THÈSE

Pour obtenir le grade de

DOCTEUR DE L'UNIVERSITÉ GRENOBLE ALPES

École doctorale : PHYS - Physique
Spécialité : Astrophysique et Milieux Dilués
Unité de recherche : Institut de Planetologie et d'Astrophysique de Grenoble

Modélisation Particle-in-cell des magnétosphères de binaires de pulsars : accélération de particules et émission électromagnétique

Particle-in-cell modeling of pulsar binary magnetospheres: particle acceleration and electromagnetic emission

Présentée par :

Valentina RICHARD--ROMEI

Direction de thèse :

Benoît CERUTTI CHARGE DE RECHERCHE HDR, CNRS DELEGATION ALPES	Directeur de thèse

Rapporteurs :

FABRICE MOTTEZ
DIRECTEUR DE RECHERCHE, CNRS ILE-DE- FRANCE MEUDON
NANDA REA
SENIOR SCIENTIST, CONSEJO SUP DE INVEST CIENTIFICAS

Thèse soutenue publiquement le **19 décembre 2025**, devant le jury composé de :

GILLES HENRI, PROFESSEUR DES UNIVERSITES, UNIVERSITE GRENOBLE ALPES	Président
FABRICE MOTTEZ, DIRECTEUR DE RECHERCHE, CNRS ILE-DE- FRANCE MEUDON	Rapporteur
NANDA REA, SENIOR SCIENTIST, CONSEJO SUP DE INVEST CIENTIFICAS	Rapporteure
CLAIRE GUEPIN, CHARGEE DE RECHERCHE, CNRS DELEGATION OCCITANIE EST	Examinatrice
LUCAS GUILLEMOT, ASTRONOME ADJOINT, OBS SCIENCES UNIVERS CENTRE VAL-DE-LOIRE	Examinateur
GUILLAUME VOISIN, CHARGE DE RECHERCHE, CNRS ILE-DE- FRANCE MEUDON	Examinateur

Acknowledgements

Ce travail marque la concrétisation de trois ans de travail de recherche, et des années d'études qui ont précédé. Je veux ici rendre hommage à toutes les personnes qui ont façonné mon chemin, de près ou de loin, dans cette quête vers le savoir, dans cette quête vers l'astrophysique.

Mon parcours universitaire a été parsemé de rencontres structurantes, parfois déterminantes. Je ne peux toutes les citer, mais je pense en particulier à Matthias González, Etienne Parizot, Jean-Noël Aqua, Guilhem Semerjian, Frédéric Chevy, Adel Bilal, Kumiko Kotera, Simon Prunet, Valentin Decoene, Claire Guépin. Merci à vous tous pour vos conseils si précieux tout au long de mon parcours et pour votre passion contagieuse pour la physique.

Benoît, tu m'as ouvert la porte d'un monde qui me faisait tant rêver : les sources astrophysiques de haute énergie. Merci pour tout ce que tu m'as appris, d'abord pour les longues réunions où tu me guidais vers la découverte et la compréhension précise des choses, puis pour celles où on tentait ensemble de résoudre des problèmes de physique. Merci également pour la relecture attentive de ce manuscrit. Et, puisque la recherche ne saurait avancer sans échanges, débats ou schémas sur des tableaux blancs, je tiens à remercier Ileyk, Benjamin, Enzo, John, Geoffroy, Gilles, Maïca, Nico, Mario, Corentin, Raphaël Duqué, Raphaël Mignon-Risse, et tous les collègues avec qui j'ai eu le plaisir de partager des discussions scientifiques. Merci également aux amis rencontrés aux Houches, qui ont rendu ces séjours d'autant plus mémorables.

Alessandro et Riccardo, collaborer avec vous à été un grand plaisir. Merci notamment à vous et à toute l'équipe des hautes énergies de l'Observatoire de Rome pour votre accueil si chaleureux, et ces semaines passées ensemble que je n'oublierai pas.

Je tiens à remercier les membres du jury pour leur présence lors de la soutenance, pour la relecture attentive du manuscrit et les discussions qui en ont découlé. Vos travaux m'ont inspirée tout au long de cette thèse, et ce fut un véritable honneur de pouvoir partager avec vous les résultats de trois années de recherche. Merci notamment à Nanda Rea et Fabrice Mottez pour avoir accepté d'être les rapporteurs de cette thèse.

Une thèse doit énormément à ceux qui concourent à créer un cadre de travail épanouissant. En ce sens, je voudrais remercier particulièrement Maïca, Nicolas, Martina et Valérie. Puis, évidemment, ceux qui ont été mes repères au laboratoire : mon acolyte Nathan; le trio du troisième étage, Juliette, Léa et Audrey; et Maxime, parti trop tôt à l'autre bout du monde. Je n'oublie pas Antoine et Valentin. Merci à vous tous pour les repas partagés, les pauses nécessaires après des heures à se battre contre un code qui ne marche pas, les soirées crêpes, le foot, les éclats de rire, les moments de doute et les moments de succès. Victor, tu as été ma famille à Grenoble, ma deuxième maison. Merci d'avoir tant partagé ensemble : les rires, les pleurs, les nombreux dîners, le sport...et même les courses à la gare. Sans oublier notre hermitage improvisé, en pleine canicule, pour rédiger.

Je suis venue seule à Grenoble, mais accompagnée de loin par nombre de personnes que j'ai la chance d'appeler amis, et qui ont illuminé ces années. En commençant par ceux de l'IAP, et notamment Clément, Aline, Maxime et Sofia; ce fut un bonheur de partager un bout de mon parcours avec vous, et un privilège de continuer à suivre vos aventures. Amis normaliens, Léo et Martin, merci pour nos discussions où on refait le monde, votre humour,

et votre compagnie pendant la rédaction. Nos escapades bretonnes où, isolés du monde, nous tentions de donner sens et cohérence à de mystérieuses équations, demeureront parmi les moments les plus excitants et stimulants que j'ai vécus. Magdy, tu as été un "parrain" pour moi, merci pour ta grande générosité. Alice, Mélina, Nico, William, Eloi, Guillaume, merci de m'avoir fait tant aimer les années universitaires, et tout ce qu'on a partagé depuis. Je ne conçois pas toutes ces années sans vous. Amis Magendiens, ce jour-là où nous découvrions les résultats du bac tous ensemble, j'avais le cœur serré à l'idée que nos chemins se séparent. Nous sommes éparpillés partout et ailleurs, mais toujours là. Merci donc à Geoffroy, Elsa, Julie, Cléa, Maïtena, Thibaut, Camille, Charlotte, Rémi. Mention spéciale à Marvin, pour avoir été mon binôme de thèse à distance, et à Elena, pour avoir partagé avec moi des moments aussi délicats que déterminants. Camille, merci d'être le frère que je n'ai jamais eu; te retrouver à Grenoble a signifié beaucoup. Sarah, un bout de notre Madrid restera toujours en moi.

Et puis il y a ces "adultes" que j'ai eu la chance de rencontrer quand j'étais petite (ou moins petite), et à qui je dois tant. Par ordre chronologique je voudrais remercier Violaine et Stéphane, Marta, Delphine, Sophie et Laurent, Philippe et Fazia, Brigitte et Thierry, Désirée et Valérie, Gilles et Kheira. Vous avez tous, d'une manière ou d'une autre, contribué à ce que j'en arrive là aujourd'hui.

Cette thèse, je la dois aussi et avant tout à ma famille. A mes grands-parents et à ma tante, qui ont été une source d'inspiration et d'admiration inégalables. À mes parents, que je ne remercierai jamais assez, pour tout ce qu'il m'ont transmis, pour avoir toujours cru en moi et attisé ma curiosité, pour leur soutien infaillible encore et toujours. Et évidemment à ma sœur, mon pilier, sans qui tout aurait beaucoup moins de sens.

Simon, merci d'avoir traversé ces années à mes côtés, malgré la distance qui nous séparait bien trop souvent. Tu as été mon plus grand soutien, ma lumière lorsque je faiblissais, le premier à célébrer mes succès. Merci pour ton approche si noble de la physique, pour ton approche si singulière de la vie : j'aime découvrir le monde à travers tes yeux et tes pensées. Et, surtout, merci pour ton amour que je ne saurais qualifier sans le limiter.

Enfin, à toi, petite Vali qui rêvais d'astrophysique, te voilà. This one is for you.

Contents

Acknowledgements ii

List of Figures vii

List of Tables x

Acronyms xi

Abstract xii

Résumé xiii

1 Introduction 1
- 1.1 Relativistic magnetospheres as sources of high-energy processes . . . 2
- 1.2 Pulsars . . . 4
  - 1.2.1 The discovery of pulsating neutron stars . . . 4
  - 1.2.2 Multi-wavelength emission . . . 5
  - 1.2.3 Classes of pulsars . . . 6
- 1.3 Gamma-ray pulsars . . . 8
  - 1.3.1 The *Fermi*-LAT revolution . . . 9
  - 1.3.2 Observational signatures . . . 9
- 1.4 Pulsars in binaries . . . 11
- 1.5 Objectives and outline of the thesis . . . 12

2 Theory of pulsar magnetospheres 13
- 2.1 Orders of magnitude . . . 14
- 2.2 Magnetospheric plasma properties and MHD waves . . . 15
- 2.3 Electrodynamics of pulsar magnetospheres . . . 17
  - 2.3.1 Unipolar inductor model and vacuum solution . . . 18
  - 2.3.2 Goldreich-Julian model and electrosphere . . . 19
  - 2.3.3 Force-free model: plasma-filled magnetosphere . . . 21
  - 2.3.4 Current understanding of pulsar magnetospheres . . . 28
- 2.4 Particle acceleration in the current sheet . . . 33
  - 2.4.1 Relativistic generalized Ohm's law in the collisionless limit . . . 33
  - 2.4.2 Magnetic reconnection . . . 33
  - 2.4.3 Instabilities in the current sheet . . . 34
  - 2.4.4 Particles spectrum . . . 35
- 2.5 Synchrotron-curvature radiation . . . 35
  - 2.5.1 Radiation reaction force . . . 37
  - 2.5.2 Effective perpendicular magnetic field . . . 38
  - 2.5.3 Radiation power . . . 39
  - 2.5.4 Power spectrum . . . 40

2.5.5 Curvature radiation 41

3 Numerical methods **43**
3.1 Motivation for PIC simulations 44
3.2 PIC principles 45
3.3 `Zeltron` code 46
3.3.1 PIC algorithm 46
3.3.2 Treatment of divergence constraints 50
3.3.3 Temporal and spatial resolutions 51
3.3.4 Parallelization 51
3.4 Global PIC simulations of pulsar magnetospheres 52
3.4.1 Rescaling 52
3.4.2 Spherical grid 53
3.4.3 Boundary conditions 53
3.4.4 Radiation modeling 54

4 Pulsar wind - companion interaction **57**
4.1 Astrophysical motivations 58
4.2 Numerical model 58
4.2.1 2D equatorial setup 58
4.2.2 Companion implementation 61
4.2.3 Orbital-modulated light curves 62
4.2.4 Parametric study to probe different regimes 63
4.3 Reference case: isolated pulsar magnetosphere 64
4.3.1 Stationary solution 64
4.3.2 Key physical properties 66
4.4 Pulsar-companion interaction 67
4.4.1 Global dynamics 67
4.4.2 Particle kinetics 69
4.4.3 High-energy electromagnetic signature 73
4.5 Radio counterparts 75
4.5.1 Radio waves from relativistic magnetic reconnection 75
4.5.2 Additional wave generation triggered by the companion 79
4.5.3 A source of (periodic) radio transients 79
4.6 Discussion and conclusion 83

5 Pulsar wind - disk interaction: application to transitional millisecond pulsars **85**
5.1 Transitional millisecond pulsars (tMSPs) 86
5.1.1 Bridging the gap between radio and accreting MSPs 86
5.1.2 The population of tMSPs 88
5.1.3 The three states of tMSPs 90
5.1.4 Optical and X-ray pulsations from PSR J1023+0038 in the sub-luminous disk state 91
5.2 Existing models in the literature 93
5.2.1 Phenomenological models of X-ray and optical pulses 93
5.2.2 Numerical simulations of disk–magnetosphere interaction 94
5.3 Our numerical model 94
5.3.1 3D setup of the pulsar magnetosphere 94
5.3.2 Disk implementation 98
5.3.3 Parametric study: different magnetic obliquities 99
5.4 Structure of the magnetosphere in the presence of the disk 100

5.4.1 Global structure . . . 102
5.4.2 Particle acceleration . . . 106
5.4.3 Plasma isotropization . . . 107
5.5 Synchrotron emission . . . 108
5.5.1 Increase of the synchrotron emission due to the disk . . . 108
5.5.2 Light curves . . . 110
5.5.3 Polarization properties . . . 113
5.6 Discussion and conclusion . . . 119

6 Towards pulsar–black hole simulations **122**
6.1 Electromagnetic precursors to neutron star mergers . . . 123
6.1.1 Observations of neutron star mergers . . . 123
6.1.2 Precursor radiative signatures . . . 124
6.1.3 The special case of black hole–neutron star binaries . . . 124
6.2 Existing models and key predictions . . . 125
6.3 Off-center pulsar on a spherical grid . . . 126
6.3.1 Electromagnetic fields implementation . . . 126
6.3.2 Particles injection . . . 128
6.4 Next steps towards binary implementation . . . 130

Conclusion and perspectives **131**

Bibliography **136**

Résumé de la thèse en français **159**

List of Figures

1.1 Examples of high-energy phenomena . . . 3
1.2 Sketch of the pulsar magnetosphere with associated light curves . . . 5
1.3 P–$\dot{P}$ diagram . . . 7
1.4 Gamma-ray luminosity as a function of the spin-down power . . . 8
1.5 SED of the Vela pulsar . . . 9
1.6 Gamma-ray light-curve of the Vela pulsar . . . 10
1.7 Gamma-ray light-curves depending on the viewing angle . . . 10

2.1 Sketch of the three main zones of the pulsar environment . . . 17
2.2 Charge distribution for the electrosphere configuration . . . 20
2.3 Split monopole solution . . . 26
2.4 Sketch of the aligned pulsar magnetospheric structure . . . 27
2.5 3D PIC simulation of the pulsar magnetosphere and inner part of the wind . . . 28
2.6 Sketch of the magnetosphere's open zone . . . 29
2.7 Sketch of a pair cascade in the polar cap . . . 31
2.8 Sketch of a magnetic X-point . . . 33
2.9 2D local PIC simulation of the reconnecting current sheet . . . 35
2.10 Instabilities in a 3D PIC simulation of the global pulsar magnetosphere . . . 36
2.11 Nonthermal particle energy spectrum generated by relativistic magnetic reconnection . . . 36
2.12 Sketch of a charged particle's motion in a uniform magnetic field . . . 39
2.13 Sketch of the angular distribution of radiation from a charged particle moving along the x-axis and accelerated perpendicularly . . . 41
2.14 Superposition of individual particles spectra producing a power-law spectrum . . . 42

3.1 Illustration of the PIC computational domain . . . 45
3.2 Illustration of the three main steps performed at each PIC timestep . . . 46
3.3 Illustration of the leapfrog integration scheme . . . 47
3.4 Illustration of the area-weighting scheme . . . 48
3.5 Illustration of the Yee algorithm . . . 50
3.6 Illustration of the spherical Yee mesh in 2D and 3D . . . 53
3.7 Sketch of the geometrical quantities used to compute light curves . . . 55

4.1 Initial numerical configuration for the pulsar wind - spherical companion interaction . . . 59
4.2 Geometrical structure of the current sheet in 3D and in the 2D equatorial plane 62
4.3 3D illustration of the eclipses implemented in our code . . . 63
4.4 Definition of the fast magnetosonic radius . . . 64
4.5 Illustration of the companion separations and sizes used in the parametric study 65
4.6 Temporal evolution of the outgoing Poynting flux . . . 65
4.7 Snapshot from the isolated pulsar simulation . . . 66
4.8 Averaged wind bulk Lorentz factor $\Gamma_{\rm wind}$, for each simulation . . . 68

4.9 Relationship between the measured opening angle of the shock cone and the Alfvénic Mach number . . . 69
4.10 Snapshot of a simulation including a companion settled outside the fast magnetosonic surface . . . 70
4.11 Snapshot of a simulation including a companion settled within the fast magnetosonic surface . . . 71
4.12 Successive maps of the synchrotron power at the companion's surface . . . 72
4.13 Radial profiles of electromagnetic energy fluxes and particle energy fluxes . . . 72
4.14 Averaged particle energy spectra and their spatial decomposition . . . 73
4.15 Averaged synchrotron spectra and their spatial decomposition . . . 74
4.16 High-energy synchrotron light curves . . . 75
4.17 Light curve characteristics as a function of the pulsar-companion separation . . . 76
4.18 Radio emission from a local 2D PIC simulation of the pulsar striped wind . . . 78
4.19 Radio emission from a global 2D PIC simulation of the pulsar striped wind . . . 78
4.20 Emission of fast magnetosonic modes in the wake of the companion . . . 80
4.21 Phase-space diagram of radio transients . . . 81
4.22 P–$\dot{P}$ including the first discovered LPTs . . . 82

5.1 Illustration of the recycling scenario in the P–$\dot{P}$ diagram . . . 86
5.2 Millisecond pulsar binaries as a function of orbital period and median donor mass . . . 87
5.3 Temporal evolution of the three confirmed tMSPS across their different states . . . 88
5.4 X-ray and optical light curves of PSR J1023+0038. . . . 91
5.5 Pulse profiles of PSR J1023+0038 as a function of the pulsar spin phase . . . 92
5.6 SED of the total and pulsed emission from PSR J1023+0038 during the high mode . . . 92
5.7 3D spherical numerical setup for the pulsar wind - disk interaction . . . 97
5.8 Sketch of the simulation setup including the disk . . . 98
5.9 Tests on the disk's boundary conditions . . . 100
5.10 3D density of isolated pulsar magnetospheres, for different magnetic obliquities 101
5.11 Temporal evolution of the outgoing Poynting flux . . . 102
5.12 3D particles density of the pulsar magnetosphere with and without the disk . . . 103
5.13 3D particles density of the pulsar's magnetosphere interacting with the disk . . . 104
5.14 Time evolution of the net outgoing Poynting flux L/L_0 and the particle density 105
5.15 2D poloidal maps of the plasma density for each magnetic obliquity . . . 106
5.16 2D equatorial map of the plasma density density . . . 107
5.17 3D rendering of the magnetic field strength . . . 107
5.18 2D maps of the magnetic field strength . . . 108
5.19 2D poloidal map of the mean Lorentz factor of particles . . . 108
5.20 2D poloidal maps of the plasma isotropization . . . 109
5.21 2D maps of the isotropic synchrotron power . . . 110
5.22 Temporal evolution of the synchrotron emission maps in the presence of the disk 111
5.23 Skymaps and associated light curves, for all simulations . . . 112
5.24 Synchrotron spectrum and frequency binning . . . 113
5.25 Skymaps and light curves for different energy bins . . . 113
5.26 Light curves for different energy bins, evaluated at the viewing angle of PSR J1023+0038 114
5.27 Reference skymaps of polarization angle and degree . . . 115
5.28 Skymaps of the polarization degree in the presence of the disk . . . 115
5.29 Skymaps of the polarization angle in the presence of the disk . . . 116
5.30 Skymaps of the polarization degree as a function of energy . . . 117
5.31 Skymaps of the polarization angle as a function of energy . . . 117

5.32 Polarization angle and degree for different energy bins, evaluated at the viewing angle of PSR J1023+0038 118
5.33 Synchrotron emission properties as a function of the magnetic obliquity 118
5.34 Energy dependence of the X-ray polarization properties measured from PSR J1023+0038 120
5.35 Measured polarization angle of PSR J1023+0038 in the high mode, as a function of the rotational phase 121

6.1 Successive phases of a neutron star merger 123
6.2 First general-relativistic MHD simulations of black hole–neutron star binaries . 125
6.3 Initial numerical configuration for the offset pulsar 127
6.4 Fields and particles maps from the offset pulsar configuration 129
6.5 Field maps of close pulsar binary systems, for different rotational regimes . . . 134

List of Tables

2.1 Typical orders of magnitude for pulsars. 15

4.1 Simulation parameters for the pulsar wind - spherical companion interaction . . 61
4.2 Labeling of each simulation involving a companion, with its corresponding parameters 63

5.1 Simulation parameters for the pulsar wind - disk interaction 97
5.2 Summary table of the various simulations for the pulsar wind - disk interaction 99

Acronyms

AGN Active Galactic Nucleus

AMXP Accreting millisecond pulsar

CFL Courant-Friedrichs-Lewy

FRB Fast radio bursts

FDTD Finite-difference time domain

LOFAR LOw Frequency ARray

LPT Long-period radio transients

MHD Magnetohydrodynamics

MSP Millisecond pulsar

PIC Particle-in-cell

RRAT Rotating radio transient

SKA Square Kilometre Array

tMSP transitional millisecond pulsar

Abstract

The 21st century has witnessed the advent of multi-messenger astronomy, accompanied by the development of ever more advanced telescopes, thereby offering new opportunities to probe the most energetic phenomena of the universe. These advances have emphasized the central role of relativistic magnetospheres in powering high-energy astrophysical processes. Pulsar magnetospheres are the archetype of relativistic magnetospheres, as they combine relativistic effects, strong magnetic fields, and rapid rotation around a compact object. Significant progress in modeling such systems has been made over the past decades, primarily driven by numerical methods made possible by high-performance computing. In particular, the particle-in-cell (PIC) approach, due to its ability to simulate plasma kinetic processes from first principles, has emerged as the predominant tool for studying particle acceleration and high-energy emission in such environments. While many studies have focused on modeling isolated pulsar winds, pulsars in binary systems remain largely unexplored, despite representing a significant fraction of the pulsar population. This thesis investigates three distinct categories of pulsar binaries through PIC simulations. I present 2D simulations of the pulsar magnetosphere and its wind interacting with an unmagnetized spherical companion. The results reveal that the presence of the companion triggers enhanced particle acceleration and high-energy radiation in the form of an orbitally modulated hollow cone, possibly associated with long-period radio counterparts. Then, I investigate, via 3D simulations, the interaction between a pulsar wind and a disk. I demonstrate that the presence of the disk significantly enhances high-energy emission, modifies polarization signatures, and broadens the light-curve pulses, which appear as either single or double per pulsar spin period depending on the pulsar's magnetic obliquity. These results successfully reproduce the main features of the optical and X-ray pulsed emission observed from the transitional millisecond pulsar J1023+0028. Finally, I initiate the development of a new setup with the `Zeltron` PIC code, aimed at performing the first 3D PIC simulation of a black hole-neutron star binary.

Résumé

Le XXIe siècle a marqué l'avènement de l'astronomie multi-messagers, accompagné du développement de télescopes toujours plus performants, ouvrant ainsi de nouvelles perspectives pour sonder les phénomènes les plus énergétiques de l'univers. Ces avancées ont mis en évidence le rôle central des magnétosphères relativistes dans les processus astrophysiques de haute énergie. Les magnétosphères de pulsars, qui combinent effets relativistes, champs magnétiques intenses et rotation rapide autour d'un objet compact, en sont l'archétype. Des progrès significatifs dans la modélisation de tels systèmes ont été réalisés au cours des dernières décennies, principalement grâce aux méthodes numériques rendues possibles par le calcul haute performance. En particulier, l'approche "Particle-in-cell" (PIC), par sa capacité à simuler les processus cinétiques du plasma à partir de principes fondamentaux, s'est imposée comme l'outil prédominant pour étudier l'accélération de particules et l'émission de haute énergie dans de tels environnements. Alors que de nombreuses études se sont concentrées sur la modélisation des vents de pulsars isolés, les pulsars en systèmes binaires restent largement inexplorés, malgré leur proportion significative dans la population de pulsars. Cette thèse explore trois catégories distinctes de binaires de pulsars à travers des simulations PIC. Je présente des simulations 2D de la magnétosphère d'un pulsar et de son vent en interaction avec un compagnon sphérique non magnétisé. Les résultats montrent que la présence du compagnon induit une augmentation de l'accélération de particules et de l'émission de haute énergie sous la forme d'un cône creux modulé par la période orbitale, avec de possibles contreparties radio associées. J'étudie ensuite, via des simulations 3D, l'interaction entre le vent d'un pulsar et un disque. Je montre que la présence du disque renforce significativement l'émission de haute énergie, modifie sa polarisation et élargit les pulsations dans les courbes de lumière. Je prédis l'émission d'une ou deux pulsations par période de rotation du pulsar, selon l'obliquité magnétique du pulsar. Ces résultats reproduisent avec succès les principales caractéristiques de l'émission pulsée optique et X observée pour le pulsar milliseconde transitionnel J1023+0028. Enfin, j'initie le développement d'une nouvelle configuration du code PIC `Zeltron`, destinée à réaliser la première simulation PIC 3D d'un système binaire trou noir–étoile à neutrons.

Chapter 1

Introduction

Contents

1.1 Relativistic magnetospheres as sources of high-energy processes . . . 2
1.2 Pulsars . . . 4
1.2.1 The discovery of pulsating neutron stars . . . 4
1.2.2 Multi-wavelength emission . . . 5
1.2.3 Classes of pulsars . . . 6
1.3 Gamma-ray pulsars . . . 8
1.3.1 The *Fermi*-LAT revolution . . . 9
1.3.2 Observational signatures . . . 9
1.4 Pulsars in binaries . . . 11
1.5 Objectives and outline of the thesis . . . 12

1.1 Relativistic magnetospheres as sources of high-energy processes

A variety of high-energy phenomena are observed across the Universe and play a central role in the recent advent of multi-messenger astronomy, as they often combine several of the four "messengers" that bring us information from the sky, namely electromagnetic signals, cosmic rays (mostly nuclei and protons propagating through space), neutrinos and gravitational waves. Most high-energy phenomena originate from extremely compact objects or from processes associated with them. White dwarfs, neutron stars and black holes form what we refer to as compact objects, listed here in order of increasing compactness, which reflects the intensity of their gravitational fields. They all represent final stages of stellar evolution, depending on the mass of their progenitor star prior to gravitational collapse, although they can also form through the merger of less compact objects; for instance, the coalescence of two white dwarfs can produce a neutron star, while the merger of white dwarfs or neutron stars can lead to the formation of a black hole.

The interplay of (general-)relativistic effects, strong magnetic fields, and rapid rotation gives rise to relativistic magnetospheres around compact objects. These magnetospheres are relativistic in several respects: they can power highly magnetized relativistic outflows (e.g., relativistic winds or collimated jets), evolve under general-relativistic effects, trigger pair creation, and efficiently accelerate particles, which in turn leads to the emission of non-thermal radiation. Neutron stars naturally combine all these ingredients and thus provide the canonical environments for such magnetospheres. White dwarfs, in contrast, may host strong magnetic fields, but these are typically weaker than those of neutron stars, and their slower rotation rates yield magnetospheres that are essentially non-relativistic. Black holes do not possess intrinsic magnetic fields; however, they can develop an induced relativistic magnetosphere when immersed in an external magnetic field and plasma, for example supplied by an accretion disk or a relativistic wind.

The high-energy phenomena involving relativistic magnetospheres can be classified into three main classes. The most evident ones are those induced by pure magnetospheric processes. Among the most significant examples are pulsars, i.e., rapidly rotating neutron stars emitting periodic pulses of radiation and producing strong relativistic winds. These winds can inflate pulsar wind nebulae – clouds of gas and dust, often appearing as diffuse, glowing regions – such as the Crab Nebula (Weekes et al., 1989). They are also sources of transient phenomena, such as giant radio pulses (Cognard et al., 1996), glitches (i.e., sudden spin-up events; Haskell and Melatos 2015) or pulsar nulling (i.e., sudden drops in the pulse intensity; Backer 1970), and are possible cosmic-rays accelerators, as investigated in Guépin et al. (2020). Other systems emblematic of magnetospheric activity are magnetars (see Figure 1.1), super-magnetized neutron stars that occasionally generate giant flares and outbursts (Coti Zelati et al., 2018). Magnetars (and, to a lesser extent, pulsar magnetospheres) have also been proposed as sources of fast radio bursts (FRBs; Lorimer et al. 2007), brief but extremely energetic pulses of radio waves. An emerging class of long-period radio transients (Hurley-Walker et al., 2022, 2023) – sources of radio pulses with periodicities from minutes to hours, sometimes accompanied by higher-energy counterparts (Anumarlapudi et al., 2025) – are most likely associated with pulsars, magnetars, or white dwarfs, either isolated or in binaries (e.g., Hurley-Walker et al. 2024; de Ruiter et al. 2025).

Accretion may also reveal or even foster magnetospheric activity. A striking example is provided by active galactic nuclei (AGN; see Figure 1.1), accreting supermassive black holes hosted at the center of galaxies. These are the most luminous persistent sources of electromagnetic radiation in the universe, with M87* and Sagittarius A* being the most prominent examples (Event Horizon Telescope Collaboration et al., 2019, 2022). Some of these black hole magnetospheres may launch highly-collimated, relativistic jets (Blandford



Figure 1.1: Conceptual representation of high-energy phenomena. *Left panel:* magnetar, with its magnetic field lines; credit: M. Rebisz. *Middle panel:* AGN, with the supermassive black hole at the center, the accretion disk and the relativistic jet; credit: ESO/M. Kornmesser. *Right panel:* neutron star binary merger; credit: NASA's Goddard Space Flight Center.

and Znajek, 1977), referred to as blazars when pointing towards the Earth. These jets are important sites of particle acceleration and radiation, promising candidates for ultra-high-energy cosmic rays, and can be associated to neutrino emission, as shown by the joint detection of a neutrino event with a blazar flare (IceCube Collaboration et al., 2018). Moreover, tidal disruption events, characterized by the disruption of stars or white dwarfs by supermassive black holes, couple transient accretion and magnetospheric activity, sometimes culminating in the ejection of relativistic jets. These are other promising sources of ultra-high-energy cosmic rays (Guépin et al., 2018) and of high-energy neutrinos (Stein et al., 2021). Lastly, X-ray binaries, which consist of a donor star and a compact-object accretor, emit intense X-ray radiation powered by accretion and are governed by the accretor's magnetosphere, which drives a broad range of phenomena: the magnetosphere can channel matter onto the magnetic poles or instead inhibit accretion, as in transitional millisecond pulsars (Papitto and Martino, 2021); it can produce X-ray pulsations, as observed in X-ray pulsars (XRPs) and ultra-luminous X-ray pulsars (ULXs); and can even trigger flares. Some X-ray binaries also produce accretion-powered relativistic jets, analogous to jets from AGN, but operating at comparatively lower power; such systems are referred to as microquasars and may serve as sources of high-energy galactic cosmic rays and neutrinos (Kaci et al., 2025).

Gravitational collapse and mergers of compact objects gather another category of magnetosphere-influenced processes. Core-collapse supernovae, powerful stellar explosions caused by the collapse of a massive star's core, are major contributors to Galactic cosmic rays and neutrinos. They include magnetorotational supernovae (Akiyama et al., 2003) and magnetar-powered supernovae (Kasen and Bildsten, 2010), both of which can be strongly influenced by the involved relativistic magnetospheres. In these events, magnetosphere-driven jets and outflows may be launched, and gravitational waves can also be emitted, with their properties potentially modulated by magnetospheric effects. According to the well-established collapsar scenario (MacFadyen and Woosley, 1999), a subset of core-collapse supernovae leads to the formation of a black hole surrounded by an accretion disk, which can power relativistic jets through magnetospheric activity, ultimately producing long gamma-ray bursts. These jets are also potential sources of ultra-high-energy cosmic rays and high-energy neutrinos. Similarly, mergers of compact objects (see Figure 1.1) trigger gravitational waves and post-coalescence electromagnetic signals, including short gamma-ray bursts, which may be associated with ultra-high-energy cosmic rays. Mergers involving at least one neutron star that result in a black hole can form transient magnetospheres which decay over time, as shown by Bransgrove et al. (2021). Precursor electromagnetic emissions arising from the interaction of binary magnetospheres are also predicted, although they have not yet been detected (Most and Philippov, 2020, 2023; Carrasco and Shibata, 2020; Carrasco et al., 2021).

Consequently, describing these high-energy phenomena and their associated processes requires a thorough understanding of the environments surrounding compact objects. Beyond the scope of high-energy astrophysics, these systems constitute excellent laboratories for extreme physics, enabling the study of strong gravity, relativistic and highly magnetized plasmas,

thereby highlighting their relevance across several theoretical domains of physics.

While astrophysical observations in previous centuries were largely limited to electromagnetic signals, first in the optical band and gradually extending across the multi-wavelength spectrum (radio, infrared, UV, X-rays, gamma-rays), the 21st century has witnessed the rise of multi-messenger astronomy, in which instruments can observe and combine different messengers from the same astrophysical event. Indeed, the past two decades have seen the first simultaneous detections of multiple messengers from a single event, such as the gravitational-wave event GW170817 (Abbott et al., 2017) accompanied by electromagnetic radiation, or the association of a high-energy neutrino with the blazar TXS 0506+056 (IceCube Collaboration et al., 2018). This new era has been enabled not only by the development of detectors for cosmic rays, neutrinos, and gravitational waves, but also by major advances in instrumentation for electromagnetic detection, including improvements in sensitivity, timing accuracy, spectral coverage, spatial and spectral resolution, and polarization measurements.

These observational advances have naturally led to an increased need for theoretical studies, aimed at deciphering the detected signals. Significant advances in modeling have been achieved over the past decades, primarily driven by the growing power of numerical approaches, which make it possible to overcome the strong limitations of purely analytical methods. Indeed, the increase in computational resources, driven by the rapid progress of high-performance computing, together with the development of advanced numerical methods– such as relativistic magnetohydrodynamics (MHD) and particle-in-cell (PIC) codes or adaptive mesh refinement–has enabled the study of increasingly sophisticated problems, including fully 3D, non-linear, relativistic, and multi-scale ones. As a result, numerical simulations have become a predominant tool for both the prediction and interpretation of astrophysical observations. As will be explained in the following, particle-in-cell simulations have gradually emerged as a crucial tool in high-energy astrophysics, as they can capture non-thermal phenomena that drive particle acceleration and high-energy radiation, producing the most energetic components of the observed spectra.

1.2 Pulsars

Pulsar magnetospheres encompass a wide range of the phenomena introduced previously and are considered the canonical case of relativistic magnetospheres. They are of particular interest as they combine extreme magnetic fields, rapid rotation, and relativistic plasma dynamics, making them ideal environments to investigate fundamental processes such as particle acceleration and electromagnetic radiation, especially at high energies.

1.2.1 The discovery of pulsating neutron stars

Neutron stars were hypothesized in 1934 by Baade and Zwicky, almost two years after the discovery of the neutron, as reported in Baade and Zwicky (1934)[1]:

> *"With all reserve we advance the view that a super-nova represents the transition of an ordinary star into a neutron star, consisting mainly of neutrons. Such a star may possess a very small radius and an extremely high density. As neutrons can be packed much more closely than ordinary nuclei and electrons, the 'gravitational packing' energy in a cold neutron star may become very large, and, under certain circumstances, may far exceed the ordinary nuclear packing fractions. A neutron star would therefore represent the most stable configuration of matter as such."*

[1] We note that Landau (1932) anticipated the existence of extremely dense stars resembling neutron stars, although previous to the discovery of neutrons (see Yakovlev et al. 2013 for a discussion).

Neutron stars long remained a theoretical concept, primarily motivating studies of their equation of state, which predicted extremely small radii on the order of ten kilometers, thereby disfavoring the prospect of thermal detection. Progress accelerated in the 1960s, when the center of the Crab Nebula was identified as a highly magnetized neutron star. Building on this, Pacini (1967) suggested that a rapidly rotating, magnetized neutron star would emit radiation and proposed that this mechanism could power the nebula itself. That same year, Jocelyn Bell Burnell, then a PhD student under the supervision of Antony Hewish, serendipitously discovered the first pulsating neutron star – hence named "pulsar" – a source emitting extremely short periodic ($P = 1.33$ s) radio pulses with exceptional, and at first disconcerting, stability (Hewish et al., 1968). In the wake of this discovery, Gold (1968) proposed a model for pulsars, consisting of a rapidly rotating, magnetized neutron star that powers beams of radiation from magnetic poles misaligned with the rotation axis, thereby extracting rotational energy from the star. This model naturally explained the pulsed pattern as resulting from the periodic sweep of the radiation beams across the sky, commonly referred to as the "lighthouse effect." Gold's model was soon supported by the discovery of pulsars, identified in the Vela (Large et al., 1968) and Crab (Staelin and Reifenstein, 1968) supernova remnants, thereby confirming supernovae as the birthplaces of neutron stars, as originally predicted by Baade and Zwicky (1934). The joint measurement of the Crab pulsar's spin and spindown, interpreted in light of this model, ultimately established the connection between pulsars and neutron stars.

1.2.2 Multi-wavelength emission

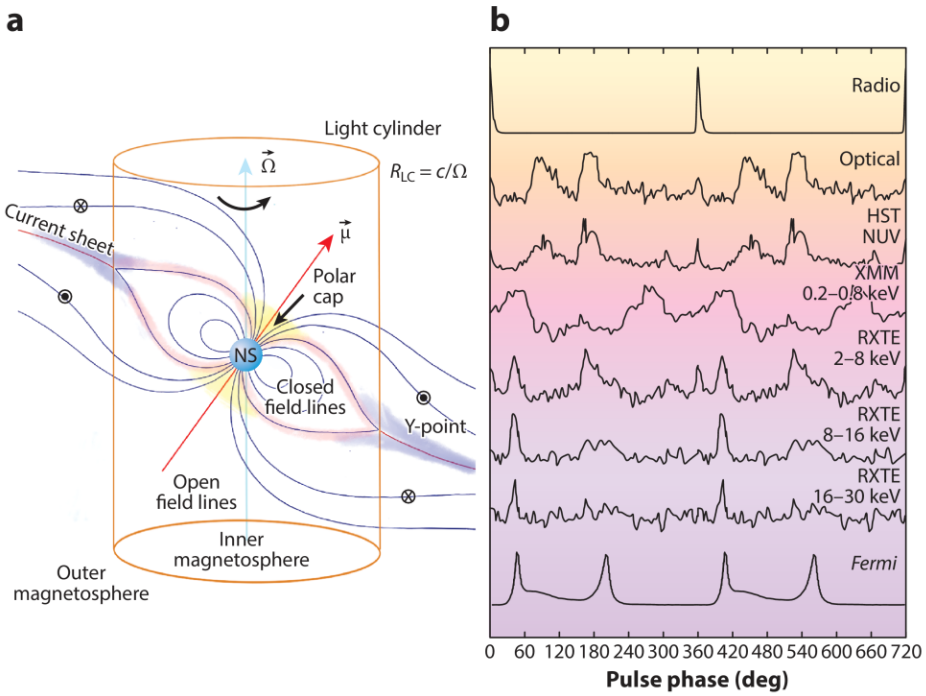

Figure 1.2: Schematic representation of the pulsar magnetosphere, with the associated electromagnetic light curves of the Vela pulsar. The magnetospheric regions responsible for radiation are highlighted on panel (a) with different colors depending on the corresponding electromagnetic frequencies shown in panel (b). We note that this is a highly simplified view of the emission regions, which will be discussed more thoroughly in the next chapter. Figure taken from Philippov and Kramer (2022).

To date, over 4000 pulsars have been discovered[2]. Although initially dicovered via radio pulses, their magnetosphere was progressively found to emit across the entire electromagnetic spectrum. The magnetospheric regions responsible for radiation are different depending on the emitted frequency (Figure 1.2), reflecting distinct emission processes. Indeed, while radio emission is thought to primarily originate from the polar cap regions near the star surface (although the current sheet also represents a secondary emitting region, as thouroughly described in Chapter 4), high-energy radiation is predominantly emitted from the outer magnetospheric regions.

1.2.3 Classes of pulsars

Although all pulsars share a common set of observational properties, the growing number discovered over time has revealed fundamental characteristics that distinguish them. The P–$\dot{P}$ diagram is a widely used tool for classifying the pulsar population based on the spin period P and its derivative $\dot{P}$, as shown in Figure 1.3. First, pulsars are divided into a set of young pulsars (sometimes referred to as "classical" pulsars) with typical periods of ~ 0.6 s and magnetic fields of $\sim 10^{12}$ G, often found in supernova remnants, and a set of older pulsars with millisecond periods and $\sim 10^{8}$ G magnetic fields, discovered later (Backer et al., 1982) and called "recycled pulsars" owing to their spin-up through the accretion of angular momentum from a companion star (lower-left region of the P–$\dot{P}$ diagram)[3]. Millisecond pulsars represent about 10% of the known pulsar population.

Neutron stars are also commonly classified based on their main source of radiation, which reflects the star's fundamental characteristics (the classes introduced below are represented in Figure 1.3):

- Rotation-powered pulsars: most pulsars are rotation-powered, meaning that they mainly owe their emission to the extraction of rotational energy from the star. Magnetospheric torques on the star surface spin down the star and allow for the extraction of Poynting flux, which is in turn converted into particle acceleration, pair creation, and electromagnetic emission, from radio to gamma-rays. Although most pulsars emit in the radio band, few pulsars have been detected in the optical band, about 100 in the X-ray band (combining a hot thermal contribution from the polar caps with the non-thermal magnetospheric signal), and about 300 in the gamma-ray band (see Philippov and Kramer 2022; Smith et al. 2023). Some pulsars, called "rotating radio transients" (RRATs), are detected only sporadically, although the periodic patterns found in their detections indicate an underlying radio pulsar source (see Chapter 4). Rotation-powered pulsars are found both among young pulsars and among millisecond pulsars, the latter most often residing in binary systems.

- Magnetically-powered pulsars: magnetars, a class of ~ 30 extremely magnetized neutron stars, usually rotating slower than the classical young pulsars, have also been linked to the radio pulsar population, following the first detection of transient radio pulsations from a magnetar (Camilo et al., 2006). They exhibit persistent X-ray luminosities ranging from $\sim 10^{31}$ to $\sim 10^{35}$ erg s^{-1}, typically exceeding their rotational energy loss rate, and attributed to thermal emission as the stellar surface is heated by the magnetic field decay in the crust (Rea and De Grandis, 2025). Magnetars also power X-ray and gamma-ray flares and outbursts. The decay and reconfiguration of their intense magnetic fields, reaching up to $\sim 10^{15}$ G and representing an enormous magnetic energy reservoir, are the leading mechanisms proposed to explain these emissions (Esposito et al., 2021).

[2] An up-to-date database of pulsars can be found in the Australia Telescope National Facility Pulsar Catalogue https://www.atnf.csiro.au/research/pulsar/psrcat/ (Manchester et al., 2005).

[3] We note that white dwarf collapsing due to accretion could also form millisecond pulsars (Gautam et al., 2022).

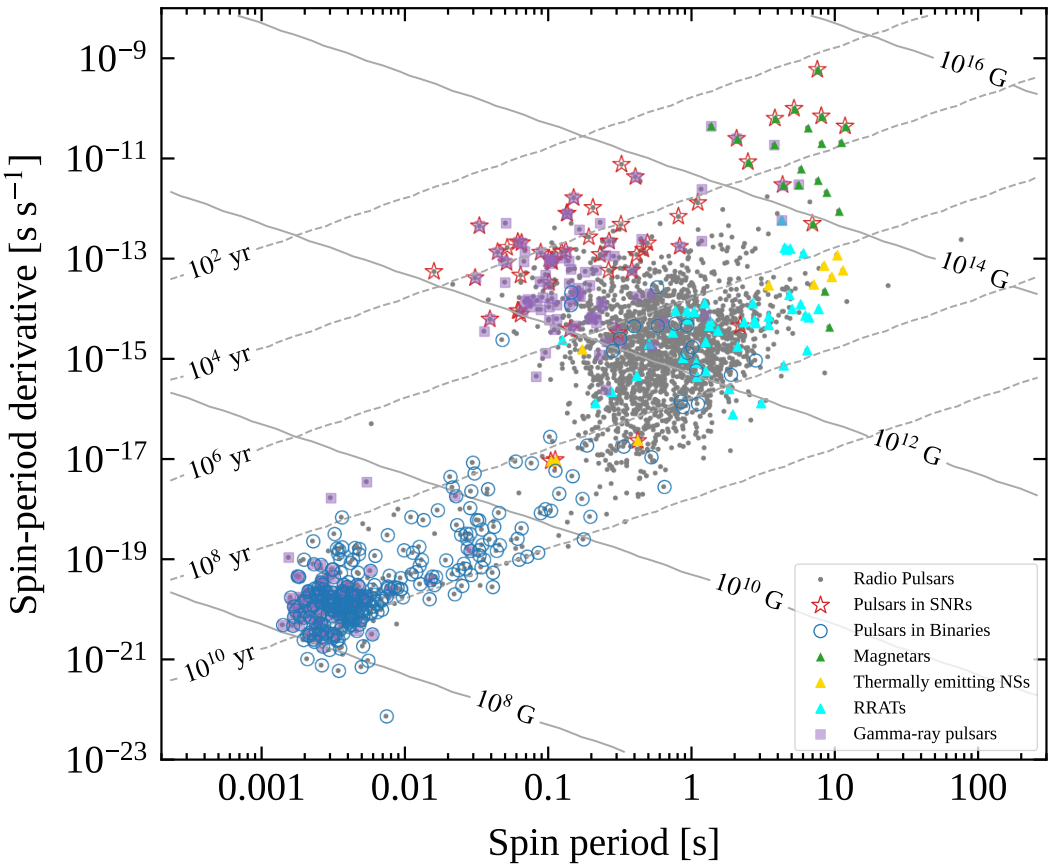

Figure 1.3: P–$\dot{P}$ diagram representing the main pulsar classes. The labels SNRs, NSs, and RRATs respectively denote supernova remnants, neutron stars and rotating radio transients. Millisecond pulsars lie in the lower left part of the diagram. The solid lines trace constant surface magnetic field at the poles, computed by assuming that the spin-down is due to dipolar losses. Dashed lines mark constant characteristic age (see Smith et al. 2023 for calculation details). Figure taken from Ronchi (2024).

- Accretion-powered pulsars: some pulsars involved in binary systems owe their emission to the release of gravitational binding energy as matter from the companion star is channeled onto the surface of the neutron star. Accretion-powered pulsars emit predominantly in X-rays, hence their common designation as "X-ray pulsars." While radio pulsations are generally quenched by accretion, these pulsars can also be associated with emission at other wavelengths (optical, UV, IR, gamma rays), though such emission usually originates from the disk, companion, or jets. Some peculiar millisecond pulsars, referred to as "transitional millisecond pulsars," have been observed to switch between accretion-powered and rotation-powered states over time (see Chapter 5).

- Thermally-powered pulsars: the internal heat of the neutron star can also serve as a primary source of radiation. This is the case for young pulsars cooling over $\sim 10^5$ years after formation, or for older pulsars reheated by external sources, typically via accretion.

1.3 Gamma-ray pulsars

This thesis primarily focuses on gamma-ray pulsars, which to date have all been detected as rotation-powered. While pulsars were historically identified through their radio emission, the majority of their radiative power is emitted in gamma rays. Indeed, 1% to 100% of their spin-down power is radiated in gamma-rays above 100 MeV (see Figure 1.4), compared to less than 10^{-6} for the radio emission (Cerutti et al., 2025). Modeling this gamma-ray emission therefore amounts to unveiling the main dissipative processes that drive high-energy phenomena, such as particle acceleration and radiation, while also providing valuable insights into the global structure and dynamics of pulsar magnetospheres.

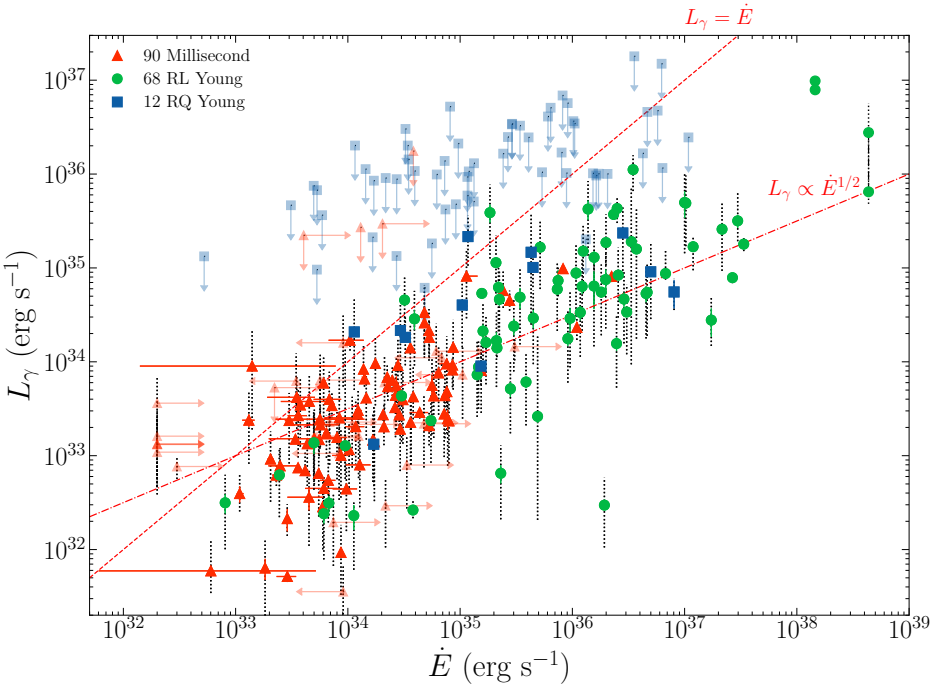

Figure 1.4: Gamma-ray luminosity L_γ (100MeV-100GeV band) as a function of the spin-down power $\dot{E}$. RL and RQ abbreviations respectively correspond to radio loud and radio quiet. Light-color points mark upper limits. Figure taken from Smith et al. 2023.

1.3.1 The *Fermi*-LAT revolution

Earth's atmosphere is opaque to gamma rays, preventing their direct detection from the ground and necessitating the use of space-based telescopes. Only the most energetic gamma rays (e.g., at TeV energies) can be detected indirectly from the ground, through Cherenkov light emitted by the extensive air showers they generate when interacting with the Earth's atmosphere.

The *Fermi* gamma-ray space telescope, launched in 2008, is the first gamma-ray telescope performing all-sky surveys each day and the most sensitive gamma-ray telescope on orbit. It aims at detecting astrophysical and cosmological phenomena ranging from solar flares, pulsars and AGN, to gamma-ray bursts, cosmic rays and dark matter. The Large Area Telescope (LAT; Atwood et al. 2009), operating in the 20 MeV - 1 TeV energy band, is the primary instrument on board the *Fermi* Gamma-ray Space Telescope. Before its launch, less than a dozen gamma-ray pulsars had been detected with high confidence. The *Fermi*-LAT telescope has revolutionized the study of high-energy gamma-ray sources. The latest released catalog (4FGL-DR4; Ballet et al. 2024) contains more than 7000 sources, among which pulsars are the largest class of Galactic gamma-ray sources. A specific pulsar catalog based on 12 years observational data (the Third Pulsar Catalog; Smith et al. 2023) reports $\sim$ 300 gamma-ray pulsars and about 45 candidates, which in total accounts for 10% of all known pulsars, and many more are expected, as suggested by the steady discovery rate since launch. Gamma-ray pulsars are found both among young pulsars and among millisecond pulsars. Figure 1.4 shows the dependence of the gamma-ray luminosity L_γ on the spin-down power $\dot{E}$, highlighting that older millisecond pulsars tend to exhibit higher gamma-ray efficiencies than young pulsars. Coordination with radio timing observations has played a crucial role in unveiling many of Fermi's pulsars, and has also established that some radio pulsars have no detectable gamma-ray counterpart. Conversely, several gamma-ray pulsars, including some millisecond pulsars, have been found to be radio-quiet.

1.3.2 Observational signatures

Despite differences in their observational signatures, gamma-ray pulsars share a number of common characteristics, which are summarized below. Their phase-averaged spectra are characterized by a hard power-law component at lower energies, transitioning to an exponential cutoff above a few GeV (see Figure 1.5). Low spin-down pulsars (e.g., millisecond pulsars) feature sharper cutoffs and higher energy peaks.

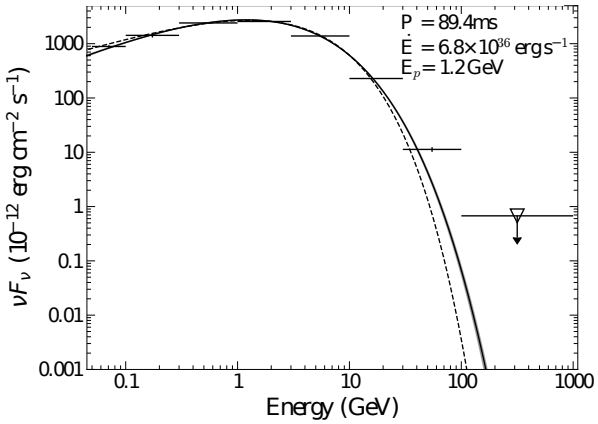

Figure 1.5: Spectral energy density (SED) of the Vela pulsar, characterized by a spin period of $P = 89.4$ ms and a spin-down power of $\dot{E} = 6.8 \times 10^{36}$ s. The SED peaks at an energy of $E_p = 1.2$ GeV. Different lines show different fits. Figure adapted from the LAT Third Pulsar Catalog (Smith et al., 2023).

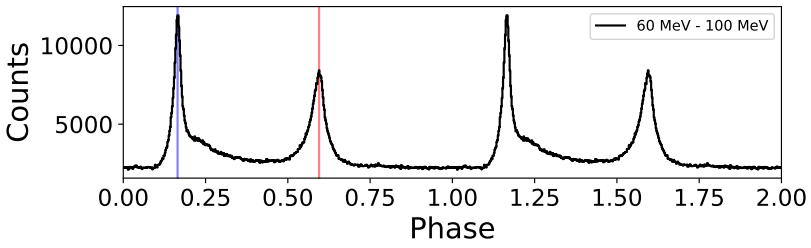

Figure 1.6: Archetypal gamma-ray light curve of the Vela pulsar, obtained in the 60–100 MeV energy band. The blue and red vertical lines indicate the phases of the first and second peaks, respectively. Figure taken from Lange et al. (2025).

Unlike radio pulses, which can be detected individually when sufficiently bright, gamma-ray pulses must be folded over many pulsar rotation periods due to poor photon statistics. Averaged light curves typically exhibit two peaks per rotation, with a peak separation equal to or smaller than half a phase (Figure 1.6). Yet, some exceptions display one or three peaks. The two peaks are sometimes connected by an additional "bridge" emission between them. They sharpen and become increasingly asymmetric with rising photon energy, while their phases remain independent of energy. Although there are exceptions, gamma-ray pulses are generally not aligned with radio pulses, which themselves typically occur once per rotation, and are significantly broader, suggesting that the two types of emission originate from distinct regions and processes within the magnetosphere.

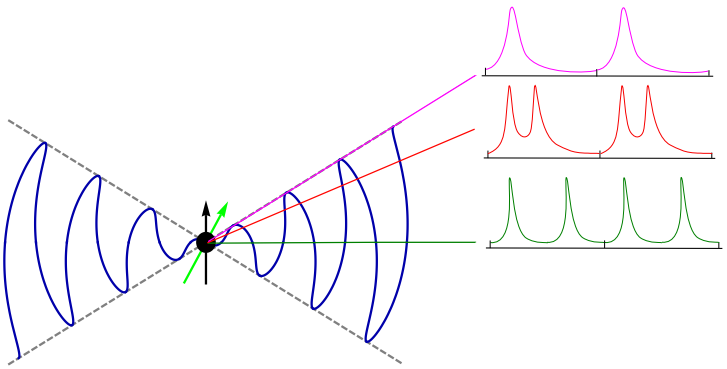

Figure 1.7: Sketch of the current sheet in the poloidal (r–z) plane, indicated by the blue line. The black sphere marks the pulsar, while the black and green arrows denote the rotation and magnetic axes, respectively. Gamma-ray emission arises from the current sheet, as illustrated by the three light curves corresponding to three different viewing angles. Figure taken from Mochol (2017).

As will be thoroughly explained in the following chapters, gamma-ray emission is now understood to primarily originate from a current sheet forming in the outer magnetosphere and pulsar wind (Figure 1.2), where particles accelerated by magnetic reconnection produce non-thermal radiation. This result is consistent with the detection of pulsed emission at energies exceeding $\sim$ 1 GeV, since the polar cap regions (see Figure 1.2) are expected to be opaque to such high-energy photons due to magnetic conversion. The "two-caustic" pulsed shape originates from geometrical effects due to the current sheet structure, represented in Figure 1.7. Each time the current sheet passes through the observer's line of sight, a pulse of light is detected (see Figure 1.7 and Cerutti et al. 2025 for further details). The pulse phases, their phase-separation, and the amplitude of the bridge emission depend on the viewing angle (see light curves in Figure 1.7). In particular, if the viewing angle does not intercept the current sheet (e.g., at lowest latitudes), no pulse is detected.

Over the past few decades, significant progress has been made in our understanding of pul-

sar magnetospheres. Numerical simulations have complemented existing theoretical models, and the advent of particle-in-cell (PIC) methods has provided new insights into these systems. In particular, they have enabled us to address fundamental questions regarding the general structure of isolated pulsar magnetospheres, the kinetic processes at play, and high-energy emission. Several studies have simulated isolated pulsar magnetospheres via the Particle-in-cell method, in both aligned (Philippov and Spitkovsky, 2014; Chen and Beloborodov, 2014; Cerutti et al., 2015; Belyaev, 2015; Hu and Beloborodov, 2022) and inclined (Philippov et al., 2015b; Cerutti et al., 2016; Kalapotharakos et al., 2018) configurations. These models have shown that a significant fraction of the spindown power is dissipated into kinetic energy, mainly through magnetic reconnection processes. They have identified the wind current sheet as the primary site of particle acceleration. Finally, these simulations have succeeded in reproducing the radiative signatures of pulsar magnetospheres, by accounting for synchrotron radiation from accelerated particles escaping the reconnection layers (Cerutti et al., 2016; Philippov and Spitkovsky, 2018; Kalapotharakos et al., 2018). However, a sizable fraction of pulsars is found in binary systems, especially among millisecond pulsars.

1.4 Pulsars in binaries

Pulsar binary systems include:

- pulsar–neutron star binaries, e.g., PSR B1913+16 (Hulse and Taylor, 1975) and the double pulsar PSR J0737-3039 (Burgay et al., 2003; Lyne et al., 2004);
- pulsar–black hole binaries (see Barr et al. 2024 and Chen and Liu 2024), for which no observations of stable systems have yet been confirmed, although two neutron star–black hole merger events have been detected via gravitational waves;
- pulsar–massive star binaries, typically observed as gamma-ray binaries (Dubus, 2013);
- pulsar–main sequence star binaries and spider pulsars, such as PSR B1957+20 (Fruchter et al., 1988) and PSR J2051−0827 (Stappers et al., 1996).
- pulsar–white dwarf binaries, e.g., PSR J1141−6545 (Kaspi et al., 2000), PSR J1909−3744 (Jacoby et al., 2003), PSR J1738+0333 (Jacoby et al., 2007), and PSR J0348+0432 (Antoniadis et al., 2013).
- pulsar–planet binaries, such as PSR J1719−1438b (see Niţu et al. 2022 and references therein).

The behavior of a pulsar binary depends sensitively on the properties of its companion, such as whether it possesses a magnetic field, whether it supplies mass and angular momentum to the pulsar, and whether it emits a (relativistic) wind. Its properties govern a variety of phenomena, such as intrabinary shocks, eclipses, accretion and ejection processes, ablation or evaporation of the companion, flares and outbursts. While several studies have investigated the magnetic coupling of neutron stars in tight binary systems (Hansen and Lyutikov, 2001; Palenzuela et al., 2013; Crinquand et al., 2019; Most and Philippov, 2020), fewer studies have focused on the interaction between a pulsar wind and its companion. Such systems are of considerable interest to the astrophysical community, as they are expected to produce multi-messenger signals and host novel sites of particle acceleration, potentially giving rise to new radiative signatures and enhanced electromagnetic emission, compared to isolated pulsar magnetospheres. Predicting their observational properties can guide future detections, help coordinate multi-wavelengths and multi-messenger campaigns, and ultimately provide valu-

able insights into the pulsar population. Moreover, these systems offer a unique opportunity to probe regions of the pulsar environment that are typically inaccessible in isolated pulsars.

1.5 Objectives and outline of the thesis

In this thesis, we aim to provide insights into a few specific cases of binary systems involving rotation-powered pulsars. In particular, the goal is to advance our understanding of their magnetospheric structure, particle acceleration mechanisms and sites, and their electromagnetic emission. Before doing so, we review the main theoretical aspects of pulsar magnetospheres in Chapter 2. Particle-in-cell simulations have emerged as the natural tool to address these questions, as they can capture both the macroscopic magnetospheric structure and the microphysical processes responsible for particle acceleration and radiation. We provide a description of this numerical method in Chapter 3. To start investigating the basics of such interacting systems, we first consider a generic scenario in which a small spherical companion orbits within a pulsar wind. This study, developed in Chapter 4, is applicable to pulsar planets or asteroids, and also serves as a first step towards modeling compact object binaries, such as pulsar–neutron star and pulsar–white dwarf systems. Although it represents a fundamental case study, it has, to the best of our knowledge, never been modeled with MHD or PIC simulations.

In contrast to systems with small, compact companions (such as planets or stellar remnants), another emblematic class of pulsar binaries involves millisecond pulsars in interaction with main-sequence stars, whose outflows can strongly interact with the pulsar wind, either through accretion disks or via wind-driven shocks. Millisecond pulsars can thereby either behave as rotation-powered pulsars or as accretion-powered pulsars, depending on the properties of the companion star. Intriguingly, since the early 21st century, several millisecond pulsar binaries, referred to as "transitional millisecond pulsars," have been observed to switch between rotation-powered and accretion-powered states, exhibiting an intermediate "sub-luminous disk state." This state is marked by the presence of an accretion disk without clear evidence of accretion, and by puzzling electromagnetic emissions which properties lie midway between those of accretion-powered and rotation-powered pulsars. Chapter 5 is devoted to the study of such peculiar systems, presenting the first ab initio PIC modeling of a pulsar wind interacting with a disk.

Adding further complexity, we may wonder what occurs when general relativity comes into play, as in pulsar-black hole binaries. Possible precursory electromagnetic emission from pulsar-black hole binaries could serve as an alert for gravitational-wave events. Several studies have already modeled such systems, predicting notable phenomena such as flares and the formation of large-scale magnetospheric structures. However, no general-relativistic PIC models of such systems exist to date, even though modeling the microphysical dissipative processes is essential to predict detectable electromagnetic signals. While general-relativistic codes exist that include a central black hole, and flat-spacetime versions exist that model a pulsar, combining both objects within a unified framework remains a numerical challenge. In Chapter 6, we present the first steps undertaken towards such a model.

Through these three case studies, this work aims to provide insights into the high-energy processes governing interacting pulsar magnetospheres and their resulting electromagnetic emissions. Accordingly, this thesis addresses the following fundamental questions:
How does the magnetosphere rearrange in the presence of the companion?
How much rotational energy of the pulsar is transferred to the pulsar wind?
Does the presence of the companion trigger enhanced particle acceleration, and what are the primary acceleration sites?
Which kinetic processes drive the resulting electromagnetic emissions?
What observational signatures, such as spectra and light curves, arise from this interaction?

Chapter 2

Theory of pulsar magnetospheres

Contents

2.1 Orders of magnitude . . . 14
2.2 Magnetospheric plasma properties and MHD waves . . . 15
2.3 Electrodynamics of pulsar magnetospheres . . . 17
2.3.1 Unipolar inductor model and vacuum solution . . . 18
2.3.2 Goldreich-Julian model and electrosphere . . . 19
2.3.3 Force-free model: plasma-filled magnetosphere . . . 21
2.3.4 Current understanding of pulsar magnetospheres . . . 28
2.4 Particle acceleration in the current sheet . . . 33
2.4.1 Relativistic generalized Ohm's law in the collisionless limit . . . 33
2.4.2 Magnetic reconnection . . . 33
2.4.3 Instabilities in the current sheet . . . 34
2.4.4 Particles spectrum . . . 35
2.5 Synchrotron-curvature radiation . . . 35
2.5.1 Radiation reaction force . . . 37
2.5.2 Effective perpendicular magnetic field . . . 38
2.5.3 Radiation power . . . 39
2.5.4 Power spectrum . . . 40
2.5.5 Curvature radiation . . . 41

2.1 Orders of magnitude

Before addressing the theoretical aspects of pulsar magnetospheres, we present some key properties common to all isolated, rotation-powered pulsars, along with their corresponding orders of magnitude.

Pulsars are neutron stars that are observed to emit regular pulses. Neutron stars result from the collapse of ordinary O and B massive stars ($\sim 8-25\,M_\odot$) at the later stages of their evolution. When no fuel for nuclear fusion remains in the stellar core, gravity is no longer balanced by radiation pressure, causing the star to collapse. Stars with degenerate core masses below the Chandrasekhar limit ($M_{\rm Ch} \sim 1.4\,M_\odot$) evolve into white dwarfs. If the core mass exceeds this limit, electron degeneracy pressure becomes insufficient to stop the collapse. At such high densities, electrons and protons combine via inverse beta decay, producing neutrons and neutrinos. Stability is ultimately provided by the repulsive component of the strong nuclear force between nucleons, which counterbalances the gravitational pressure. The resulting neutron star is an extremely hot ($T_\star \sim 10^6$) compact object, mainly composed of degenerate neutrons, with typical masses $M_{\rm NS} \sim 1.4\,M_\odot$ and radii $R_{\rm NS} \sim 10$ km. White dwarfs in binary systems can also evolve into neutron stars by accreting mass from their companion and surpassing the Chandrasekhar limit. Neutron stars thus represent the most compact stellar remnants that remain stable under gravity, with compactness given by:

$$\Xi = \frac{GM_{\rm NS}}{R_{\rm NS}c^2} \sim 0.2 \left(\frac{M_{\rm NS}}{1.4M_\odot}\right)\left(\frac{R_{\rm NS}}{10{\rm km}}\right)^{-1}, \tag{2.1}$$

where $M_\odot$ is the Sun mass.

The conservation of angular momentum during core collapse produces rapidly rotating neutron stars, with typical spin periods $\sim 0.01-10$ s, although millisecond pulsars ($\sim 1-10$ ms) are also observed, likely due to subsequent acquisition of angular momentum through accretion from a companion star. While this provides a zeroth-order explanation of such high rotation frequencies, a variety of additional mechanisms operating during and after the supernova explosion may influence the rotation of the newly-formed neutron star, either accelerating or decelerating it. Moreover, neutron stars are observed to spin down over time, at typical rates 10^{-21}–$10^{-12}\,{\rm s\,s^{-1}}$. Their rotational energy ($E_{\rm rot}$) can be expressed as

$$E_{\rm rot} = 2\pi^2 I P^{-2} \tag{2.2}$$

where $I = 2M_{\rm NS}R_{\rm NS}^2/5$ is the moment of inertia of the star, assuming it is spherical. Hence, the rate of rotational energy loss is given by

$$\dot{E}_{\rm rot} = -4\pi^2 I \dot{P} P^{-3} \sim -4\times 10^{31}{\rm erg.s^{-1}} \left(\frac{I}{10^{45}\ {\rm g\,cm^2}}\right)\left(\frac{P}{1\,{\rm s}}\right)\left(\frac{\dot{P}}{10^{-15}}\right). \tag{2.3}$$

The magnetic field at the poles can be inferred from their P and $\dot{P}$ measurements, assuming that the neutron star can be modeled as a rotating magnetic dipole, misaligned with respect to the rotation axis (Jackson, 1975; Lyne and Graham-Smith, 1990)[1]:

$$B = \frac{2\mu}{R_{\rm NS}^3} = \sqrt{\frac{3c^3 I P \dot{P}}{2\pi^2 R_{\rm NS}^6}} \sim 2\times 10^{12}{\rm G} \left(\frac{I}{10^{45}\ {\rm g\,cm^2}}\right)\left(\frac{P}{1\,{\rm s}}\right)\left(\frac{\dot{P}}{10^{-15}}\right), \tag{2.4}$$

where μ is the norm of the magnetic dipole moment. The magnetic flux conservation during collapse amplifies the progenitor's field, and internal dynamical processes (e.g., dynamo

[1]We note that this magnetic dipole braking model is a simplified assumption that cannot account for several observed radiative properties, and therefore needs to be revised in light of our current understanding of magnetospheres. Instead, the spin-down results from a braking torque applied at the stellar surface, caused by strong surface currents subjected to the Laplace force arising from a toroidal magnetic field.

process) may further enhance the field, overall leading to typical field strengths $10^9 - 10^{15}$ at the star surface. In addition, the magnetic field decays over time (e.g., see De Grandis et al. 2020; Viganò et al. 2021; Dehman et al. 2023 for recent works).

Although the internal structure of neutron stars remains an open field of research, it is commonly accepted that, as a first approximation, they can be considered perfect conductors due to the abundance of free charges in their interior.

Table 2.1 summarizes the typical orders of magnitude for the fundamental properties of pulsars.

Table 2.1: Typical orders of magnitude for pulsars.

Quantity	**Symbol**	**Order of magnitude**
Neutron star mass	$M_\star$	$1.4\ M_\odot$
Neutron star radius	$R_\star$	10^6 cm
Compactness	Ξ	0.2
Average mass density	$\rho_\star = 3M_\star/(4\pi R_\star^3)$	$10^{14}\ \mathrm{g\,cm^{-3}}$
Surface temperature	$T_\star$	10^6 K
Rotation period	P	1 ms − 10 s
Spin period derivative	$\dot{P}$	$10^{-21} - 10^{-12}$
Angular frequency	$\Omega = 2\pi/P$	$0.6 - 6 \times 10^3\ \mathrm{rad\,s^{-1}}$
Surface magnetic field	$B_\star$	$10^8 - 10^{15}$ G
Light cylinder radius	$R_{\rm LC} = c/\Omega$	$5 \times 10^6 - 5 \times 10^{10}$ cm
Moment of inertia	I	$10^{45}\ \mathrm{g\,cm^2}$
Spin-down power	$\dot{E}_{\rm rot} = 4\pi^2 I \dot{P} P^{-3}$	$10^{31} - 10^{38}\ \mathrm{erg\,s^{-1}}$
Typical particle Lorentz factor	γ	$10 - 10^7$
Typical magnetospheric particle density	n	$10^{12} - 10^{17}\ \mathrm{cm^{-3}}$

2.2 Magnetospheric plasma properties and MHD waves

Prior to modeling pulsar magnetospheres, it is important to emphasize that they are filled with plasma, whose properties play a crucial role in shaping their structure and dynamics. We recall here some key properties of such plasmas, which will form the basis for the following sections:

- *Quasi-neutral pair plasma* – the active magnetosphere is filled with quasi-neutral plasma, mostly populated by electrons and positrons (assuming pair creation in the magnetosphere; see Section 2.3.4), although some ions are extracted from the neutron star surface. The role of ions in the plasma composition remains controversial and not well constrained.

- *Relativistic* – particles are accelerated to (ultra-)relativistic energies, which implies the need to take into account relativistic effects. In particular, we recall the Lorentz transformations applying to the electromagnetic fields. In a reference frame ($\mathcal{R}'$) moving with velocity $\mathbf{v}$ with respect to a frame ($\mathcal{R}$), the fields read (Jackson, 1975):

$$\mathbf{E}' = \gamma(\mathbf{E} + \boldsymbol{\beta} \times \mathbf{B}) - \frac{\gamma^2}{\gamma+1}\boldsymbol{\beta}(\boldsymbol{\beta}\cdot\mathbf{E}) \tag{2.5}$$

$$\mathbf{B}' = \gamma(\mathbf{B} - \boldsymbol{\beta} \times \mathbf{E}) - \frac{\gamma^2}{\gamma+1}\boldsymbol{\beta}(\boldsymbol{\beta}\cdot\mathbf{B}) \tag{2.6}$$

- *Collisionless* – akin to most astrophysical plasmas, the plasma around pulsars is very dilute (typical particle densities of $n \sim 10^{17}\,\mathrm{cm^{-3}}$), making the frequency of particle-particle collisions negligible compared to the plasma frequency, $w_{\rm p} = \sqrt{4\pi n_e e^2/m_e}$

(where e, n_e and m_e are respectively the charge, the number density and the mass of the electrons), defined as the characteristic frequency at which electric charges oscillate in a conductive medium when thermal motion is neglected. As a result, its particle distribution is not thermalized and can emit non-thermal radiation. Particles still interact with each other indirectly via the electromagnetic fields.

- *Cold plasma wind* – the pulsar wind consists predominantly of cold plasma, except within narrow, hot current sheets (see Section 2.3.4).

- *Magnetically dominated* – the magnetospheric plasma is highly magnetized. In ideal MHD, the electric field vanishes in the proper frame: $\mathbf{E}' = \mathbf{E} + \mathbf{v} \times \mathbf{B}/c = \mathbf{0}$, where $\mathbf{E}'$ denotes the electric field proper frame (i.e., the frame comoving with the bulk flow of the pulsar wind) and $\mathbf{E}$, $\mathbf{B}$ are respectively the electric and magnetic fields in the observer's frame (i.e., the frame in which the neutron star's center of mass is at rest). We can define the magnetization parameter (σ) as the ratio, in the proper frame, of the magnetic to particle enthalpy densities (Kirk et al., 2009):

$$\sigma \equiv \frac{\mathbf{B}'^2}{4\pi\omega c^2}\,, \tag{2.7}$$

where ω is the proper enthalpy density of the plasma and $\mathbf{B}'$ the magnetic field in the proper frame. This expression can be simplified by making two assumptions. First, we assume that the plasma is cold, which is true in most of the magnetosphere, as discussed in the previous point. This allows us to reduce the enthalpy density expression to the rest mass energy density: $\omega = m_e c^2 n/\Gamma$, where n and Γ are respectively the particle's density and the Lorentz factor of the wind in the observer's frame. Secondly, if we assume that the magnetic field $\boldsymbol{B}$ is perpendicular to the bulk velocity of the plasma wind, which is globally a good approximation in the wind zone where the flow is radial and the field predominantly toroidal, the Lorentz transformation given in Eq. (2.6), coupled to the ideal condition, reduces to $\mathbf{B}' = \mathbf{B}/\Gamma$. Thus, the magnetization parameter can be recast as the ratio of electromagnetic to particle kinetic energy:

$$\sigma = \frac{B^2}{4\pi m_e c^2 n \Gamma}\,. \tag{2.8}$$

This parameter will be used extensively throughout this thesis. Within pulsar magnetospheres, $\sigma \gg 1$ everywhere except inside the current sheet, so that the plasma is magnetically dominated. The dynamics are governed by the interplay between electromagnetic fields and strong currents carried by the particles.

A dilute magnetized plasma can, in principle, sustain a variety of electromagnetic modes. Nevertheless, we assume that, near the light-cylinder radius, the plasma density is high enough to cause strong damping of low-frequency electromagnetic waves (Kirk et al., 2009), which implies that only MHD waves survive and propagate through the outer pulsar wind. In ideal MHD, plasma perturbations decompose into three fundamental linear wave modes[2]:

- Alfvén waves: plasma particles oscillations in response to the restoring force provided by magnetic field tension. They are incompressible, low-frequency, dispersionless, transverse waves that propagate at the Alfvén speed (V_A; Kirk and Duffy 1999; Kirk et al. 2009):

$$V_\mathrm{A} = \frac{cB'}{\sqrt{4\pi\omega + B'^2}}\cos\Phi = c\sqrt{\frac{\sigma}{\sigma+1}}\cos\Phi\,, \tag{2.9}$$

where Φ is the angle between the wavevector and the magnetic field.

[2] In non-ideal MHD, the same three modes remain, but their dispersion relations can be modified by dissipative effects.

- Magnetosonic waves: compressible, low-frequency waves driven by a combination of thermal pressure, magnetic pressure and magnetic tension. Their dispersion relation has two roots, leading to two distinct wave modes (Kirk and Duffy, 1999): slow magnetosonic modes, of phase velocity $v_{\rm slow}$, and fast magnetosonic modes, of phase velocity $v_{\rm fast} = c\sqrt{\sigma/(1+\sigma)}$. Their motion involves both longitudinal and transverse components relative to the magnetic field, with fast modes propagating obliquely or perpendicular to the field and slow modes propagating primarily along it. We note that one generally has $v_{\rm slow} \leq V_A \leq v_{\rm fast}$.

2.3 Electrodynamics of pulsar magnetospheres

This section introduces the theoretical framework and fundamental models that form the basis of our current understanding of pulsar magnetospheres, and concludes with an up-to-date description of their global structure. Before proceeding, we define the characteristic length scales considered in this thesis. We can split the environment of a pulsar into three main parts, as shown in Figure 2.1:

- the *magnetosphere*[3] or *light-cylinder zone*, which radius $R_{LC} = c/\Omega$ is defined as the distance at which a corotating object would reach the speed of light, c being the speed of light and Ω the angular velocity of the pulsar;

- the *wind zone*, that goes from the light cylinder to the termination shock, where a nearly standing shock wave is generated as the pulsar wind encounters the surrounding medium;

- the *pulsar wind nebula*, that extends beyond the termination shock.

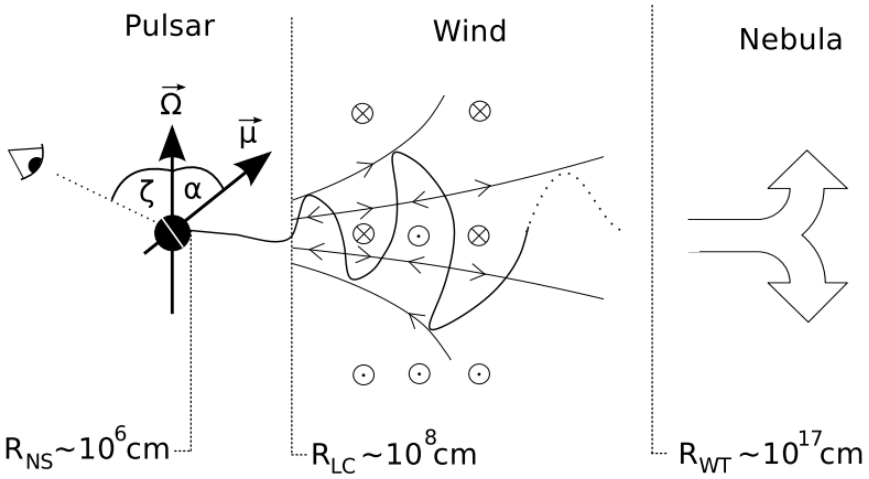

Figure 2.1: Sketch of the three main zones of the pulsar environment, in the poloidal plane. $R_{\rm NS}$, $R_{\rm LC}$ and $R_{\rm WT}$ name respectively the neutron star radius, the light-cylinder radius and the wind termination shock radius, and the corresponding lengthscales are given for the Crab pulsar. The α angle defines the inclination of the magnetic dipole ($\boldsymbol{\mu}$) and the ζ angle defines the observer angle with respect to the rotation vector ($\boldsymbol{\Omega}$). The solid line in the wind zone traces the current layer. Figure taken from Bühler and Blandford (2014).

[3] Although the term is sometimes extended to encompass the inner wind region, in this manuscript we adopt the formal definition of the magnetosphere, confining it to the light cylinder.

Our focus is restricted to the inner regions of the pulsar environment, from the light-cylinder zone out to the pulsar wind. Consequently, we do not address the physics of the termination shock nor that of the pulsar wind nebula (see, however, Kirk et al. 2009; Amato 2020 for reviews).

2.3.1 Unipolar inductor model and vacuum solution

We start by considering the simplest case of a rotating, perfectly conductive neutron star, in vacuum, hosting a dipolar magnetic moment at its center, aligned with the rotation axis. In spherical coordinates $(r,\,\theta,\,\phi)$ the magnetic field reads:

$$B_r(r,\theta,\phi) = \frac{B_\star r_\star^3}{r^3}\,2\,\cos\,\theta \tag{2.10}$$

$$B_\theta(r,\theta,\phi) = \frac{B_\star r_\star^3}{r^3}\,\sin\,\theta \tag{2.11}$$

$$B_\phi(r,\theta,\phi) = 0 \tag{2.12}$$

where $r_\star$ is the star radius and $B_\star = \mu/r_\star^3$ is the magnetic field at the stellar equator, μ being the norm of the magnetic moment.

The perfectly conducting assumption implies a vanishing electric field inside the star, $\mathbf{E}'^{\rm in} = \mathbf{0}$, in the corotating frame $(\mathcal{R}')$. Transforming this condition into the non-rotating, observer's frame $(\mathcal{R})$ leads to:

$$\mathbf{E}^{\rm in} + \mathbf{v}\times\mathbf{B}^{\rm in} = \mathbf{0} \;\;\text{with}\;\; \mathbf{v} = \mathbf{\Omega}\times\mathbf{r}\,, \tag{2.13}$$

where $\mathbf{\Omega}$ is the angular velocity of the neutron star, $\mathbf{r}$ is the position vector and $\mathbf{E}^{\rm in}$, $\mathbf{B}^{\rm in}$ are respectively the electric and magnetic fields inside the star. Charges rearrange so as to compensate the Lorentz force $\mathbf{F}_{\rm L} = \mathbf{v}\times\mathbf{B}/c$, leading to an excess of positive charges at the equator and negative charges at the poles[4]. By doing so, they create a potential difference, hence an electric field $\mathbf{E}_{\rm in}$ inside the star, which components are the following:

$$E_r^{\rm in}(r,\theta,\phi) = \frac{r\sin\theta}{R_{\rm LC}}B_\theta = \frac{r}{\mathrm{R_{LC}}}\frac{B_\star r_\star^3}{r^3}\sin^2\theta \tag{2.14}$$

$$E_\theta^{\rm in}(r,\theta,\phi) = -\frac{r\sin\theta}{R_{\rm LC}}B_r = -\frac{r}{\mathrm{R_{LC}}}\frac{B_\star r_\star^3}{r^3}\sin 2\theta \tag{2.15}$$

$$E_\phi^{\rm in}(r,\theta,\phi) = 0 \tag{2.16}$$

where $\mathrm{R_{LC}} = c/\Omega$ is the light cylinder radius.

The electric field outside the star $(\mathbf{E})$ can be computed by assuming that the star is in vacuum, the Poisson equation for the electric potential hence becoming $\nabla^2\Phi = 0$, where Φ is the electric potential, and by using $E_\theta = E_\theta^{\rm in}$ as the boundary condition. For an aligned rotator and assuming that the star has no net charge, the electric field is given by (Deutsch, 1955; Michel, 1982):

$$E_r(r,\theta,\phi) = \frac{B_\star r_\star^5}{r^4\,\mathrm{R_{LC}}}\,(1-3\cos^2\theta) \tag{2.17}$$

$$E_\theta(r,\theta,\phi) = -\frac{B_\star r_\star^5}{r^4\,\mathrm{R_{LC}}}\sin 2\theta \tag{2.18}$$

$$E_\phi(r,\theta,\phi) = 0\,. \tag{2.19}$$

[4]This model very much resembles that of a Faraday disk, which consists of a rotating conducting disk embedded in a uniform magnetic field, parallel to its rotation axis.

In this case, the net outgoing Poynting flux was shown to be equal to (Pacini, 1968; Ostriker and Gunn, 1969):

$$L_{\rm vacuum} = \frac{2}{3}\frac{\mu^2\Omega^4}{c^3}\sin^2\chi\,, \tag{2.20}$$

χ being the angle between the magnetic moment $\boldsymbol{\mu}$ and the rotation axis. We note that, for a null inclination, no Poynting flux is emitted and the star does not spin down.

2.3.2 Goldreich-Julian model and electrosphere

From the vacuum solution (Eqs. 2.17; 2.18; 2.19), we notice that there is an unscreened surface electric field parallel to the magnetic field: $E_\parallel = \mathbf{E}\cdot\mathbf{B}/B^2 \neq 0$. At the star surface, the electric field is of the order $E \sim B_\star r_\star/R_{\rm LC} \sim B_\star r_\star 2\pi/cP \sim 10^8$ statV.cm^{-1}, for a pulsar spin period $P = 1$s, $r_\star = 10^6$ cm and $B_\star = 10^{12}$ G. Such strong resulting electric force was shown to overcome gravitational and molecular attractions (Goldreich and Julian, 1969; Ruderman, 1974; Jones, 1986; Medin and Lai, 2007), therefore being able to lift electrons and ions from the stellar surface.

Goldreich and Julian (1969), who were the first ones to highlight this point, developed a model based on the extraction of both electrons and ions from the pulsar surface, until the charge density is high enough to screen the parallel electric field. The model is developed in the framework of axisymmetric, steady-state, ideal MHD and assumes a perfectly conducting plasma corotating with the star. Starting from the Maxwell-Gauss equation, the charge density (ρ) reads

$$\rho = \frac{1}{4\pi}\nabla\cdot\mathbf{E} \tag{2.21}$$

and plugging into it the corotation electic field given by the ideal condition

$$\mathbf{E} = -\frac{\mathbf{v}\times\mathbf{B}}{c} = -\frac{(\boldsymbol{\Omega}\times\mathbf{r})\times\mathbf{B}}{c} \tag{2.22}$$

leads to

$$\rho = -\frac{1}{4\pi c}\nabla\cdot((\boldsymbol{\Omega}\times\mathbf{r})\times\mathbf{B})\,, \tag{2.23}$$

which can be rewritten as[5]

$$\rho = -\frac{1}{4\pi c}\left[\mathbf{B}\cdot(\nabla\times(\boldsymbol{\Omega}\times\mathbf{r})) - (\boldsymbol{\Omega}\times\mathbf{r})\cdot(\nabla\times\mathbf{B})\right]\,. \tag{2.24}$$

The first terms simplifies as[6]

$$\nabla\times(\boldsymbol{\Omega}\times\mathbf{r}) = \boldsymbol{\Omega}\,(\nabla\cdot\mathbf{r}) + (\mathbf{r}\cdot\nabla)\,\boldsymbol{\Omega} - \mathbf{r}\,(\nabla\cdot\boldsymbol{\Omega}) - (\boldsymbol{\Omega}\cdot\nabla)\,\mathbf{r} = 2\boldsymbol{\Omega} \tag{2.25}$$

since $\boldsymbol{\Omega}\,(\nabla\cdot\mathbf{r}) = 3\boldsymbol{\Omega}$, $(\mathbf{r}\cdot\nabla)\,\boldsymbol{\Omega} = 0$ (due to $\boldsymbol{\Omega}$ constant), $\mathbf{r}\,(\nabla\cdot\boldsymbol{\Omega}) = 0$ (due to $\boldsymbol{\Omega}$ constant) and $(\boldsymbol{\Omega}\cdot\nabla)\,\mathbf{r} = \boldsymbol{\Omega}$. The second term can be rewritten using the Maxwell-Ampère equation, by assuming a steady-state:

$$\nabla\times\mathbf{B} = \frac{4\pi}{c}\mathbf{J} \tag{2.26}$$

where $\mathbf{J}$ is the current induced by the rotating charge density,

$$\mathbf{J} = \rho\mathbf{v} = \rho(\boldsymbol{\Omega}\times\mathbf{r})\,. \tag{2.27}$$

From equations (2.24), (2.26) and (2.27), we obtain the so-called "Goldreich-Julian density" ($\rho_{\rm GJ}$):

$$\rho_{\rm GJ} \equiv -\left(\frac{\boldsymbol{\Omega}\cdot\mathbf{B}}{2\pi c}\right)\frac{1}{1-(\boldsymbol{\Omega}\times\mathbf{r})^2/c^2}\,. \tag{2.28}$$

[5] We make use of the vector identity $\nabla\cdot(\mathbf{a}\cdot\mathbf{b}) = \mathbf{b}\cdot(\nabla\times\mathbf{a}) - \mathbf{a}\cdot(\nabla\times\mathbf{b})$.

[6] We make use of the vector identity $\nabla\times(\mathbf{a}\times\mathbf{b}) = \mathbf{a}(\nabla\cdot\mathbf{b}) + (\mathbf{b}\cdot\nabla)\mathbf{a} - \mathbf{b}(\nabla\cdot\mathbf{a}) - (\mathbf{a}\cdot\nabla)\mathbf{b}$.

For a dipolar magnetic field and a rotation axis along the $z-$axis, Eq. (2.28) reads

$$\rho_{\rm GJ} = -\frac{\Omega B_\star}{2\pi c}\left(\frac{r_\star}{r}\right)^3 \left(\frac{3\cos^2\theta - 1}{1 + \left(\frac{\Omega r \sin\theta}{c}\right)^2}\right) . \tag{2.29}$$

The relativistic term $(\Omega r \sin\theta/c)$ appearing in the denominator becomes important near the light cylinder but can reasonably be neglected near the stellar surface, which leads to

$$\rho_{GJ} \approx \frac{-\boldsymbol{\Omega}\cdot\mathbf{B}}{2\,\pi\,c} = -\frac{\Omega\,B_\star}{2\,\pi\,c}\left(\frac{r_\star}{r}\right)^3 (3\cos^2\theta - 1)\,. \tag{2.30}$$

The Goldreich-Julian density corresponds to a number density of about $n_{\rm GJ} = \rho_{\rm GJ}/e \sim 10^{11}{\rm cm}^{-1}$ near the star surface, for a pulsar spin period $P = 1$s and a surface magnetic field $B_\star = 10^{12}$G.

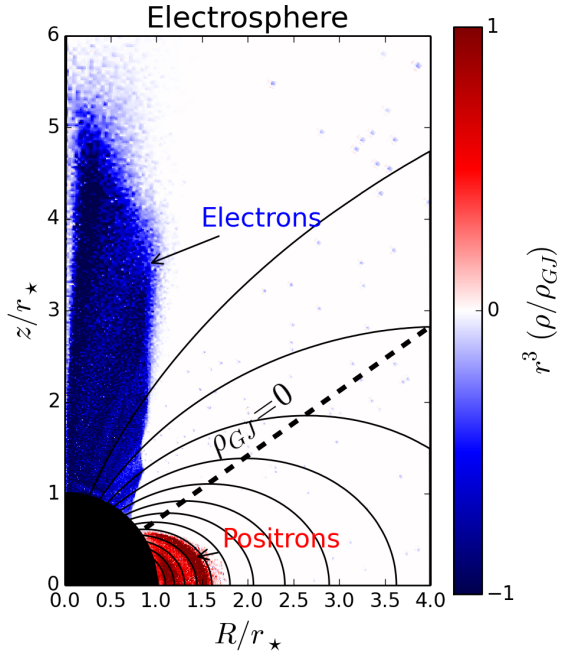

Figure 2.2: Charge distribution for the electrosphere configuration, obtained from a 2D axisymmetric PIC simulation. Electrons are lifted from the poles, forming a dome, while positrons form a torus around the equator. In the simulation, positrons represent the positive charges, replacing the ions. Figure taken form Cerutti and Beloborodov (2017).

In the Goldreich-Julian picture, the magnetosphere was supposed to be filled everywhere with just the right amount of charges to ensure $\mathbf{E}\cdot\mathbf{B} = 0$. However, under their assumptions, which in particular do not consider pair creation, the resulting solution for an aligned rotator differs from what was expected (Jackson, 1975; Krause-Polstorff and Michel, 1985a,b; Mottez, 2024). Compensating currents develop in response to the external parallel electric field (predicted by the vacuum model), generating opposing electric fields, so as to achieve $\mathbf{E}\cdot\mathbf{B} = 0$. Once enough charges are extracted to screen out the parallel electric field at the pulsar surface, plasma extraction stops and a steady solution establishes. The corotation electric field (Eq. 2.22) imposes the corotation of the plasma with the star. For a magnetic dipole, $\boldsymbol{\Omega}\cdot\mathbf{B} > 0$ at the poles and $\boldsymbol{\Omega}\cdot\mathbf{B} < 0$ at the equator, therefore leading to an accumulation of electrons above the poles ($\rho_{\rm GJ} > 0$; the "dome") and of ions in the equatorial region ($\rho_{\rm GJ} < 0$; the "disk"). The overall size of the charged clouds spans only a few stellar radii. Although

in the plasma-filled regions the electric field is screened, particles can be accelerated in the vacuum regions between the domes and the disk. In the case of oblique rotators, we recover qualitatively the same structure. This charge-separated configuration, called the "electrosphere" (see Figure 2.2), was shown to be unstable (Pétri et al., 2002; Spitkovsky and Arons, 2002). Moreover, although this solution leads to the emission of Poynting flux and therefore a non-zero spin-down power, it fails to reproduce the observed magnetospheric behavior of active pulsars. Indeed, even if the Poynting flux were to be converted into kinetic energy, the absence of pair cascades would leave the radiation far below the detection threshold. Nevertheless, this solution remains worth discussing, as it is considered a potential model for old, inactive pulsars, lying below the death line (see Section 2.3.4 and Figure 4.22).

2.3.3 Force-free model: plasma-filled magnetosphere

The previous section suggests that pair production is at play in active pulsar magnetospheres. This is confirmed by observations and models of pulsar wind nebulae, indicating that magnetospheres should feature plasma densities greater than the Goldreich-Julian density. In such case, the expected amount of charges cannot all be extracted from the star surface and pair creation is indeed required in the magnetosphere.

Although the persistence of small, localized regions with unscreened parallel electric fields is required for pair creation, this regime, based on a plasma-filled magnetosphere, is well described by a highly magnetized limit of relativistic ideal MHD, called "force-free electrodynamics". The force-free model has been proven to be a good approximation in the case of pulsar magnetospheres (see Cerutti and Philippov 2017 and references therein). This limit relies on the assumption that the Lorentz force dominates over all the other terms in the conservation of momentum MHD equation (i.e., $U_{\rm B} = B^2/8\pi \gg U_{\rm plasma}$, where $U_{\rm B}$ is the magnetic energy density and $U_{\rm plasma}$ is the plasma energy density), implying the following force-free condition:

$$\rho\mathbf{E} + \mathbf{J} \times \mathbf{B} = \mathbf{0}\,, \tag{2.31}$$

where ρ and $\mathbf{J}$ are the charge and current densities. The force-free limit therefore requires a compromise concerning the plasma density (Komissarov, 2002): the plasma should be sufficiently dense, in order to screen the parallel electric field and verify

$$\mathbf{E} \cdot \mathbf{B} = \mathbf{0}\,, \tag{2.32}$$

but diffuse enough so that its inertia can be overlooked. To ensure that poloidal currents flow along the poloidal magnetic field lines, unless the force-free approximation would break down, the electromagnetic field must be magnetically dominated (i.e., $B^2 - E^2 > 0$).

Gruzinov (1999) and Blandford (2002) demonstrated that the equations of force-free electrodynamics can be expressed entirely in terms of the electromagnetic fields and their derivatives, without explicit reference to the plasma, by showing that the force-free current takes the form:

$$\mathbf{J} = c\frac{\nabla \cdot \mathbf{E}}{4\pi} \cdot \frac{\mathbf{E} \times \mathbf{B}}{B^2} + \frac{c}{4\pi}\frac{(\nabla \times \mathbf{B}) \cdot \mathbf{B} - (\nabla \times \mathbf{E}) \cdot \mathbf{E}}{B^2}\mathbf{B}\,. \tag{2.33}$$

The force-free magnetosphere, under the assumptions of stationarity and axisymmetry, is governed by the solution of a non-linear partial differential equation, known as "the pulsar equation". Hereafter, we derive the pulsar equation, in cylindrical coordinates (R,ϕ,z). The magnetic field can be expressed in terms of the vector potential $\mathbf{A}$. Under the assumption of axisymmetry ($\partial/\partial\phi = 0$), the expression simplifies to

$$\mathbf{B} = \nabla \times \mathbf{A} = -\frac{\partial A_\phi}{\partial z}\,\mathbf{e}_{\rm R} + \left(\frac{\partial A_R}{\partial z} - \frac{\partial A_z}{\partial R}\right)\mathbf{e}_\phi + \frac{1}{R}\frac{\partial (RA_\phi)}{\partial R}\,\mathbf{e}_z\,. \tag{2.34}$$

We can reformulate Eq. (2.34) by defining:

- the poloidal magnetic flux function (ψ), corresponding to the total magnetic flux that passes through a disk of radius R in a plane perpendicular to the z-axis,

$$\psi(R,z) \equiv \frac{1}{2\pi}\iint \mathbf{B}\cdot \mathrm{d}\mathbf{S} = RA_\phi \tag{2.35}$$

- the current function, giving the total electric current crossing the same surface,

$$I(R,z) \equiv \frac{c}{2}\iint \mathbf{J}\cdot \mathrm{d}\mathbf{S} = RB_\phi \tag{2.36}$$

so as to obtain

$$\mathbf{B} = \frac{\nabla\psi \times \mathbf{e}_\phi}{R} + \frac{I}{R}\mathbf{e}_\phi\,. \tag{2.37}$$

Making use of the Maxwell-Gauss equation (Eq. 2.21) together with the stationary Ampère-Maxwell's law,

$$\mathbf{J} = \frac{c}{4\pi}\nabla\times\mathbf{B}\,, \tag{2.38}$$

the force-free condition (Eq. 2.31) can be rewritten as follows:

$$(\nabla\cdot\mathbf{E})\mathbf{E} + (\nabla\times\mathbf{B})\times\mathbf{B} = \mathbf{0}\,. \tag{2.39}$$

To obtain the pulsar equation, we must substitute $\mathbf{E}$ and $\mathbf{B}$ in Eq. (2.39) as a function of ψ, I and their spatial coordinates (R, z). Before proceeding, we explicitly write

$$\nabla\psi\times\mathbf{e}_\phi = -\frac{\partial\psi}{\partial z}\mathbf{e}_R + \frac{\partial\psi}{\partial R}\mathbf{e}_z\,, \tag{2.40}$$

which will be used extensively in the following. We start from deriving the expression of $(\nabla\cdot\mathbf{E})\mathbf{E}$. The ideal MHD condition (Eq. 2.22) reads

$$\mathbf{E} = -\frac{(\mathbf{\Omega}\times\mathbf{R})\times\mathbf{B}}{c} = -\left(\frac{R}{R_{\rm LC}}\right)\mathbf{e}_\phi\times\mathbf{B}\,. \tag{2.41}$$

Combining it with Eq. (2.37) and using Eq. (2.40) yields

$$\mathbf{E} = -\left(\frac{R}{R_{\rm LC}}\right)\mathbf{e}_\phi\times\left(\frac{\nabla\psi\times\mathbf{e}_\phi}{R}\right) = -\frac{1}{R_{\rm LC}}\nabla\psi\,. \tag{2.42}$$

The divergence of the electric field hence reads:

$$\begin{aligned}\nabla\cdot\mathbf{E} &= -\frac{1}{R_{\rm LC}}\nabla\cdot\nabla\psi \\ &= -\frac{1}{R_{\rm LC}}\left(\frac{1}{R}\frac{\partial}{\partial R}\left(R\frac{\partial\psi}{\partial R}\right) + \frac{\partial}{\partial z}\frac{\partial\psi}{\partial z}\right) \\ &= -\frac{1}{R_{\rm LC}}\left(\frac{1}{R}\frac{\partial\psi}{\partial R} + \frac{\partial^2\psi}{\partial R^2} + \frac{\partial^2\psi}{\partial z^2}\right)\,.\end{aligned} \tag{2.43}$$

We next derive $(\nabla\times\mathbf{B})\times\mathbf{B}$. For readability, we decompose $\nabla\times\mathbf{B}$ into two terms:

$$\nabla\times\mathbf{B} = \nabla\times\left(\frac{\nabla\psi\times\mathbf{e}_\phi}{R}\right) + \nabla\times\left(\frac{I}{R}\mathbf{e}_\phi\right) \tag{2.44}$$

Using Eq. (2.40), the curl of the poloidal magnetic field takes the form:

$$\begin{aligned}\nabla\times\left(\frac{\nabla\psi\times\mathbf{e}_\phi}{R}\right) &= \left[\frac{\partial}{\partial z}\left(\frac{-1}{R}\frac{\partial\psi}{\partial z}\right) - \frac{\partial}{\partial R}\left(\frac{1}{R}\frac{\partial\psi}{\partial R}\right)\right]\mathbf{e}_\phi \\ &= \left[\frac{1}{R^2}\frac{\partial\psi}{\partial R} - \frac{1}{R}\left(\frac{\partial^2\psi}{\partial R^2} + \frac{\partial^2\psi}{\partial z^2}\right)\right]\mathbf{e}_\phi\,.\end{aligned} \tag{2.45}$$

The curl of the toroidal magnetic field can also be rewritten:

$$\begin{aligned}\nabla\times\left(\frac{I}{R}\mathbf{e}_\phi\right) &= -\frac{\partial}{\partial z}\frac{\partial\psi}{\partial R}\left(\frac{I}{R}\right)\mathbf{e}_R+\frac{1}{R}\frac{\partial}{\partial R}\left(R\frac{I}{R}\right)\mathbf{e}_z\\ &= -\frac{1}{R}\frac{\partial I}{\partial z}\mathbf{e}_R+\frac{1}{R}\frac{\partial I}{\partial R}\mathbf{e}_z\,.\end{aligned}\tag{2.46}$$

Taking the cross product of Eq. (2.45) with $\mathbf{B}$ yields:

$$\left[\nabla\times\left(\frac{\nabla\psi\times\mathbf{e}_\phi}{R}\right)\right]\times\mathbf{B}=\left[\frac{1}{R^2}\frac{\partial\psi}{\partial R}-\frac{1}{R}\left(\frac{\partial^2\psi}{\partial R^2}+\frac{\partial^2\psi}{\partial z^2}\right)\right]\frac{\nabla\psi}{R}\tag{2.47}$$

and performing the same operation on Eq. (2.46) gives:

$$\begin{aligned}\left[\nabla\times\left(\frac{I}{R}\mathbf{e}_\phi\right)\right]\times\mathbf{B} &= \frac{1}{R^2}\frac{\partial I}{\partial z}\frac{\partial\psi}{\partial R}\mathbf{e}_\phi-\frac{1}{R^2}\frac{\partial I}{\partial R}\frac{\partial\psi}{\partial z}\mathbf{e}_\phi-\frac{I}{R^2}\frac{\partial I}{\partial z}\mathbf{e}_z-\frac{I}{R^2}\frac{\partial I}{\partial R}\mathbf{e}_R\\ &= \frac{1}{R^2}\left(\frac{\partial I}{\partial z}\frac{\partial\psi}{\partial R}-\frac{\partial I}{\partial R}\frac{\partial\psi}{\partial z}\right)\mathbf{e}_\phi-\frac{I}{R^2}\frac{\partial I}{\partial\psi}\nabla\psi\,.\end{aligned}\tag{2.48}$$

Adding Eqs. (2.47) and (2.48) leads to:

$$(\nabla\times\mathbf{B})\times\mathbf{B}=\left[\frac{1}{R^3}\frac{\partial\psi}{\partial R}-\frac{1}{R^2}\left(\frac{\partial^2\psi}{\partial R^2}+\frac{\partial^2\psi}{\partial z^2}\right)-\frac{I}{R^2}\frac{\partial I}{\partial\psi}\right]\nabla\psi+\frac{1}{R^2}\left(\frac{\partial I}{\partial z}\frac{\partial\psi}{\partial R}-\frac{\partial I}{\partial R}\frac{\partial\psi}{\partial z}\right)\mathbf{e}_\phi\,.\tag{2.49}$$

We finally obtain the pulsar equation by plugging Eqs. (2.43) and (2.49) into Eq. (2.39) and keeping the poloidal component:

$$\left(1-\frac{R^2}{R_{\rm LC}^2}\right)\left(\frac{\partial^2\psi}{\partial R^2}+\frac{\partial^2\psi}{\partial z^2}\right)-\left(1+\frac{R^2}{R_{\rm LC}^2}\right)\frac{1}{R}\frac{\partial\psi}{\partial R}+I\frac{\partial I}{\partial\psi}=0\,.\tag{2.50}$$

Michel (1973) proposed an analytical solution to the pulsar equation, applied to a rotating monopole and called the "split monopole solution". This solution has been shown to provide an accurate approximation of the pulsar wind beyond the light cylinder ($r\gg R_{\rm LC}$) and continues to be employed in modern studies (e.g., see Chapter 4). We therefore derive this solution below. We make use of the spherical coordinate system (r, θ, ϕ) and the cylindrical coordinate system (R, ϕ, z), where the cylindrical coordinates are related to the spherical coordinates by $R=r\sin\theta$, $z=r\cos\theta$, $\phi=\phi$ and, conversely, $r=\sqrt{R^2+z^2}$, $\tan\theta=r/z$. The solution is based on the assumption that the poloidal magnetic field is purely radial and decays as $1/r^2$, i.e., $B_r=B_\star(r_\star/r)^2$ and $B_\theta=0$. We first derive the magnetic flux function. According to Eq. (2.37), we can express the poloidal magnetic field as follows:

$$\mathbf{B}_p(r,\theta)=\frac{\nabla\psi\times\mathbf{e}_\phi}{r\sin\theta}=\left(\frac{1}{r\sin\theta}\frac{\partial\psi}{r\partial\theta};-\frac{1}{r\sin\theta}\frac{\partial\psi}{\partial r};0\right)\,.\tag{2.51}$$

Hence, we can identify the poloidal components:

$$B_r = B_\star\left(\frac{r_\star}{r}\right)^2=\frac{1}{r\sin\theta}\frac{\partial\psi}{r\partial\theta}\tag{2.52}$$

$$B_\theta = 0=-\frac{1}{r\sin\theta}\frac{\partial\psi}{\partial r}\,.\tag{2.53}$$

The last equation shows that ψ does not depend on the radius ($\psi(r,\theta)=\psi(r)$) and rearranging Eq. (2.52) yields

$$\frac{\partial\psi}{\partial\theta}=B_\star r_\star^2\sin\theta\tag{2.54}$$

Integrating, we obtain

$$\psi(r,\theta) = B_\star r_\star^2 (1-\cos\theta) \tag{2.55}$$

which, in cylindrical coordinates, reads:

$$\psi(R,z) = B_\star r_\star^2 \left(1 - \frac{z}{\sqrt{r^2+z^2}}\right) . \tag{2.56}$$

Therefore, we can evaluate the derivatives of ψ appearing in the first two terms of the pulsar equation (Eq. 2.50), which allows us to express the first term as

$$\left(1-\frac{R^2}{R_{\rm LC}^2}\right)\left(\frac{\partial^2\psi}{\partial R^2}+\frac{\partial^2\psi}{\partial z^2}\right) = \left(1-\frac{R^2}{R_{\rm LC}^2}\right)\frac{B_\star R_\star^2 z}{(R^2+z^2)^{3/2}} \tag{2.57}$$

and the second term as

$$-\left(1+\frac{R^2}{R_{\rm LC}^2}\right)\frac{1}{R}\frac{\partial\psi}{\partial R} = -\left(1+\frac{R^2}{R_{\rm LC}^2}\right)\frac{B_\star R_\star^2 z}{(R^2+z^2)^{3/2}} . \tag{2.58}$$

so that their sum equals:

$$\left(1-\frac{R^2}{R_{\rm LC}^2}\right)\left(\frac{\partial^2\psi}{\partial R^2}+\frac{\partial^2\psi}{\partial z^2}\right) - \left(1+\frac{R^2}{R_{\rm LC}^2}\right)\frac{1}{R}\frac{\partial\psi}{\partial R} = -\frac{B_\star R_\star^2}{R_{\rm LC}^2}\frac{2zr^2}{(R^2+z^2)^{3/2}} \tag{2.59}$$

Substituting it in the pulsar equation (Eq. 2.50) yields:

$$I(\psi)\frac{\partial I}{\partial\psi} = \frac{2B_\star r_\star^2}{R_{\rm LC}^2}\frac{R^2 z}{(R^2+z^2)^{3/2}} \tag{2.60}$$

which, in spherical coordinates, becomes

$$I(\theta)\frac{{\rm d}I}{{\rm d}\theta}\frac{1}{B_\star r_\star^2\sin\theta} = \frac{2B_\star r_\star^2}{R_{\rm LC}^2}\cos\theta\sin^2\theta \tag{2.61}$$

$$\Rightarrow I(\theta)\frac{{\rm d}I}{{\rm d}\theta} = \frac{2B_\star^2 r_\star^4}{R_{\rm LC}^2}\cos\theta\sin^3\theta . \tag{2.62}$$

Defining $u=\sin\theta$, $K=\frac{2B_\star^2 r_\star^4}{R_{\rm LC}^2}$, and integrating, we obtain

$$\int_{I(0)}^{I(\theta)} \tilde{I}{\rm d}\tilde{I} = K\int_{\sin(0)}^{\sin(\theta)} u^3{\rm d}u . \tag{2.63}$$

Hence,

$$\frac{1}{2}\left[I(\theta)^2 - I(0)^2\right] = \frac{K}{4}\sin^4\theta \quad\Rightarrow\quad I(\theta)^2 = I(0)^2 + \frac{K}{2}\sin^4\theta . \tag{2.64}$$

Setting the axial current to zero ($I(0)=0$) yields

$$I(\theta) = \pm\sqrt{\frac{K}{2}}\sin^2\theta = \pm\frac{B_\star r_\star^2}{R_{\rm LC}}\sin^2\theta . \tag{2.65}$$

The sign of $I(\theta)$ is determined by the Goldreich–Julian charge density (Eq. 2.30), since charges are assumed to stream outward along open field lines, meaning that $I(\theta)<0$ in the aligned case ($\mathbf{\Omega}\cdot\mathbf{B}>0$) and $I(\theta)>0$ in the anti-aligned case ($\mathbf{\Omega}\cdot\mathbf{B}<0$), sometimes referred to as the "anti-pulsar" solution. In the following, we assume an aligned pulsar.

With $I(\theta)$ known, the electromagnetic field components can now be explicitly derived. By definition (Eq. 2.36),

$$B_\phi = \frac{I}{R} = \frac{I}{r\sin\theta} = -\frac{B_\star r_\star^2\sin\theta}{R_{\rm LC} r} . \tag{2.66}$$

In order to find the electric field components, we first determine the corresponding current density:

$$\mathbf{J} = \frac{c}{4\pi}(\nabla \times \mathbf{B}) = \frac{c}{4\pi}\frac{1}{r\sin\theta}\frac{\partial}{\partial\theta}(\sin\theta B_\phi) = -\frac{c}{2\pi R_{\rm LC}}B_\star\frac{r_\star^2}{r^2}\cos\theta\,\mathbf{e}_r\,. \tag{2.67}$$

Since the current density is purely radial, the radial component of the electric field, E_r, can be inferred from the force-free condition (Eq. 2.31), which imposes $\mathbf{E}$ perpendicular to $\mathbf{J}$:

$$\mathbf{E}\cdot\mathbf{J} = 0 \Rightarrow E_r\,J_r = 0 \Rightarrow E_r = 0\,. \tag{2.68}$$

The screening condition (Eq. 2.32) can be used to deduce the toroidal electric field:

$$\mathbf{E}\cdot\mathbf{B} = 0 \Rightarrow E_\phi\,B_\phi = 0 \Rightarrow E_\phi = 0\,. \tag{2.69}$$

Finally, we resort to the ideal MHD condition (Eq. 2.22) to infer the last electric component:

$$\mathbf{E} = -\frac{1}{c}(\mathbf{\Omega}\times\mathbf{r})\times\mathbf{B} = -\frac{\Omega r\sin\theta B_r}{c}\mathbf{e}_\theta = -\frac{B_\star r_\star^2\sin\theta}{rR_{\rm LC}} = B_\phi\mathbf{e}_\theta\,. \tag{2.70}$$

Hence, the final monopole solution takes the form (in spherical coordinates):

$$B_r = B_\star\left(\frac{r_\star}{r}\right)^2 \tag{2.71}$$

$$B_\theta = 0 \tag{2.72}$$

$$B_\phi = -B_\star\left(\frac{r_\star^2}{rR_{\rm LC}}\right)\sin\theta \tag{2.73}$$

$$E_r = 0 \tag{2.74}$$

$$E_\theta = B_\phi \tag{2.75}$$

$$E_\phi = 0\,. \tag{2.76}$$

In order to still satisfy $\nabla\cdot\mathbf{B} = 0$, we consider a "split monopole", anti-symmetric about the equatorial plane. The solution in the opposite hemisphere is therefore given by reversing the fields and current vectors across the equator: $\mathbf{E}\to-\mathbf{E}$, $\mathbf{B}\to-\mathbf{B}$ and $\mathbf{J}\to-\mathbf{J}$ (see Figure 2.3). An equatorial current sheet arises from this reversal of the magnetic field across the equator. It carries the return current to ensure a null net current through the stellar surface and therefore a neutral stellar charge. The ratio $B_\phi/B_r = r\sin\theta/R_{\rm LC}$ tells us that, near the star surface, magnetic field lines are almost radial. Close to the light-cylinder radius, poloidal and toroidal components are of the same order. And far in the pulsar wind, the magnetic field becomes almost purely toroidal. The split monopole solution allows for a non-vanishing outflowing Poynting flux ($\mathbf{\Pi} = c\mathbf{E}\times\mathbf{B}/4\pi$), corresponding to the spin-down power extracted from the star:

$$L_{\rm monopole} = \iint\mathbf{\Pi}\cdot{\rm d}\mathbf{S} = \frac{c}{4\pi}\iint(E_\theta B_\phi - E_\phi B_\theta)r^2\sin\theta{\rm d}\theta{\rm d}\phi = \frac{2\,c\,B_\star^2\,{\rm r}_\star^4}{3\,{\rm R}_{\rm LC}^2}\,. \tag{2.77}$$

Bogovalov (1999) extended the split-monopole solution to inclined configurations and proved that the spin-down expression holds for oblique magnetic moments.

Because of the complexity of the pulsar equation, no analytical solution exists for the case of an aligned rotating dipole; however, several numerical solutions have been obtained (Contopoulos et al., 1999; Contopoulos, 2005; Goodwin et al., 2004; Gruzinov, 2005; Timokhin, 2006). These simulations establish the basis of the currently accepted structure of pulsar magnetospheres. The magnetosphere is characterized by three main regions: (i) a closed zone around the equatorial region, extending up to the light-cylinder radius and corotating with the pulsar; (ii) an open zone, with open field lines emerging from the polar caps and

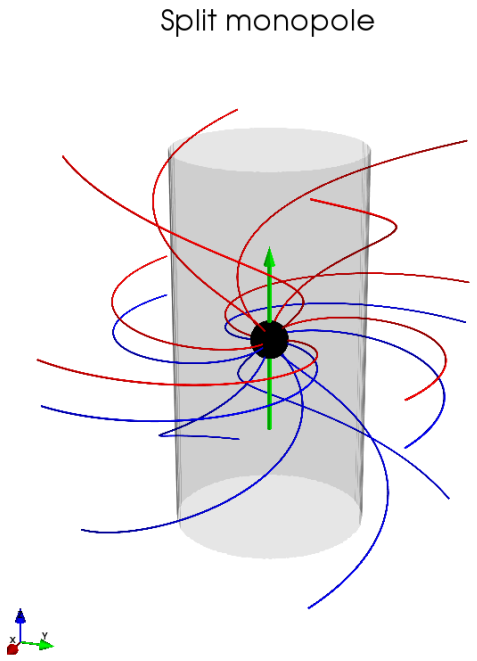

Figure 2.3: Split monopole solution. The green arrow represents the rotation vector. Red lines correspond to the outgoing field lines while blue lines represent the incoming field lines. The field reverses polarity across the equator. The grey cylinder marks the light cylinder radius. Figure taken from Cerutti and Beloborodov (2017).

driving direct volume currents; and (iii) a Y-shaped current layer driving return currents, which separates the open and closed zones inside $R_{\rm LC}$, and which beyond $R_{\rm LC}$ divides open field lines of opposite polarity across the equatorial plane (see Figure 2.4). The spin-down rate of an aligned dipolar rotator can be assessed by estimating the net Poynting flux through the light-cylinder radius, $L_{\rm dipole} \sim cR_{\rm LC}^2 E_\theta B_\phi$, and by considering that at the light cylinder $E_\theta \sim B_\phi \sim 0$, so that:

$$L_{\rm dipole,\ aligned} \approx \frac{\mu^2 \Omega^4}{c^3}\,. \tag{2.78}$$

Time-dependent force-free simulations performed subsequently for both aligned (Komissarov, 2006; McKinney, 2006; Spitkovsky, 2006; Parfrey et al., 2012) and oblique (Spitkovsky, 2006; Kalapotharakos and Contopoulos, 2009; Pétri, 2012; Tchekhovskoy et al., 2013) rotators confirm the overall structure of the stationary axisymmetric solution. However, they reveal a different, wobbling current sheet geometry in the inclined case, compared to the flat current sheet in the aligned solution.

Inside the current sheet, the magnetic field vanishes (as it reverses across the current sheet) and the force-free approximation, based on magnetic dominance and neglecting plasma pressure and inertia, breaks down. Force-free models attempt to circumvent this difficulty by introducing an artificial resistivity, while an alternative approach consists in adopting full relativistic MHD descriptions (that include plasma inertia and pressure). However, these models are not adapted to capture the kinetic processes at play in these regions. Moreover, as previoulsy mentioned, the presence of electric gaps and the physics of pair production cannot be accounted for within the force-free framework. This motivates the development of kinetic approaches (Particle-in-cell method), capable of self-consistently modeling the global magnetosphere along with particle acceleration, pair production, and radiation (Philippov and Spitkovsky, 2014; Chen and Beloborodov, 2014; Philippov et al., 2015a,b; Cerutti et al., 2015, 2016; Belyaev, 2015). We emphasize that global magnetospheric models are essential, since the problem is inherently non-local: for instance, particle acceleration and pair creation

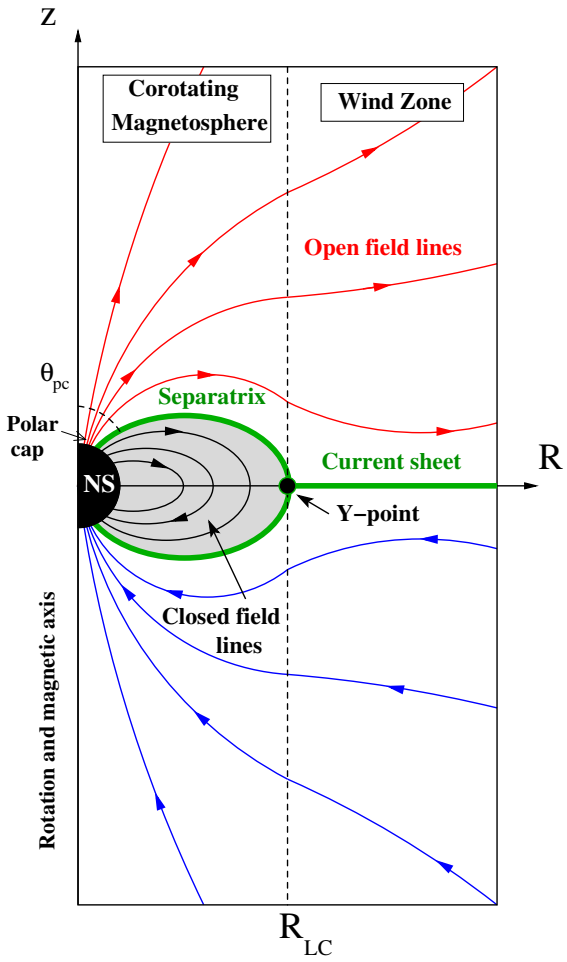

Figure 2.4: Sketch of the aligned pulsar magnetospheric structure obtained by numerical solutions of the pulsar equation. We can distinguish three main zones: (i) The closed field line zone (grey, and black field lines) before the light-cylinder radius. (ii) The open field line zone (red and blue field lines), which extends beyond $R_{\rm LC}$. It carries the ouflowing Poynting flux and the relativistic pulsar wind. (iii) The equatorial current sheet (green) in the wind zone, that lies between opposite magnetic fluxes. Before the light cylinder, it splits into two separatrix current sheets that separate the last open field lines from the first closed field lines. Figure taken from Cerutti and Beloborodov (2017).

at the polar caps are influenced by the global magnetospheric currents, which are themselves regulated by processes in the current sheet.

2.3.4 Current understanding of pulsar magnetospheres

This section outlines the main characteristics of pulsar magnetospheres, based on the current understanding. It integrates results from both force-free models and particle-in-cell simulations to provide a unified global picture that incorporates dynamical and kinetic properties. While not intended as an exhaustive review, this section focuses on introducing the key concepts needed for the following chapters.

As demonstrated by force-free models, three main regions can be distinguished in the magnetosphere: the closed zone, the open zone, and the current sheet, as illustrated in Figure 2.5. Accordingly, our description is divided into three parts, based on this classification.

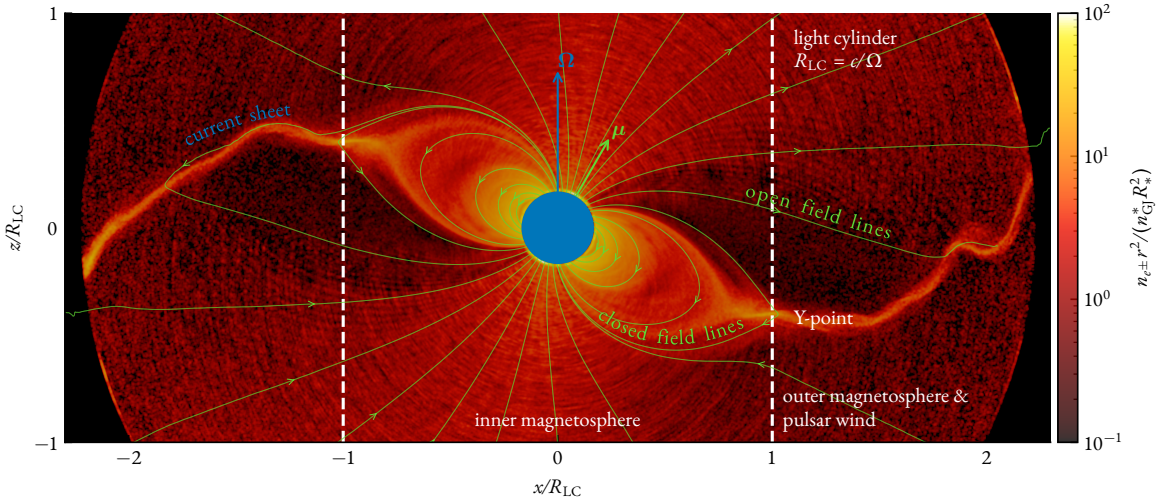

Figure 2.5: Structure of the pulsar magnetosphere and inner part of the wind. 3D Particle-in-cell simulation of an inclined ($\chi = 30°$) pulsar. Colors indicate the density. The neutron star surface and its rotation axis are in blue. Magnetic field lines and the magnetic moment are indicated in green. The white dashed lines trace the light-cylinder radius, separating the magnetosphere from the pulsar wind. Figure taken from Hakobyan et al. (2023).

Closed zone

This region, that constitutes the main structural difference with the split-monopole solution, is characterized by closed magnetic field lines, similar to dipolar field lines, that co-rotate with the star and enforce corotation of the trapped plasma (with charge density ρ_{GJ} to maintain corotation). The absence of poloidal current ($\mathbf{J_p} = 0$) and toroidal magnetic field ($B_\phi = 0$) implies that this zone does not contribute to the pulsar's activity. Corotation is only possible within the light-cylinder radius, hence the closed region is confined inside R_{LC}. More precisely, it is bounded by the Y-point, defined as the location where the last closed magnetic field line connects to the equatorial current sheet. Although expected at R_{LC}, the Y-point has been found to lie at $r \leq R_{LC}$ (see, for example, Hakobyan et al. 2023). In addition to the trapped corotating plasma, some pair plasma produced by photons emitted in the current sheet near the Y-point may leak into and become trapped within the closed zone.

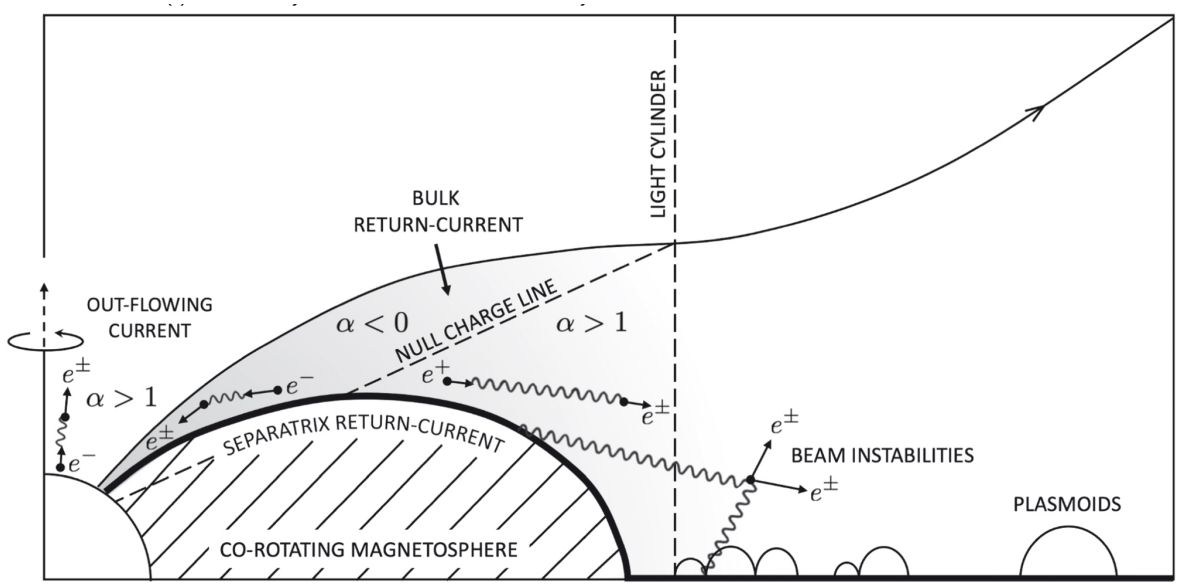

Figure 2.6: Schematic representation of currents and pair production in the magnetosphere. The thick black line marks the current sheet and the separatrix. The hatched region indicates the closed zone. A volume return current flows in the grey shaded area. Figure taken from Bransgrove et al. (2023).

Open zone

Magnetic field lines anchored near the stellar poles extend beyond the light cylinder and, due to rotation, open to infinity. Indeed, since the field is frozen into the plasma, corotation outside $R_{\rm LC}$ would require an azimuthal velocity of the plasma $v_\phi = \Omega r \sin\theta$ exceeding the speed of light. The region on the stellar surface from which these open field lines originate is referred to as the "polar cap", and its angular aperture $\theta_{\rm pc}$ can be estimated by assuming a dipolar magnetic field in the closed zone and magnetic flux conservation:

$$\sin^2\theta_{\rm pc} \approx \frac{\mathrm{r}_\star}{\mathrm{R}_{\rm LC}}\,, \tag{2.79}$$

so that the polar cap radius is $R_{\rm pc} \approx r_\star\sqrt{r_\star/R_{\rm LC}}$. This region is characterized by the presence of a direct volume current from the poles ($\mathbf{J_p} \neq \mathbf{0}$), with plasma flowing outwards from the surface along magnetic field lines, and a non-zero toroidal magnetic field ($B_\phi \neq 0$), which becomes increasingly dominant with radius. As a result, a poloidal electric field is induced in the wind zone and a Poynting flux is carried outward at nearly the speed of light, driving the relativistic pulsar wind. It is the active part of the magnetosphere, mostly responsible for the pulsar spin-down:

$$\dot{E} = -L\,, \tag{2.80}$$

where L is the net radial Poynting flux. An approximate formula for the spin-down power of the oblique rotator magnetosphere in the force-free limit was obtained from 3D time-dependent simulations (Spitkovsky, 2006):

$$L_{\rm dipole} \approx \frac{\mu^2\Omega^4}{c^3}(1+\sin^2\chi)\,. \tag{2.81}$$

Near the pulsar surface, the magnetization is very high and particles predominantly flow along magnetic field lines. They also experience a drift ($v_{\rm D}$) perpendicular to magnetic field lines

$$v_{\rm D} = c\frac{\boldsymbol{E}\times\mathbf{B}}{B^2}\,. \tag{2.82}$$

Its corresponding Lorentz factor is rather small near the light cylinder, but progressively increases with radius. In the outer parts of the wind, where the magnetic field becomes predominantly toroidal and plasma mainly flows radially, the plasma motion is dominated by the drift velocity (before reaching the fast magnetosonic point).

In regions where the plasma fails to supply the required current, or carries it with the wrong sign of charge, Ampère's law induces a parallel electric field $E_\parallel$. In particular, some plasma-starved regions can form at the pulsar surface. In these regions, particles (mainly electrons) are extracted from the surface and are accelerated along the curved field lines by the strong parallel electric fields (see Figure 2.6). Doing so, they emit a high-energy curvature radiation which converts into electron-positron pairs in the strong magnetic field present at the star surface, via the $\gamma + B \to e^- + e^+$ channel (Erber, 1966). The newly-produced pairs radiate via synchrotron processes (or inverse-Compton scattering of X-ray photons radiated from the star surface), thereby leading to the production of supplementary pairs (via both $\gamma + B$ conversion and $\gamma - \gamma$ collisions), themselves subsequently accelerated. In the outer parts of the magnetosphere, pairs are primarily created via $\gamma - \gamma$ photon collisions, due to the decrease of the magnetic field strength with radius. This turns into a cascade of gamma-rays and secondary particle pairs, referred to as "pair cascade" or "pair discharge" (see Figure 2.7), until the density of plasma allows it to almost fully screen the parallel electric field, nearly satisfying the $E_\parallel = \mathbf{E} \cdot \mathbf{B}/B = 0$ condition. Once this condition is fulfilled, pair creation stops momentarily, and restarts when the newly formed plasma is accelerated away, thus leading to the appearance of new electric gaps. Hence, pair cascades are intermittent (Timokhin, 2010; Timokhin and Arons, 2013). This procces mostly happens at the polar caps, over a distance of about $r_\star$ above the surface, and can be quantified by the cascade multiplicity parameter

$$\kappa = \frac{n}{n_{\rm GJ}}\,, \tag{2.83}$$

which typical values range from 10^3 and 10^6. General relativistic effects have been shown to be important in the activation of pair production close to the magnetic poles (Philippov et al., 2015a; Gralla et al., 2016; Belyaev and Parfrey, 2016; Philippov and Spitkovsky, 2018; Torres et al., 2024). Radio emission originating in the inner magnetosphere is associated with pair cascades occurring above the polar caps. To avoid the accumulation of net electric charge on the star surface, positive return currents compensate the negative charge extracted from the polar cap. The current sheet and the separatrix (see next section) carry part of the return current, while another fraction originates from the outer regions of the polar cap, before $R_{\rm LC}$ (see the grey area in Figure 2.6).

The maximum energy that an electron can reach from the voltage drop at the polar cap is

$$\gamma_{\rm pc} = \frac{e\Phi_{\rm pc}}{m_e c^2}\,, \tag{2.84}$$

where, due to Eq. (2.79),

$$\Phi_{\rm pc} = \int_0^{\theta_{\rm pc}} E_\theta(r_\star) r_\star {\rm d}\theta = \frac{B_\star r_\star^3}{R_{\rm LC}^2} = \frac{\mu\Omega^2}{c^2}\,. \tag{2.85}$$

As mentioned in Section 2.1, the magnetic field and rotation frequency of isolated pulsars decay over time. Hence, this potential drop decays accordingly and primary particles accelerated in old enough pulsars may not reach high enough Lorentz factors to produce pairs via the $\gamma - \gamma \to e^+ + e^-$ channel. In such case, pair production can still occur near the surface (via $\gamma + B \to e^+ + e^-$). If a pulsar slows down sufficiently (and depending on its magnetic field decay, structure, and other magnetospheric factors), it crosses a theoretical boundary in the P–$\dot{P}$ diagram called the "death line," beyond which pair production ceases and, under the standard radio emission model, the neutron star can no longer generate observable radio signals (Chen and Ruderman, 1993).

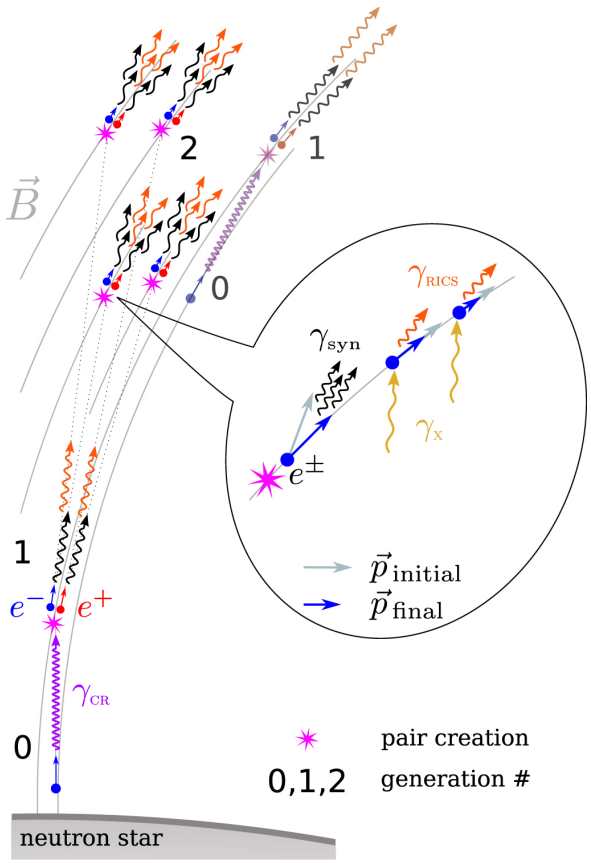

Figure 2.7: Sketch of a pair cascade in the polar cap of a young pulsar with a strong magnetic field. The labels $\gamma_{\rm CR}$, $\gamma_{\rm syn}$, and $\gamma_{\rm RICS}$ denote photons produced via curvature, synchrotron, and resonant inverse Compton processes, respectively. Figure taken from Timokhin and Harding (2019).

Current layer

Before the Y-point, the jump in B_ϕ at the boundary between opened and closed field lines creates a thin return current layer, called the "separatrix". Beyond the Y-point, an equatorial current sheet arises from the reversal of the magnetic field across the equator. Both the separatrix and the current sheet carry most of the return current that compensates the opposite current originating from the polar caps, thereby ensuring a null net current through the stellar surface and therefore a neutral stellar charge. The return current flowing along the separatrix is mostly sustained by pair creation around the Y-point (Hu and Beloborodov, 2022). Electrons are mainly found near the Y-point and along the separatrix. Indeed, after being extracted in the polar caps, they flow out in the wind until they are attracted by the equatorial current sheet, that accelerates them back to the stellar surface. On the other hand, positrons mainly lie in the current sheet beyond the Y-point. They flow outwards along the separatrix, reach the Y-point where they gain most of their energy, and pursue outwards along the current sheet. Overall, the separatrix is negatively charged, while the current sheet is positively charged.

While aligned dipoles develop a planar equatorial current sheet beyond the light cylinder, inclined magnetic moments produce a current sheet oscillating in θ around the equatorial plane, with an amplitude set by the inclination angle χ and a wavelength of $2\pi R_{\rm LC}$ (see Figure 2.5). In the equatorial plane, the current sheet takes the form of two inspiral branches separating magnetic stripes of alterning polarity, hence the appellation "striped wind".

PIC simulations have shown that the current sheet beyond the Y-point is the primary site of Poynting flux dissipation into particle acceleration in pulsar magnetospheres (Chen and Beloborodov, 2014; Philippov et al., 2015b), due to magnetic reconnection (see Section 2.4 for details). About 1 to 10% of the spin-down power is dissipated in the current sheet (Cerutti et al., 2020), with most of the dissipation occurring in the inner wind region, from the Y-point out to a few $R_{\rm LC}$. Magnetic reconnection efficiently accelerates particles, producing a power-law energy spectrum. The mean energy reached by particles in the current sheet was shown (Philippov and Spitkovsky, 2014; Cerutti et al., 2015) to be controlled by the magnetization parameter at $R_{\rm LC}$ evaluated upstream of the current sheet ($\sigma_{\rm LC}$), which can also be expressed in terms of the polar cap potential drop (Eq. 2.84):

$$\langle\gamma\rangle \sim \sigma_{\rm LC} \sim \frac{\gamma_{\rm pc}}{\kappa\Gamma}\,, \tag{2.86}$$

where κ is the multiplicity parameter (Eq. 2.83) assessed upstream of the current sheet, and Γ is the bulk Lorentz factor of the wind.

Cerutti et al. (2020) argue that, in isolated pair producing pulsars, dissipation proceeds efficiently at all radii up to $\sim 10^2 - 10^4\ R_{\rm LC}$. This implies that the striped structure of the wind may disappear before the wind reaches the termination shock radius, $R_{\rm TS}$ (e.g., for the Crab pulsar, $R_{\rm TS}/R_{\rm LC} \sim 10^9$). This finding is particularly interesting, as it highlights the relevance of pulsar binary systems in which the companion lies at much smaller radii. Indeed, in such systems, the pulsar wind is truncated by the companion's surface, stellar wind, or accretion disk, allowing us to probe the inner wind regions, and therefore the striped wind itself.

Particles accelerated in the current sheet radiate via synchrotron processes. Their cooling time is short, which leads to the emission of high-energy photons and the powering of most of the high-energy emission originating from pulsar magnetospheres, with radiative efficiencies of the order of $L_\gamma/L_{\rm spin-down} \sim 1 - 10\%$. The current understanding of the magnetospheric structure enables to explain the observed pulsed GeV and TeV emission (Bai and Spitkovsky, 2010; Cerutti et al., 2016; Philippov and Spitkovsky, 2018; Hakobyan et al., 2023). Radio pulses observed simultaneously to the high-energy ones are also related to magnetic dissipation in the current sheet, although attributed to a different radiative mechanism (see Chapter 4;

and also Uzdensky and Spitkovsky 2014; Lyubarsky 2019; Philippov et al. 2019; Bransgrove et al. 2023).

The two following sections describe in further details: (i) the Poynting flux dissipation into particle acceleration inside the current sheet; and (ii) the radiative processes responsible for the high-energy radiation emitted by pulsar magnetospheres.

2.4 Particle acceleration in the current sheet

2.4.1 Relativistic generalized Ohm's law in the collisionless limit

Magnetic reconnection is a powerful mechanism of non-thermal particle acceleration. It refers to a topological rearrangement of the large-scale magnetic field driven by microscopic plasma processes, in particular the breaking and reconnection of magnetic field lines of opposite polarities. Magnetic reconnection corresponds to a breakdown of the frozen-in flux condition, i.e., it requires going beyond the ideal Ohm's law. Moreover, for high magnetizations ($\sigma \gg 1$), magnetic reconnection proceeds in the relativistic regime, as $V_A = c\sqrt{\sigma/1+\sigma} \sim c$. For each species, the relativistic generalized Ohm's law in the collisionless limit is the following:

$$\boldsymbol{E} + \frac{\langle \boldsymbol{v} \rangle}{c} \times \boldsymbol{B} = \frac{\nabla \cdot \boldsymbol{P}}{qn} + \frac{m}{q}\left(\frac{\partial \langle \boldsymbol{u} \rangle}{\partial t} + (\langle \boldsymbol{v} \rangle \cdot \nabla)\langle \boldsymbol{u} \rangle\right) \tag{2.87}$$

where m and q are respectively the specie mass and charge, n is the particle number density, $\langle \boldsymbol{u} \rangle$ the mean particle 4-velocity, and $\boldsymbol{P}$ the pressure tensor (Sironi et al., 2025). In collisionless pair plasmas (and in electron–ion plasmas at the X-point), reconnection is mediated by the off-diagonal terms of the particle's pressure tensor (Bessho and Bhattacharjee, 2005).

2.4.2 Magnetic reconnection

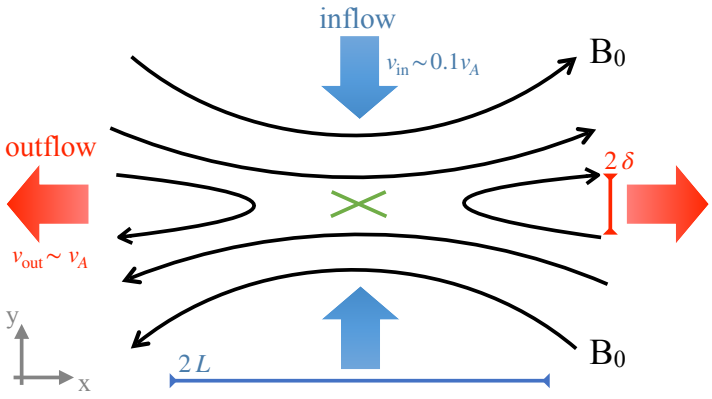

Figure 2.8: Sketch of a magnetic X-point. The green cross marks the X-point. Blue arrows represent the approaching magnetic field lines and inflowing plasma, while red arrows represent the direction in which reconnected field lines and plasma are expelled. B_0 denotes the upstream magnetic field strength. Figure taken from Sironi et al. 2025.

Magnetic reconnection proceeds in regions called "X-points" (see green cross in Figure 2.8). At the X-point, magnetic field lines of opposite polarities, frozen into the plasma, come together due to plasma experiencing an $\boldsymbol{E} \times \boldsymbol{B}$ drift at speed $v_{\rm in}$ into the current layer. As they reach the X-point, non-ideal microscopic effects become important and allow the magnetic field lines to reconnect and be expelled, thus releasing magnetic tension, in the perpendicular direction at speed $v_{\rm out} \sim V_{\rm A}$, where $V_{\rm A}$ is the Alfvén speed corresponding to the upstream

magnetic field B_0. Particles carried by the reconnecting field lines are accelerated at the X-point. Indeed, according to ideal MHD, the upstream electric field, directed along the z-axis (see Figure 2.8), reads:

$$E_{\rm upstream} = \frac{v_{\rm in} B_0}{c} \,. \tag{2.88}$$

A non-ideal electric field $E_{\rm rec}$ emerges at the X-point[7], in the z-direction and can be shown to be $\boldsymbol{E}_{\rm rec} = \boldsymbol{E}_{\rm upstream}$ (Sironi et al., 2025). This electric field induces currents directed along the z-axis, through non-ideal effects. The Poynting's theorem states:

$$\partial_t(u_e) + \nabla \cdot \mathbf{\Pi} = -\mathbf{J} \cdot \mathbf{E} \,, \tag{2.89}$$

where $u_e = (\mathbf{E}^2 + \mathbf{B}^2)/8\pi$ is the electromagnetic energy density and $\Pi = (\mathbf{E} \times \mathbf{B}/4\pi)$ is the Poynting flux. Hence, between two successive spherical surfaces, if the total electromagnetic energy density is conserved, the emergence of a non-zero $\mathbf{J} \cdot \mathbf{E}$ term implies Poynting flux dissipation into particles kinetic energy. A particle of energy ϵ and charge e gains energy at a rate $\dot{\epsilon} \sim e v_{\rm in} B_0$. Particles accelerated by magnetic reconnection in the current layer ultimately form a power-law distribution.

The dimensionless reconnection rate is defined as the ratio between the speed at which the upstream magnetic flux and its associated plasma are carried towards the reconnecting current sheet due to a magnetic X-point, and the outflowing velocity from the X-point. Assuming mass-conservation allows us to express it as the aspect ratio of the layer:

$$\beta_{\rm rec} = \frac{v_{\rm in}}{v_{\rm out}} = \frac{v_{\rm in}}{V_{\rm A}} = \frac{\delta}{L} \,, \tag{2.90}$$

where δ and L respectively are the typical thickness and length of the current layer. In the relativistic limit, $V_{\rm A} \sim c$ and, according to Eqs. (2.88) and (2.90), the relativistic reconnection rate can also be expressed as the ratio between the upstream electric and magnetic fields.

According to the original model of magnetic reconnection (i.e., the Sweet-Parker model in non-relativistic MHD; Sweet 1958; Parker 1963), the layer thickness is microscopic, while the layer length is expected to be of the order of the system size, hence macroscopic. As a result, Eq. (2.90) tells us that the reconnection rate should be $\beta_{\rm rec} \ll 1$, since $\delta \ll L$. This is in strong contradiction with observations of the solar corona and the Earth's magnetosphere, where $v_{\rm in} \sim 0.1 V_{\rm A}$ (Isobe et al., 2005; Phan et al., 2007). These measurements would imply $v_{\rm in} \sim 0.1c$ in a relativistic regime, which appears to be corroborated by simulations of relativistic magnetic reconnection in collisionless plasmas. However, current sheets have been shown to be subject to a nonlinear interplay of several plasma instabilities, which enhance the reconnection rate and thereby resolve this apparent inconsistency. Relativistic magnetic reconnection in collisionless plasmas has been extensively studied over the past decades, especially since the advent of kinetic (PIC) simulations, providing strong progress in the understanding of the processes at play (see Sironi et al. 2025 for a review).

2.4.3 Instabilities in the current sheet

The current sheet is unstable to various instabilities. Here, we present the main ones.

The tearing instability (also referred to as "plasmoid instability") inherently triggers fast reconnection, as it tears apart a thin current layer, causing it to fragment into a chain of magnetic loops, called "magnetic islands" (or "flux ropes" in 3D), separated by secondary current layers. These magnetic loops are filled with plasma, so that they are also referred to as "plasmoids" (Figure 2.9). In pulsar magnetospheres, the tearing instability extends to a non-linear, dynamical phase, where the current sheet fragments into a hierarchical chain

[7] The location where the electric field first develops - within the current sheet or in the ideal region - depends on whether reconnection is externally induced or occurs spontaneously.

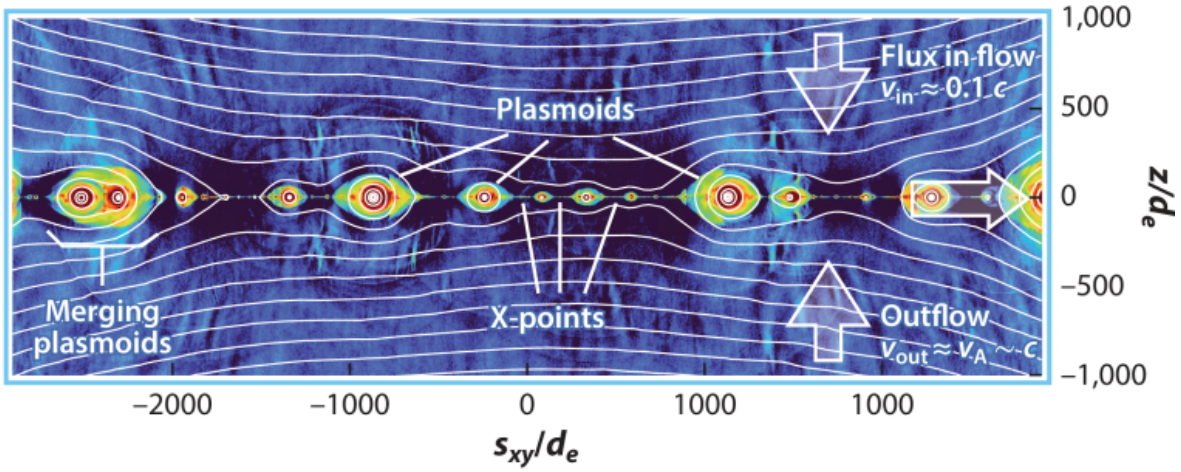

Figure 2.9: Reconnecting current sheet, from a local 2D PIC simulation. Colors indicate the plasma density and white lines trace the magnetic field lines. d_e denotes the plasma skin depth. Figure taken from Philippov and Kramer (2022).

of plasmoids. Secondary current layers feed the adjacent plasmoids. Plasmoids grow and eventually merge, thereby stretching the secondary current layers and causing them to become unstable. Mergers of plasmoids sometimes also lead to the appearance of secondary current sheets at the merger interface, i.e., perpendicular to the primary current sheet.

The current sheet is also unstable to the relativistic drift-kink instability, an ideal instability that causes the rippling of the current sheet in the z-direction. In 3D, flux ropes of sufficiently large sizes created by the tearing instability become unstable to the corresponding kink instability ("flux-rope kink instability"), which causes their displacement in the z-direction. Figure 2.10 provides a visualization of the tearing and kink instabilities arising in a 3D PIC simulation.

2.4.4 Particles spectrum

Over the past two decades, several independent studies have shown that reconnection in high-σ plasmas efficiently produces nonthermal particles, resulting in hard power-law energy spectra that extend over a wide energy range (Zenitani and Hoshino, 2001; Cerutti et al., 2012; Sironi and Spitkovsky, 2014; Werner et al., 2016). Figure 2.11a shows the particle energy spectra for different plasma magnetizations. The spectrum hardens with increasing magnetization, with power-law indices approaching ~ 1, as shown in Figure 2.11. In the ultra-relativistic limit, the acceleration of pairs and ions proceeds in a similar manner, yielding comparable energy spectra.

2.5 Synchrotron-curvature radiation

Pulsars emit across the entire electromagnetic spectrum, from radio waves to γ-rays. Radio emission is primarily produced through coherent processes in the open-field-line regions near the polar caps, as well as near the light cylinder through magnetic reconnection processes for pulsars with strong magnetic fields, but its generation mechanisms are not discussed here. Instead, we concentrate on incoherent, non-thermal emission from accelerated particles throughout the magnetosphere, which accounts for the observed high-energy emission. The primary source of high-energy emission beyond the light cylinder is synchrotron radiation (Cerutti et al., 2016), which is the relativistic counterpart of cyclotron radiation. Curvature radiation can also be important, in particular near the star surface. Hence, we limit our study

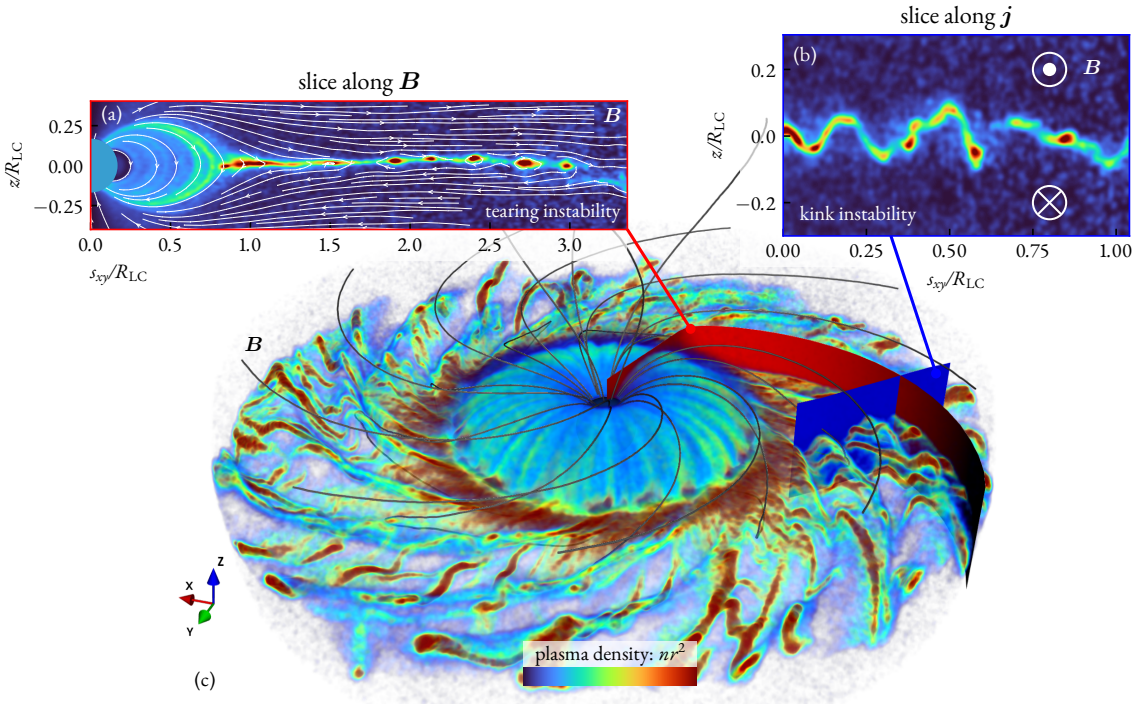

Figure 2.10: 3D PIC simulation of a global pulsar magnetosphere, for an aligned rotator. Colors indicate the density, compensated by r^2. Panel (c) shows the current sheet, whth the densest regions corresponding to flux ropes. Gray lines trace open field lines. Panel (a) shows a slice along the magnetic field lines, so as to highlight the tearing instability. Panel (b) shows a slice along the currents perpendicular to the magnetic field, so as to highlight the kink instability. Figure taken from Hakobyan et al. (2023).

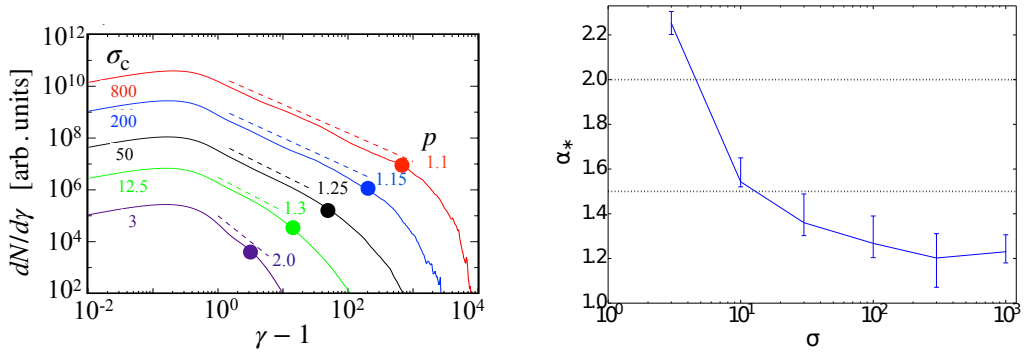

Figure 2.11: Energy spectrum of particles accelerated by relativistic magnetic reconnection, in a pair plasma. Panel (a) shows the spectra obtained from 2D PIC simulations and the hardening of the spectrum with increasing magnetization (σ_c). Figure taken from Sironi et al. (2025). Panel (b) shows the power-law index ($\alpha_\star$) of the spectrum as a function of the upstream magnetization (σ). Figure taken from Werner et al. (2016).

to synchrotron-curvature radiation, and neglect other radiative processes, such as inverse Compton, synchrotron self-Compton or bremsstrahlung.

As we will see, this radiation is emitted by accelerated particles evolving in an electromagnetic field, and thus carries away energy and momentum from the emitting particles. Before presenting the various properties of synchrotron-curvature radiation, we therefore introduce the radiation reaction force that accounts for the feedback of radiation on particle motion.

2.5.1 Radiation reaction force

According to classical electrodynamics, the equation of motion of a charged particle evolving in an electromagnetic field reads:

$$\frac{\mathrm{d}p^\mu}{\mathrm{d}\tau} = m\frac{\mathrm{d}u^\mu}{\mathrm{d}\tau} = \frac{q}{c}F^{\mu\nu}u_\nu \,, \tag{2.91}$$

where u^ν and p^μ are respectively the 4-velocity and the 4-momentum of the particle, τ the proper time of the particle, q its charge, and $F_{\mu\nu}$ the covariant electromagnetic tensor, given by :

$$F_{\mu\nu} = \begin{pmatrix} 0 & E_x & E_y & E_z \\ -E_x & 0 & -B_z & B_y \\ -E_y & B_z & 0 & -B_x \\ -E_z & -B_y & B_x & 0 \end{pmatrix}$$

with the (+,-,-,-) metric signature.

However, when a particle is subject to radiative energy losses, an additional force, called radiation-reaction force, must be taken into account. Such motion of a classical charged particle in the presence of an external electromagnetic field was first described by Lorentz in a non-relativistic limit, extended to the relativistic case by Abraham (Abraham, 1902, 1904) and then re-expressed in a covariant form by Dirac (Dirac, 1938), finally giving the so-called Lorentz-Abraham-Dirac equation:

$$m\frac{\mathrm{d}u^\mu}{\mathrm{d}\tau} = \frac{q}{c}F^{\mu\nu}u_\nu + g^\mu \,, \tag{2.92}$$

where g^μ is the radiation-reaction force, given by

$$g^\mu = \frac{2q^2}{3c^3}\left(\frac{\mathrm{d}^2u^\mu}{\mathrm{d}\tau^2} - u^\mu u^\nu \frac{\mathrm{d}^2u_\nu}{\mathrm{d}\tau^2}\right) . \tag{2.93}$$

Equation (2.92) was shown to be defective for various mathematical and physical reasons (see, for example, Piazza 2008). In particular, by containing the time derivative of the acceleration of the charge, it lead to solutions displaying an exponential increase of the particle acceleration even in the absence of any external field (i.e., “runaway”solutions). Landau and Lifschitz (1975) proposed a new expression of the radiation-reaction force contained in the Lorentz-Abraham-Dirac equation, for a particle evolving in an external electromagnetic field[8], that had the advantage of avoiding the above problems. Indeed, they reformulated the reaction force (Eq. 2.93) so that Eq. (2.92) becomes a second-order differential equation. To do so, they assumed that, in the rest frame of the charged particle, the reaction force is negligible compared to the Lorentz force, so that the derivatives of the four-velocity appearing in Eq. (2.93) can be inferred from the zero-order expression of the equation of motion (Eq. 2.91). As a result, they obtained:

$$g^\mu = \frac{2q^3}{3mc^3}\left(\partial_\alpha F^{\mu\nu}u_\nu u^\alpha\right) - \frac{2q^4}{3m^2c^5}F^{\mu\nu}F_{\alpha\nu}u^\alpha + \frac{2q^4}{3m^2c^5}\left(F_{\nu\beta}u^\beta\right)\left(F^{\nu\alpha}u_\alpha\right)u^\mu \,. \tag{2.94}$$

[8]The Lorentz-Abraham-Dirac equation is more general and could apply to other external forces than those induced by electromagnetic fields.

A mathematical approach to this problem (Spohn, 2000) also corroborated this result, by considering, among all possible solutions of the Lorentz-Abraham-Dirac equation, a sub-manifold of physical solutions characterized by asymptotically vanishing acceleration, which can all be obtained by perturbation expansion (Rohrlich, 2008). We recall that these are classical equations that stay valid only until quantum effects remain negligible.

The corresponding three-dimensional expression, accounting for the reaction force induced by synchrotron and curvature radiation, is:

$$\begin{aligned}\mathbf{g} = \frac{2q^3}{3m_e c^3}\gamma\left[(\partial_t + c\boldsymbol{\beta}\cdot\nabla)\,\mathbf{E} + \boldsymbol{\beta}\times(\partial_t + c\boldsymbol{\beta}\cdot\nabla)\mathbf{B}\right] \\ +\frac{2}{3}\frac{q^4}{m^2c^4}\left[(\mathbf{E}+\boldsymbol{\beta}\times\mathbf{B})\times\mathbf{B} + (\boldsymbol{\beta}\cdot\mathbf{E})\mathbf{E}\right] \\ -\frac{2}{3}\frac{q^4}{m^2c^4}\gamma^2\left[(\mathbf{E}+\boldsymbol{\beta}\times\mathbf{B})^2 - (\boldsymbol{\beta}\cdot\mathbf{E})^2\right]\boldsymbol{\beta}\,. \end{aligned} \tag{2.95}$$

The first term of Eq. (2.95) has been shown to be negligible compared to the others (Tamburini et al., 2010). For ultra-relativistic particles, $\gamma \gg 1$ and the third term of Eq. (2.95) is dominant. It acts as a drag force opposite to the particle velocity and is proportional to the radiative power (Eq. 2.107). However, it is worth mentioning that the second term was shown to be important to properly model curvature radiation (Cerutti et al., 2016).

2.5.2 Effective perpendicular magnetic field

The general motion of a charged particle in an electromagnetic field, when neglecting the radiation reaction force, is given by Eq. (2.91). Considering respectively the first component ($\mu = 0$) and the spatial component ($\mu = 1, 2, 3$), we obtain the following system (Rybicki and Lightman, 1979):

$$\frac{(\mathrm{d}\gamma)mc}{\mathrm{d}t} = q\mathbf{E}\cdot\boldsymbol{\beta} \tag{2.96}$$

$$\frac{\mathrm{d}(\gamma mc\boldsymbol{\beta})}{\mathrm{d}t} = q(\mathbf{E}+\boldsymbol{\beta}\times\mathbf{B})\,. \tag{2.97}$$

Developping Eq. (2.97) yields

$$\frac{\mathrm{d}\gamma}{\mathrm{d}t}mc\boldsymbol{\beta} + \gamma mc\frac{\mathrm{d}\boldsymbol{\beta}}{\mathrm{d}t} = q(\mathbf{E}+\boldsymbol{\beta}\times\mathbf{B})\,, \tag{2.98}$$

and, by injecting Eq. (2.96) into Eq. (2.98), we obtain

$$\frac{\mathrm{d}\boldsymbol{\beta}}{\mathrm{d}t} = \frac{q}{\gamma mc}(\mathbf{E}+\boldsymbol{\beta}\times\mathbf{B} - (\boldsymbol{\beta}\cdot\mathbf{E})\boldsymbol{\beta})\,. \tag{2.99}$$

In the usual synchrotron regime, where the electric field can be neglected ($\mathbf{E} = \mathbf{0}$), the equation of motion of a charged particle reads

$$\frac{\mathrm{d}\boldsymbol{\beta}}{\mathrm{d}t} = \frac{q}{\gamma mc}(\boldsymbol{\beta}\times\mathbf{B})\,, \tag{2.100}$$

and the particle undergoes a helical motion (see Figure 2.12) of gyration frequency

$$\omega = \frac{qB}{\gamma mc}\,. \tag{2.101}$$

Identifying the right-hand terms of Eq.(2.100) and Eq.(2.99), we can define a new effective perpendicular magnetic field $\tilde{\mathbf{B}}_\perp$ so that

$$\tilde{\mathbf{B}}_\perp = \mathbf{E}+\boldsymbol{\beta}\times\mathbf{B} - (\boldsymbol{\beta}\cdot\mathbf{E})\boldsymbol{\beta}\,, \tag{2.102}$$

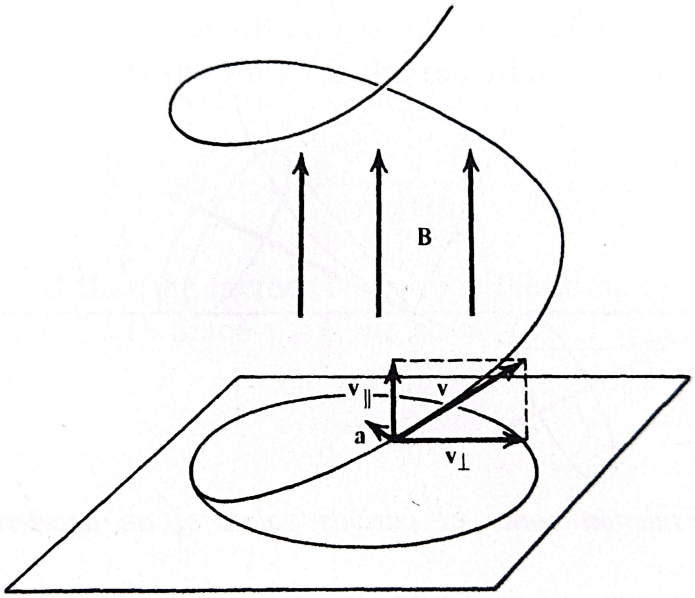

Figure 2.12: Schematic view of a charged particle undergoing helical motion in a uniform magnetic field ($\boldsymbol{B}$). The labels $\boldsymbol{a}$, $\boldsymbol{v}$, $\boldsymbol{v}_{\parallel}$ and $\boldsymbol{v}_{\perp}$ respectively denote the particle acceleration, velocity, parallel velocity and perpendicular velocity (with respect to the magnetic field). Figure taken from Rybicki and Lightman (1979).

where $\tilde{\mathbf{B}}_{\perp}$ is the perpendicular magnetic field for an arbitrary electromagnetic field (i.e., $\boldsymbol{E} \neq 0$). In pulsar environments, the electric and magnetic field strengths are comparable, so we will consistently use this expression in our work. We neglect quantum electrodynamical effects reached above the critical magnetic field, $B_{\rm QED} = m_e^2 c^3/\hbar e$, since we globally have $\gamma\tilde{\mathbf{B}}_{\perp} \ll B_{\rm QED}$ in the magnetosphere. It is worth mentioning that, in the relativistic limit, one can show:

$$\tilde{\mathbf{B}}_{\perp} \cdot \boldsymbol{\beta} = 0\,, \tag{2.103}$$

meaning that the acceleration and velocity are perpendicular, according to Eq. (2.100).

2.5.3 Radiation power

Accelerated charges radiate. The total power radiated by a non-relativistic charge is given by the Larmor formula:

$$\mathcal{P}_{\rm Larmor} = \frac{2}{3}\frac{q^2\mathbf{a}^2}{c^3}\,, \tag{2.104}$$

where $\mathbf{a}$ is the 3-acceleration of the particle. The Lorentz invariant generalization of this formula, valid in particular for relativistic charges, reads:

$$\mathcal{P}_{\rm Larmor,relat} = \frac{2q^2}{3m^2c^3}\left(\frac{{\rm d}p^{\mu}}{{\rm d}\tau}\frac{{\rm d}p_{\mu}}{{\rm d}\tau}\right)\,. \tag{2.105}$$

This result is independent of the accelerating force. For a particle evolving in an electromagnetic field, we substitute ${\rm d}p^{\mu}/{\rm d}\tau$ by the Lorentz force $(q/c)F^{\mu\nu}u_{\nu}$:

$$\mathcal{P}_{\rm rad} = \frac{2q^4}{3m^2c^5}(F^{\mu\nu}u_{\nu})(F_{\mu\rho}u^{\rho})\,. \tag{2.106}$$

The Lorentz-invariant expression can be rewritten in terms of the electric and magnetic fields in the laboratory frame, yielding the following three-dimentional formulation of the radiated power:

$$\mathcal{P}_{\rm rad} = \frac{2}{3}\frac{q^4}{m^2c^3}\gamma^2\left[(\mathbf{E}+\boldsymbol{\beta}\times\mathbf{B})^2 - (\boldsymbol{\beta}\cdot\mathbf{E})^2\right]\,. \tag{2.107}$$

In the ultra-relativistic limit ($\beta \sim 1$), one can show that

$$(\mathbf{E} + \boldsymbol{\beta} \times \mathbf{B})^2 - (\boldsymbol{\beta} \cdot \mathbf{E})^2 = \tilde{\mathbf{B}}_\perp^2 \,, \tag{2.108}$$

enabling us to recast Eq. (2.107) into the form

$$\mathcal{P}_{\rm rad} = \frac{2}{3}\frac{q^4}{m^2c^3}\gamma^2 \tilde{B}_\perp^2 \,. \tag{2.109}$$

We note that, in a pure magnetic field (i.e., $\mathbf{E} = \mathbf{0}$), Eq. (2.107) reduces to the well-known Larmor expression (Rybicki and Lightman, 1979):

$$\mathcal{P} = \frac{2}{3}\frac{q^4}{m^2c^3}\gamma^2\beta^2 B^2 \sin^2\alpha \tag{2.110}$$

$$= \frac{2}{3}\frac{q^4}{m^2c^3}\gamma^2\beta^2 B_\perp^2 \,, \tag{2.111}$$

where $B_\perp^2 = B^2 \sin^2\alpha$ and α is the pitch angle, i.e., the angle between the magnetic field and the particle's velocity. For an isotropic distribution of velocities, by averaging over all the pitch angles,

$$\langle \sin\alpha \rangle = \frac{1}{4\pi}\int \sin^2\alpha \mathrm{d}\Omega = \frac{2}{3} \,, \tag{2.112}$$

and Eq. (2.110) becomes

$$\langle \mathcal{P} \rangle_\alpha = \left(\frac{2}{3}\right)^2 \frac{q^4}{m^2c^3}\gamma^2\beta^2 B^2 \,. \tag{2.113}$$

The radiative power scales as $1/m^2$, making radiation from electrons much more efficient than that from protons. Substituting the charge q by the electron charge, we can reformulate Eq. (2.113) as follows:

$$\langle \mathcal{P} \rangle_\alpha = \frac{4}{3}\sigma_{\rm T} c \beta^2 \gamma^2 U_{\rm B} \,, \tag{2.114}$$

where $\sigma_{\rm T} = 8\pi r_e^2/3$ is the Thomson cross section, $r_e = e^2/m_e c^2$ is the classical radius of the electron, and $U_{\rm B} = B^2/8\pi$ is the magnetic energy density. This allows us to express the synchrotron cooling time ($t_{\rm sync}$) as a function of the magnetic energy density:

$$t_{\rm sync} = \frac{\gamma m_e c^2}{\langle \mathcal{P} \rangle_\alpha} = \frac{3 m_e c}{4\sigma_{\rm T} U_{\rm B} \gamma \beta^2} \,. \tag{2.115}$$

2.5.4 Power spectrum

The radiative power emitted by a charged particle in its rest frame can be expressed in terms of the angle between the acceleration and the direction of emission (ζ'):

$$\frac{\mathrm{d}\mathcal{P}'_{\rm rad}}{\mathrm{d}\Omega'} = \frac{q^2 a'^2}{4\pi c^3}\sin^2\zeta' \,, \tag{2.116}$$

where primed quantities are evaluated in the rest frame of the particle. The $\sin^2\zeta'$ dependance indicates that the radiation has a dipolar pattern. Yet, due to relativistic beaming effects, the emission in the observer's frame is strongly beamed along the particle's velocity direction. For a particle accelerated perpendicularly with respect to its motion (as it is the case here; see Eq. 2.103), the resulting angular distribution of the radiation is illustrated in Figure 2.13. The radiation is mainly contained within a cone of aperture angle $2/\gamma \ll 1$, so that the observed pulse duration is much shorter than the gyration period. As a result, contrary to the cyclotron radiation, for which the emission frequency equals the gyration frequency of the particle in the magnetic field, the synchrotron radiation can extend to frequencies many times greater

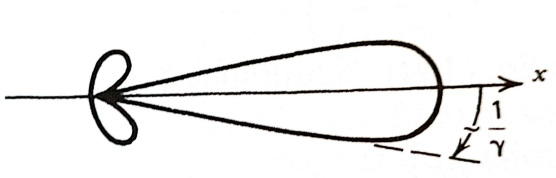

Figure 2.13: Representation of the angular distribution of radiation emitted by a charged particle moving along the x-axis and accelerated perpendicularly. Figure taken from Rybicki and Lightman (1979).

than the particle's gyration frequency, thereby spreading and complexifying considerably the resulting spectrum.

The synchrotron power spectrum emitted by an individual charged particle is given by (Blumenthal and Gould, 1970):

$$\frac{\mathrm{d}P}{\mathrm{d}\nu} = \frac{\sqrt{3}q^3\tilde{B}_\perp}{mc^2}\left(\frac{\nu}{\nu_c}\right)\int_{\nu/\nu_c}^{\infty} K_{5/3}(x)\mathrm{d}x\,, \tag{2.117}$$

where $K_{5/3}$ is the modified Bessel function of order 5/3, ν is the radiation frequency and ν_c is the critial frequency

$$\nu_c = \frac{3q\tilde{B}_\perp\gamma^2}{4\pi mc}\,. \tag{2.118}$$

The total synchrotron spectrum results from summing the emission spectra of individual particles. We know from Sections 2.3.4 and 2.4 that the emitting particles are mainly accelerated via magnetic reconnection, which is a non-thermal process of particle acceleration, leading to a power-law distribution of particles. For a power-law distribution of emitting electrons $N(\gamma) \propto \gamma^{-p}$, the synchrotron spectrum can be expressed as

$$P(\omega) \propto \omega^{-(p-1)/2}\,, \tag{2.119}$$

where $\omega = 2\pi\nu$. Hence, even though the spectrum of a single particle is not a power law, the integrated spectrum from an ensemble of particles with a power-law energy distribution follows itself a power law (see Figure 2.14).

2.5.5 Curvature radiation

Curvature radiation is emitted when charged particles follow curved magnetic field lines. The curvature radius (r_C) can be obtained from the centripetal acceleration formula by equating:

$$a = \frac{v_\mathrm{sync}^2}{r_\mathrm{L}} = \frac{v_\mathrm{curv}^2}{r_\mathrm{C}} \tag{2.120}$$

To describe curvature radiation, we refer to the same formalism as that employed for synchrotron radiation. Since synchrotron radiation is inherently due to transverse motion, $v_\mathrm{sync} = v_\perp$. Conversely, as curvature radiation applies to parallel motion, $v_\mathrm{curv} = v$. Hence,

$$\frac{v_\perp^2}{r_\mathrm{L}} = \frac{v^2}{r_\mathrm{C}}\,. \tag{2.121}$$

In the ultra-relativistic limit ($\beta \sim 1$), we obtain

$$r_\mathrm{C} = \frac{\gamma mc^2}{qB\sin\alpha}\,, \tag{2.122}$$

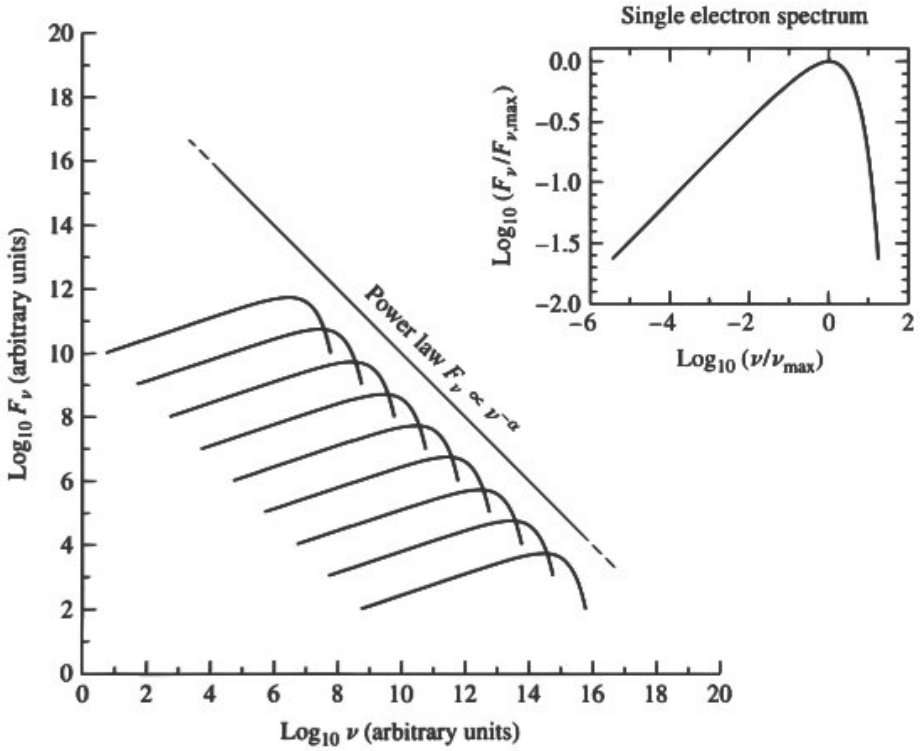

Figure 2.14: Superposition of individual particles spectra producing a power-law spectrum. Figure taken from Carroll and Ostlie (2017).

and substituting r_{C} into Eq. (2.110) yields the following curvature power:

$$\mathcal{P}_{\mathrm{curv}} = \frac{2}{3}\frac{q^2 c \gamma^4}{r_{\mathrm{C}}^2}\,. \tag{2.123}$$

In pulsar magnetospheric models (see Section 2.3), primary photons emitted near the polar caps are produced via curvature radiation. More generally, in the inner magnetosphere, the intense magnetic field causes efficient synchrotron cooling, which reduces particle pitch angles and transverse motion. Particles predominantly slide along magnetic field lines and curvature radiation becomes important near the stellar surface, where field lines are most strongly curved.

Chapter 3

Numerical methods

Contents

3.1 Motivation for PIC simulations 44
3.2 PIC principles 45
3.3 `Zeltron` code 46
3.3.1 PIC algorithm 46
3.3.2 Treatment of divergence constraints 50
3.3.3 Temporal and spatial resolutions 51
3.3.4 Parallelization 51
3.4 Global PIC simulations of pulsar magnetospheres 52
3.4.1 Rescaling 52
3.4.2 Spherical grid 53
3.4.3 Boundary conditions 53
3.4.4 Radiation modeling 54

3.1 Motivation for PIC simulations

The variety of physical processes involved in relativistic magnetospheres, combined with the complex and non-linear interplay between fields and particles, makes an analytical treatment extremely challenging, if not impossible. As discussed in Chapter 2, only highly simplified or very specific configurations can be treated analytically. All other, more complex problems can only be addressed numerically. The numerical treatment consists of sampling time and space and iterate in time to approximate the solution of differential equations at each timestep, based on the solution at the previous time. By employing computational resources capable of handling a very large number of timesteps and grid points, one can, provided stability and convergence criteria are satisfied, construct representative models (i.e., "simulations") of relativistic magnetospheres.

For plasma models, two main approaches are commonly considered: MHD or force-free electrodynamics simulations, which treat the plasma as a fluid, and kinetic simulations, which model the dynamics of individual particles and their interactions through the electromagnetic field. MHD approaches were employed before kinetic ones, as they were much less computationally demanding and still proved very instructive in reproducing the macroscopic structure of relativistic magnetospheres. For instance, they manage to estimate the rotational energy extracted from pulsars, and converted into outflowing Poynting flux. However, as shown in Chapter 3 for the case of pulsars, they fail to capture the microphysical processes at play, responsible for particle acceleration, pair creation and non-thermal radiation. In particular, they cannot estimate the amount of spin-down energy converted into high-energy radiation. Instead, kinetic simulations are particularly well suited to the collisionless plasmas that populate relativistic magnetospheres, as they can self-consistently capture the magnetosphere's dynamics and the processes related to particle acceleration and radiation, that operate at microscopic scales (i.e., skindepth, Larmor radius, and cooling scales), referred to as "kinetic scales."

The evolution of collisionless plasma is governed, for each species s, by the Vlasov equation:

$$\frac{\partial f_s}{\partial t} + \frac{\mathbf{p}}{\gamma m_s} \cdot \frac{\partial f}{\partial \mathbf{r}} + q_s \left(\mathbf{E} + \frac{\mathbf{v} \times \mathbf{B}}{c} \right) \cdot \frac{\partial f_s}{\partial \mathbf{p}} = 0 \tag{3.1}$$

where $f_s \equiv \mathrm{d}N/\mathrm{d}\mathbf{r}\mathrm{d}\mathbf{p}$ is the particle distribution function, $\mathbf{r}$ the position, $\mathbf{p}$ the relativistic momentum, γ, m_s and q_s the Lorentz factor, mass and charge respectively. The Vlasov equation is coupled to Maxwell's equations:

$$\boldsymbol{\nabla} \cdot \mathbf{E} = 4\pi\rho \tag{3.2}$$

$$\boldsymbol{\nabla} \cdot \mathbf{B} = 0 \tag{3.3}$$

$$\boldsymbol{\nabla} \times \mathbf{E} = -\frac{1}{c}\frac{\partial \mathbf{B}}{\partial t} \tag{3.4}$$

$$\boldsymbol{\nabla} \times \mathbf{B} = \frac{4\pi}{c}\mathbf{J} + \frac{1}{c}\frac{\partial \mathbf{E}}{\partial t}\,. \tag{3.5}$$

Numerical kinetic approaches consist either in directly solving the Vlasov equation (Vlasov codes) or in solving it indirectly through a particle approximation, by sampling the distribution function with a set of "macro-particles" (Particle-in-cell codes). Vlasov codes are grid-based solvers of the Vlasov equation, in which the particle distribution function is evolved on a phase-space grid. Several numerical schemes can be employed for this purpose, including spectral methods, conservative finite-volume or finite-difference methods, and semi-Lagrangian methods (see Filbet and Sonnendrücker 2003 for a review). Although Vlasov codes involve lower numerical noise than particle methods, as they do not sample the plasma with macro-particles, the six-dimensional nature of the problem (three spatial plus three momentum dimensions) leads to a tremendously high computational and memory cost for systems as large as magnetospheres, especially in 2D or 3D. Consequently, particle-based methods are much more

commonly used. Among particle-based approaches, the Particle-in-cell (PIC) approach is by far the most widely used in astrophysics[1].

3.2 PIC principles

Reformulating the Vlasov equation as an advection equation and applying the method of characteristics allows one to solve it along the characteristic curves, which correspond to particle trajectories obeying the equations of motion (Sironi and Cerutti, 2017). Each plasma species (s) is approximated by a set of N charged macro-particles characterized by their position $\mathbf{r}_\alpha$ and momentum $\mathbf{p}_\alpha$:

$$f(\mathbf{r}, \mathbf{p}, t) \approx \sum_{\alpha=1}^{N} w_\alpha \, \delta(\mathbf{r} - \mathbf{r}_\alpha(t)) \, \delta(\mathbf{p} - \mathbf{p}_\alpha(t)) \,, \tag{3.6}$$

where δ is the Dirac delta function. Due to numerical costs, simulating all plasma particles is impossible and, instead, each simulated particle (i.e., each macro-particle) represents a huge number of physical particles, given by the weight w_α, with the same q/m ratio and therefore following the same trajectory in phase space.

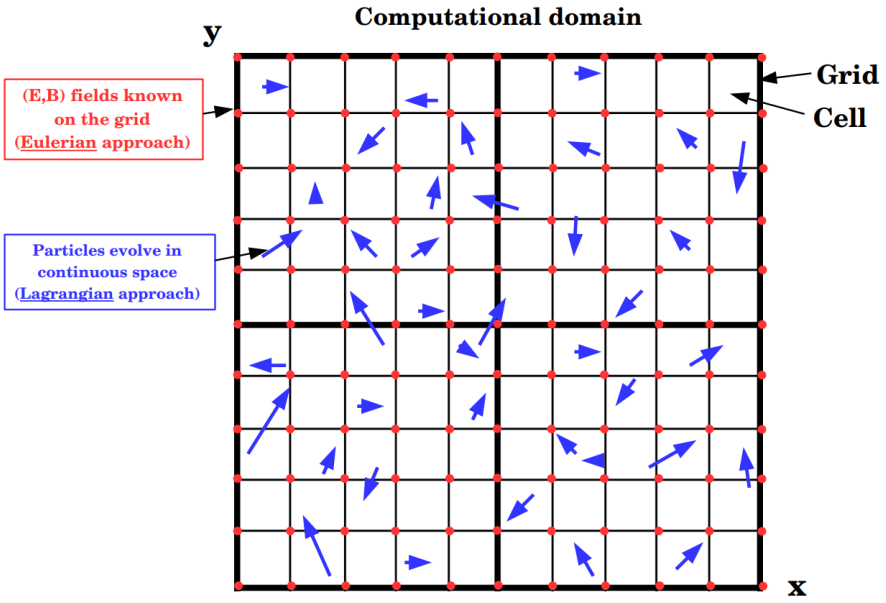

Figure 3.1: Illustration of the PIC computational domain, for a cartesian grid. Figure taken from Cerutti (2021).

As shown in Figure 3.1, the essence of the PIC approach is to represent macro-particles in continuous phase space (Lagrangian approach) while computing moments of the distribution (charge densities and currents) and electromagnetic fields on a grid (Eulerian approach). This allows to drastically reduce the numerical cost of interactions from $\sim N^2$, in the case of binary interactions, to N, when considering particles interacting only indirectly via electromagnetic fields, which is well-justified in the case of collisionless plasmas.

Although this method presents many advantages, such as its lower computational cost compared to Vlasov codes and its easy scalability to a large number of cores, it also comes with some drawbacks. The most significant is the presence of shot noise, inherently due to

[1]Other particle methods exist, such as the finite-size particle method, which can be appropriate for some small-scale problems, and the delta-f method, designed for studying deviations from an equilibrium distribution in weakly perturbed plasmas.

the sampling of the particle distribution, which can mask low-amplitude effects. In addition, sparsely populated regions of the distribution may be undersampled.

The PIC method relies on three main computational stages per each timestep (see Fig. 3.2):

i- solving Newton's equation for each particle and obtaining the new phase space position;

ii- depositing charge and current densities coming from particles on the grid;

iii- solving Maxwell equations to evolve the fields on the grid.

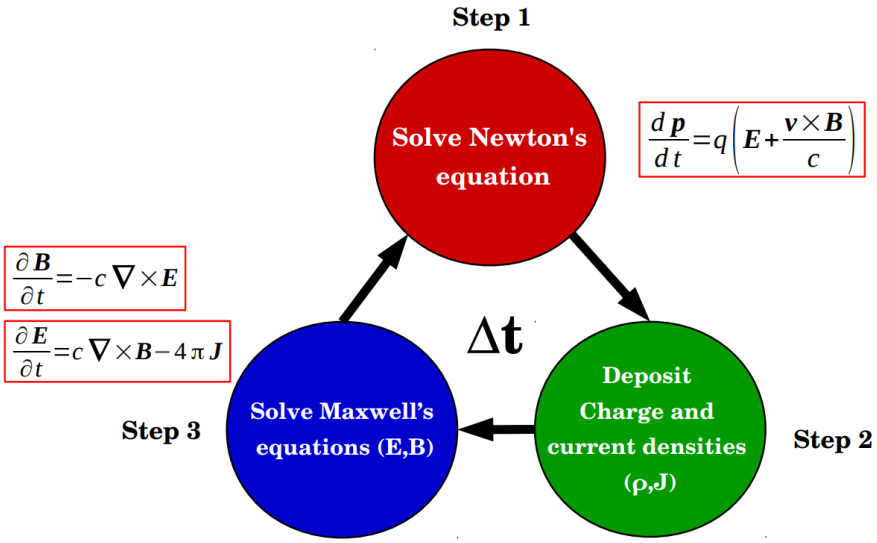

Figure 3.2: Illustration of the three main steps performed at each PIC timestep. Figure taken from Sironi and Cerutti (2017).

In the next section, we detail these three steps. For each step, specific numerical issues arise, which can be addressed by different numerical methods. In such cases, we describe the algorithms implemented in the `ZELTRON` code, which is the code used throughout this thesis.

3.3 `Zeltron` code

The `ZELTRON` code is a PIC code developed in 2012 for astrophysical plasma applications, in particular to incorporate the radiation reaction force that was missing in standard PIC codes at the time (Cerutti et al., 2013).

3.3.1 PIC algorithm

We define the following notation: $t^n \equiv n\Delta t$, where Δt is the timestep of the simulation and n the number of iterations. Similarly, for readability purposes, we note A^n any quantity A evaluated at time t^n.

Particle motion

The evolution of particles is governed by the following system of equations of motion:

$$\frac{\mathrm{d}\mathbf{u}}{\mathrm{d}t} = \frac{q}{m_\mathrm{e}c}\left(\mathbf{E}+\frac{\mathbf{u}\times\mathbf{B}}{\gamma}\right) \tag{3.7}$$

$$\frac{\mathrm{d}\mathbf{r}}{\mathrm{d}t} = \frac{c\mathbf{u}}{\gamma} \tag{3.8}$$

where $\mathbf{u} = \gamma\mathbf{v}/c$ is the four-velocity of particles divided by c, and $\gamma = \sqrt{1+\boldsymbol{u}^2}$ is the particle's Lorentz factor. To solve them numerically, we employ a standard method called "Boris push" (Birdsall and Langdon, 1991) which is fast, stable and based on the leapfrog integration scheme. The leapfrog integration method is a finite-difference, time-centered scheme, accurate to second order, according to which positions and velocities are staggered in time by half a timestep (see Figure 3.3): positions are defined at time t^n and velocities at time $t^{n+1/2}$.

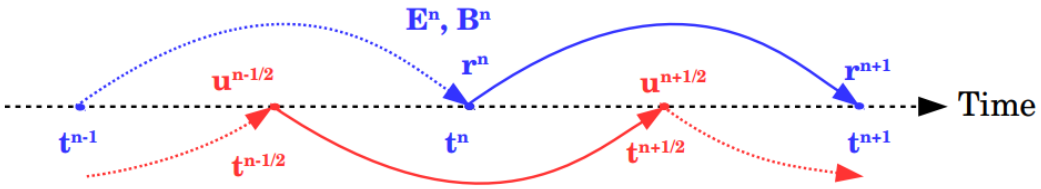

Figure 3.3: Illustration of the leapfrog integration scheme used to numerically solve the Newton equations via the Boris push method. Particle positions and fields are computed for each timestep (t^n) and particle velocities are computed for times shifted by half a timestep ($t^{n+1/2}$). Figure taken from Sironi and Cerutti (2017).

Hence, Eq. (3.7) can be re-expressed as a time-centered finite difference and the velocity appearing in its right-hand term can be rewritten as a time-centered mean:

$$\frac{\mathbf{u}^{n+1/2}-\mathbf{u}^{n-1/2}}{\Delta t} = \frac{q\mathbf{E}^n}{\mathrm{mc}} + \frac{q}{\mathrm{mc}}\left(\frac{\mathbf{u}^n\times\mathbf{B}^n}{\gamma^n}\right) \tag{3.9}$$

$$\mathbf{u}^n = \frac{\mathbf{u}^{n-1/2}+\mathbf{u}^{n+1/2}}{2}\,. \tag{3.10}$$

The fields appearing in the right-hand side of Eq. (3.9) are evaluated at the particle's position. Since they are initially defined on the grid, an interpolation is needed to obtain their corresponding value at any particle position in continuous space. To do so, we employ a first-order linear interpolation method based on an area-weighting scheme, illustrated in Figure 3.4. In a 2D Cartesian grid, the total effective field "felt" by a particle located at P(x,y) inside a cell defined by the nodes $[x_i, x_{i+1}]$ and $[y_j, y_{j+1}]$ is the sum of the contributions from each node surrounding the cell. The contribution of a node (i,j) is given by the ratio of the $(x_{i+1}-x)(y_{i+1}-y)$ surface over the total cell suface (see S_4 in Figure 3.4).

Now, assuming that fields are known at time t^n at the particles locations, and velocities are known at time $t^{n-1/2}$, the value of $\mathbf{u}^{n+1/2}$ can be extracted from Eqs. (3.9) and (3.10). This can be achieved by defining

$$\mathbf{u}^- = \mathbf{u}^{n-1/2} + \frac{q\Delta t\mathbf{E}^n}{2mc} \tag{3.11}$$

$$\mathbf{u}^+ = \mathbf{u}^{n+1/2} - \frac{q\Delta t\mathbf{E}^n}{2mc} \tag{3.12}$$

and showing that

$$\mathbf{u}^+ = \mathbf{u}^+ + \mathbf{u}^-\times\mathbf{s} + (\mathbf{u}^-\times\mathbf{w})\times\mathbf{s}\,, \tag{3.13}$$

where

$$\mathbf{w} = \frac{q\Delta t\mathbf{B}^n}{2mc\gamma^n} \quad \text{and} \quad \mathbf{s} = \frac{2\mathbf{w}}{1+\mathbf{w}^2}\,. \tag{3.14}$$

Finally, the position at time t^{n+1} is easily obtained by expressing Eq. (3.8) as a time-centered finite difference:

$$\frac{\mathbf{r}^{n+1}-\mathbf{r}^n}{\Delta t} = c\frac{\mathbf{u}^{n+1/2}}{\gamma^{n+1/2}}\,. \tag{3.15}$$

The radiation reaction force is added to this scheme according to the prescription given by Tamburini et al. 2010.

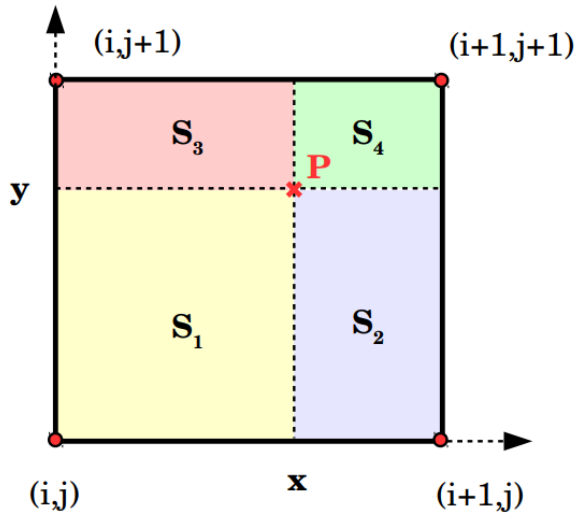

Figure 3.4: Illustration of the area-weighting scheme applied to a 2D cartesian grid cell, used to deposit charges and currents on the grid and to interpolate fields for a particle located at P(x,y). Figure taken from Sironi and Cerutti (2017).

Current and charge deposition

Once the new particle positions and velocities are known, the charge and current densities need to be deposited on the grid, so as to further calculate the field values. For any deposition scheme based on a shape function S, we can express the current and charge densities at the grid point $\mathbf{r}_i$ as follows:

$$\rho(\mathbf{r}_i) = \sum_{\alpha=1}^{N} q_\alpha \, w_\alpha \, S(\mathbf{r}_i - \mathbf{r}_\alpha) \tag{3.16}$$

$$\mathbf{J}(\mathbf{r_i}) = \sum_{\alpha=1}^{N} q_\alpha \, w_\alpha \, \mathbf{v}_\alpha \, S(\mathbf{r}_i - \mathbf{r}_\alpha) \, . \tag{3.17}$$

Even if the particles are point-like, the shape function employed for the deposition of source terms attributes them an effective size. We use the same interpolation scheme as the one presented for the fields interpolation, which allows us to rewrite, in 2D Cartesian coordinates, the charge and current densities as a sum on the number of particles (N_{cell}) contained in the cell (x_i, y_j):

$$\rho_{i,j} = \sum_{\alpha=1}^{N_{\text{cell}}} q_\alpha w_\alpha (1 - C_x)(1 - C_y) \tag{3.18}$$

$$\rho_{i+1,j} = \sum_{\alpha=1}^{N_{\text{cell}}} q_\alpha w_\alpha C_x (1 - C_y) \tag{3.19}$$

$$\rho_{i,j+1} = \sum_{\alpha=1}^{N_{\text{cell}}} q_\alpha w_\alpha (1 - C_x) C_y \tag{3.20}$$

$$\rho_{i+1,j+1} = \sum_{\alpha=1}^{N_{\text{cell}}} q_\alpha w_\alpha C_x C_y \tag{3.21}$$

$$\mathbf{J}_{i,j} = \sum_{\alpha=1}^{N_{\rm cell}} q_\alpha w_\alpha \mathbf{v}_\alpha (1-C_x)(1-C_y) \tag{3.22}$$

$$\mathbf{J}_{i+1,j} = \sum_{\alpha=1}^{N_{\rm cell}} q_\alpha w_\alpha \mathbf{v}_\alpha C_x (1-C_y) \tag{3.23}$$

$$\mathbf{J}_{i,j+1} = \sum_{\alpha=1}^{N_{\rm cell}} q_\alpha w_\alpha \mathbf{v}_\alpha (1-C_x) C_y \tag{3.24}$$

$$\mathbf{J}_{i+1,j+1} = \sum_{\alpha=1}^{N_{\rm cell}} q_\alpha w_\alpha \mathbf{v}_\alpha C_x C_y \,, \tag{3.25}$$

where

$$C_x = \frac{x_\alpha - x_i}{x_{i+1} - x_i} \quad \text{and} \quad C_y = \frac{y_\alpha - y_i}{y_{i+1} - y_i} \,. \tag{3.26}$$

Field evolution

After depositing currents and charges on the grid, we can lastly evolve the electromagnetic fields, by solving the Maxwell-Ampère and the Maxwell-Faraday equations:

$$\frac{\partial \mathbf{E}}{\partial t} = c\nabla \times \mathbf{B} - 4\pi \mathbf{J} \tag{3.27}$$

$$\frac{\partial \mathbf{B}}{\partial t} = -c\nabla \times \mathbf{E} \,. \tag{3.28}$$

To solve this system, the ZELTRON code resorts to the finite-difference time domain (FDTD) method, which is stable and fast. The fields are shifted in both space and time, in order to guarantee second order accuracy in space and in time. The staggering in time is done according to the leapfrog scheme and the staggering in space relies on the Yee mesh (Yee, 1966), as illustrated in Figure 3.5 for a 2D Cartesian grid. The **E**-components are edge-centered while the **B**-components are face-centered on the Yee cell. This fields configuration allows to solve the integral form of Eqs. (3.27) and (3.28) at the scale of a cell. For instance, the integral form of Eq. (3.28) reads:

$$\frac{\partial}{\partial t} \iint \mathbf{B} \cdot \mathbf{dS}_{\rm cell} = -\, c \oint \mathbf{E} \cdot \mathbf{dl}_{\rm cell} \,, \tag{3.29}$$

where we used the Stokes theorem on the face of the cell, for the right-hand side of the equation. Expressing the derivatives as centered finite differences, one obtains the following relation for the z-component of Eq. (3.29):

$$\frac{(B_z)^{n+1/2}_{i+1/2,j+1/2,k} - (B_z)^{n-1/2}_{i+1/2,j+1/2,k}}{\Delta t} = -c\,\frac{(E_y)^n_{i+1,j+1/2,k} - (E_y)^n_{i,j+1/2,k}}{\Delta x} + c\,\frac{(E_x)^n_{i+1/2,j+1,k} - (E_x)^n_{i+1/2,j,k}}{\Delta y} \tag{3.30}$$

where (i,j,k) gives the spatial coordinates on the grid and Δx, Δy the grid spatial intervals. The flux of B_z through the cell face is equal to the closed line integral of the electric field along the edges of that face.

Fields are staggered in time but must both be known at integer timesteps to start the next loop in time and push de particles again. We overcome this problem by splitting the timestep

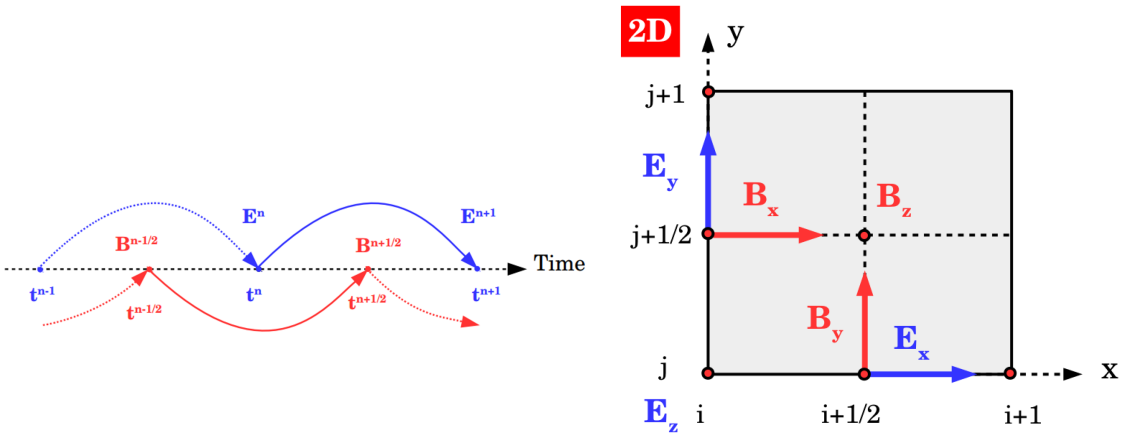

Figure 3.5: Illustration of the Yee algorithm, taken from Sironi and Cerutti (2017). *Left:* Staggering in time of the electric and magnetic fields. *Right:* Staggering in space of the fields, shown for a 2D frame.

into two half-steps when advancing the magnetic field:

$$\boldsymbol{B}^{n+1/2} = \boldsymbol{B}^{n} - \frac{c\Delta t}{2}(\nabla \times \boldsymbol{E})^{n} \tag{3.31}$$

$$\mathbf{E}^{n+1} = \mathbf{E}^{n} + c\Delta t(\boldsymbol{\nabla} \times \mathbf{B})^{n+1/2} - 4\pi\Delta t\mathbf{J}^{n+1/2} \tag{3.32}$$

$$\boldsymbol{B}^{n+1} = \boldsymbol{B}^{n+1/2} - \frac{c\Delta t}{2}(\boldsymbol{\nabla} \times \boldsymbol{E})^{n+1} \tag{3.33}$$

In addition, the current density is computed as the average of its values evaluated before and after updating the particle positions. Assuming all quantities are known for $t \leq t^n$, the final algorithm performed over one timestep reads:

Operation 1 - Compute $\boldsymbol{u}^{n+1/2}$ from $\boldsymbol{u}^{n-1/2}$, $\mathbf{E}^n$ and $\mathbf{B}^n$

Operation 2 - Compute $\mathbf{J}_a$ from $\boldsymbol{r}^n$ and $\boldsymbol{u}^{n+1/2}$

Operation 3 - Compute $\boldsymbol{r}^{n+1}$ from $\boldsymbol{r}^n$ and $\boldsymbol{u}^{n+1}$

Operation 4 - Compute $\mathbf{J}_b$ from $\boldsymbol{r}^{n+1}$ and $\boldsymbol{u}^{n+1/2}$ $\Rightarrow \mathbf{J}^{n+1/2} = \boldsymbol{J}_a + \boldsymbol{J}_b$

Operation 5 - Compute $\boldsymbol{B}^{n+1/2}$ from $\boldsymbol{B}^n$ and $\boldsymbol{E}^n$

Operation 6 - Compute $\boldsymbol{E}^{n+1}$ from $\boldsymbol{E}^n$ and $\boldsymbol{B}^{n+1/2}$ and $\boldsymbol{J}^{n+1/2}$

Operation 7 - Correct $\boldsymbol{E}^{n+1}$ with the Poisson solver

Operation 8 - Compute $\boldsymbol{B}^{n+1}$ from $\boldsymbol{B}^{n+1/2}$ and $\boldsymbol{E}^{n+1}$

The seventh operation has not been motivated so far; it is the purpose of the next section.

3.3.2 Treatment of divergence constraints

In theory, Eqs. (3.2) and (3.3) are enforced by solving the time-dependent Maxwell-equations. However, the discretization of space and time implemented to solve these equations numerically can lead to truncation errors.

Fortunately, the divergence-free constraint on the magnetic field (Eq. 3.3) is verified at all times, provided it is satisfied at $t = 0$ in the simulation. Indeed, the FDTD scheme has the advantage of conserving this quantity to machine roundoff precision.

Conversely, the Gauss law (Eq. 3.2) is not satisfied automatically by the Zeltron algorithm presented so far and the charge is not conserved when deposited on the grid (i.e., $\partial_t \rho = \boldsymbol{\nabla} \cdot \boldsymbol{J}$ is not always verified). Here again, several methods exist to address this problem and avoid the accumulation of unphysical charge. The choice that was made in Zeltron consists in correcting the electric field periodically[2]. We want to find $\delta \boldsymbol{E}$ so that

$$\boldsymbol{\nabla} \cdot (\boldsymbol{E} + \delta \boldsymbol{E}) = 4\pi\rho \,. \tag{3.34}$$

By defining the electric potential φ such that $\delta \boldsymbol{E} = -\boldsymbol{\nabla}\delta\varphi$, Eq. (3.34) can be recast as

$$\boldsymbol{\Delta}(\delta\varphi) = \boldsymbol{\nabla} \cdot \boldsymbol{E} - 4\pi\rho \,. \tag{3.35}$$

Hence, correcting $\boldsymbol{E}$ amounts to solving the above Poisson equation. To do so, we use the Gauss–Seidel iterative method, performing 500 iterations per cycle, and apply one cleaning cycle every 25 timesteps, which has proven sufficient.

3.3.3 Temporal and spatial resolutions

To ensure the numerical stability of the FDTD method, the Courant-Friedrichs-Lewy (CFL) condition must be satisfied, which in 2D reads:

$$(c\Delta t)^2 \left(\frac{1}{\Delta x^2} + \frac{1}{\Delta y^2} \right) < 1 \,. \tag{3.36}$$

In addition to this purely numerical constraint, the accurate capture of microphysical plasma processes requires two further resolution conditions. First, the Debye length must be resolved. This is the characteristic scale over which electrostatic fields are screened by charged particles. In the relativistic regime, the Debye length approaches the plasma skin depth (d_e), namely the characteristic distance over which low-frequency electromagnetic waves can propagate in the plasma:

$$d_\mathrm{e} = \sqrt{\frac{mc^2}{4\pi q^2 n}} \,, \tag{3.37}$$

where n is the plasma number density. Second, the plasma frequency,

$$\omega_\mathrm{p} = \frac{c}{d_e} \,, \tag{3.38}$$

must also be resolved in time. In practice, once the spatial resolution requirement and the CFL condition are satisfied, the temporal resolution of ω_p is automatically ensured.

3.3.4 Parallelization

Global PIC codes designed to model relativistic magnetospheres must be parallelized to handle both the large spatial domains and long integration times.

For global astrophysical problems, parallelization is commonly achieved through spatial decomposition of the grid, which is the strategy adopted in the Zeltron code. The simulation domain is divided into subdomains, each assigned to a processor (or core), which advances the particles and fields contained within in. After completing the operations of each timestep independently, processors exchange boundary information with their nearest neighbours via the Message Passing Interface (MPI) library. This communication involves both the transfer of particles crossing subdomain boundaries, and the synchronization of electromagnetic fields through ghost cells at processor interfaces.

[2] Other current deposition schemes have been developed to enforce charge conservation, but the present method is preferred for its ease of implementation on different grid geometries.

Grid-based domain decomposition has the advantage of scaling efficiently to a large number of processors, which is essential for astrophysical applications. However, its performance critically depends on load balancing, i.e., the distribution of particles across sub-domains. Since the computational cost is largely dominated by the update of particles and currents, an uneven distribution can significantly slow down the entire simulation: processors assigned to nearly empty subdomains must wait for heavily loaded ones to complete each timestep. For this reason, the partitioning of subdomains must be chosen carefully.

3.4 Global PIC simulations of pulsar magnetospheres

So far, we have presented the PIC method and, in particular, its implementation in the `Zeltron` code. The code exists in several versions; in this thesis we focus on configurations designed to model a pulsar magnetosphere, to which we add a different companion in each of the following chapters. Hence, it is worth outlining some properties common to all pulsar magnetosphere setups, whether in 2D or 3D.

3.4.1 Rescaling

Global PIC simulations of pulsar magnetospheres must cover an enormous range of length scales, from kinetic scales up to the macroscopic dimensions of the system. Achieving such realistic scale separations is computationally impossible, which necessitates rescaling key physical parameters, such as the neutron star radius, the magnetic field strength, and the particles mass ratio, to reduce the scale separation by several orders of magnitude. However, the key requirement is to preserve the realistic hierarchy of both spatial and energy scales.

Since we focus on the inner regions of the pulsar wind, the light-cylinder radius ($R_{\rm LC}$) represents the largest scale of interest. The light-cylinder radius is smallest for millisecond pulsars, with $R_{\rm LC} \sim 5r_\star$. The electron plasma skin depth ($d_{\rm e}$) reaches its minimum at the star surface, defining the smallest relevant scale ($d_{\rm e}^\star$), while the current sheet thickness is set by the skin depth at the light cylinder ($d_{\rm e}^{\rm LC}$), providing an additional characteristic scale. Ultimately, the relevant hierarchy of scales satisfies

$$d_{\rm e}^\star \ll d_{\rm e}^{\rm LC} \ll r_\star \ll R_{\rm LC}\,. \tag{3.39}$$

Regarding energy scales, the maximum achievable energy corresponds to an electron experiencing the full potential drop ($\gamma_{\rm pc}$; see Section 2.3.4 for a definition). A second chacacteristic energy ($\gamma_{\rm th}$) is defined as the particle energy required to emit curvature photons capable of producing pairs, while the energy of the resulting secondary particles naturally defines a third scale. The maximum energy attainable by a particle under strong radiative cooling, when the accelerating electric force is balanced by the radiation reaction force ($f_{\rm rad} = eE_\parallel$), defines an additional important energy scale, known as the synchrotron burnoff limit:

$$\gamma_{\rm rad} = \sqrt{\frac{3eE_\parallel}{2r_{\rm e}^2\tilde{B}_\perp^2}}\,, \tag{3.40}$$

where $\tilde{B}_\perp^2$ is the effective perpendicular magnetic field (see Section 2.5.2). This quantity is typically estimated at the light cylinder by assuming that $E_\parallel \sim \tilde{B}_\perp$ and $\tilde{B}_\perp \sim B_{\rm LC}$, yielding

$$\gamma_{\rm rad}^{\rm LC} \approx \sqrt{\frac{3eR_{\rm LC}^3}{2r_e^2 B_\star r_\star^3}}\,. \tag{3.41}$$

The resulting hierarchy of scales is given by:

$$\gamma_{\rm sec} < \gamma_{\rm rad}^{\rm LC} < \gamma_{\rm th} \ll \gamma_{\rm pc}\,. \tag{3.42}$$

We note that the downscaling of the magnetic field by several orders of magnitude would almost suppress radiative cooling. A numerical factor $\kappa_{\rm rad} \gg 1$ is introduced to artificially enhance it, thereby significantly reducing $\gamma_{\rm rad}$ and preserving the correct hierarchy of energy scales.

An important consequence of this rescaling procedure is the compression of the resulting spectral boundaries, a point that must be kept in mind when interpreting the spectra. More generally, relating PIC simulation results to pulsar observations requires a careful extrapolation of certain physical quantities.

3.4.2 Spherical grid

Section 3.3.1 provides a generic description of the PIC algorithm implemented in the `Zeltron` code, illustrated with a 2D Cartesian grid for explanatory purposes. In practice, however, the version of the code used for pulsar modelling employs a spherical grid, which is much better suited to this application, with the pulsar modelled as a sphere at the center of the simulation domain. While the underlying principles remain the same, certain aspects of the algorithm are adapted accordingly. Figure 3.6 shows the spherical Yee mesh in both 2D and 3D. Consistently with Section 3.3.1, the fields are advanced using the integral form of the time-dependent Maxwell equations. The complete list of 3D integrated components adapted to the spherical grid is provided in Cerutti et al. (2016). The CFL condition and the Poisson solver are reformulated to account for the spherical geometry. Similarly, the charge and current deposition schemes rely on the same linear interpolation as in the Cartesian case, but are adapted to the spherical grid.

3.4.3 Boundary conditions

The boundary conditions specific to each problem will be detailed in the corresponding chapters. However, some general features deserve to be discussed beforehand.

The inner boundary of the spherical grid coincides with the stellar surface, modeled as a perfectly conducting sphere with the magnetic field frozen into it. The sphere is set in rotation, with its rotation axis aligned with the polar axis. At the outer boundary, located in the pulsar

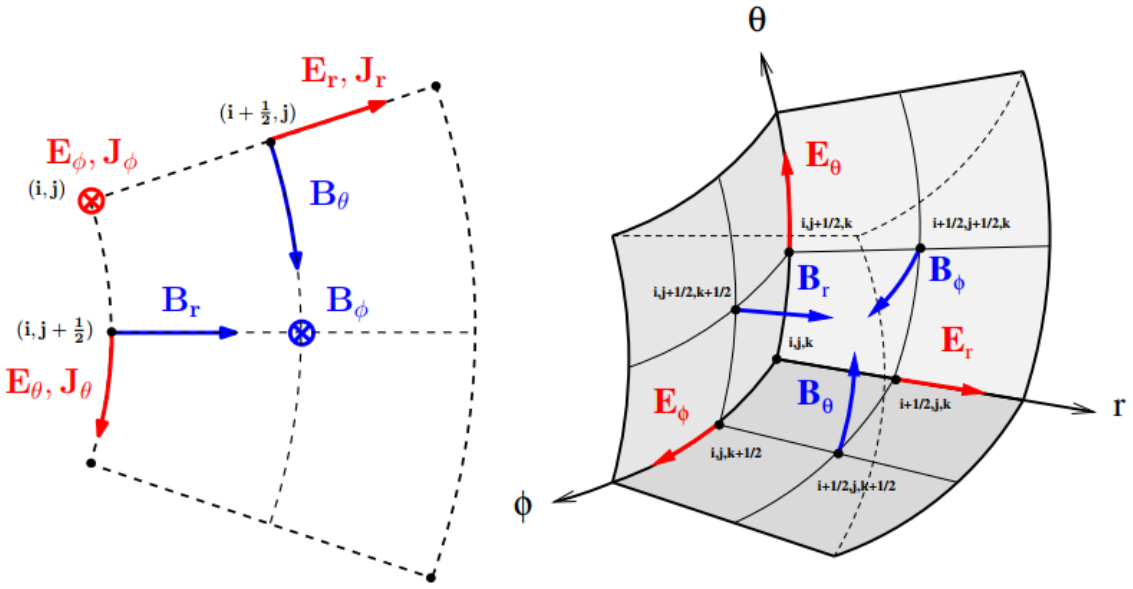

Figure 3.6: Illustration of the spherical Yee mesh for the 2D axisymmetric case (left) and full 3D case (right). Figure taken from Cerutti (2021).

wind, all fields and particles are absorbed to prevent reflection, thereby mimicking an open boundary. This is achieved by introducing artificial dissipation into Maxwell's equations, which exponentially damps the fields within a spherical shell extending from $r_{\rm abs}$ to the outer edge $r_{\rm max}$. Accordingly, the time-dependent Maxwell equations are modified as follows (Birdsall and Langdon, 1991):

$$\frac{\partial \boldsymbol{E}}{\partial t} = -\lambda(r)\,\boldsymbol{E} + c\,(\boldsymbol{\nabla}\times\boldsymbol{B}) - 4\pi\boldsymbol{J} \tag{3.43}$$

$$\frac{\partial \boldsymbol{B}}{\partial t} = -\lambda(r)\,\boldsymbol{B} - c\,(\boldsymbol{\nabla}\times\boldsymbol{E})\,, \tag{3.44}$$

where $\lambda(r)$ is the conductivity of the absorption layer, non-zero only within the layer. The absorption must increase gradually to avoid partial reflection of waves, while remaining steep enough to minimize the fraction of the simulation domain it occupies. The conductivity profile was determined empirically according to these two criteria and is given (for $r \geq r_{\rm abs}$) by

$$\lambda = \frac{A_{\rm damp}}{\Delta t}\left(\frac{r - r_{\rm abs}}{r_{\rm max} - r_{\rm abs}}\right)^3, \tag{3.45}$$

where $A_{\rm damp} > 1$ is a numerical factor controlling the damping efficiency, and the layer thickness is typically set to $r_{\rm max} - r_{\rm abs} = 0.1 r_{\rm max}$. A standard zero-gradient boundary condition ($\partial F/\partial r = 0$), applied to all field components F, complements the damping provided by the absorption layer by preventing reflections at the outer boundary.

A direct consequence of the open outer boundary is the need to continuously supply plasma to the simulation domain. As discussed in Chapter 2, magnetospheric plasma originates from the stellar surface and from pair creation, with the latter clearly dominating the plasma supply. While the modelling of particles extracted from the surface follows a similar approach across studies (although some models simulate the entire star rather than just its surface, filling the interior with particles; see Philippov and Spitkovsky 2014; Chen and Beloborodov 2014), there exists a variety of pair production prescriptions, mainly due to persistent uncertainties regarding this process, such as the exact location of particle creation. In our studies, we employ different prescriptions depending on the problem; the specific details of plasma injection are therefore deferred to the following chapters. Similarly, the remaining boundary conditions are problem-dependent and are detailed later.

3.4.4 Radiation modeling

The modelling of synchrotron-curvature radiation relies on the calculation of the effective perpendicular magnetic field (Eq. 2.102), radiation power (Eq. 2.109) and power spectrum (Eq. 2.117) derived in Chapter 2, and on the following assumptions. Each macro-particle radiates a macro-photon, which represents a large number of physical photons, determined by the weight of the macro-particle. The contribution of each macro-photon to the total radiation is given by Eq. (2.109), scaled by its weight, while its spectral distribution follows Eq. (2.117). The emission of photons is aligned with the particle's momentum, which is a good approximation due to the strong relativistic beaming, focusing the radiation in a cone of aperture $\sim 2/\gamma \ll 1$. Photons then travel freely on straight lines at the speed of light, without interacting with each other or with the magnetic field (optically thin approximation). General relativistic effects on the photon trajectories are neglected. Photons are eclipsed (i.e., absorbed and removed from the simulation) if they hit the star. Otherwise, photons are collected on a screen perpendicular to the observer's line of sight and tangent to the simulation domain ($r_{\rm max}$), which acts as a proxy for a screen at infinity (see Figure 3.7).

The construction of light curves requires correcting for the phase shift introduced by the finite propagation time of photons to the observer. To calculate the phase shift, we first compute the time delay between a photon emitted at a point P (r, θ, ϕ) along $\boldsymbol{e}_{\rm obs}$ and a

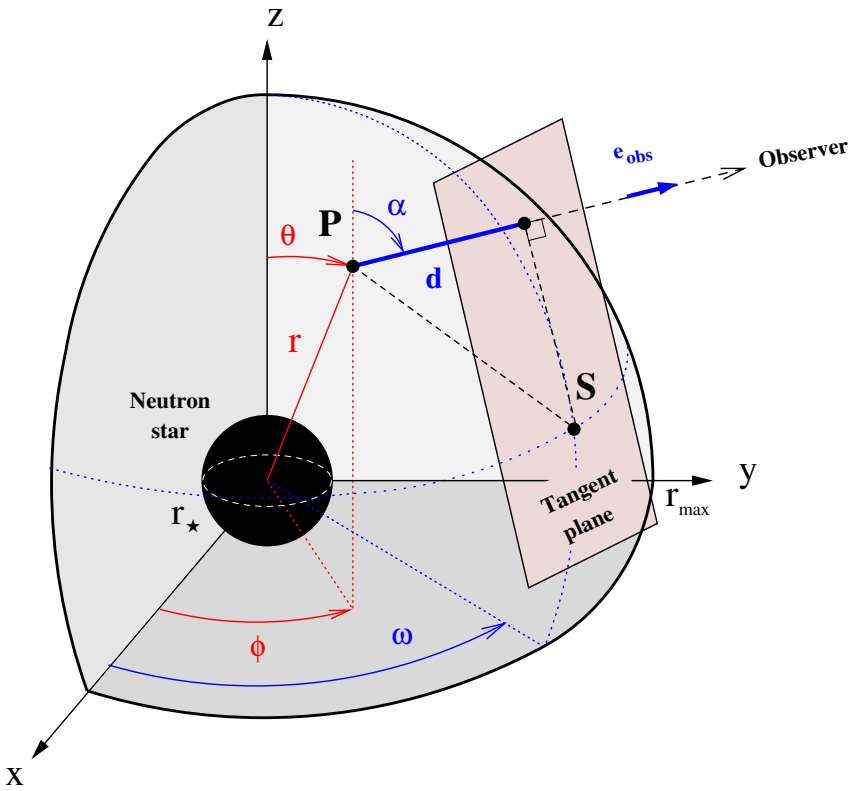

Figure 3.7: Schematic representation of the geometrical quantities used to compute light curves. A particle located at point P (r, θ, ϕ) emits a photon in the direction of the observer (α, ω), defined by the unit vector $\boldsymbol{e}_{\rm obs}$. The photon is then collected on a screen perpendicular to the observer's line of sight and tangent to the simulation domain, after a time delay $t_{\rm d} = d/c = (\boldsymbol{PS} \cdot \boldsymbol{e}_{\rm obs})/c$ measured relative to the point S ($r_{\rm max}$, α, ω), which is the closest point to the observer along the line of sight. Figure taken from Cerutti et al. (2016).

photon emitted at S ($r_{\rm max}$, α, ω) in the same direction, where the point S is defined as the location in the simulation domain closest to the observer along the given line of sight, serving as the reference point for measuring photon travel times (see the schematic representation of these quantities in Figure 3.7). Hence, the travel distance between both photons is given by the projection of $\boldsymbol{PS}$ along the $\boldsymbol{e}_{\rm obs}$ direction, and the delay time ($t_{\rm d}$) reads:

$$t_{\rm d} = \frac{\boldsymbol{PS} \cdot \boldsymbol{e}_{\rm obs}}{c} \,. \tag{3.46}$$

Transforming $\boldsymbol{PS}$ and $\boldsymbol{e}_{\rm obs}$ in Cartesian coordinates yields

$$\boldsymbol{PS} = \begin{bmatrix} r_{\rm max} \sin\alpha \cos\omega - r \sin\theta \cos\phi \\ r_{\rm max} \sin\alpha \sin\omega - r \sin\theta \sin\phi \\ r_{\rm max} cos\alpha - r \cos\theta \end{bmatrix} \tag{3.47}$$

and

$$\boldsymbol{e}_{\rm obs} = \begin{bmatrix} \sin\alpha \cos\omega \\ \sin\alpha \sin\omega \\ \cos\alpha \end{bmatrix} \,, \tag{3.48}$$

so that

$$\boldsymbol{PS} \cdot \boldsymbol{e}_{\rm obs} = r_{\rm max} - r[\sin\alpha \sin\theta \cos(\omega - \phi) + \cos\alpha \cos\theta] \,. \tag{3.49}$$

The resulting phase shift $\Phi_{\rm p}$ is then given by

$$\Phi_{\rm p} \equiv \omega - \Omega t_{\rm d} \pmod{2\pi} \,, \tag{3.50}$$

where $\Phi_{\rm p} = 0$ lies in the plane defined by the magnetic moment $\boldsymbol{\mu}$ and the rotation vector $\boldsymbol{\Omega}$.

Synthetic light curves are finally constructed by summing the contributions of individual photons as a function of their phase, for any given observer's line of sight.

Chapter 4

Pulsar wind - companion interaction

Contents

4.1 Astrophysical motivations . . . 58
4.2 Numerical model . . . 58
4.2.1 2D equatorial setup . . . 58
4.2.2 Companion implementation . . . 61
4.2.3 Orbital-modulated light curves . . . 62
4.2.4 Parametric study to probe different regimes . . . 63
4.3 Reference case: isolated pulsar magnetosphere . . . 64
4.3.1 Stationary solution . . . 64
4.3.2 Key physical properties . . . 66
4.4 Pulsar-companion interaction . . . 67
4.4.1 Global dynamics . . . 67
4.4.2 Particle kinetics . . . 69
4.4.3 High-energy electromagnetic signature . . . 73
4.5 Radio counterparts . . . 75
4.5.1 Radio waves from relativistic magnetic reconnection . . . 75
4.5.2 Additional wave generation triggered by the companion . . . 79
4.5.3 A source of (periodic) radio transients . . . 79
4.6 Discussion and conclusion . . . 83

This chapter is based on Richard-Romei and Cerutti (2024), which has been slightly reorganized for better integration into the manuscript. Additional explanations and details have been included, along with a discussion on potential radio signatures.

4.1 Astrophysical motivations

Pulsar winds have been shown to be preferred sites for particle acceleration and high-energy synchrotron radiation falling in the gamma-ray energy band. Many studies have been conducted in order to better characterize the general structure of such relativistic plasmas in isolated systems (see Chapter 2). However, a few percent of galactic pulsars are found in binary systems (Lorimer, 2008; Breton, 2009). While numerous studies have explored the magnetic coupling of neutron stars in close binary systems (Hansen and Lyutikov, 2001; Palenzuela et al., 2013; Crinquand et al., 2019; Most and Philippov, 2020), far fewer have addressed pulsar wind–companion interactions. As of today, the fundamentals of such interactions remain unclear, leaving open questions regarding the possible rearrangement of the magnetosphere, the strength and location of particle acceleration, and the high-energy emission generated within these systems. Ultimately, we wonder whether a pulsar wind interacting with a companion may lead to a new class of long-period high-energy (and radio) transients.

In this work, we aim to model an inclined pulsar magnetosphere, along with the inner regions of its wind, interacting with a spherical companion embedded in the pulsar wind. To the best of our knowledge, such systems have not yet been modeled using either MHD or PIC simulations. The spider pulsar regime (i.e., the regime where a millisecond pulsar has a low-mass companion star) has been investigated through 2D PIC simulations by Cortés and Sironi (2022, 2024, 2025), where they model the pulsar wind as a plane parallel striped wind, thereby focusing on its outer parts. We focus on a spherical, unmagnetized companion embedded in the pulsar wind, with a diameter smaller than the half-wavelength of the striped wind, thereby excluding the spider pulsar regime. This configuration is intended to represent a generic case that can be applied to various companions. Among them are planets orbiting pulsars, such as PSR J1719−1438b (see Wolszczan 2012, Niţu et al. 2022 and references therein). Characteristic signatures from such systems are expected (see, for example, Mottez and Heyvaerts 2012), analogously to those observed in the Solar System from planets and moons (e.g., the Jupiter-Io interaction; Neubauer 1980), as suggested by Mishra et al. (2023). Another relevant application involves asteroids interacting with a pulsar wind, which have been proposed to trigger repeating fast radio bursts (Dai et al., 2016; Mottez et al., 2020; Decoene et al., 2021). Finally, the companion may also serve as a proxy for compact object binaries, such as pulsar-neutron star binaries (e.g., PSR B1913+16, Hulse and Taylor 1975 or the double pulsar system PSR J0737-3039, Burgay et al. 2003; Lyne et al. 2004) and pulsar-white dwarf binaries, e.g., PSR J1141−6545 (Kaspi et al., 2000), PSR J1909−3744 (Jacoby et al., 2003), PSR J1738+0333 (Jacoby et al., 2007), and PSR J0348+0432 (Antoniadis et al., 2013).

We investigate how the presence of the companion affects the magnetospheric structure, enhances particle acceleration, and gives rise to high-energy emission. In addition, we explore how varying the companion's size and distance influences these diagnostics. Finally, we discuss potential radio counterparts to the high-energy emission. To capture both the global dynamics of the magnetosphere and the microphysical plasma processes responsible for particle acceleration and non-thermal emission, we resort to PIC simulations.

4.2 Numerical model

4.2.1 2D equatorial setup

We use the 2.5D version of the relativistic electromagnetic `Zeltron` code (Cerutti et al., 2013; Cerutti and Werner, 2019), implemented in spherical coordinates and restricted to the equatorial plane (Cerutti et al., 2015, 2016). Our simulation setup closely follows that of (Cerutti and Philippov, 2017), with the addition of a companion placed in the pulsar wind.

The computational domain consists of a disk composed of (4096 x 4096) cells. Particles

are confined to the $r\phi$-plane, while all three spatial components of both the electromagnetic fields and particle velocities are retained. The spherical grid is linear in ϕ and logarithmic in r, ensuring a constant cell aspect ratio across radii. This is well suited for modeling pulsar winds, as both the particle density and field amplitudes decrease with radius. Consequently, the relativistic plasma skin depth, c/ω_p (where ω_p is the plasma frequency), and the Larmor radius, r_L, increase with distance from the pulsar.

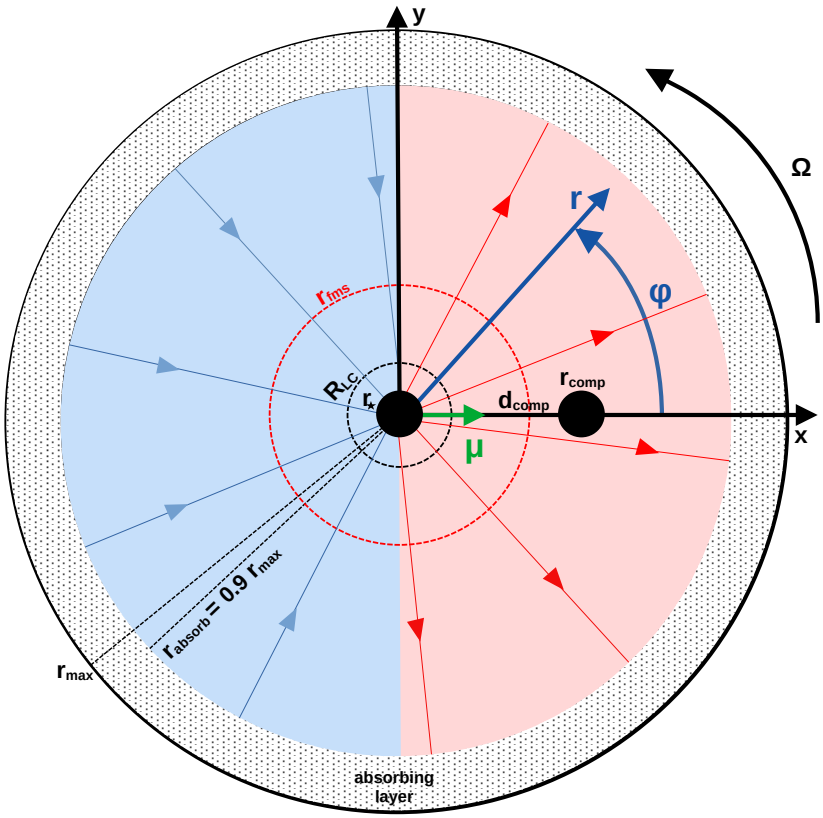

Figure 4.1: Initial numerical configuration. The pulsar, defined by its radius $r_\star$ and angular velocity Ω, is positioned at the center of a spherical simulation domain defined in coordinates (r,ϕ). The domain extends to a radius $r_{\rm max}$, with an absorbing layer applied at $r_{\rm absorb} = 0.9\ r_{\rm max}$. A companion body with radius $r_{\rm comp}$ is placed at a fixed radial distance $d_{\rm comp}$ along the $\phi = 0$ direction. The domain is initially devoid of particles. Magnetic field lines (indicated by blue and red arrows) follow a split-monopole geometry: they are radially outward in one hemisphere (light red region) and radially inward in the other one (light blue region). The hemispheres are separated by a plane orthogonal to the magnetic moment vector $\boldsymbol{\mu}$ (green arrow) and parametrized by $\phi = \Omega t \pm \pi/2$. The light-cylinder radius $R_{\rm LC}$ is marked by a black dashed circle, while the fast magnetosonic radius $r_{\rm fms}$ (defined in Section 4.2.4) is denoted by a red dashed circle. Figure taken from Richard-Romei and Cerutti (2024).

The surface of the star, $r = r_\star$, defines the inner boundary of the computational domain, which extends radially out to 24 $R_{\rm LC}$, where the light-cylinder radius is set to $R_{\rm LC} = 3\ r_\star$. The inner boundary absorbs all incoming particles, and an absorbing layer is implemented at $r_{\rm absorb} = 0.9\ r_{\rm max}$ for both particles and fields to mimic an open boundary, beyond which no information can go back inwards (Cerutti et al., 2015; Belyaev, 2015). This assumption is reasonable, as the fast magnetosonic point is located well within the simulation domain (see Section 4.2.4).

The central neutron star is modeled as a spherical perfect conductor rotating at a constant angular velocity of $\boldsymbol{\Omega}_{\rm spin} = \Omega\,\mathbf{u}_z = (c/R_{\rm LC})\,\mathbf{u}_z$, where $\mathbf{u_z}$ is the unit vector pointing out of

the simulation plane. The simulation begins with the star in vacuum and magnetic field lines anchored at its surface. It was shown in Cerutti and Philippov (2017) that implementing a dipolar magnetic field in this equatorial setup is inadequate. We therefore adopt a split-monopole configuration (see Section 2.3.3; Michel 1973; Bogovalov 1999), in which the initial magnetic field is purely radial. By construction of the equatorial setup, the magnetic axis must be inclined at an angle $\chi = \pi/2$. The perfect conductor condition applied to the pulsar surface in the corotating frame implies, by Lorentz transformation, a non-zero electric field in the simulation frame:

$$\mathbf{E}_\star = -\frac{(\mathbf{\Omega}_{\rm spin} \times \mathbf{r}_\star) \times \mathbf{B}_\star}{c}\,, \tag{4.1}$$

where $\mathbf{E}_\star$ and $\mathbf{B}_\star$ are the electric and magnetic fields at the star surface. This condition initiates the rotation of the magnetic field lines at $t = 0$. The steady-state electromagnetic field recovers the split monopole solution (Eq. 2.71). We recall that, the electromagnetic field reverses across the magnetic equator, defined by $\phi = \Omega t \pm \pi/2$, in order to satisfy $\boldsymbol{\nabla} \cdot \mathbf{B} = 0$ (see Figure 4.1). The split-monopole configuration is a good approximation of the pulsar wind at $R \gg R_{\rm LC}$, making it well suited for our study, which focuses on large distances from the star.

The magnetosphere is initially empty and is gradually filled with electron-positron pairs, which are uniformly injected from the surface of the star at a rate of one macroparticle per cell per timestep for each species. This prescription accounts for polar cap discharge and pair creation processes (Sturrock, 1971; Ruderman and Sutherland, 1975; Timokhin and Arons, 2013; Philippov et al., 2020). Indeed, we neglect any additional pair creation mechanism beyond the stellar surface, given that pair production predominantly occurs in the inner magnetosphere. The potential presence of ions, whose number density is largely dominated by that of pairs, would not significantly affect the magnetospheric structure, and their radiative contribution would be negligible compared to pair losses. This justifies our choice to omit ion extraction from the surface. We impose a high surface multiplicity of $\kappa_\star = n_\star/n_{\rm GJ} = 10$, where $n_\star$ is the density of plasma injected at the stellar surface, and $n_{\rm GJ} = \Omega B_\star/2\pi ec$ is the Goldreich-Julian density (Eq. 2.28; Goldreich and Julian 1969) at the same location. This prescription ensures that the plasma is dense enough to effectively screen the parallel electric field, i.e., $\mathbf{E} \cdot \mathbf{B} = 0$. We also set a high plasma magnetization at the star surface, defined as $\sigma_\star = B_\star^2/4\pi\Gamma_\star n_\star m_e c^2$, where $\Gamma_\star$ is the bulk Lorentz factor of the surface plasma. Maintaining both a high multiplicity and a high plasma magnetization (i.e., $\kappa \gg 1$ and $\sigma \gg 1$) ensures that the magnetosphere and the wind approach the quasi-force-free regime (see Section 2.3.3), except for deviations within the current sheet. The injection of pair plasma occurs along magnetic field lines, with the initial velocity set to the drift velocity ($\mathbf{v}_{\rm D}$) predicted by the force-free monopole solution (Eq.2.71):

$$\begin{aligned}
\mathbf{v}_{\rm D} &= \frac{c\mathbf{E}\times\mathbf{B}}{B^2} && (4.2)\\
&= \frac{c}{B^2}\left(\frac{B_\star^2 r_\star^4}{r^2 R_{\rm LC}^2}\mathbf{e}_r + \frac{B_\star^2 r_\star^4}{r^3 R_{\rm LC}}\mathbf{e}_\phi\right) && (4.3)\\
&= \frac{c}{B_\star^2 r_\star^4\left(\frac{1}{r^4}+\frac{1}{r^2R_{\rm LC}^2}\right)}\left(\frac{B_\star^2 r_\star^4}{r^2 R_{\rm LC}^2}\mathbf{e}_r + \frac{B_\star^2 r_\star^4}{r^3 R_{\rm LC}}\mathbf{e}_\phi\right) && (4.4)\\
&= \frac{c}{1+\left(\frac{R_{\rm LC}}{r}\right)^2}\mathbf{e}_r + \frac{r\Omega}{1+\left(\frac{r}{R_{\rm LC}}\right)^2}\mathbf{e}_\phi\,. && (4.5)
\end{aligned}$$

To properly resolve kinetic plasma scales, the scale separation in our computational domain is reduced by several orders of magnitude relative to realistic pulsar environments. As a result,

our simulations are best suited to modeling millisecond pulsars. The plasma skin depth, d_e, reaches its minimum value at the stellar surface ($d_e^\star$), where it is resolved by 1.14 cells (Δr). At the light-cylinder radius, this resolution increases to approximately $(d_e/\Delta r)_{LC} \sim 10$, and continues to grow with radius, reaching about 24 cells near the outer boundary. The current sheet that develops in the magnetosphere (see Section 4.3) has a thickness on the order of d_e. At $r = R_{LC}$, the Larmor radius is resolved by ~ 1 cell in the wind region, and by up to ~ 70 cells within the current sheet. The Larmor radius resolution increases with radius, reaching ~ 10 cells in the wind at the edge of the computational box. A list of the numerical and physical parameters used in the simulations is provided in Table 4.1.

Table 4.1: Simulation parameters. The values at R_{LC} or r_{fms} are those derived for the isolated pulsar magnetosphere. r_{fms} and Γ_{fms} are defined in Section 4.2.4. Table taken from Richard-Romei and Cerutti (2024).

Parameter	Value
Number of cells	$4096\,(r) \times 4096\,(\phi)$
Inner boundary	$r_\star$
R_{LC}	$3\ r_\star$
r_{absorb}	$24\ R_{LC}$
$(d_e/\Delta r)_{LC}$	16.2
σ_{LC}	60
$P_{spin}/\Delta t$	4.3×10^4
r_{fms}	$5.1\ R_{LC}$
Γ_{fms}	3.9
$d_e^\star/r_\star$	1.8×10^{-3}
Plasma composition	electrons and positrons
Injection model	from the star surface

Particles and electromagnetic fields evolve self-consistently via a computation loop performed at each timestep (see Section 3.3.1 for a full description of the methodology). The particle dynamics follow the Abraham-Lorentz-Dirac equation, which includes the Lorentz force and radiative energy losses (see Eq. 2.92). The timestep is set to half the CFL stability limit. General relativistic corrections to the system's electrodynamics are not included in this study (see, however, Philippov et al. 2015a; Philippov and Spitkovsky 2018; Chen et al. 2020; Torres et al. 2024).

4.2.2 Companion implementation

A companion is added in the pulsar wind, i.e., $d_{comp} > R_{LC}$, where d_{comp} labels the separation of the companion (see Figure 4.1). For simplicity, the companion is modeled as an unmagnetized, non-rotating perfect conductor with no intrinsic wind. Particles impacting its surface are absorbed.

The inclination of the magnetic axis relative to the rotation axis (we recall that $\chi = \pi/2$ in this study) causes the current sheet to oscillate in the θ-direction, hence producing a striped wind (Coroniti, 1990; Bogovalov, 1999), characterized by a spatial periodicity of $\lambda = 2\pi R_{LC}$ and angular extent of 2χ (see Figure 4.2, left panel). A two-dimensional equatorial cross-section of this structure features two Archimedean spirals, separated by stripes πR_{LC} wide of alterning magnetic field polarities, that carry the outflowing cold relativistic wind (see Figure 4.2, right panel). We restrict our study to companion radii smaller than the semi-stripe wavelength, ensuring that its entire diameter fits between two successive reconnection layers: $\delta_{cs} < r_{comp} < \pi R_{LC}$, where δ_{cs} is the current sheet width. Given the chosen companion

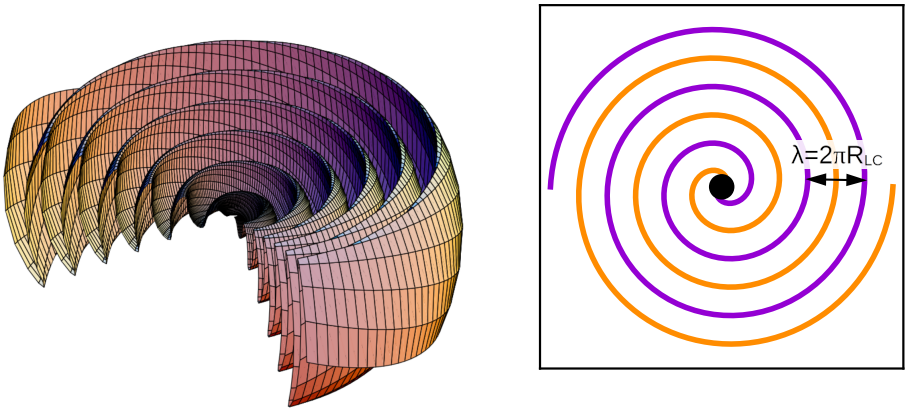

Figure 4.2: *Left:* 3D structure of the current sheet obtained for the oblique split-monopole solution (Bogovalov, 1999), representing the striped wind of isolated pulsars. Figure taken from Kirk et al. (2009). *Right:* 2D equatorial cut of the 3D structure shown on the left. The black disk represents the region inside the light cylinder radius. The current sheet emerges at $\sim R_{\rm LC}$ in the form of two Archimedean spirals, offset by half an angular phase. The radial separation between the two branches is uniform and equal to $\lambda/2 = \pi R_{\rm LC}$, where λ is the stripe wavelength.

separations and radii (see Table 4.2), the ratio $\delta_{\rm cs}/r_{\rm comp}$ spans from 0.15 (run D2R1) to 0.9 (run D9R05).

The pulsar-companion separation is assumed to remain constant over time. This is justified even in the case of a compact object binary containing millisecond pulsars: for our smallest considered separation ($d_{\rm comp} = 2\ R_{\rm LC}$), the merger timescale due to gravitational wave emission is roughly 300 times the pulsar spin period ($P_{\rm spin}$) and 30 times the orbital period ($P_{\rm orb}$), based on the analytical estimate from Iorio et al. (2023). The companion is set at rest in the simulation. Indeed, even at the smallest separation considered, the Keplerian orbital period of a millisecond pulsar binary exceeds the pulsar spin period by roughly an order of magnitude. Combined with the assumption of a perfectly conducting companion, this justifies setting the electric field to zero inside the companion and at its surface, i.e., $\mathbf{E}_{\rm companion} = \mathbf{0}$.

4.2.3 Orbital-modulated light curves

Synchrotron emission is the primary source of high-energy radiation beyond the light cylinder (Cerutti et al., 2016). Each simulated macroparticle (k) radiates a macrophoton, which represents a group of physical photons and carries the following power (Blumenthal and Gould, 1970):

$$\mathcal{P}_{\rm rad} = \frac{2}{3} w_k r_e^2 c \gamma^2 \tilde{B}_\perp^2 \,, \tag{4.6}$$

where w_k is the macroparticle's weight, $r_e = e^2/m_e c^2$ is the classical electron radius, γ is the particle's Lorentz factor and $\tilde{B}_\perp^2$ is the effective perpendicular magnetic field, defined in Eq. (2.102).

In this study, we focus on the orbital modulation of the light curves. As mentioned earlier, the companion is assumed to be stationary in the simulation, based on the condition that the orbital period ($P_{\rm orb}$) is much longer than the pulsar spin period ($P_{\rm spin}$). Nevertheless, if we assume a circular orbit, we can simulate orbital-modulated light curves by positioning observers all around the computational domain. The arrival time delays of photons emitted

from different locations in the simulation domain when they reach the observer's screen are negligible compared to the orbital timescales. This justifies neglecting them here, unlike in studies of isolated pulsars where modeling the pulsed emission modulated by the spin period requires taking them into account (Cerutti et al., 2016). We account for eclipses caused by both the star and the companion by removing all photons that lie behind these objects for a given line of sight (see Figure 4.3 for an illustration).

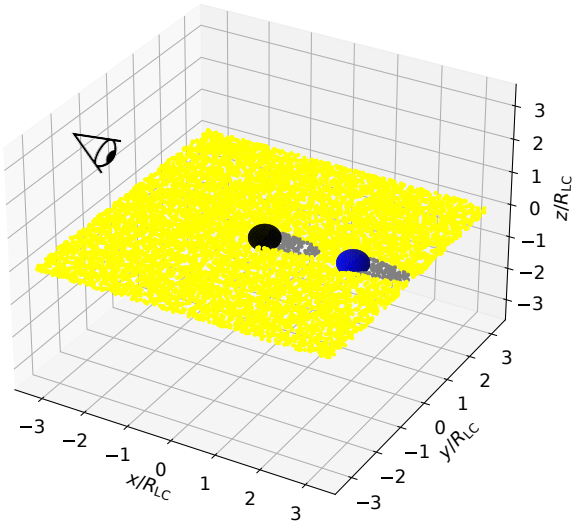

Figure 4.3: 3D illustration of the eclipses implemented in our code. The black and the blue spheres respectively correspond to the neutron star and the companion. For a given line of sight (indicated by the eye symbol), yellow points represent non-eclipsed photons, while grey points indicate photons that are eclipsed.

4.2.4 Parametric study to probe different regimes

We perform different simulations for different binary separations ($d_{\rm comp}$) and companion radii ($r_{\rm comp}$), so as to study their impact on the rearrangement of the wind and on the resulting kinetic processes. The full list of parameters is compiled in Table 4.2.

Table 4.2: Labeling of each simulation involving a companion, with its corresponding parameters. Table taken from Richard-Romei and Cerutti (2024).

Run	$d_{\rm comp}$ ($R_{\rm LC}$)	$r_{\rm comp}$ ($r_\star$)
D2R1	2	1
D5R1	5	1
D9R05	9	0.5
D9R1	9	1
D9R2	9	2
D15R1	15	1

By varying the binary separation, we can probe different regions of the pulsar wind, and in particular, explore two distinct regimes depending on whether the companion lies inside or outside the fast magnetosonic radius ($r_{\rm fms}$). This point defines the causal boundary in the pulsar wind. It corresponds to the radius beyond which the wind velocity surpasses the Alfvén speed, i.e., $\Gamma = \Gamma_{\rm fms}$, where Γ is the Lorentz factor of the wind and $\Gamma_{\rm fms}$ is the Lorentz factor of fast magnetosonic waves. We know from Section 2.2 that $v_{\rm fms} = c\sqrt{\sigma/(1+\sigma)}$, so that

$\Gamma_{\rm fms} = \sqrt{1+\sigma} \sim \sqrt{\sigma}$. Substituting the expression of the plasma magnetization (σ; Eq. 2.7) into this expression, we obtain:

$$\Gamma_{\rm fms} = \sqrt{\frac{B^2}{4\pi n m c^2 \Gamma_{\rm fms}}}\,. \tag{4.7}$$

Rearranging yields:

$$\Gamma_{\rm fms} = \left(\frac{B^2}{4\pi n m_e c^2}\right)^{1/3} = (\Gamma\sigma)^{1/3} = \mu_{\rm M}^{1/3}\,, \tag{4.8}$$

where $\mu_{\rm M}^{1/3}$ is the magnetization parameter introduced by Michel (1969). In order to investigate both regimes, the fast magnetosonic radius must be located at an intermediate distance between the light cylinder and the outer edge of the domain. To satisfy this condition, we impose a magnetization of $\sigma_\star = 250$ at the surface of the star, yielding a value of $\sigma_{\rm LC} \sim 60$ at the light-cylinder radius outside the current sheet. With this choice of parameters, the fast magnetosonic point is located around $5R_{\rm LC}$, as shown in Figure 4.4. In Figure 4.5, we illustrate the various companion sizes and their positions relative to the fast magnetosonic point.

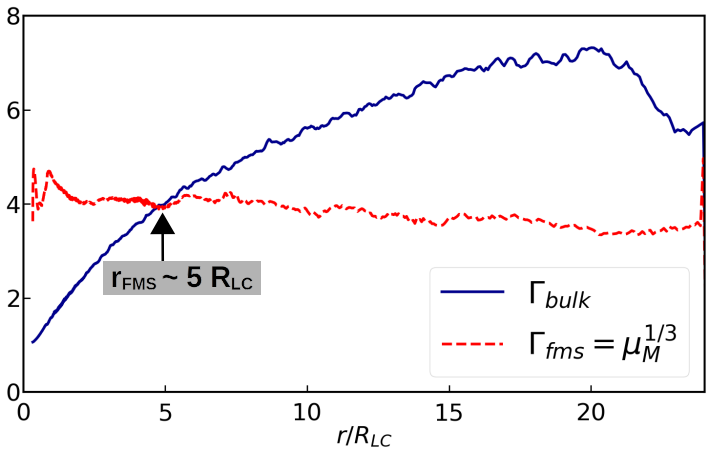

Figure 4.4: Definition of the fast magnetosonic radius. It is the radius at which the bulk Lorentz factor of the wind (blue line) intersects that of the fast magnetosonic modes (red line). The curves are computed from the isolated pulsar simulation. In our setup, the fast magnetosonic radius is located at approximately $5\,R_{\rm LC}$. This result remains unchanged when adding a companion in the magnetosphere, with deviations in some specific cases (see Section 4.4.1).

4.3 Reference case: isolated pulsar magnetosphere

As a reference for assessing the effects of the companion and to ensure that our setup reproduces the well-established features of isolated pulsars, we conduct a simulation of an isolated pulsar magnetosphere using identical numerical parameters to those employed in the companion-interaction runs. We begin by describing its structure before presenting the results of the wind–companion interaction.

4.3.1 Stationary solution

The initial split-monopole configuration illustrated in Figure 4.1 evolves rapidly once the simulation begins ($t > 0$), as the magnetic field lines start rotating to satisfy the perfect

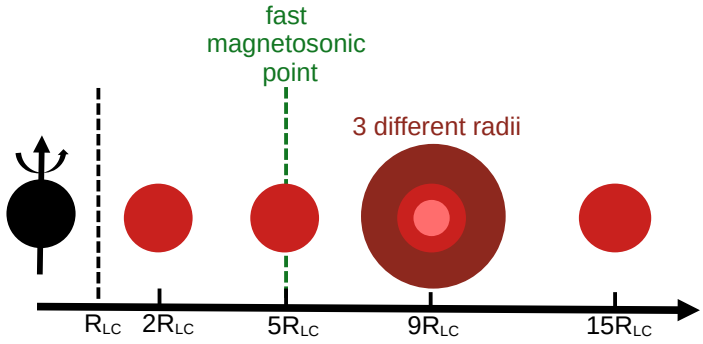

Figure 4.5: Illustration of the companion separations and sizes used in the parametric study. The black sphere represents the pulsar, and the black arrow indicates its rotation axis. The dashed black and green lines mark the light-cylinder radius and fast magnetosonic radius, respectively. Red spheres represent the companion; different shades correspond to different sizes.

conductor condition at the stellar surface (see Section 4.2.1). Electron-positron pairs injected from the surface progressively populate the domain, and the magnetosphere reaches a steady-state configuration after approximately 4.5 $P_{\rm spin}$. To assess this, we compute the radial profiles of the outgoing Poynting flux ($L_{\rm EM}$) by integrating over spherical surfaces of radius r:

$$L_{\rm EM}(r) = \frac{c}{4\pi}\int\int(\mathbf{E}\times\mathbf{B})\cdot\mathrm{d}\mathbf{S} = \frac{c}{2\pi}\int(E_\theta B_\phi - E_\phi B_\theta)r^2\mathrm{d}\phi\,. \tag{4.9}$$

In Figure 4.6, we can see the initial transient moving outwards until it exits the simulation box, and the solution becomes stationary.

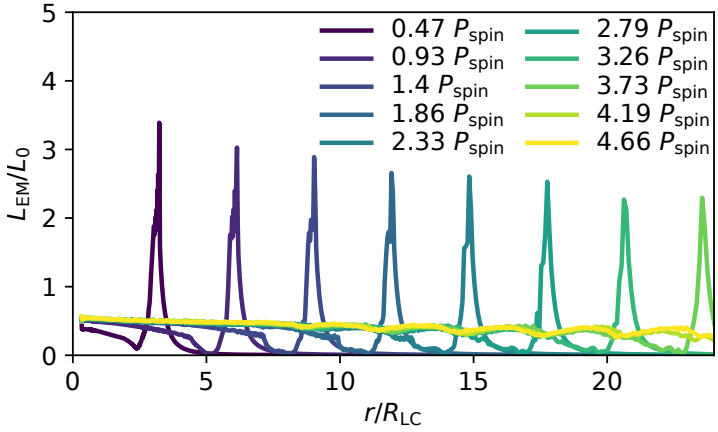

Figure 4.6: Temporal evolution of the outgoing Poynting flux ($L_{\rm EM}/L_0$), computed by integrating over spheres of radius r, with data from the D9R1 simulation run. The Poynting flux is normalized to $L_0 = (2/3)(cB_\star^2 r_\star^4)/R_{\rm LC}^2$, corresponding to the net radial Poynting flux for a split monopole (Eq. 2.77). At the beginning of the simulation, a transient arises at the center of the box and progressively exits the computational domain, leading to the convergence of the Poynting flux after about 4.5 $P_{\rm spin}$. All simulation runs follow a similar evolutionary pattern and reach convergence at approximately the same time.

Inside the light cylinder, closed magnetic field lines near the magnetic equator co-rotate with the star, thereby confining the plasma. Conversely, at the polar caps, rotation-driven open field lines extend beyond the light cylinder and reconnect along the current sheet (Kirk et al., 2009; Arons, 2012; Pétri, 2016; Cerutti and Philippov, 2017). As expected from the inclination of the magnetic axis, the two-dimensional equatorial view reveals alternating stripes

of opposite magnetic polarity, separated by the two spiral arms of the current sheet (see Section 4.2.2 and Figure 4.2).

4.3.2 Key physical properties

Figure 4.7 displays the main diagnostics of interest for this study, taken from a snapshot of the isolated pulsar simulation at $t = 12.4$ pulsar spin periods.

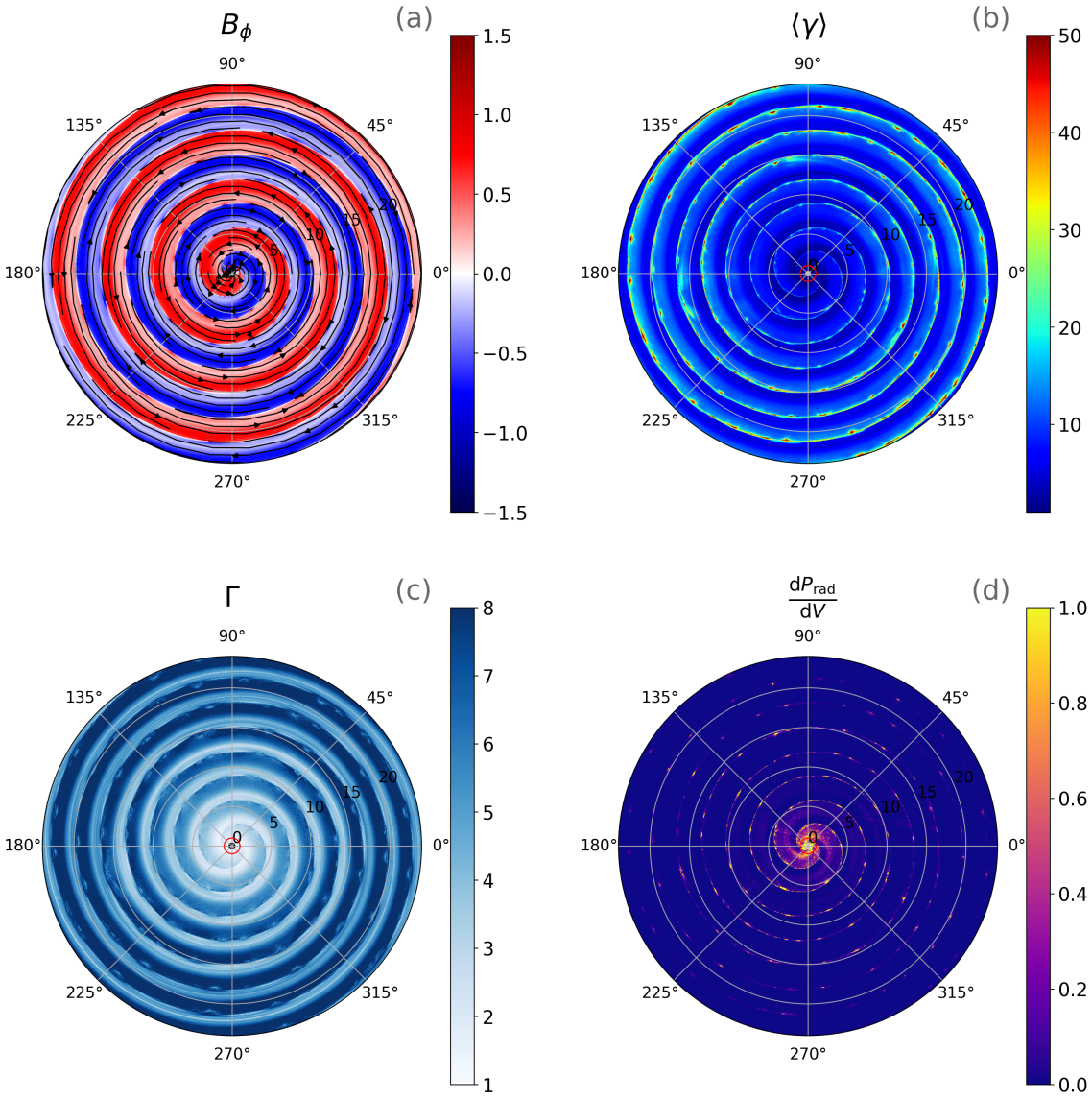

Figure 4.7: Snapshot from the isolated pulsar simulation at 12.4 pulsar spin periods. The central pulsar appears as a black disk in the left panels and a white disk in the right panels, for visualization clarity. *From top left to bottom right:* toroidal magnetic field $(B_\phi/B_\star)(R_{\rm LC}r/r_\star^2)$, with solid lines showing magnetic field lines; mean particle Lorentz factor $\langle\gamma\rangle$; plasma bulk Lorentz factor Γ; isotropic synchrotron power emitted per unit volume $({\rm d}P_{\rm rad}/{\rm d}V)(r^2/r_\star^2)$. All distances are expressed in units of the light-cylinder radius, marked by the red circle. Figure taken from Richard-Romei and Cerutti (2024).

In the top left panel (Figure 4.7a), we represent the toroidal magnetic field (B_ϕ), where we recover the stripes of alternating polarities (blue and red stripes), separated by thin white spirals corresponding to the reconnection layers. Given that $E_\theta \sim B_\phi$ and $E_\phi \sim B_\theta \sim 0$ (see Eqs. 2.71), Eq. (4.9) indicates that the radial Poynting flux can be approximated as

$L_{\rm EM}(r) \propto B_\phi^2$, making the toroidal magnetic field a reliable tracer of the outgoing Poynting flux.

Figure 4.7c shows a snapshot of the wind's bulk Lorentz factor at time $t = 12.4\ P_{\rm spin}$. On average, the Lorentz factor increases nearly linearly with radius until the fast magnetosonic point located at $r_{\rm FMS} = 5.1\ R_{\rm LC}$, where it reaches $\Gamma = 3.9$. Beyond this point, the wind continues to accelerate, albeit more gradually, reaching $\Gamma \sim 7.5$ at the edge of the simulation domain. Magnetic reconnection locally modulates the acceleration due to the current layer's attraction of particles: it slows down the wind on the leading edge of the current sheet and enhances its acceleration on the trailing edge.

Following their acceleration at X-points through magnetic reconnection, particles are trapped within plasmoids. These plasmoids can be identified on Figure 4.7b, which shows a map of the mean particle Lorentz factor ($\langle\gamma\rangle$). They result from the fragmentation of the current sheet under the relativistic tearing mode, as explained in Chapter 2. As expected, they grow over time through successive mergers as they propagate outward along the spiral-shaped current sheet. Magnetic reconnection dissipates $\sim 24\%$ of the available Poynting flux (corresponding to the spindown power extracted from the star) between the light-cylinder radius and the outer edge of the simulation, with maximum efficiency within the inner parts of the wind (for $r < 2\ R_{\rm LC}$).

Lastly, a significant fraction of the wind's kinetic energy is converted into synchrotron radiation within the current sheet (see Fig. 4.7d). The synchrotron luminosity decreases with distance from the source, consistent with the $1/r^2$ decline in both particle density and effective perpendicular magnetic field $\tilde{B}_\perp^2$. In total, 0.7% of the pulsar's spindown power is radiated as high-energy synchrotron emission. Time-delay effects lead to a pulsed synchrotron signal, characterized by two short, bright pulses per stellar spin period (Lyubarskii, 1996; Pétri, 2012; Arka and Dubus, 2013; Cerutti et al., 2016; Philippov and Spitkovsky, 2018; Kalapotharakos et al., 2018; Kalapotharakos et al., 2023). To enable comparison with orbitally modulated light curves computed in the presence of the companion (Section 4.4.3), we define the "reference flux" as the synchrotron emission averaged over one pulsar rotation.

Before discussing the effects of a companion, we emphasize that the magnetosphere of an isolated pulsar is, to a good approximation, globally axisymmetric, if averaged over a pulsar spin period.

4.4 Pulsar-companion interaction

Having characterized the magnetospheric structure, particle acceleration, and high-energy emission in the isolated pulsar case, we now examine how these properties are altered by the presence of a companion.

4.4.1 Global dynamics

For each simulation, Figure 4.8 displays the wind's bulk Lorentz factor, averaged over multiple pulsar rotations, with the fast magnetosonic surfaces overplotted. By averaging over multiple spin periods, we eliminate the wind's striped structure and local inhomogeneities, retaining only the large-scale bulk flow. When the companion is located within the fast magnetosonic surface, i.e., $d_{\rm comp} \leq 5\ r_{\rm fms}$ (runs D2R1 and D5R1), the wind is decelerated throughout the entire domain, with the effect becoming more isotropic and pronounced for closer orbital separations. In this case, we observe that the fast magnetosonic surface becomes disrupted, yet still encloses the companion. The localized enhancement of Γ in the companion's wake arises from numerical artifacts caused by the extremely low plasma density in that region. When the companion lies beyond the fast magnetosonic surface, a sharp drop in the Lorentz factor systematically appears along a cone trailing the companion, marking the formation of

a shock.

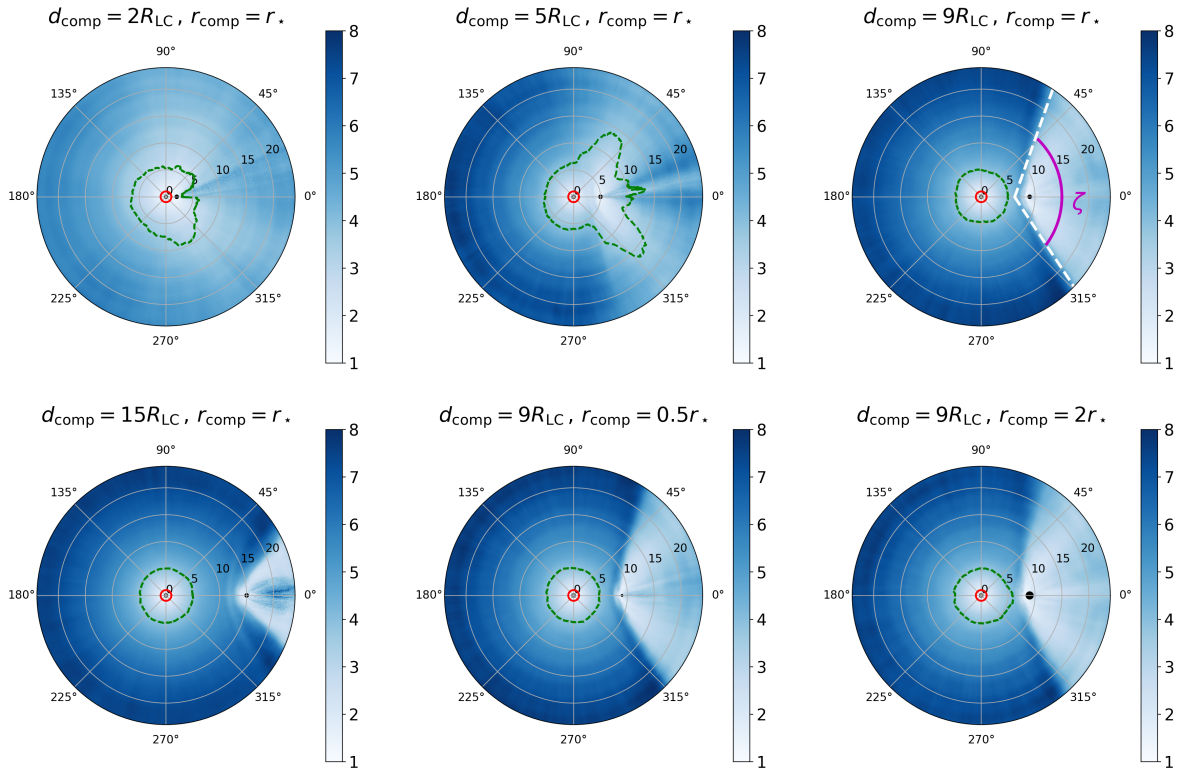

Figure 4.8: Wind bulk Lorentz factor $\Gamma_{\rm wind}$ averaged over several spin periods, shown for each simulation. Distances are expressed in units of the light cylinder, marked by the red circle. The dashed green line indicates the location of the fast magnetosonic surface. When the companion distance $d_{\rm comp}$ exceeds $r_{\rm fms}$, a shock forms with an angular opening ζ (refer to upper-right panel). In contrast, if $d_{\rm comp} < r_{\rm fms}$, no shock develops, and the entire magnetosphere experiences deceleration. Figure taken from Richard-Romei and Cerutti (2024).

When a shock forms in a plane-parallel, uniform flow, the cone opening angle (see ζ in the top-right panel of Fig.4.8) can be related to the relativistic Alfvénic Mach number ($\mathcal{M}$) evaluated at the cone's apex through the following relation:

$$\sin\left(\frac{\zeta}{2}\right) \sim \frac{1}{\mathcal{M}}\,. \tag{4.10}$$

The Mach number is defined as

$$\mathcal{M} = \frac{\beta\Gamma}{\beta_{\rm A}\Gamma_{\rm A}}\,, \tag{4.11}$$

where $\beta_{\rm A} = \sqrt{\sigma/(1+\sigma)}$ (Eq.2.9) and $\Gamma_{\rm A}$ are the Alfvén velocity and the Alfvén Lorentz factor, respectively. As can be seen in Figure 4.9, the values of $\sin(\zeta/2)$ measured in the simulation show reasonably good agreement with the theoretical relation given in Eq.(4.10), with relative deviations remaining below 28%. The concordance is particularly remarkable given the strong inhomogeneity of the striped wind and the tilt of the cone direction, which result in different wind velocities being reached at the same distance from the cone's apex. The red curve in Figure 4.9 shows the radial profile of $1/\mathcal{M}$, averaged over the ϕ-direction, where the Mach number is computed for the reference isolated pulsar magnetosphere. It can be seen that, despite some deviations, the wind properties of the isolated case provide a reasonable approximation for estimating the shock cone opening angle across different binary separations.

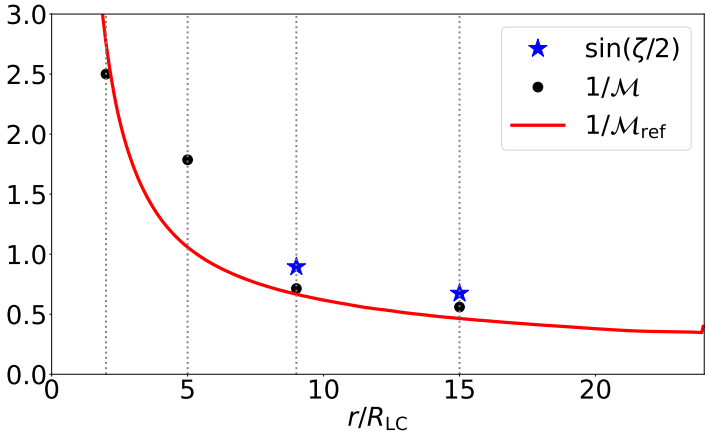

Figure 4.9: Comparison between the measured $\sin(\zeta/2)$ (blue stars), where ζ is the measured opening angle of the shock cone, and the inverse Alfvénic Mach number ($1/\mathcal{M}$; black dots), evaluated at each binary separation, to test the theoretical prediction of Eq. (4.10). Vertical dotted lines indicate the companion locations. For $d_{\rm comp} = 2\ R_{\rm LC}$ and $d_{\rm comp} = 5\ R_{\rm LC}$, no shock forms, and therefore no opening angle can be measured. The red curve shows the radial profile of $1/\mathcal{M}$, averaged over the azimuthal direction, computed from the reference simulation of the isolated pulsar magnetosphere.

Figure 4.10 presents the same set of diagnostics as in Section 4.3, now in the presence of a companion with radius $r_{\rm comp} = r_\star$ and located at $d_{\rm comp} = 9\ R_{\rm LC}$, hence beyond the fast magnetosonic point (run D9R1). In particular, panel (c) shows a snapshot of the bulk Lorentz factor of the wind, which exhibits the characteristic striped structure of the pulsar wind and the shocked cone expected since $d_{\rm comp} > r_{\rm fms}$. Consistent with this, panel (a) shows that the magnetic field is altered, but that all perturbations remain confined within a cone trailing the companion, as they are advected by the pulsar wind. Although a shock is present, we note that the high magnetization of the magnetosphere suppresses large discontinuities in the magnetic field and density, which would be indicative of significant compression (Coroniti, 1990). On the other hand, Figure 4.11 presents the toroidal magnetic field (left panel) and the mean Lorentz factor weighted by the plasma density (right panel) for the regime in which the companion is settled inside the fast magnetic surface (i.e., $d_{\rm comp} \leq r_{\rm fms}$; runs D2R1 and D5R1). In this regime, perturbations propagate faster than the outflowing wind, thereby affecting the entire magnetosphere and preventing the formation of a shock (Figure 4.11, left panel).

4.4.2 Particle kinetics

Regardless of shock formation, the companion's presence enhances particle acceleration at all binary separations. This results from the compression of magnetic field lines that reach the companion's surface as the wind expands, leading to forced reconnection. Figure 4.12 illustrates this effect by showing the time evolution of a current sheet branch (white dashed line) approaching the companion's surface. At first, the leading edge of the current sheet begins to decelerate upon approaching the companion, starting at a distance of roughly $1\ r_{\rm comp}$. It subsequently bends backward but continues to progress toward the companion's surface due to the overall radial motion of the sheet. After contact, the current sheet breaks apart around the obstacle, and two branches of enhanced particle acceleration emerge and propagate outward, forming two distinct radial streams. Actually, the entire cone enclosed between these two streams becomes a favorable region for particle acceleration. The resulting cone of enhanced particle acceleration is shown in Figure 4.10b, for the simulation in which the com-

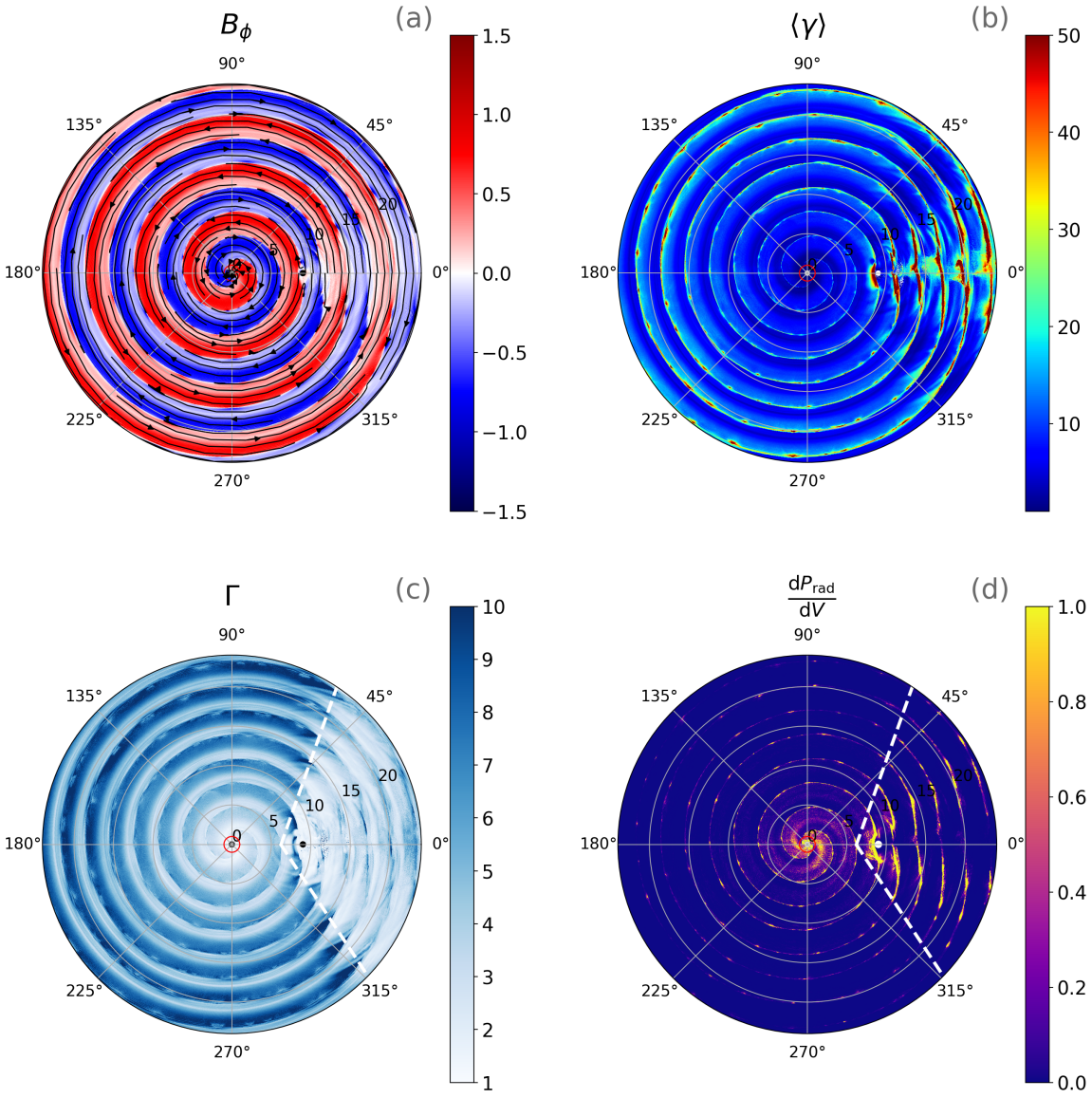

Figure 4.10: Snapshot of a simulation including a companion ($d_{\rm comp} = 9\ R_{\rm LC}$ and size $r_{\rm comp} = r_\star$), at 11.7 pulsar spin periods. The central pulsar and the companion appear as black disks in the left panels and white disks in the right panels, for visualization clarity. *From top left to bottom right:* toroidal magnetic field $(B_\phi/B_\star)(R_{\rm LC}r/r_\star^2)$, with solid lines showing magnetic field lines; mean particle Lorentz factor $\langle\gamma\rangle$; plasma bulk Lorentz factor Γ; isotropic synchrotron power emitted per unit volume $({\rm d}P_{\rm rad}/{\rm d}V)(r^2/r_\star^2)$. All distances are expressed in units of the light-cylinder radius, marked by the red circle. The aperture angle of the shocked region, shown by white dashed lines in panel (c), is replicated in panel (d) for comparison with the hollow emission cone. Figure taken from Richard-Romei and Cerutti (2024).

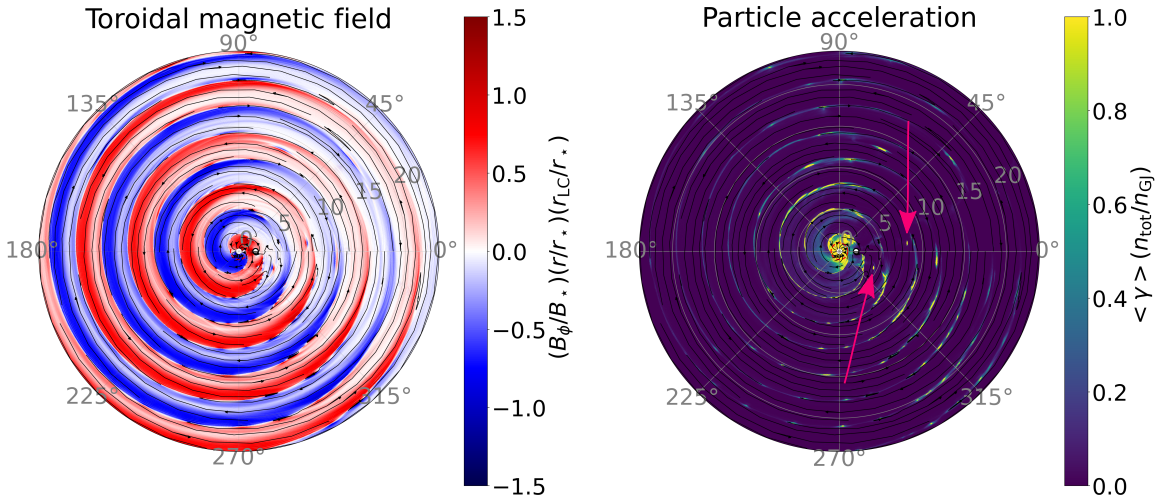

Figure 4.11: Snapshot of a simulation including a companion settled within the fast magnetosonic surface ($d_{\rm comp} = 2\ R_{\rm LC}$ and size $r_{\rm comp} = r_\star$), at 4.9 pulsar spin periods. The central pulsar and the companion appear as white disks. *Left:* toroidal magnetic field $(B_\phi/B_\star)(R_{\rm LC}r/r_\star^2)$, with solid lines showing magnetic field lines. *Right:* mean particle Lorentz factor weighted by the plasma density $\langle\gamma\rangle(n_{\rm tot}/n_{\rm GJ})$, where $n_{\rm GJ}$ is the Goldreich-Julian density at the surface of the star. All distances are expressed in units of the light-cylinder radius, marked by the red circle. Pink arrows highlight plasmoids located between the spiral arms of the disrupted current sheets.

panion is located beyond the fast magnetosonic point. Since the density in the companion's wake is extremely low, the majority of the highly accelerated particles stream along the edges of the cone, which explains the hollow cone structure seen in the corresponding synchrotron power ($P_{\rm rad}$) map, where the mean Lorentz factor ($\langle\gamma\rangle$) is weighted by the local density. In the sub-magnetosonic regime, although no shock is formed, we still observe two preferential directions along which the accelerated particles propagate (Figure 4.11, right panel). Interestingly, the current sheet is so violently disrupted that some plasmoids are ejected between the spiral arms of the current sheet (see pink arrows in Figure 4.11, right panel). The synchrotron emission from these plasmoids is expected to modify the light curves over the pulsar's spin period, introducing an additional peaked component between the two classical caustics.

A significant fraction of the outflowing electromagnetic energy ($L_{\rm EM}$) is converted into outflowing particle's kinetic energy ($L_{\rm kin}$), defined as

$$L_{\rm kin}(r) = \int\int (\gamma - 1) n m_e c^2 v_r r^2 \sin\theta {\rm d}\theta {\rm d}\phi\,, \tag{4.12}$$

where v_r is the radial velocity of the pulsar wind. Figure 4.13 represents radial profiles of the electromagnetic energy flux ($L_{\rm EM}$; full lines) and particle kinetic energy ($L_{\rm kin}$; dashed lines), and their sum ($L_{\rm EM} + L_{\rm kin}$; thick full lines) for the two regimes - depending on whether the companion is located inside (orange lines) or outside (blue lines) the fast magnetosonic point. In both regimes, we observe a decrease in electromagnetic energy flux accompanied by an increase in particle kinetic energy, particularly near the location of the companion ($d_{\rm comp}$; vertical dotted lines). When $d_{\rm comp} = 9\ R_{\rm LC} > r_{\rm fms}$, the total energy flux $L_{\rm EM} + L_{\rm kin}$ (blue thick lines) remains approximately constant, indicating that most of the dissipated Poynting flux is converted into particle acceleration. The slight decrease in the total flux can be attributed to other energy loss mechanisms, such as synchrotron radiation or numerical dissipation. Conversely, when $d_{\rm comp} = 2\ R_{\rm LC} < r_{\rm fms}$, a sharp drop in the electromagnetic energy flux is observed near the companion's surface, likely caused by the reflection of outgoing electromagnetic waves at the companion's surface. Beyond the companion's location, the sum of

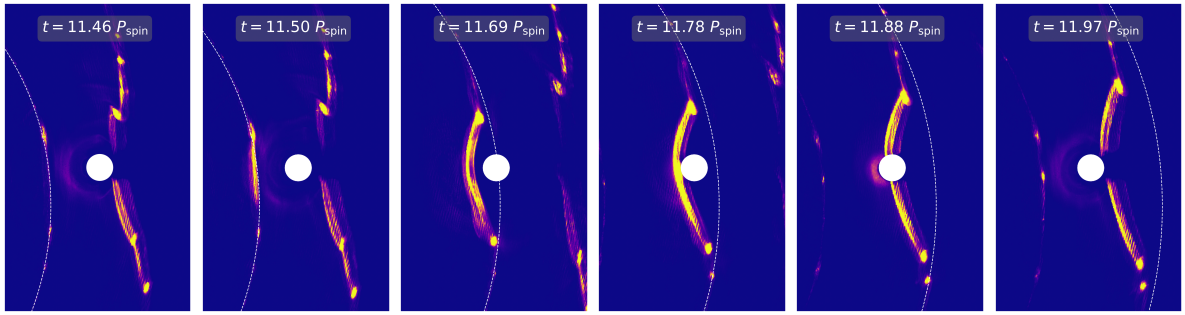

Figure 4.12: Synchrotron power per unit volume ($\mathrm{d}P_{\mathrm{rad}}/\mathrm{d}V$) shown in successive snapshots of run D9R1, zoomed in on the region surrounding the companion during an interaction with the current sheet. Shown as a white dashed line, the Archimedean spiral marks the expected structure of the current sheet in the companion-free case. The current sheet propagates nearly radially, but upon encountering the companion's surface, it bends, brightens, and eventually breaks apart. Figure taken from Richard-Romei and Cerutti (2024).

the electromagnetic energy flux and of the particle kinetic energy remains approximately constant. As magnetic reconnection persists and radiative losses weaken with distance, particle acceleration increases up to the boundary of the computational box. In total, between the inner and outer edges of the computational domain, 57% and 35% of the Poynting flux are consumed for $d_{\mathrm{comp}} = 2\ R_{\mathrm{LC}} < r_{\mathrm{fms}}$ and $d_{\mathrm{comp}} = 9\ R_{\mathrm{LC}} > r_{\mathrm{fms}}$, respectively.

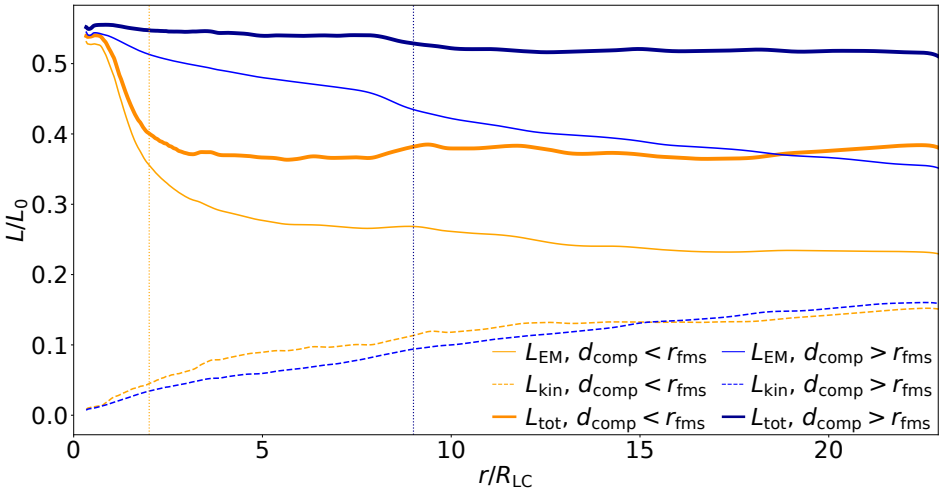

Figure 4.13: Radial profiles of electromagnetic energy fluxes (full lines), particle energy fluxes (dashed lines), and their sum (thick full lines), for the two regimes $d_{\mathrm{comp}} = 2\ R_{\mathrm{LC}} < r_{\mathrm{fms}}$ (orange lines) and $d_{\mathrm{comp}} = 9\ R_{\mathrm{LC}} > r_{\mathrm{fms}}$ (blue lines). Dotted vertical lines indicate the respective locations of the companion. All fluxes are normalized by $L_0 = (2/3)(cB_\star^2 r_\star^4)/(R_{\mathrm{LC}}^2)$, the analytical expression for the outgoing Poynting flux in the split-monopole solution.

Figure 4.14 displays the particle energy spectra for all simulations. The introduction of the companion generates a localized spectral bump, with the peak energy varying according to the binary separation. A separation of 5 R_{LC} (red line) appears to be the most favorable for reaching the highest particle energies, with the spectral bump centered around $\gamma \sim 200$. The companion size has little impact on the particle energy spectra (see orange lines on Figure 4.14, left panel). By decomposing the domain into shocked and unshocked regions (Figure 4.14, right panel), we demonstrate that the observed spectral hardening arises exclusively from the shocked portion of the wind, when a shock is present. Outside the shocked region, the spectral shape remains consistent with that of an isolated pulsar.

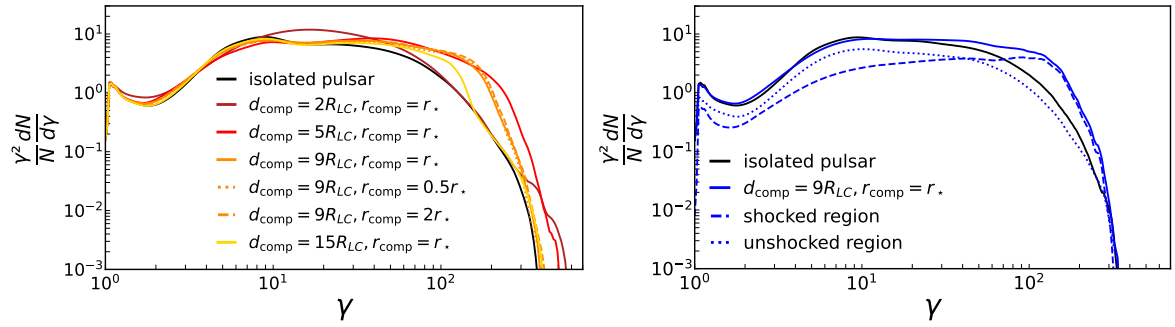

Figure 4.14: *Left:* Particle energy spectra averaged over several spin periods for all simulation runs. The black solid line represents the spectrum of the isolated pulsar magnetosphere. Colored solid lines correspond to binary configurations, with different colors indicating different binary separations. Orange dashed and dotted lines represent variations in companion size. *Right:* Spatial decomposition of the particle energy spectrum for the D9R1 run. The total spectrum (solid blue curve) is separated into contributions from the shocked region (dashed blue curve) and the unshocked region (dotted blue curve). For comparison, the spectrum from the isolated pulsar case is shown (solid black curve). Figures taken from Richard-Romei and Cerutti (2024).

4.4.3 High-energy electromagnetic signature

As previously discussed (Section 3.4.4), synchrotron losses represent the dominant contribution to the system's high-energy radiation. These losses are particularly significant in the inner parts of the wind, where the magnetic field strength ($B \propto 1/r$) and particle density ($n \propto 1/r^2$) are highest. In the isolated pulsar case, synchrotron losses arise from particles that were accelerated in reconnection layers and subsequently trapped within plasmoids along the current sheet (Figure 4.7).

The addition of a companion introduces a new component to the synchrotron emission. Indeed, the companion acts as an obstacle, triggering additional particle acceleration through forced reconnection (see previous section) and causing the current sheet to brighten further. This emission becomes the dominant contribution, significantly exceeding that produced in the isolated pulsar configuration, as illustrated by the synchrotron spectra presented in Figure 4.15 (left panel). As the binary separation increases, the excess synchrotron emission diminishes, primarily due to the radial decrease in both particle density and magnetic field strength, despite the Lorentz factor (γ) continuing to rise with distance, albeit more slowly. Doubling the companion's radius ($r_{\rm comp} = 2\ r_\star$) produces a modest upward shift in the spectrum, while reducing it to $r_{\rm comp} = 0.5\ r_\star$ causes a slighter downward shift. In addition to enhancing the synchrotron emission, the presence of the companion shifts the spectral peaks to higher frequencies. Once again, the configuration with a separation of $d_{\rm comp} = 5\ R_{\rm LC}$ appears to be the most efficient at shifting the spectral peak to higher frequencies, compared to the other cases. Figure 4.15 (right panel) compares, for run D9R1, the synchrotron spectra originating from the shocked and unshocked regions of the magnetosphere. The unshocked region exhibits a spectrum consistent with that of the isolated pulsar case, confirming that the excess emission arises solely from the shocked region.

The orbital light curves obtained for all simulation runs are displayed in Figure 4.16. We focus on high-energy synchrotron radiation, selecting emission above the reference frequency $\nu_0 = 3eB_\star/4\pi mc$, which has been established in earlier works (e.g., Cerutti et al. 2016) as a reliable lower limit for isolating synchrotron emission from the current sheet. The light curves are integrated over the entire polar angle range and normalized to a reference flux, defined as the phase-averaged synchrotron emission over one spin period ($P_{\rm spin}$) from the isolated pulsar configuration (see Section 4.3). All light curves exhibit a marked increase in

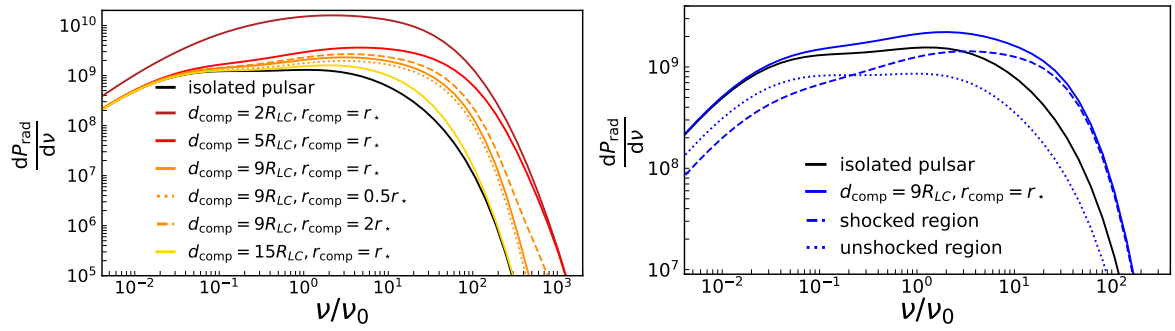

Figure 4.15: *Left:* Synchrotron spectra averaged over several spin periods for all simulation runs. The black solid line represents the spectrum of the isolated pulsar magnetosphere. Colored solid lines correspond to binary configurations, with different colors indicating different binary separations. Orange dashed and dotted lines represent variations in companion size. *Right:* Spatial decomposition of the synchrotron spectrum for the D9R1 run: the total spectrum (solid blue curve) is separated into contributions from the shocked region (dashed blue curve) and the unshocked region (dotted blue curve). For comparison, the spectrum from the isolated pulsar case is shown (solid black curve). Figures taken from Richard-Romei and Cerutti (2024).

radiation flux, characterized by two broad peaks. These peaks correspond to the observer's line of sight intersecting the edges of the hollow emission cone (see Figure 4.10d). The peak intensity ranges from 3.5 to 14 times the reference flux, depending on the companion's size and separation. Larger companion radii (orange curves in Figure 4.16) result in stronger peaks and larger orbital phase separations between them. The binary separation affects several key characteristics of the light curves, including the peak intensities, their widths, the phase separation between them ($\Delta\Phi$), and the angular offset of the emission cone with respect to the pulsar–companion axis ($\delta_{\rm offset}$).

Figure 4.17 illustrates the dependence of these quantities on the pulsar–companion separation. According to the upper panel, the total synchrotron emission integrated over one orbit decreases with increasing separation, following a power law proportional to $d_{\rm comp}^{-0.56}$ (see red line).

The orbital phase separation between the two peaks (Figure 4.17, middle panel) decreases with increasing binary separation, following a power-law scaling of $d_{\rm comp}^{-0.68}$ (light blue line). We show that these scalings closely follow the corresponding $1/\Gamma$ values calculated at the apex of the shocked cone for each run (dark blue points in the middle panel of Figure 4.17), indicating that relativistic beaming plays a key role in determining the peak separation. In fact, in Figure 4.17, the $1/\Gamma$ scaling (dark blue points) is normalized by a factor of 0.55 to match the measured peak separations. This adjustment accounts for the fact that the Γ values are derived from temporally averaged maps (see Fig.4.8), which smooth out local variations, whereas Fig.4.10c shows that Γ can locally reach up to twice the averaged value within the current sheet near the companion. Additionnally, we note that the altered region of the magnetosphere (Figure 4.10a), where particle acceleration and radiation are enhanced, is contained within the shocked zone. As a result, the opening angle of the shock cone provides an upper limit for the aperture of the emission cone (see Figure 4.10d, white dashed lines).

Another interesting property to quantify is the angular offset between the center of the hollow emission cone and the pulsar-companion axis, referred to as $\delta_{\rm offset}$. In Figure 4.17 (lower panel), we show that $\tan(\delta_{\rm offset})$, measured for each companion separation (green crosses), matches the drift velocity (see Eq. 4.5) ratio computed at the corresponding companion loca-

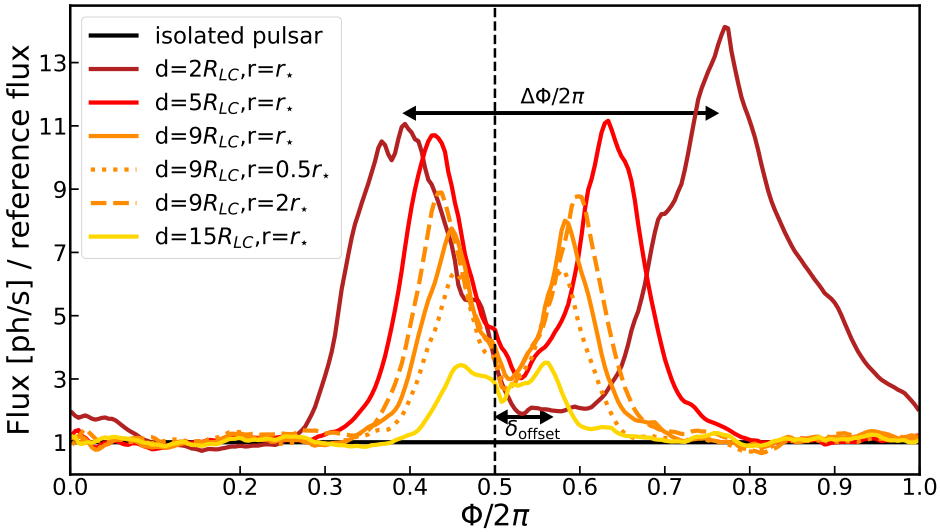

Figure 4.16: High-energy ($\nu > \nu_0 = 3eB_\star/4\pi mc$) synchrotron light curves for all simulation runs, plotted as a function of orbital phase Φ. Fluxes are integrated over the full range of polar angles and normalized to the reference flux from the isolated pulsar magnetosphere (black solid line). Colored solid lines correspond to different binary separations, while orange dashed and dotted lines represent variations in companion size. The vertical black dashed line indicates the pulsar-companion axis. Two broad and intense peaks—arising from a hollow emission cone in 3D—are generated by the pulsar-companion interaction, with different properties depending on the companion size and separation. The angular separation between the peaks is denoted $\Delta\Phi$, and the cone's tilt relative to the pulsar-companion axis is labeled $\delta_{\rm offset}$. Figure taken from Richard-Romei and Cerutti (2024).

tion and obtained from the monopole analytical solution of Michel (1973) (green line):

$$\frac{V_\phi}{V_r} = \left(\frac{r\Omega}{1+\left(\frac{r}{R_{\rm LC}}\right)^2}\right)\left(\frac{c}{1+\left(\frac{R_{\rm LC}}{r}\right)^2}\right)^{-1} = \frac{R_{\rm LC}}{r}\,. \tag{4.13}$$

Hence, the plasma drift velocity evaluated at the companion's radial position governs the angular tilt of the hollow emission cones relative to the pulsar-companion axis. We also verify that the angular offset of the emission cone closely matches that of the shock cone (light green crosses), whenever a shock is present.

4.5 Radio counterparts

Thus far, we have investigated the high-energy emission produced by the interaction between the pulsar wind and a small companion. In this section, we focus on its potential radio counterparts.

4.5.1 Radio waves from relativistic magnetic reconnection

Apart from the radio emission originating from the polar caps of isolated pulsars, there are hints that an additional radio emission mechanism operates in pulsar magnetospheres exhibiting strong magnetic fields ($> 10^3$G at $R_{\rm LC}$; e.g., the Crab pulsar, other energetic young pulsars, and millisecond pulsar). Indeed, such pulsars exhibit several characteristics that are difficult to reconcile with a polar cap emission origin, including the presence of two well-separated peaks in the light curve, which are difficult to explain without specific geometries

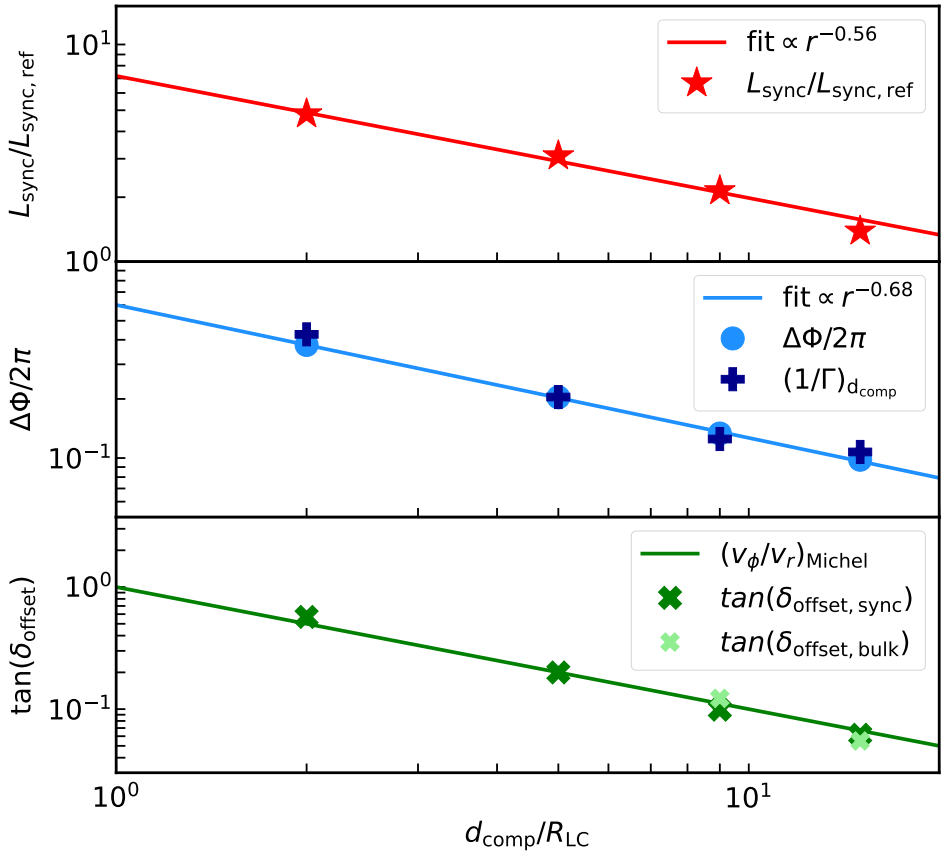

Figure 4.17: Light curve characteristics as a function of the pulsar-companion separation. *Upper panel:* Total synchrotron power integrated over one orbit (red points), normalized to that of the isolated pulsar case, and scaling as $d_{\rm comp}^{-0.56}$ (red line). *Middle panel:* Orbital phase separation between the two light curve peaks (light blue points), scaling as $d_{\rm comp}^{-0.68}$ (light blue line). Dark blue crosses indicate the corresponding $1/\Gamma$ values, calculated upstream of the companion and normalized by a factor 0.55. *Lower panel:* Angular offsets of the emission cone (green crosses) and the shock cone (light green crosses) relative to the pulsar-companion axis, plotted alongside the theoretical drift velocity ratio of the wind $V_\phi/V_r = R_{\rm LC}/r$ (green line), derived from the monopole solution of Michel (1973). Figure adapted from Richard-Romei and Cerutti (2024).

(e.g., orthogonal or aligned rotators with hollow-cone beams); the phase alignment with high-energy emission from the current sheet (Johnston et al., 2004; Johnson et al., 2014; Ng et al., 2014; Eilek and Hankins, 2016); the absence of pulse broadening at lower frequencies, contrary to expectations from standard models; the nanosecond duration of the pulses ("nanoshots"; Eilek and Hankins 2016); and the occurrence of exceptionally bright single pulses, known as giant pulses (Bilous et al., 2015).

Lyubarsky (2019) presents a theoretical model predicting radio wave emission resulting from relativistic magnetic reconnection, described hereafter. When magnetic reconnection occurs (see Section 2.4.2 for a detailed description), a chain of magnetic islands (i.e., closed loops of magnetic field) trapping plasma is formed between reconnection X-points. It is well known that plasmoids merge over time, with coalescence speeds approaching a significant fraction of the speed of light in relativistic magnetospheres, hence forming progressively larger magnetic islands. As a result, the magnetic field is perturbed near the coalescence points, giving rise to MHD waves. Contrary to Alfvén waves, which propagate along magnetic field lines, fast magnetosonic waves propagate across magnetic field lines, thereby carrying energy in the radial direction. In regions where the plasma density vanishes, fast magnetosonic waves transition into vacuum electromagnetic waves. Although these waves are eventually absorbed if they remain in the plasma, pulsar magnetospheres contain gap regions (i.e., plasma-depleted zones) that enable their escape. Pulses originating from separate coalescence events intersect above the current sheet, initiating non-linear interactions that generate Alfvén waves and lower the efficiency of radiation escape. Indeed, these newly formed Alfvén waves cascade most of their energy to smaller scales, heating the plasma, until the characteristic interaction timescale approaches the escape time ($\tau \sim R_{\rm LC}/c$), allowing the remaining radiation to eventually escape the magnetosphere. The pulses are expected to last for a few nanoseconds, depending on the sizes of the magnetic islands, which themselves scale with the width of the current sheet. Such durations correspond to a frequency of approximately 100 MHz, placing them in the radio frequency range. This model successfully reproduces both the luminosity and duration of the Crab pulsar's giant radio pulses.

In the same year, Philippov et al. (2019) supported this scenario through kinetic plasma simulations that successfully reproduced the coherent radio emission mechanism and provided a detailed visualization of the processes at play. According to previous studies (e.g., Cerutti and Philippov 2017), the current sheet is unstable to the relativistic tearing mode, which causes its fragmentation and the formation of plasmoids separated by secondary current sheets. These secondary sheets themselves undergo further fragmentation on progressively smaller scales through a hierarchical process driven by the plasmoid instability (Uzdensky et al., 2010). Using a global 2D PIC simulation with a setup closely resembling that of our study, they predict the formation of a large number of plasmoids between 1 and 2 $R_{\rm LC}$. They observe plasmoid mergers throughout the current sheet. Near the light cylinder, the current sheet is populated primarily by small plasmoids, while progressively larger plasmoids appear at greater distances. Beyond a certain threshold radius, however, the plasmoid structure does not evolve anymore, as mergers cease due to the nearly radial expansion of the wind. Local 2D PIC simulations of relativistic magnetic reconnection are employed to provide a more detailed analysis of the plasmoid merging process. As plasmoids grow through successive mergers, they eventually become large enough to generate secondary current sheets perpendicular to the primary one, which themselves undergo fragmentation due to secondary tearing instabilities (see Figures 4.18a, 4.18b). The plasmoids formed in the perpendicular current sheets subsequently collide with the upstream magnetic field. In such environments, plasmoids reach relativistic velocities; their mergers or collisions with the surrounding magnetic field generate perturbations in the magnetosphere in the form of fast magnetosonic waves (see Figures 4.19a, 4.19b), which transition into vacuum electromagnetic waves in higly magnetized regions (see circular arcs propagating outwards from the reconnection layer in Figure 4.18c). The resulting light

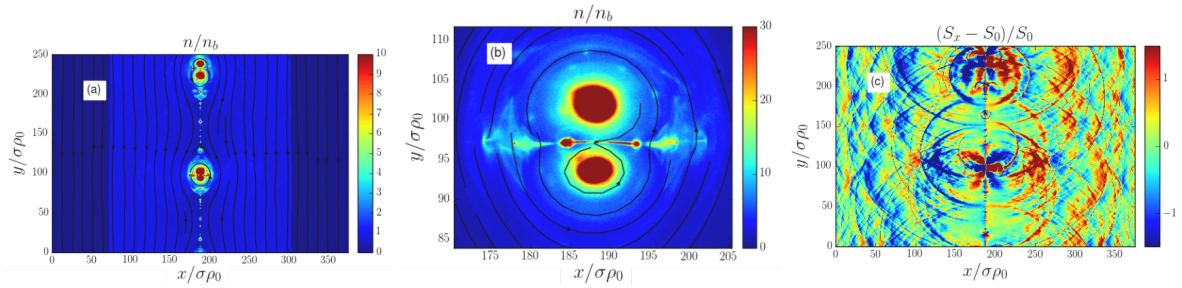

Figure 4.18: Local 2D PIC simulation of relativistic magnetic reconnection. *Panel a:* Plasma density, illustrating the fragmentation of the current sheet into a chain of plasmoids. *Panel b:* A zoomed-in view of two merging large plasmoids, showing the formation of a perpendicular secondary current sheet. *Panel c:* Outflowing (x-component) Poynting flux arcs produced by the collision of plasmoids with each other or with the magnetic field, with the average reconnection-induced Poynting flux subtracted. Figure adapted from Philippov et al. (2019).

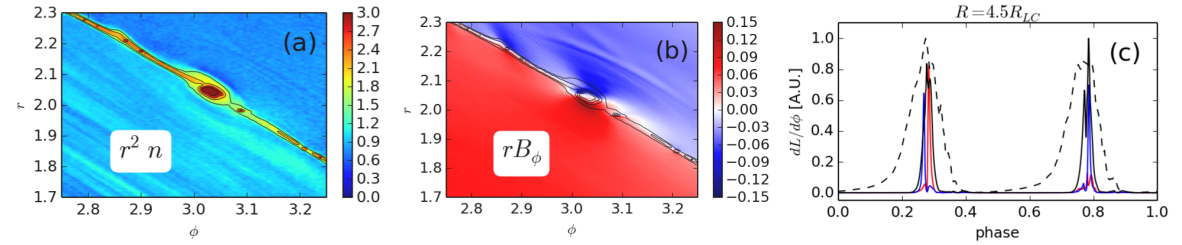

Figure 4.19: Global 2D equatorial PIC simulation of the pulsar striped wind. Radii are given in units of the light cylinder. *Panel a:* Zommed-in view of the plasma density showing a plasmoid chain. *Panel b:* Zoomed-in view of the toroidal magnetic field in the same region. Around $r = 2.2$, $\phi = 3.1$, we observe the emission of a fast magnetosonic wave originating from the plasmoid merger just below. *Panel c:* Time-averaged radio lightcurve (black solid line) and gamma-ray light curve (black dashed line). Two radio pulses are shown in red and blue. The radio pulses are phase-aligned with the gamma-ray pulses and exhibit narrower profiles. Figure adapted from Philippov et al. (2019).

curve features several bright, short peaks clustered around two phases, which align with the high-energy peaks generated by synchrotron emission from the current sheet (Figure 4.19c). For pulsars displaying strong magnetic fields at $R_{\rm LC}$, this low-frequency radiation is expected to fall in the $\gtrsim$ 100 MHz radio band, potentially detectable by the LOw Frequency ARray (LOFAR; van Haarlem et al. 2013) and the Square Kilometre Array (SKA; Dewdney et al. 2009), while weaker magnetic fields may yield lower-frequency signatures.

4.5.2 Additional wave generation triggered by the companion

Our simulations show evidence of the mechanism discussed above. More importantly, we find that, when the companion is embedded in the pulsar wind, the emission of fast magnetosonic modes is substantially increased. Indeed, the presence of the companion perturbs the current sheet, triggering further fragmentation and forced reconnection in the portion of the sheet reaching the upstream side of the companion, thereby resulting in the formation of numerous plasmoids at the companion's location. These newly formed plasmoids propagate radially along the edges of the perturbed cone (see Section 4.4.2) and eventually merge with each other or collide with the upstream magnetic field, generating fast magnetosonic waves. Figure 4.20 shows a zoomed-in view of the toroidal magnetic field in the perturbed region of the magnetosphere. Numerous fast magnetosonic waves, identifiable as white arcs, originate from merged plasmoids and propagate outwards. According to the studies discussed in the previous section, these waves are expected to escape the pulsar wind as low-frequency electromagnetic radiation falling within the radio band. Considering that the typical size of plasmoids is dictated by the current sheet thickness, and that the current sheet thickness grows linearly with radius (Cerutti and Philippov, 2017), plasmoids formed near the companion's surface located at $\sim 10\,R_{\rm LC}$ should be roughly an order of magnitude larger than those formed around $R_{\rm LC}$. The fast magnetosonic waves resulting from such plasmoid mergers should therefore exhibit lower frequencies than the usual ones originating from plasmoids mergers around $R_{\rm LC}$. Although relativistic beaming at these separations would be stronger, and hence contract the wavelengths, it is not expected to be sufficient to compensate the significant increase in the plasmoids size, particularly in the fast magnetosonic regime as the wind significantly slows down in the shocked zone.

This result indicates that the presence of a companion in the pulsar wind can significantly enhance the coherent radio emission associated with the current sheet, i.e., the radio emission phase-aligned with the gamma-ray emission. When the companion lies beyond the fast magnetosonic surface (as in Figure 4.20), the newly formed plasmoids remain within the current sheet. Consequently, the expected radio signature consists of two pulses per pulsar rotation, similar to those in Figure 4.19c but with highly enhanced amplitudes. This additional radio signature would be visible only when the perturbed region crosses the line of sight. When the companion lies within the fast magnetosonic surface, plasmoids still predominantly flow along two specific directions (see Figure 4.11), leading to a similar amplification of the spin-modulated radio pulses. However, in this case, the perturbations induced in the pulsar wind propagate more isotropically, implying that the radio signal could be detected over a broader portion of the orbit. Additionnally, in this sub-magnetosonic regime, some plasmoids are ejected between successive spirals of the current sheet (see pink arrows in Figure 4.11), which could produce additional pulses in the light curves between the two main radio and gamma-ray pulses per rotation phase associated with the current sheet.

4.5.3 A source of (periodic) radio transients

Although not fully quantified, we predict radio transients originating from the pulsar wind interacting with a small, wind-free companion. Most of this emission should be periodic, modulated by the orbit of the companion. Nevertheless, if the companion is close enough to the

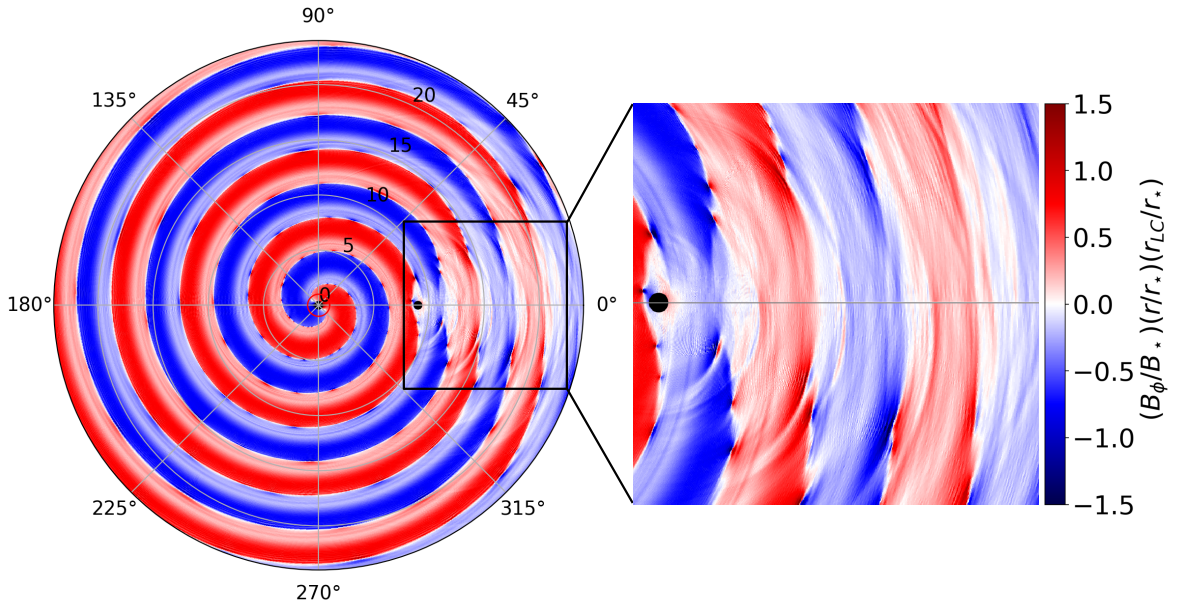

Figure 4.20: Zoomed-in snapshot of the toroidal magnetic field (B_ϕ) from the D9R1 simulation, highlighting the emission of fast magnetosonic modes (visible as white arcs) along the edges of the perturbed cone. On the left, we show a global view of the pulsar's striped wind, with the pulsar at the center and the companion (black disk) located at $d_{\rm comp} = 9\ R_{\rm LC}$. Radii are expressed in units of the light-cylinder radius, indicated by the red circle.

pulsar to lie inside the fast magnetosonic surface, further perturbations of the magnetosphere could also produce sporadic, non-periodic radio bursts.

The theoretical prediction of periodic radio transients holds particular relevance for various classes of transient events, including long-period radio transients (LPTs), rotating radio transients (RRATs), and repeating fast radio bursts (FRBs), all of which exhibit intermittent or quasi-periodic emission. Figure 4.21 provides an informative classification of these events by placing them in phase space (L_ν; $\nu \cdot W$).

LPTs (see purple stars in Figure 4.21) constitute a recently discovered class ($\sim$ 12 confirmed so far) of Galactic periodic radio sources displaying unusually long periodicities, ranging from minutes to hours (e.g., Hurley-Walker et al. 2022, 2023; Caleb et al. 2022; Caleb et al. 2024; Dong et al. 2024; de Ruiter et al. 2025). These place them in a region of the P–$\dot{P}$ diagram where no pulsar is expected according to standard magnetic field evolution models, i.e., beyond the death line (see Figure 4.22). The radio pulses last from seconds to minutes and are highly polarized. Given their long durations, sub-structures can be identified within the pulses, sometimes exhibiting millisecond-period oscillations. Multi-wavelength searches have been conducted, leading to the first detections of higher-energy counterparts from several sources within the past year. X-ray counterparts were detected from ASKAP J1832−0911 (Wang et al., 2025) and from ASKAP J144834−685644 (Anumarlapudi et al., 2025), while ILT J1101+5521 and GLEAM-X J0704−37 were observed at optical wavelengths (Hurley-Walker et al., 2024; de Ruiter et al., 2025). Some sources have been observed to remain active for months, while others have persisted for decades. Their characteristics appear distinct from those of any previously known sources, leaving their physical origin an open question. Although such long periods could be explained by supernova fallback accretion (Ronchi et al., 2022; Tong, 2023), their high luminosities seem too large to be powered solely by the pulsar's rotational energy, possibly indicating magnetar-like emission mechanisms. A variety of source candidates have been proposed, including isolated white dwarfs, neutron stars, magnetars,

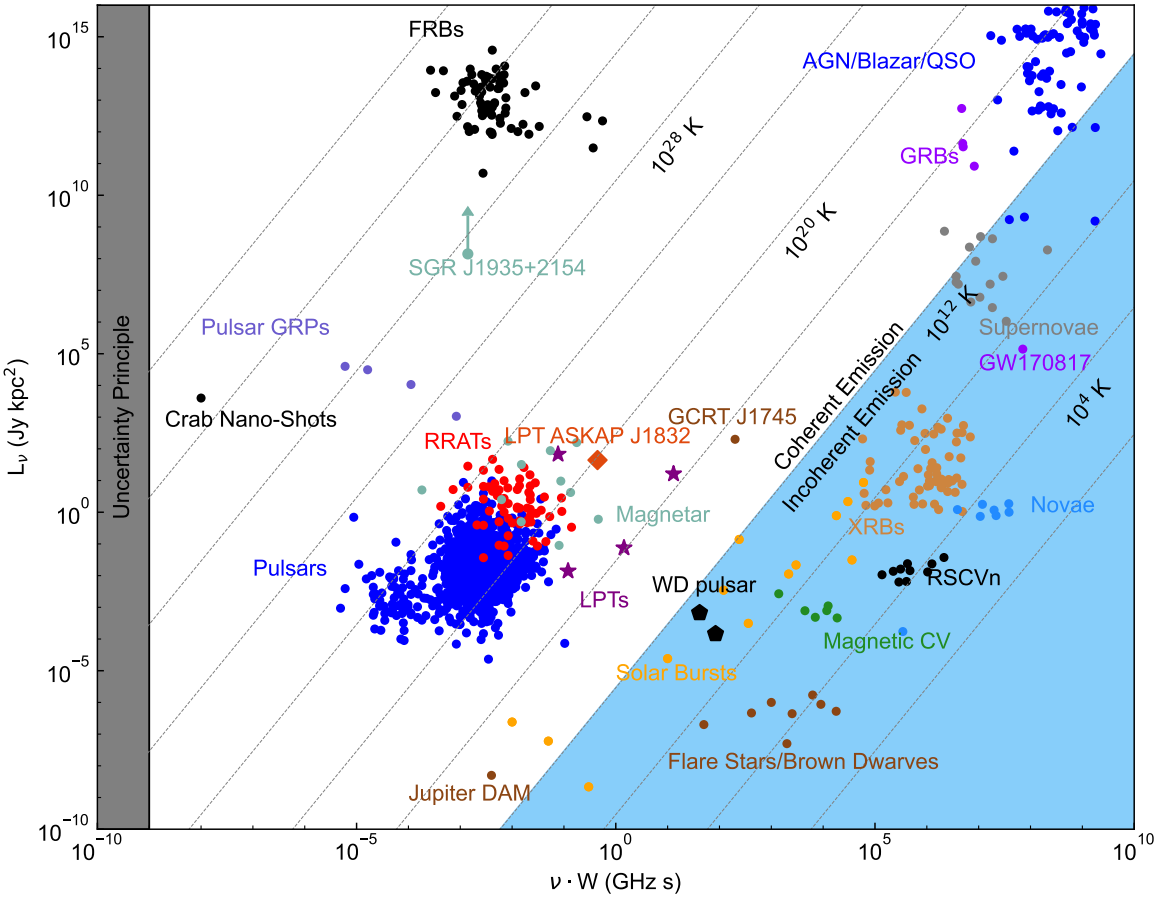

Figure 4.21: Phase-space diagram of radio transients. LPTs are shown as purple stars (the orange diamond marks the brightest sub-pulse from ASKAP J1832–0911), RRATs as red dots, and FRBs as black dots. Figure taken from Wang et al. (2025).

and binary systems involving white dwarfs, brown dwarfs, neutron stars, or exoplanets orbiting stars. Among these, magnetars and binary white dwarf scenarios are currently favored. Two LPTs (ILT J1101+5521; de Ruiter et al. 2025 and GLEAM−X J0704−37; Hurley-Walker et al. 2024; Rodriguez 2025) were recently identified as originating from white dwarf–M dwarf binary systems. Further searches will be necessary to better understand the mechanisms driving the radio emission and to determine whether all LPTs arise from magnetars, white dwarf binary systems, a combination of both, or new different sources. It is worth noting that intermediate-period radio transients are also being discovered; a recent example is the 41-second-period source reported by Wang et al. (2025).

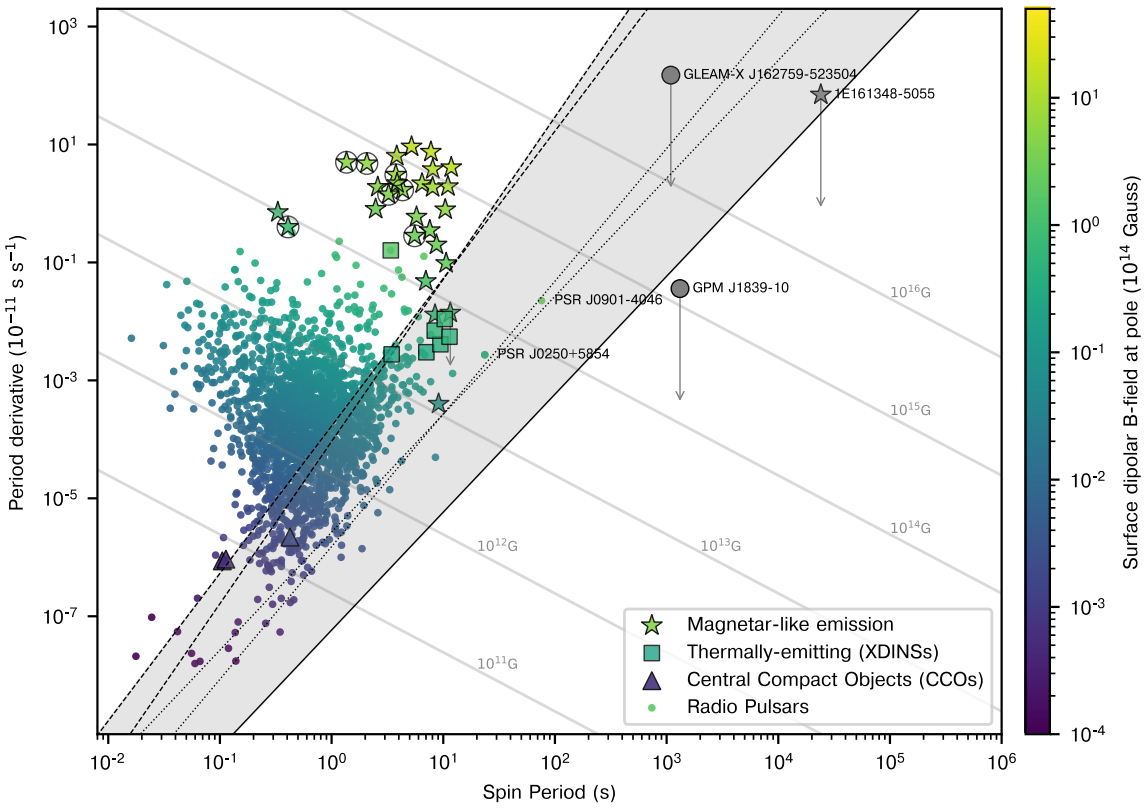

Figure 4.22: P–$\dot{P}$ diagram displaying neutron stars and the first discovered LPTs (grey circles). Theoretical death lines for a pure dipole are indicated with dashed lines, while dotted lines correspond to a twisted dipole and solid lines to a twisted multiple. The shaded area marks the death valley, taking into account all these different boundaries. GPM J1839−10 lies below the death valley and GLEAM−X J162759.5−523504.3 is below the classical dipolar death line. Figure taken from Hurley-Walker et al. (2023).

RRATs (see red dots in Figure 4.21; McLaughlin et al. 2006) are transients characterized by millisecond to second, sporadic radio bursts, separated by minutes-to-hours intervals, instead of the regular, periodic pulses seen from typical radio pulsars. A secular variation in periodicity has been observed in some RRATs. Their duty cycle is extremely low ($< 1\%$). They are detected through single-pulse searches, although they exhibit underlying periodicities similar to those of neutron stars (ranging from 45ms to 7.7s). Their surface magnetic fields range from $\sim 10^{11}$ to $\sim 5 \times 10^{13}$ G (Abhishek et al., 2022). An X-ray counterpart was found for one of them (Rea et al., 2009), but no gamma-ray counterparts were reported so far. RRATs are believed to originate from neutron stars, although their properties differ from those of the classical population (Burgay et al., 2007), leaving their exact nature an open question.

FRBs (see black dots in Figure 4.21; Lorimer et al. 2007) are brief but extremely intense

flashes of radio waves, mostly originating from extragalactic sources (except from one that was dectected in the Milky Way; Bochenek et al. 2020). FRBs have typical durations of a few milliseconds. Their extreme brightness indicates coherent emission mechanisms. Some of them are "repeaters", meaning that they emit multiple bursts over time, while others are "non-repeaters", with a single burst detected so far. Although most repeaters are not periodic, periodicity has been detected in at least one source (Chime/Frb Collaboration et al., 2020), and another FRB exhibits quasi-periodic sub-pulses (Andersen et al., 2022), pointing to a possible origin within a neutron star's magnetosphere. The origin of FRBs is still under investigation, although young magnetars are currently the leading model. Some other sources are considered, such as rapidly rotating neutron stars or black holes, compact object mergers, pulsar-planet interactions, or other more exotic possibilities. Several theoretical works have predicted the emission of repeating FRBs from small bodies orbiting pulsars (Mottez and Zarka, 2014; Mottez et al., 2020; Decoene et al., 2021). They invoke different coherent mechanisms of radio emission than those presented in Section 4.5.1, such as the cyclotron maser instability, and are based on the theory of Alfvén wings (Neubauer, 1980; Mottez and Heyvaerts, 2011).

4.6 Discussion and conclusion

Thanks to the PIC method, we were able, for the first time, to simulate a pulsar magnetosphere and its wind interacting with a small spherical companion. This allowed us to provide a comprehensive view of the resulting magnetospheric restructuring, assess particle acceleration processes, and predict the associated electromagnetic emission from such systems.

We show that introducing a companion (of comparable size to the pulsar) in the pulsar wind substantially modifies its dynamical and energetic characteristics. When the companion is located inside the fast magnetosonic point, the pulsar wind experiences a relatively isotropic deceleration. In contrast, if the companion lies beyond this critical point, a shock forms, and the perturbations are carried downstream in a cone-shaped region trailing the companion. Regardless of the presence of a shock, each time the outgoing current sheet encounters the companion's surface, forced magnetic reconnection occurs, resulting in a marked increase in particle acceleration. Following reacceleration, particles predominantly stream along two branches surrounding the companion, thereby forming an orbital-modulated hollow cone of high-energy synchrotron radiation. The intensity and aperture of such radiation decrease with increasing orbital separation and increase with the companion's size. However, in all cases, this new non-thermal component radically exceeds the pulsed synchrotron flux emitted by an isolated pulsar magnetosphere.

Despite its contributions, this study has some limitations that deserve to be mentioned. First, adopting a 2D simulation framework introduces some inherent artifacts. Indeed, constraining the magnetic field to the equatorial plane may alter the topology of the field lines. In particular, the equatorial setup inherently forces all magnetic field lines piling up in front of the companion to undergo reconnection, which may lead to an overestimation of the energy dissipated into particle kinetic energy. Therefore, our results should be interpreted as upper bounds on particle acceleration and high-energy radiation. Moreover, in two dimensions, particles escaping from reconnection X-points are trapped within neighboring plasmoids. In contrast, a third spatial dimension would permit some of these accelerated particles to leak out of the plasmoids (Zhang et al., 2021; Chernoglazov et al., 2023), potentially modifying the structure of the resulting hollow cone of radiation. As noted at the outset of this work, the scale separation achieved in our PIC simulations is several orders of magnitude smaller than that of a realistic pulsar magnetosphere. This computational constrain restricts the modeled radiation's energy range, introducing uncertainties in the synchrotron spectrum, particularly regarding its spectral bounds and overall shape. However, the total radiated energy flux

remains conserved and unaffected by this limitation. We decided not to include a wind for the companion; indeed, the companion's wind is primarily expected to increase the effective surface area of the companion, but not to substantially alter our results. Lastly, the inclusion of the companion's orbital motion could introduce a dynamic distortion of the wake and cause the companion's surface to intersect the current sheet not only radially but also azimuthally. As a result, the existing asymmetry between the opposite branches of the hollow emission cone could be exacerbated or diminished, depending on the direction of the companion's orbital motion, thereby affecting the asymmetry reflected in the two peaks of the light curves. The angular offset of the cone relative to the pulsar-companion axis could also be altered. However, these effects are likely to remain minor given the significant difference between the orbital velocity of the companion and the pulsar's rotational speed.

To conclude, we predict a new orbital-modulated high-energy component that arises when a small companion—such as a planet, asteroid, or weakly magnetized neutron star—orbits the pulsar. This emission is expected to be detectable primarily in systems viewed close to edge-on. We predict that the characteristic frequency of this non-thermal component lies in the soft gamma-ray regime. Consequently, these transients are likely to be detectable only within galactic distances. Our model also predicts associated radio counterparts, although not yet fully quantified. We demonstrate that the presence of a companion triggers abundant fast magnetosonic wave emission (significantly more than in isolated pulsars), mostly along two specific orbital directions. Since previous studies have shown that such waves can escape the magnetosphere as coherent radio emission, this combined mechanism predicts periodic radio transients observable at two distinct orbital phases. Such galactic periodic radio counterparts would be of significant interest, especially in light of the various observed radio transient classes whose origins remain uncertain (e.g., LPTs, RRATs, repeating FRBs).

Chapter 5

Pulsar wind - disk interaction: application to transitional millisecond pulsars

Contents

5.1 Transitional millisecond pulsars (tMSPs) 86
5.1.1 Bridging the gap between radio and accreting MSPs 86
5.1.2 The population of tMSPs 88
5.1.3 The three states of tMSPs 90
5.1.4 Optical and X-ray pulsations from PSR J1023+0038 in the sub-luminous disk state 91
5.2 Existing models in the literature 93
5.2.1 Phenomenological models of X-ray and optical pulses 93
5.2.2 Numerical simulations of disk–magnetosphere interaction 94
5.3 Our numerical model 94
5.3.1 3D setup of the pulsar magnetosphere 94
5.3.2 Disk implementation 98
5.3.3 Parametric study: different magnetic obliquities 99
5.4 Structure of the magnetosphere in the presence of the disk 100
5.4.1 Global structure 102
5.4.2 Particle acceleration 106
5.4.3 Plasma isotropization 107
5.5 Synchrotron emission 108
5.5.1 Increase of the synchrotron emission due to the disk 108
5.5.2 Light curves 110
5.5.3 Polarization properties 113
5.6 Discussion and conclusion 119

This chapter is based on Richard-Romei et al. (2026), in prep.

5.1 Transitional millisecond pulsars (tMSPs)

5.1.1 Bridging the gap between radio and accreting MSPs

Classical radio pulsars are usually isolated objects with spin periods ranging from ~ 0.1 s to ~ 10 s, and magnetic fields on the order of 10^{11}-10^{13} G. They populate the central region of the P–$\dot{P}$ diagram (Figure 5.1). Millisecond pulsars (MSPs), by contrast, are old neutron stars with much weaker magnetic fields ($\sim 10^{7}$-10^{8} G) and very short spin periods (< 30 ms), often found in globular clusters. They are usually found in binary systems. According to the recycling scenario, MSPs are thought to originate from low-mass X-ray binaries (LMXBs), in which a neutron star accretes matter from a low-mass donor star ($\leq 1 M_{\odot}$). The companion star orbits the compact object on timescales ranging from ~ 10 minutes to about a day, with the orbit gradually circularized by tidal forces. Accretion proceeds over $\sim 10^{7} - 10^{9}$ years through the formation of an accretion disk, as matter passes the inner Lagrangian point and enters the Roche lobe of the neutron star. The inflowing matter rotates at relativistic Keplerian velocities, thereby transferring angular momentum to the neutron star. As a result, the pulsar is spun up to millisecond periods and ends up in the lower-left corner of the P–$\dot{P}$ diagram (see the circled area of Figure 5.1).

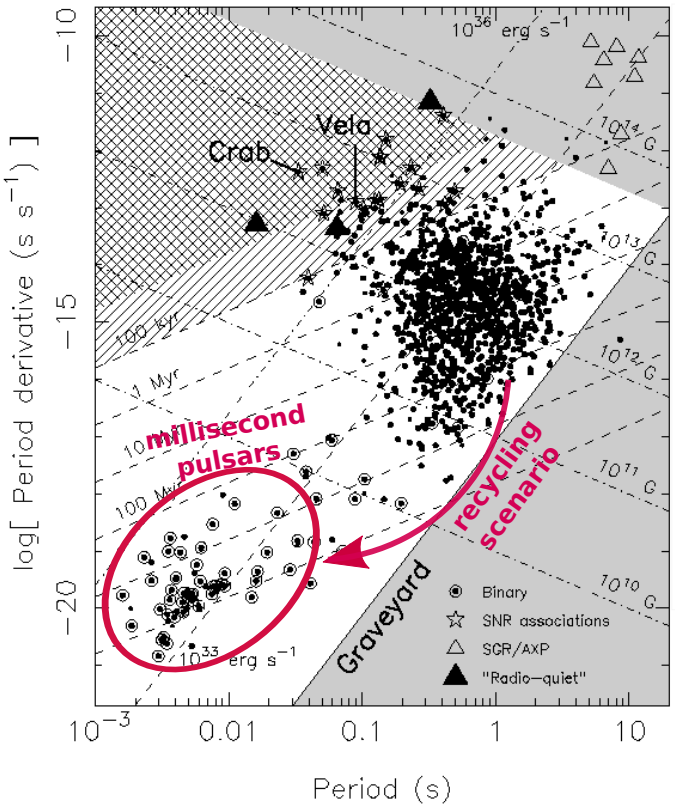

Figure 5.1: P–$\dot{P}$ diagram classifying the pulsar population by their spin period P and period derivative $\dot{P}$. Each black dot represents an individual pulsar, while circled dots indicate pulsars found in binary systems. The pink-circled region highlights the millisecond pulsars, and the pink arrow illustrates their evolutionary path. Figure adapted from Lorimer and Kramer (2004).

We distinguish two main classes of millisecond pulsar binaries: accreting millisecond pulsars (AMXPs, see orange symbols in Figure 5.2), a subclass of LMXBs, and rotation-powered millisecond pulsars (see blue and grey symbols in Figure 5.2). AMXPs are compact binary systems with orbital periods $P_{\rm orb} < 1$ day, alternating between X-ray outbursts ($L_{\rm X,outburst} \sim 10^{36}$–$10^{38}$ erg s^{-1}) and extended quiescent phases ($L_{\rm X,quiescence} \sim 10^{31}$–$10^{32}$ erg s^{-1}). Rotation-

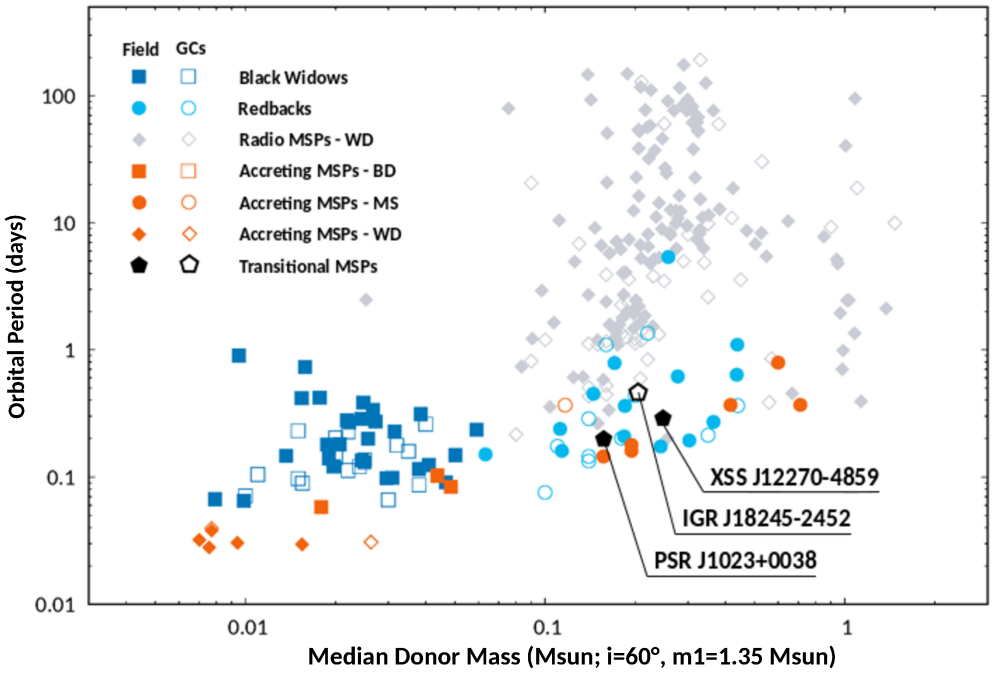

Figure 5.2: The population of millisecond pulsar binaries is shown as a function of orbital period and median donor mass (computed assuming an inclination of 60° and neutron star masses of 1.35 $M_\odot$). Accreting millisecond X-ray pulsars (AMXPs) are represented in orange, with different symbols indicating the companion type: squares for brown dwarf companions, circles for main-sequence stars, and diamonds for white dwarfs. Spiders are shown in blue, with black widows indicated by dark blue squares and redbacks by cyan circles. Non-interacting radio MSPs with white dwarf companions are represented in grey. Transitional millisecond pulsars (tMSPs) are plotted in black. Filled symbols correspond to sources located in the Galactic field, while empty symbols indicate those found in globular clusters. Figure taken from Papitto and Martino (2021).

powered MSPs are significantly more numerous than AMXPs, with 471 systems identified compared to only about 25 AMXPs as of today. They can reach much longer orbital periods, up to approximately 100 days, and are typically observed in the radio band (or in gamma rays, when intrabinary material eclipses the radio emission). They are typically found in systems with white dwarf or main-sequence companions, as well as in the so-called class of "spiders." Spider pulsars are subdivided into "black widows," which host very low-mass companions ($< 0.1\,M_\odot$) that are often nearly evaporated by the pulsar wind, and "redbacks," which host heavier companions with masses in the 0.1–0.5 $M_\odot$ range (see Koljonen and Linares 2025 for a newly available catalog of spider pulsars and more peculiar systems such as transitional millisecond pulsars).

Since the early 2000s, some millisecond pulsar binaries have been observed to transition between accretion-powered and rotation-powered states. This newly identified class of objects (see black points in Figure 5.2), referred to as transitional millisecond pulsars (tMSPs), bridges the gap between radio millisecond pulsars and accreting ones (see Jaodand et al. 2017; Campana and Di Salvo 2018 and Papitto and Martino 2021 for reviews). It remains unclear whether they are destined to become rotation-powered pulsars after completely consuming their companion, or if they follow an alternative evolutionary path.

It is worth noting that millisecond pulsar binaries may further evolve into isolated systems, either as isolated neutron stars, if the companion's mass is entirely accreted or lost through ablation or evaporation, or as isolated black holes if the neutron star accretes enough mass to exceed the maximum gravitational mass for rotating neutron stars. While no observational evidence exists for the latter scenario to date, it has been discussed in various theoretical studies (see, for example, Lavagetto et al. 2004; Dermer and Atoyan 2006; Giacomazzo and Perna 2012).

5.1.2 The population of tMSPs

To date, only three sources have been confirmed as transitional millisecond pulsars. Figure 5.3 represents the evolution of their states over time.

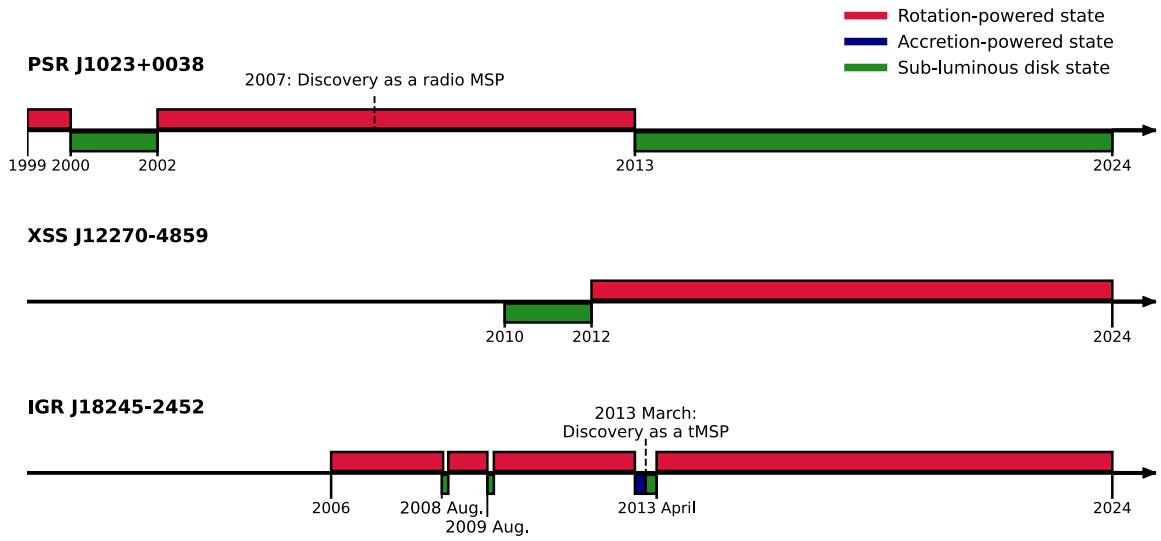

Figure 5.3: Temporal evolution of the three confirmed tMSPs across their different states. Note that the sub-luminous disk episode indicated for IGR J18245−2452 in April 2013 still requires confirmation. Figure from A. Miraval Zanon.

The first identified source is PSR J1023+0038, located at a distance of ~ 1.37 kpc. It was

initially observed in May 2000 as a disk-accreting binary, and named FIRST J102347.6−00384 (Bond et al., 2002; Szkody et al., 2003; Wang et al., 2009). In early 2002, the system underwent a dramatic transformation, marked by the disappearance of the accretion disk and the emergence of features characteristic of a redback radio millisecond pulsar (Archibald et al., 2009). Its spin period was measured to be 1.69 milliseconds, and its companion was identified as a $0.2M_{\odot}$ main-sequence star, in a 4.75-hour orbit. From June 2013 to the present, radio pulsations have once again vanished (Stappers et al., 2014), while, in contrast, double-peaked Hα emission lines reappeared (Halpern et al., 2013), accompanied by enhanced high-energy emission (X-rays, UV, and gamma rays; see Patruno et al. 2014; Stappers et al. 2014), indicating the renewed presence of an accretion disk. Notably, during both disk-present episodes, the average X-ray luminosity remained relatively low ($L_X \sim 10^{33}$–10^{34} erg, s^{-1}), thus leading to the designation of this regime as the "sub-luminous disk state" (see next section for a detailed description).

The second identified tMSP is IGR J18245−2452, located in the globular cluster M28 at a distance of 5.5 kpc and hosting a main-sequence companion star. Initially classified as a radio millisecond pulsar (PSR J1824−2452I; Bégin 2006), it exhibited a month-long X-ray accretion outburst in March 2013, with a luminosity of $L_{\rm X,outburst} \sim 10^{36}$ erg, s^{-1} (Eckert et al., 2013), thereby revealing its AMXP nature (Papitto et al., 2013), before transitioning back to a radio MSP state. This makes it the first system ever observed subsequently in a typical accretion-powered and a typical rotation-powered pulsar state. Archival observations identified two additional outbursts in 2008 and 2009 (Pallanca et al., 2013; Linares, 2013; Linares et al., 2014), whose characteristics are consistent with those of a sub-luminous disk state.

The third identified tMSP is XSS J12270−4859, located at a distance of $\sim$ 1.1 kpc. From 2010 to 2012, it exhibited properties characteritic of the sub-luminous disk state (Saitou et al., 2009; de Martino et al., 2010; Hill et al., 2011; de Martino et al., 2013; de Martino et al., 2014), in particular with the presence of a disk and quite low X-ray luminosity ($L_X \sim 10^{33}$ erg, s^{-1}). Since the end of 2012 and up to the present day, the system transitioned to a radio redback state (Bassa et al., 2014), characterized by a 1.69 ms spin period and the detection of radio pulsations, although eclipsed over a large fraction of the orbit (Roy et al., 2015).

Since these new discoveries, many searches have been conducted in order to increase the sample of confirmed tMSPs, therefore leading to the identification of many candidates. A few of the most promising sources are the following: 3FGL J1544.6−1125 (Bogdanov and Halpern, 2015), CXOU J110926.4−650224 (Coti Zelati et al., 2019), 4FGL J0407.7−5702 (Miller et al., 2020), 3FGL J0427.9−6704 (Strader et al., 2016), 4FGL J0540.0−7552 (Strader et al., 2021), CXOU J174805.05−244641.0 (Bahramian et al., 2018), CXOU 174802.26−244637.5 (Bogdanov et al., 2021), XMM J174457−2850.3 (Degenaar et al., 2014). The past year alone has seen the identification of several new transitional MSP candidates (see Pattie et al. 2024; Thongmeearkom et al. 2024; Turchetta et al. 2025; Kyer et al. 2025; Zyuzin et al. 2025) and their number can reasonably be expected to increase in the future, especially by using the Fermi-LAT catalog (Ballet et al., 2024) to cross-chek unidentified gamma-ray sources with X-ray variable counterparts.

However, although many sources show behaviours that closely resemble those of the well-established tMSPs, confirming their nature remains challenging. In particular, confirming a system as a tMSP requires observing it in at least two of the three characteristic states. Yet, transitions between states can occur very rapidly, making them difficult to capture, and can be very infrequent, as sources may spend decades in a single state. This partly explains why their confirmed population remains scarce.

5.1.3 The three states of tMSPs

Transitional millisecond pulsars alternate between three distinct states, with transitions occurring on timescales of a few days, driven by variations in the mass accretion rate from the low-mass companion star.

In the accretion-powered state, matter lost by the companion star is accreted onto the neutron star, leading to outbursts of intense X-ray emission (with typical luminosities of $L_{\rm X} \sim 5 \times 10^{36}\,{\rm erg\,s^{-1}}$), comparable in intensity and duration to those observed in other AMXPs. These outbursts are interspersed with quiescent phases during which the X-ray luminosity drops by several orders of magnitude ($L_{\rm X} \sim 10^{31}-10^{33}\,{\rm erg\,s^{-1}}$). During quiescence, radio pulsations (so far observed only in IGR J18245−2452) and gamma-ray emission may be detected.

In the rotation-powered state, the three known transitional millisecond pulsars are classified as redbacks. The inflowing matter from the companion star quenches the pulsar wind, resulting in the formation of an intrabinary shock. Ionised material blown off by the pulsar wind, either from the donor's surface or from the Lagrangian point, enshrouds the system and causes irregular, wavelength-dependent eclipses of the radio pulses. Additionally, the pulsar wind heats the donor star, and irradiation by high-energy emission from the pulsar magnetosphere imprints distinctive orbital-modulated optical signatures. The X-ray emissions observed in this state are mainly non-thermal (likely due to synchrotron emission at the intrabinary shock), among the most luminous within the redback population ($L_X \sim 10^{32}$ erg, s^{-1}), and exhibit orbital modulation, consistent with observations of other redbacks. Non-thermal gamma-ray emissions were also detected during this state, with some systems exhibiting pulsed signals aligned in phase with the radio pulsations.

As previously mentioned, tMSPs are also found in a third intermediate state, called the "sub-luminous disk state." This state owes its name to its X-ray luminosity of $L_X \sim 10^{33}$–10^{34} erg s^{-1}, which is brighter than that found for rotation-powered MSPs and quiescent AMXPs ($L_X \sim 10^{30}$–10^{32} erg s^{-1}), but fainter than X-ray outbursts of AMXPs ($L_X \sim 10^{36}$–10^{37} erg s^{-1}). One particularly striking feature of these systems is their switching between two X-ray intensity modes, termed the "high" and "low" modes, accompanied by occasional and (most probably) independent flares. Figure 5.4 shows the light curves of PSR J1023+0038, where a clear distinction can be seen between the X-ray high (blue points) and low modes (red points), as well as the flaring mode (green points). Transitions occur on timescales of $\sim$ 10 s and each mode lasts between $\sim$ 10 s to a few hours. It is worth noting that IGR J18245−2452 exhibited much longer transition times ($\sim 500 - 1000$ s) and mode durations (up to 20 hours), but these values should be interpreted with caution since shorter timescales could not be probed for this source. The X-ray luminosity is relatively constant among modes and is of $L_{\rm X,diskhigh} \sim 10^{33}$–$10^{34}$ erg s^{-1} in the high mode and drops by about one order of magnitude in the low mode ($L_{\rm X,disklow} \sim 0.1 L_{\rm X,diskhigh}$), remaining still a few times brighter than that detected in the rotation-powered state ($L_{\rm X,disklow} \leq 0.1 L_{\rm X,rot}$). No modulation with the orbital period was reported so far. However, in the high mode, both PSR J1023+0038 and XSS J12270−4859 exhibit X-ray pulsations modulated by the neutron star spin period. These pulsations disappear in the low mode and the flaring mode. The X-ray spectrum in the high mode is mostly non-thermal, with a softer power-law than in the rotation-powered state, and becomes even softer in the low mode. A faint thermal component is visible in the high mode and disappears in the low mode. The high and low mode behaviour is also observed in the UV band. The optical emission and the gamma-ray emission are a few times brighter than in the rotation-powered state, i.e., $L_{\rm opt,disk} \sim$ few times $L_{\rm opt,rot}$ and $L_{\gamma,\rm disk} \sim$ few times $L_{\gamma,\rm rot}$. A radio continuous emission is present (both for PSR J1023+0038 and XSS J12270−4859), with and anti-correlated variability compared to the X-rays and no pulsations (for PSR J1023+0038). Flares, lasting between a few minutes to a few hours, are observed across the whole spectrum (radio, near-infrared, optical, UV and X-ray bands),

although they are dominated by the X-rays, which luminosity can even exceed the spindown luminosity of the pulsar.

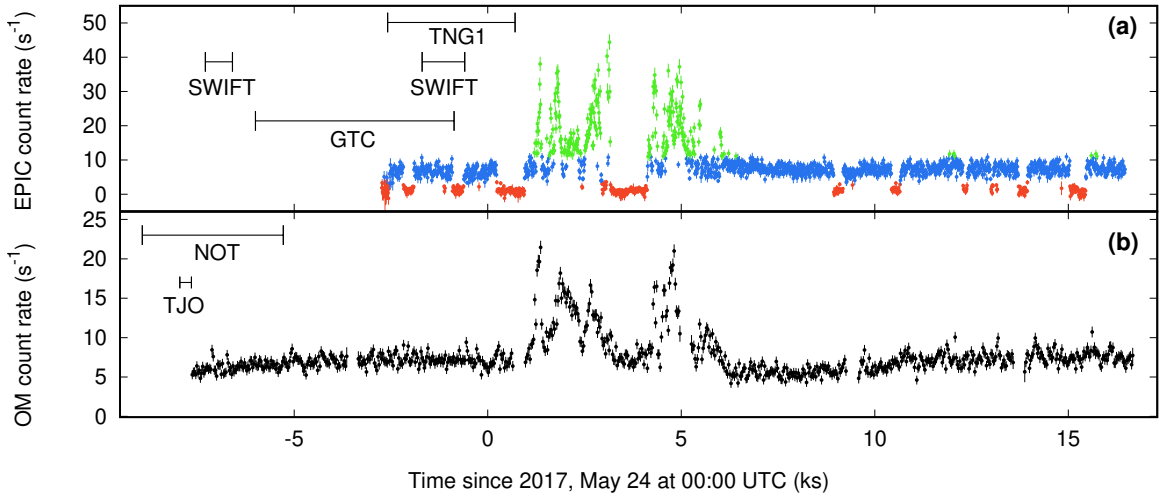

Figure 5.4: *Panel (a):* X-ray (0.3-10 keV) light curve observed during XMM1 (with EPIC), binned every 10 s. Blue, red and green points respectively correspond to the high, low and flaring mode. *Panel (b):* optical light curve observed by the Optical Monitor on board XMM-Newton, binned every 30 s. Horizontal bars illustrate the intervals of simultaneous observations by other instruments. Figure taken from Papitto et al. (2019).

5.1.4 Optical and X-ray pulsations from PSR J1023+0038 in the sub-luminous disk state

PSR J1023+0038 is observed in the high mode during $\sim 80\%$ of the time. During the high mode, X-ray and optical coherent quasi-simultaneous pulsations are detected, making it the first MSP discovered to pulsate in the optical band (since then, optical and UV pulsations have also been detected from the AMXP SAX J1808.4−3658; Ambrosino et al. 2021). They both disappear in the low mode, while pulses are also found during flares, with lower amplitudes than those detected in the high mode. Figure 5.5 shows the X-ray pulse profiles in the high mode (blue curve), the optical pulse profiles in the high mode (red curve) and the optical pulse profiles in the flaring mode (green curve), as a function of the pulsar spin phase. We can see that the optical and X-ray pulse profiles (in the high mode) are similar, with two broad peaks $\sim 180^\circ$ apart per pulsar spin period. The optical pulsations lag the X-ray pulsations by ~ 150 μs, corresponding to $0.11 P_{\rm spin}$ (there is a small variability between the two pulses of the light curve; see Illiano et al. 2023). Optical and X-ray pulses are shown to originate from regions located within a few tens of kilometers, as indicated by their compatible orbital Doppler shifts. The rms pulsed fraction of the pulses varies over time (see Miraval Zanon et al. 2022; Illiano et al. 2023); X-ray pulsations have rms amplitudes of ~ 4.3–10.8% while optical pulsations have rms amplitudes of ~ 0.1–0.8% (see Illiano et al. 2023 and references therein). Interestingly, both the optical and the X-ray pulsed spectra can be fitted by the same power-law (Figure 5.6). Recent polarimetric observations find polarization properties that differ significantly from the polarization properties observed in other accreting or rotation-powered pulsars. Strikingly, the polarized emission spectrum corresponds to the pulsed emission spectrum, in optical and in X-rays (see Section5.6 for further details).

Taken together, these observational properties point to a common mechanism as the origin of both the X-ray and optical pulsed emission. Numerous studies have attempted to uncover this underlying mechanism, which will be the focus of the next section.

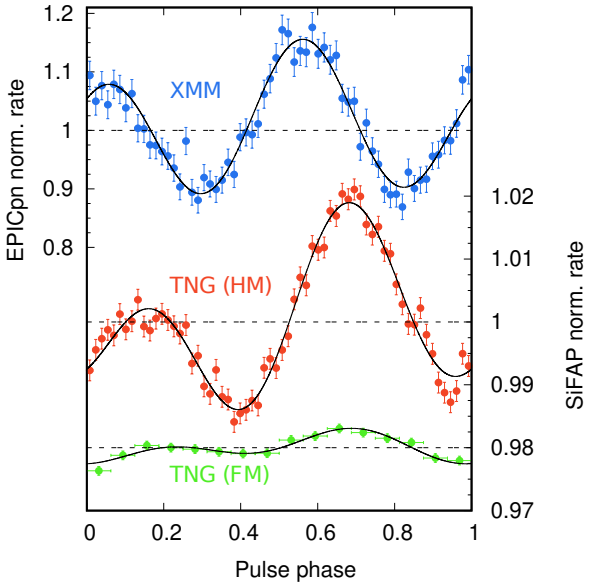

Figure 5.5: Pulse profiles as a function of the pulsar spin phase. The X-ray profile is shown as the blue curve (left $y-$axis) and was obtained by folding the high-mode intervals of the XMM-Newton/EPIC-pn data. The optical profile, shown in red (right $y-$axis), was obtained by folding the high-mode intervals of the TNG/SiFAP data. The green curve (right $y-$axis, arbitrarily shifted) represents the optical pulse profile during the flaring mode, obtained by folding the flaring-mode intervals of the TNG/SiFAP data. Figure taken from Papitto et al. (2019).

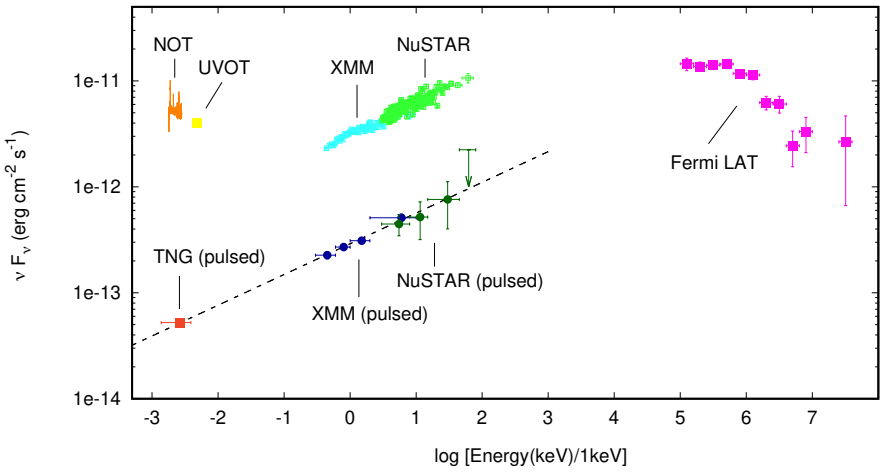

Figure 5.6: Spectral energy distribution of the total and pulsed emission from PSR J1023+0038 detected during the high mode (and corrected for interstellar extinction). Figure taken from Papitto et al. (2019). Different colors correspond to different instruments. The total NOT optical spectrum is plotted in orange, the total Swift/UVOT UVW1 spectrum is plotted with a yellow square. The average pulsed TNG/SiFAP optical flux is plotted with a red square. The total and pulsed XMM-Newton X-ray spectra are plotted with light and dark blue points, respectively. The total and pulsed NuSTAR X-ray spectra are plotted with light and dark green points, respectively. The average Fermi-LAT spectrum measured by Torres et al. (2017) is plotted with the magenta squares. The dashed line corresponds to a cutoff power-law $\nu F_\nu \sim \nu^{0.3}$, normalized so as to match the observed pulsed flux.

5.2 Existing models in the literature

5.2.1 Phenomenological models of X-ray and optical pulses

The simultaneous detection of unexpectedly bright optical and X-ray pulsations from PSR J1023+0038 has prompted numerous efforts to identify the physical mechanisms responsible for such emissions. In this section, we outline the main scenarios that have been proposed over the past few years, without aiming to be fully comprehensive, and refer the reader to the review by Papitto et al. (2019) for further details.

First, the X-ray pulsations were thought to originate from radiation emitted by matter accreted onto the magnetic poles through accretion columns (Archibald et al., 2015). However, the discovery of additionnal optical pulses discarded this scenario since the observed luminosities of the optical pulses were ~ 30 times brighter than what could be expected from such scenario (Ambrosino et al., 2017). This latter discovery also ruled out, by energy arguments, the hypothesis of optical emission originating from accretion-powered X-ray emission being reprocessed at the surface of the star or by the disk.

Papitto and Torres (2015) considered a propeller model, where most of the inflowing matter is expelled by the rapidly-rotating inner parts of the magnetosphere (Shvartsman, 1971; Illarionov and Sunyaev, 1975), instead of being accreted onto the neutron star surface. In this scenario, the accretion rate is very low and only accounts for a small fraction of the X-ray luminosity, even though it remains sufficient to account for the X-ray pulsations. The rest of the emission is due to synchrotron radiation at the boundary between the magnetosphere and the disk and additional emission comes from material outflowing from the system. The propeller regime bridges the accretion-powered and rotation-powered states. However, here again, the discovery of optical pulsations that cannot be explained by accretion, combined with their strong similarity to the X-ray pulsations and the resulting hypothesis of a common underlying mechanism (Papitto et al., 2019; Miraval Zanon et al., 2022), called into question an accretion-driven origin.

In contrast to the accretion-based model, Ambrosino et al. (2017) proposed that the optical and X-ray pulsations originate from rotation-powered synchro-curvature emission from the pulsar magnetosphere. However, this mechanism would require an extremely high conversion efficiency from the pulsar's spin-down energy to optical and X-ray radiation, much higher than in any known pulsar (Papitto et al., 2019).

Another scenario, proposed by Papitto et al. (2019), favours the emission of optical and X-ray pulsations at the shock front between the pulsar wind and the accretion disk. In this model, the relativistic plasma wind is shocked and hence accelerated at the inner edge of the accretion disk, at ~ 100 km from the neutron star surface, thereby producing synchrotron radiation (ranging from optical to X-rays) modulated by the pulsar's spin period. The disappearance of pulsations in the low mode is attributed to the inner disk boundary being pushed outward by the pulsar wind. Further works, such as Campana et al. (2019); Illiano et al. (2023); Baglio et al. (2024), support this model.

Veledina et al. (2019) proposed a related yet distinct model in which the accretion disk is truncated outside the light cylinder during the high mode, allowing the pulsar wind to form and propagate before interacting with the disk. In this scenario, the pulsar wind heats the inner regions of the disk, and the energized particles cool via synchrotron emission, producing radiation across the X-ray to optical bands. Pulsations arise naturally due to modulation by the rotating pulsar wind. In contrast to the model by Papitto et al. (2019), the disappearance of pulsations during the X-ray low mode is attributed to a transition to the propeller regime, wherein the disk penetrates the light cylinder and suppresses the pulsar wind.

Measurements of the spin-down rate, which reveal a slight increase in the presence of the disk compared to the isolated case (Jaodand et al., 2016; Burtovoi et al., 2020), suggest that accretion is not occurring; otherwise, a much stronger spin-down change would be expected.

At the same time, they imply that the disk must be located close to the neutron star, since a more distant disk would have no noticeable effect on the spin-down. These observations therefore support the most recent scenarios discussed.

5.2.2 Numerical simulations of disk–magnetosphere interaction

While significant efforts have been made to uncover the mechanisms responsible for the optical and X-ray pulsations observed in transitional millisecond pulsars (see Section 5.2.1), all proposed models rely fundamentally on the global dynamics of the interaction between the neutron star's magnetosphere and the accretion flow. This interaction has been extensively investigated through numerical simulations, predominantly using magnetohydrodynamic methods. Analytical approaches have also contributed to our understanding of disk–magnetosphere coupling, notably the work by Ekşİ and Alpar (2005).

Early studies focused on the interaction between rotating magnetized stars and their surrounding accretion disks (Miller and Stone, 1997), particularly in the case of T-Tauri stars, i.e., young stellar objects with strong magnetic fields and surrounded by accretion disks (Hayashi et al., 1996; Romanova et al., 2002, 2003b, 2008; Zanni and Ferreira, 2009, 2013; Takasao et al., 2018; Romanova et al., 2021). These works provided the foundations for models of disk-magnetosphere coupling in the more extreme compact object regime. Simulations of accreting neutron stars explored disk survival, spin-down torques, and state transitions by modelling aligned dipolar rotators (Romanova et al., 2003a; Çıkıntoğlu et al., 2022), with some studies including general-relativistic effects (Parfrey et al., 2017; Parfrey and Tchekhovskoy, 2017, 2024). More recent works extended theses models to oblique dipolar rotators (Das and Porth, 2024; Murguia-Berthier et al., 2024) and multipolar magnetic fields (Das et al., 2022).

Over the past year, new studies have addressed transitional millisecond pulsars specifically. In Guerra et al. (2024), the interaction between pulsar winds and companion-star outflows is investigated using hydrodynamic simulations. Vurgun et al. (2025) studies the disk stability through MHD simulations, based on energy arguments.

However, none of these approaches simultaneously capture the global dynamics of the pulsar–disk interaction and the kinetic processes governing particle acceleration and radiation. Such a combined treatment is essential to reproduce the non-thermal emission observed in transitional millisecond pulsars (tMSPs), and in particular, to explain their peculiar X-ray and optical pulsations. This constitutes the primary motivation for our work and justifies our use of PIC simulations to capture both the global dynamics and kinetic processes.

5.3 Our numerical model

In order to investigate the non-thermal processes at play when the pulsar magnetosphere interacts with a disk, we resort to PIC simulations. Unlike the previous study where the pulsar magnetosphere interacted with a spherical companion (Chapter 4), here, the pulsar magnetosphere interacts with a disk that covers the full azimuthal angle. Hence, if we want to allow the plasma to flow around the disk, a 2D equatorial approach no longer suffices. This is why we add a third dimension for this study.

5.3.1 3D setup of the pulsar magnetosphere

We perform 3D PIC simulations with the flat spacetime version of the `Zeltron` code. We use a spherical system of coordinates (r, θ, ϕ) with $1024 \times 128 \times 256$ cells in the respective directions. The grid is uniformly spaced in θ and ϕ but logarithmically spaced in r, which ensures the conservation of the cell aspect ratio with radius. Such grids are well adapted to model pulsar magnetospheres, where densities and fields amplitudes decrease with radius, leading to an increase in plasma skin depth and Larmor radius as the radius increases. The inner

boundary is given by the neutron star surface ($r = r_\star$), which lies at the center of the box, and the light cylinder radius equals $R_{\rm LC} = 5\,r_\star$. The simulation box is spherical and extends up to $r_{\rm max} = 5.6\,R_{\rm LC}$. However, an absorbing layer is implemented at $r_{\rm absorb} = 0.9\,r_{\rm rmax}$ for fields and particles (see Cerutti et al. 2015 for more details), so as to mimic an open boundary. Indeed, given the parameters chosen for these simulations, the fast magnetosonic point (see Section 4.2.4) approximately coincides with the outer boundary of the simulation domain, so it is reasonable to assume that the wind propagates freely to infinity beyond this point. Particles traveling back to the star surface are also absorbed, while elastic reflection is implemented at the two θ-boundaries, and boundary conditions are periodic in the ϕ-direction. As for the fields, axisymmetry constrains their behavior in the θ-direction, and periodic boundary conditions are applied in the ϕ-direction.

Initially, the star is in vacuum with a dipolar magnetic field anchored at its surface. The rotation axis is along the $\theta = 0$ direction and the magnetic obliquity (χ) denotes the angle between the magnetic moment ($\boldsymbol{\mu}$) and the rotation axis ($\boldsymbol{\Omega}/\Omega$). Let us define a system of cartesian coordinates (x, y, z), such that the z-direction corresponds to the $\theta = 0$ direction and the x-axis is set to be along the $\phi = 0$ direction. At $t = 0$, the magnetic moment $\boldsymbol{\mu} = \mu \mathbf{u}_z$ is inclined in the (xz)-plane according to the rotation matrix

$$\mathcal{R}(\chi) = \begin{pmatrix} \cos\chi & 0 & \sin\chi \\ 0 & 1 & 0 \\ -\sin\chi & 0 & \cos\chi \end{pmatrix} . \tag{5.1}$$

We impose a perfect conductor condition at the stellar surface which, due to the Lorentz transformation, leads to a non-zero poloidal electric field in the simulation frame:

$$\boldsymbol{E} = -\frac{(\boldsymbol{\Omega} \times \boldsymbol{r}_\star) \times \boldsymbol{B}}{c} . \tag{5.2}$$

This condition starts the rotation of the magnetic field lines at $t = 0$. At any later time ($t > 0$), the magnetic moment spins around the z-axis at the neutron star angular speed (Ω), as expressed by the rotation matrix

$$\mathcal{R}(\Omega t) = \begin{pmatrix} \cos(\Omega t) & -\sin(\Omega t) & 0 \\ \sin(\Omega t) & \cos(\Omega t) & 0 \\ 0 & 0 & 1 \end{pmatrix} \tag{5.3}$$

therefore giving

$$\boldsymbol{\mu}(t) = \mu \left(\sin(\chi) \cos(\Omega t)\, \mathbf{u}_x + \sin(\chi) \sin(\Omega t)\, \mathbf{u}_y + \cos(\chi)\, \mathbf{u}_z \right) , \tag{5.4}$$

or, in spherical coordinates,

$$\begin{aligned} \boldsymbol{\mu}(t) = {} & \mu \left(\sin(\chi) \sin(\theta) \cos(\Omega t - \phi) + \cos(\chi) \cos(\theta) \right) \mathbf{u}_r \\ & + \mu \left(\sin(\chi) \cos(\theta) \cos(\Omega t - \phi) - \cos(\chi) \sin(\theta) \right) \mathbf{u}_\theta \\ & + \mu \sin(\chi) \sin(\Omega t - \phi)\, \mathbf{u}_\phi . \end{aligned} \tag{5.5}$$

Then, the expression of the magnetic field at the star surface at any time is the following:

$$\begin{aligned} \boldsymbol{B}(\boldsymbol{r}) = {} & \frac{3(\boldsymbol{\mu} \cdot \boldsymbol{r})\,\boldsymbol{r}}{r^5} - \frac{\boldsymbol{\mu}}{r^3} \\ = {} & \frac{\mu}{r^3} \left(2 \sin(\chi) \sin(\theta) \cos(\Omega t - \phi) + 2 \cos(\chi) \cos(\theta) \right) \boldsymbol{u}_r \qquad (5.6) \\ & + \frac{\mu}{r^3} \left(-\sin(\chi) \cos(\theta) \cos(\Omega t - \phi) + \cos(\chi) \sin(\theta) \right) \boldsymbol{u}_\theta \\ & - \frac{\mu}{r^3} \sin(\chi) \sin(\Omega t - \phi)\, \boldsymbol{u}_\phi . \qquad (5.7) \end{aligned}$$

The magnitude of the magnetic moment is related to the surface polar magnetic field by the expression $\mu = B_\star r_\star^3$. The plasma magnetization at the surface of the star is fixed to be $\sigma_\star = B_\star^2/4\pi\Gamma_\star n_\star m_e c^2 \sim 8000$, where $\Gamma_\star$ and $n_\star$ are respectively the bulk the Lorentz factor and the particles density at the surface of the star.

At first, there is no plasma in the simulation. Plasma is supplied via two complementary methods. The first supply mechanism consists of injecting pairs uniformly over the whole surface at a rate of one particle per cell with a probability injection rate of 20%, which roughly corresponds to injecting every five timesteps. The injected surface charge density (Σ) is determined by the difference at the star surface between the radial electric field and the corotation radial electric field given by Eq.(5.2), ΔE_r:

$$\Sigma = \frac{\Delta E_r}{4\pi} \,. \tag{5.8}$$

In fact, charges are injected only if the plasma density is lower than the Goldreich–Julian density (see Eq. 2.28). In such case, a fraction (10%) of the charge density computed in Eq.(5.8) is released every timestep. Particles are injected in corotation with the star ($v_\phi = r_\star \Omega \sin\theta$), with no need of any initial poloidal velocity since the sub-Goldreich Julian density of the cells ensures the presence of electric gaps which will serve to accelerate particles.

The second injection mechanism consists of creating pairs anywhere in the simulation domain whenever the Lorentz factor of the primary particle exceeds a specific threshold. This threshold is defined as $\gamma_{\rm th} = 0.005\,\gamma_{\rm pc}$, where $\gamma_{\rm pc} = e\mu\Omega^2/m_e c^4$ is the maximum energy that can be gained by a particle from the polar cap potential drop (see Eq. 2.84). The electron-positron pairs form at the same point as the parent particle, without the emission of an intermediate photon, assuming that the photon mean free path is negligible. They are emitted in the same direction as the primary particle. All new pairs are created with the same energy, equal to 10% of $\gamma_{\rm th}$, and the primary particle is cooled by the same amount of energy. Here again, if the charge density in the cell containing the primary particle is too high, plasma injection is inhibited. The density threshold for pair creation is fixed at 10 times the Goldreich-Julian density. This density criterion guarantees that kinetic scales remain resolved everywhere, therefore ensuring the stability of the simulation. In reality, the density rarely exceeds such values, except in the current sheet. Pairs are thus created around the current sheet and may subsequently be accreted into it. Ions are not included in the simulation, due to their poor contribution to radiation (attributable to the high mass ratio between ions and pairs) and are not expected to significantly affect the dynamics of the magnetosphere (see Chen and Beloborodov 2014 and Guépin et al. 2020 for further details). Figure 5.7 summarizes the initial conditions on the three-dimensional spherical grid.

We make sure that the kinetic scales are resolved in the simulation: the skin-depth ($d_{\rm e} = \sqrt{\langle\gamma\rangle m_e c^2/4\pi n e^2}$) is resolved by $\sim$ 2 cells at the star surface, by $\sim$ 18 cells at the light cylinder radius and then progressively saturates with radius up to $\sim$ 20 cells. At $R_{\rm LC}$, the Larmor radius ($r_{\rm L} = \langle\gamma\rangle m_e c^2/eB$) is resolved by $\sim$ 13 cells in the current sheet and $\sim$ 1 cell in the wind. Its resolution in the wind increases radially up to $\sim$ 5 cells at $r_{\rm max}$. As previously discussed in Section 3.4.1, PIC simulations are necessarily rescaled due to the huge scale difference between kinetic scales (e.g., skin depth and Larmor radius) and macroscopic quantities (such as $R_{\rm LC}$). Here, the ratio between the skin depth at the star surface and the star radius is given by $d_{\rm e}^\star/r_\star \sim 7\times10^{-3}$, which implies a rescaling of the simulation by about 3 orders of magnitude compared to realistic spatial scales.

Curvature and synchrotron radiation are the main cooling channels and the dominant sources of non-thermal emission. The power emitted via synchrotron and curvature radiation scales as $P_{\rm sync} \propto \gamma^4/r_{\rm L}^2$ and $P_{\rm curv} \propto \gamma^4/r_{\rm C}^2$ respectively, where $r_{\rm L}$ is the Larmor radius and $r_{\rm C}$ (typically $\gtrsim R_{\rm LC}$) is the curvature radius. Sychrotron power dominates over curvature power, as $P_{\rm sync}/P_{\rm curv} \sim r_{\rm C}^2/r_{\rm L}^2 \gg 1$. A detailed description of their implementation is provided in Section 3.4.4.

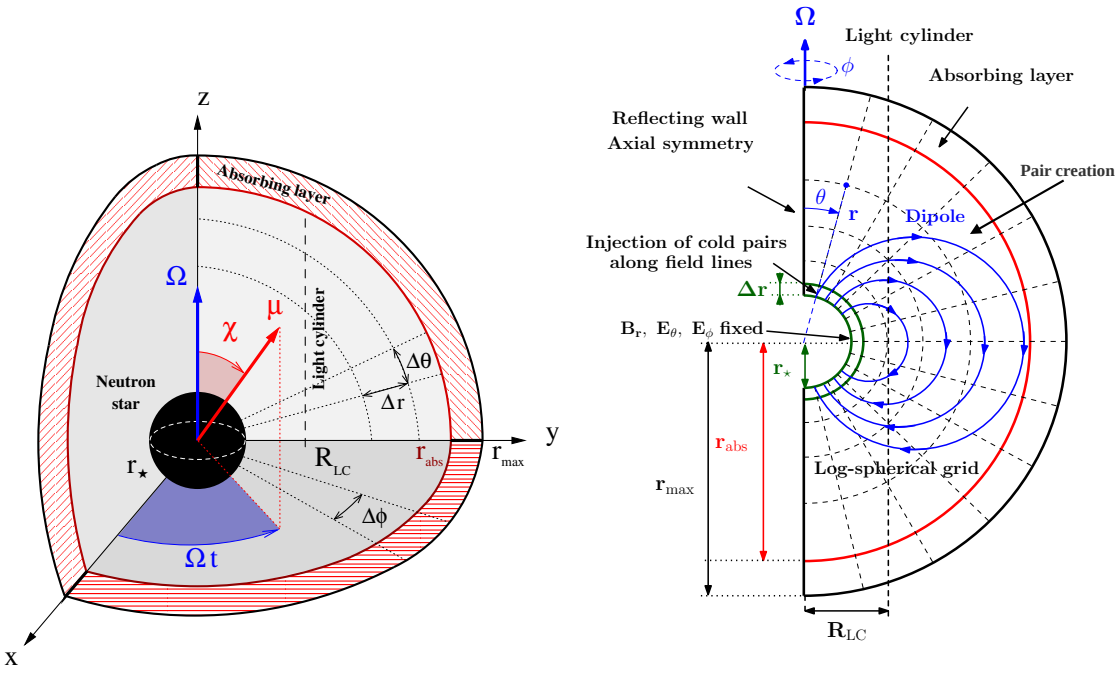

Figure 5.7: 3D numerical setup. *Left:* 3D illustration of the geometrical setup. The obliquity angle, χ, is defined as the angle between the magnetic moment $\boldsymbol{\mu}$ and the spin axis $\boldsymbol{\Omega}$. The inner boundary of the box corresponds to the radius of the neutron star, $r_\star$, the outer boundary is given by $r_{\rm max}$, and an absorbing layer for fields and particles is implemented between $r_{\rm abs}$ and $r_{\rm max}$. Figure taken from Cerutti et al. (2016). *Right:* Detailed 2D poloidal plane. The initial configuration displays a magnetic dipole anchored at the star surface, in vacuum. The star is modelled as a perfect conductor and rotates at $\Omega = c/R_{\rm LC}$. The grid is logarithmically spaced in r and uniformly spaced in θ and ϕ. Plasma is supplied via injection of cold pairs at the inner boundary and via pair creation anywhere in the simulation domain. For visualization purposes, the dipole is shown aligned, unlike in the actual simulation setup. Figure adapted from Cerutti et al. (2015).

Table 5.1: Simulation parameters.

Parameter	Value
Number of cells	$1024\,(r) \times 128\,(\theta) \times 256\,(\phi)$
Inner boundary	$r_\star$
$R_{\rm LC}$	$5\ r_\star$
$r_{\rm max}$	$5.6\ R_{\rm LC}$
$(d_{\rm e}/\Delta r)_{\rm LC}$	18
$P_{\rm spin}/\Delta t$	9.5×10^4
$d_{\rm e}^\star/r_\star$	6.7×10^{-3}
Plasma composition	electrons and positrons
Injection model	from star surface + pair creation

Fields and particles evolve self-consistently at each timestep (see Section 3.3.1 for more details). One timestep (Δt) corresponds to half the Courant-Friedrich-Lewy critical condition and $P_{\rm spin} \sim 9.5 \times 10^4 \Delta t$. Particles evolution follows the Abraham-Lorentz-Dirac equation (see Section 2.5.1), which accounts for radiative losses through the addition of a radiation-reaction

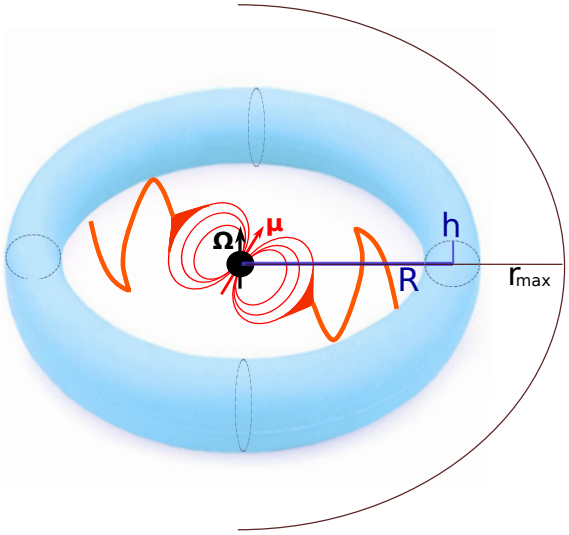

Figure 5.8: Sketch of the simulation setup including the disk. The disk is modeled as a torus which separation is R and which height is h. The inner edge of the torus is located at $R - h = 2.5\,R_{\rm LC}$. The aspect ratio of the torus is $h/R = 0.3$. Thin red lines indicate magnetic field loops, while thicker orange curved lines represent the current sheet. The magnetic moment $\boldsymbol{\mu}$ is inclined by an angle χ relative to the rotation axis $\boldsymbol{\Omega}$.

term in the equation of motion. We neglect general relativistic effects in this work since we focus on the pulsar wind rather than on the regions close to the stellar surface (see, however, Philippov et al. 2015a, Philippov and Spitkovsky 2018, Chen et al. 2020, Torres et al. 2024).

5.3.2 Disk implementation

Our main goal is to understand how the presence of a disk around a pulsar alters the dynamical and energetic properties of the pulsar wind, with a particular focus on its electromagnetic emission. Thus, we need to add a disk around the pulsar in the simulation domain. The smooth geometry of a torus is adopted to avoid any field enhancement effect at sharp edges. Within the framework of transitional pulsars, we expect the disk to reach the inner parts of the pulsar wind, i.e., $r_{\rm in} \sim$ few $R_{\rm LC}$ (Papitto et al., 2019). Such distances are well adapted for our model since our simulation box extends up to $5.6\,R_{\rm LC}$. It is important that the current sheet is properly formed before it reaches the disk, while also maintaining sufficient space beyond the inner edge of the torus to observe the reconfiguration of the magnetosphere. To satisfy this compromise, the inner edge of the disk is set at $2.5\,R_{\rm LC}$, at the equator. The aspect ratio of the disk, defined as h/R, where h is the disk height and R is the radial distance of the disk (see Figure 5.8), is not well constrained observationnally (Papitto et al., 2019). We set $h/R = 0.3$, with $R = 3.572\,R_{\rm LC}$, in agreement with previous models (Parfrey and Tchekhovskoy, 2017; Veledina et al., 2019). The torus is modeled as a perfect conductor, i.e., $\boldsymbol{E}_{\rm torus} = \boldsymbol{0}$. Moreover, we neglect the disk magnetic field, and we impose $\boldsymbol{B}_{\rm torus} = \boldsymbol{0}$ inside the disk. The orbital motion of the disk is also neglected as its Keplerian period is much longer than the spin period of the pulsar. The torus acts as an absorbing boundary for particles: any particle hitting its surface is removed from the simulation. Concerning the calculation of synchrotron emission, the rear of the torus is extended to the outer boundary of the simulation domain to ensure that any photon whose path crosses the torus or its extension is eclipsed.

Finding the most appropriate boundary conditions proved quite challenging. Indeed, we initially decided not to constrain the magnetic field inside the disk. Though it seemed to work well for aligned pulsars, the asymmetry in the ϕ-direction induced by the inclination of the magnetic moment at $t = 0$ was maintained throughout the entire simulation because

of $\partial \boldsymbol{B}/\partial t = \nabla \times \boldsymbol{E} = \boldsymbol{0}$ (see Figure 5.9, left panel). This asymmetry lead to the appearance of preferred directions along which the plasma tended to flow. Hence, we attempted to circumvent this issue through various methods. First, we initialized the simulation with a magnetic moment aligned with the rotation axis and progressively inclined it until reaching the desired value of χ. This strategy imposed a symmetric configuration of the magnetic field in the ϕ-direction at $t = 0$, thereby ensuring its preservation at all subsequent times. Unfortunately, this approach proved unsuccessful, as the simulation systematically became unstable and crashed. The ideal boundary conditions for a perfect conductor would have been the following: $\boldsymbol{B}_\perp = \boldsymbol{0}$ and $\boldsymbol{E}_\parallel = \boldsymbol{0}$ at the disk surface and $\boldsymbol{E} = \boldsymbol{0}$ inside the torus. Due to the spherical nature of our numerical grid, a toroidal geometry would not have permitted the definition of surfaces aligned with the computational grid; therefore, implementing such boundary conditions was not feasible. Yet, such boundary conditions could have been implemented if we had modified the disk geometry by adopting a geometry that conforms to the grid contours, as shown in the right panel of Figure 5.9. But this geometry has the drawback of featuring sharp edges, which could introduce numerical artifacts in the simulation, and implementing such a setup is far more demanding due to the code parallelization. Based on these considerations, we chose a toroidal geometry with both electric and magnetic fields set to zero within the torus. This choice has the advantage of avoiding any artificial asymmetry in the simulation and of forcing the magnetic field lines to contour the torus, similarly to what occurs with perfectly conducting obstacles. We also tested various boundary conditions for the particles. In particular, we implemented perfect specular reflection for particles hitting the torus surface. We noticed that such condition lead to resonances between the spin frequency and the trajectories of reflected particles in some specific directions. Some stationary structures were thus established, within which the plasma became trapped and could no longer flow freely. The development of nonlinear instabilities from small initial accumulations of plasma was also suspected. Therefore, we decided to absorb all particles hitting the surface of the torus. Provided there is sufficient plasma in the magnetosphere, this condition proved satisfactory. For future studies, an appropriate alternative could be to implement partial absorption coupled with partial isotropic reflection of particles.

5.3.3 Parametric study: different magnetic obliquities

Run	magnetic obliquity $\chi(^\circ)$
REF_15	15
REF_30	30
REF_60	60
REF_75	75
DISK_15	15
DISK_30	30
DISK_60	60
DISK_75	75

Table 5.2: Summary table of the various simulations. We perform 8 different simulations: 4 reference simulations of an isolated pulsar for 4 different magnetic obliquities (denoted with the prefix "REF"), and the corresponding simulations in the presence of the disk (denoted with the prefix "DISK").

As discussed in Chapter 2, the current sheet is the densest region of the magnetosphere beyond the light cylinder radius. While it lies along the equatorial plane in aligned pulsars, it takes on a curved shape when the pulsar's magnetic moment is inclined. The magnetic obliquity (χ) governs the structure of the current sheet and in particular its latitudinal opening

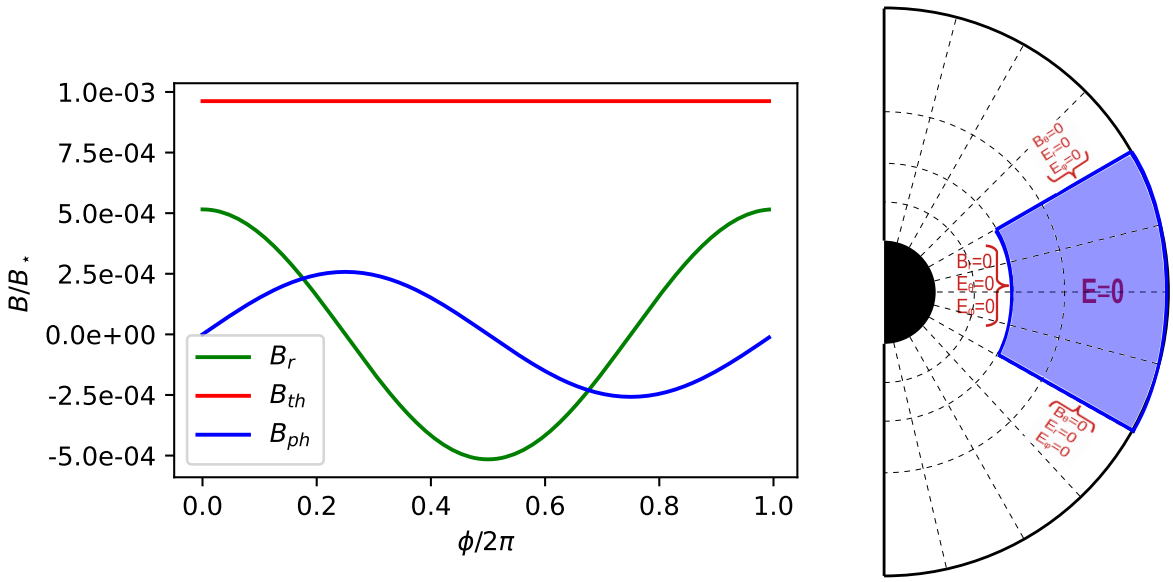

Figure 5.9: *Left:* Magnetic field components evaluated at the equator inside the torus, for the case of an unconstrained magnetic field. The fields remain constant over time in the simulation, leading to the establishment of an asymmetry in the global dynamics of the magnetosphere. Note that B_θ does not vary over time because we represent the fields at $\theta = \pi/2$, and goes to zero for the last cell in the ϕ direction. *Right:* An alternative geometry for the disk – shown in the $(r-\theta)$ plane – that would allow the implementation of the following boundary conditions: $\boldsymbol{B}_{\perp,\mathrm{surf}} = \mathbf{0}$, $\boldsymbol{E}_{\parallel,\mathrm{surf}} = \mathbf{0}$, and $\boldsymbol{E}_{\mathrm{in}} = \mathbf{0}$.

angle ($\Delta\theta$), such that $\Delta\theta = 2\chi$. The angular fraction of the current sheet intercepted by the disk is expected to play a role in this study, both for the rearrangement of the magnetosphere and the electromagnetic emission arising from such interaction. Hence, we run different simulations for different pulsar's magnetic obliquities, while the aspect ratio of the disk is set to $h/R = 0.3$ for all simulations. Overall, we run 8 simulations: 4 simulations of the pulsar interacting with the disk for 4 different magnetic obliquities ranging from 15° to 75°, and the respective reference simulations of isolated pulsars. Table 5.2 lists all the simulations and their associated magnetic obliquities and Figure 5.10 illustrates the resulting magnetospheric structures of isolated pulsars, corresponding to the four obliquities explored in this study. The central black sphere represents the neutron star, and the colors indicate the density, normalized by $(r/r_\star)^2$ to compensate for the decrease in density due to expansion. What is actually observed is the current sheet, because of its markedly higher density compared to the rest of the magnetosphere. The current sheet structure is a 3D spiral Archimedean spiral characterized by a wavelength of $2\pi R_{\mathrm{LC}}$. We can see that, as expected, higher magnetic obliquities induce a higher poloidal curvature of the current sheet, that spans an angle of 2χ in the θ-direction. The filamentary structure that is observed is due to the relativistic tearing instability (Zelenyi and Krasnoselskikh, 1979; Pétri and Kirk, 2007) that causes the fragmentation of the current sheet rapidly after its formation (see Section 2.4.3). This results in the formation of entangled flux ropes of plasma.

5.4 Structure of the magnetosphere in the presence of the disk

We were able to run each simulation up to about five pulsar's spin periods. On average, simulations converged after $1.1\,P_{\mathrm{spin}}$. This can be seen by representing the outgoing radial Poynting flux, as a function of the radius from the center of the star. Indeed, Figure 5.11

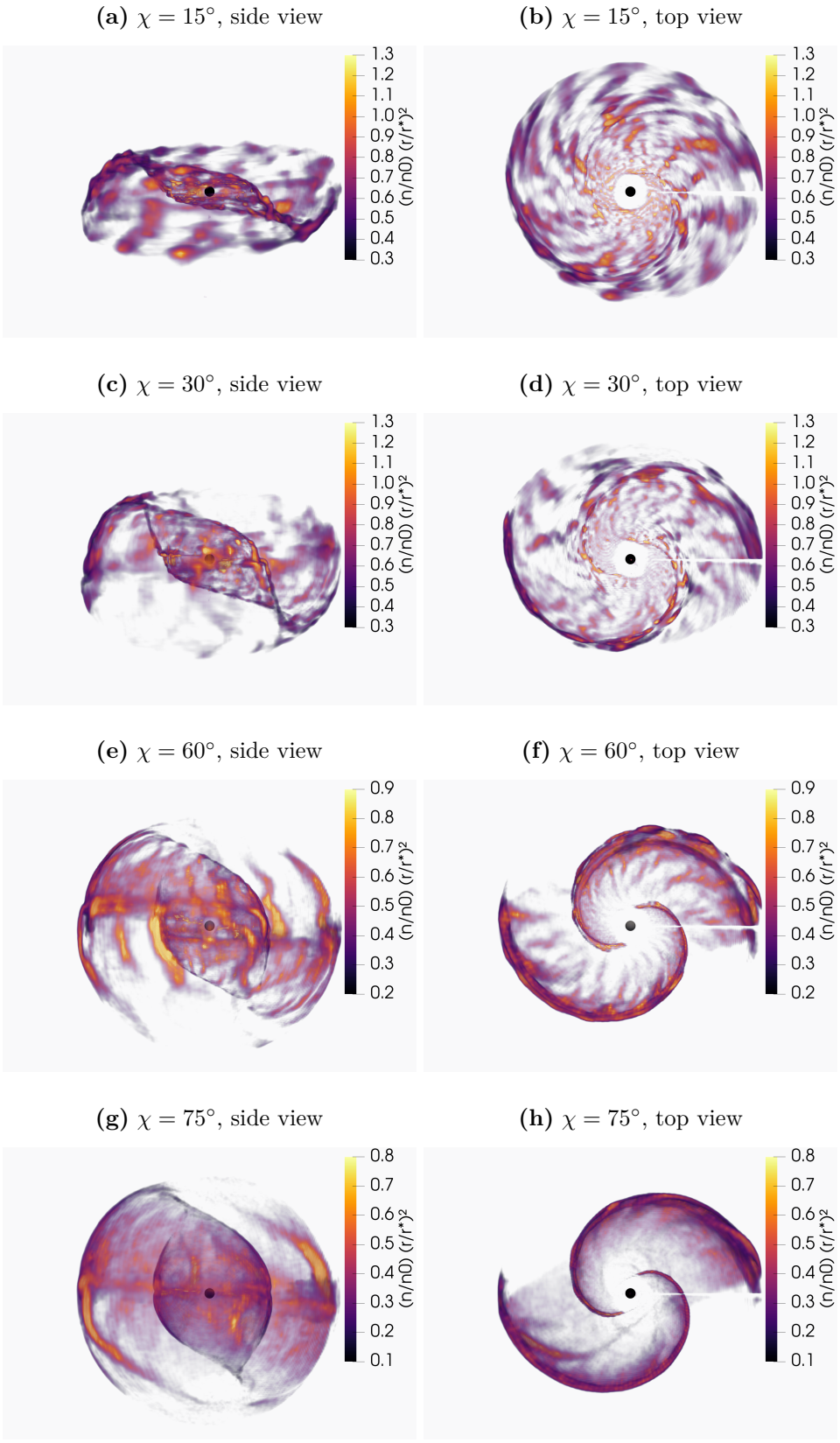

Figure 5.10: 3D density $(n/n_0)(r/r_\star)^2$ for isolated pulsars with magnetic obliquities of 15°, 30°, 60° and 75° (from top to bottom). The density is normalized by $n_0 = \kappa\, n_{\rm GJ}$, where $\kappa = 10$ is the plasma multiplicity and $n_{\rm GJ}$ is the Goldereich-Julian density, computed at the magnetic poles of the neutron star. The left panels correspond to a side view while the right panels show a top view. As the obliquity increases, the current sheet deviates further from the equatorial plane, exhibiting enhanced curvature and spanning a wider range of latitudes.

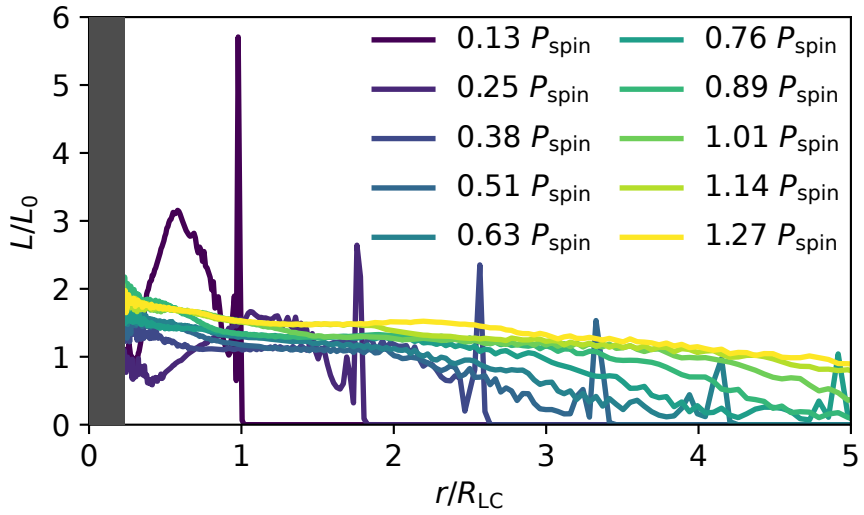

Figure 5.11: Temporal evolution of the outgoing Poynting flux (L/L_0), computed by integrating over spheres of radius r for the DISK_15 simulation. The Poynting flux is normalized by $L_0 = \mu^2\Omega^4/c^3$, the net radial Poynting flux for an aligned dipole (Eq. 2.78). At the beginning of the simulation, a transient arises at the center of the box, then exits the computational domain, leading to the convergence of the Poynting flux around $1.1P_{\rm spin}$.

shows a transient originating from the star surface and escaping the box after about $1\,P_{\rm spin}$. Then, the outgoing Poynting flux converges around $1.1\,P_{\rm spin}$.

5.4.1 Global structure

When adding the disk, we perturb the pulsar wind and MHD waves may be generated in response to this perturbation. Fast magnetosonic waves are the fastest MHD waves that can arise in such systems (Section 2.2). Beyond the fast magnetosonic radius, the pulsar wind's speed exceeds the speed of fast magnetonosic waves, thereby advecting any perturbation with it. In our case, the inner border of the disk is set at $2.5\,R_{\rm LC}$ and is expected to fall inside the fast magnetosonic radius. Since the disk's inner edge lies inside this point, any perturbation occurring at the inner disk surface can propagate back to the star and affect the entire computational domain, rather than being confined to the disk surface and its wake. The difference between both regimes is addressed and illustrated in Chapter 4.

As previously discussed, the disk is modelled by a torus which lies at the equator. Figure 5.12 illustrates the magnetosphere of an isolated pulsar with a magnetic obliquity of 15° (top panels), and the same pulsar's magnetosphere to which we added a torus (bottom panels). The volume occupied by the torus is illustrated in grey. We can see that the whole magnetosphere is altered and rearranges around the torus. While the filamentary structure of the current sheet is recovered, the presence of the torus significantly increases the plasma density by hindering its radial propagation, thereby extending the plasma residence time between the star and the torus. The plasma flows around the torus, thereby forming a flared conical structure. From Figure 5.12d, it can be seen that the resulting structure is globally axisymmetric.

Now that we have in mind where the torus is implemented and how it can affect the global structure of the magnetosphere, we present in Figure 5.13 the new magnetospheric structures obtained for each magnetic obliquity (χ). The left panels show the plasma density and the magnetic field lines for the reference case without the torus, while the right panels show the corresponding densities and fields in the presence of the torus. On the left panels, open field lines wind up around the pulsar and become increasingly toroidal with distance. On the

(a) isolated pulsar, $\alpha = 90°$

(b) isolated pulsar, $\alpha = 45°$

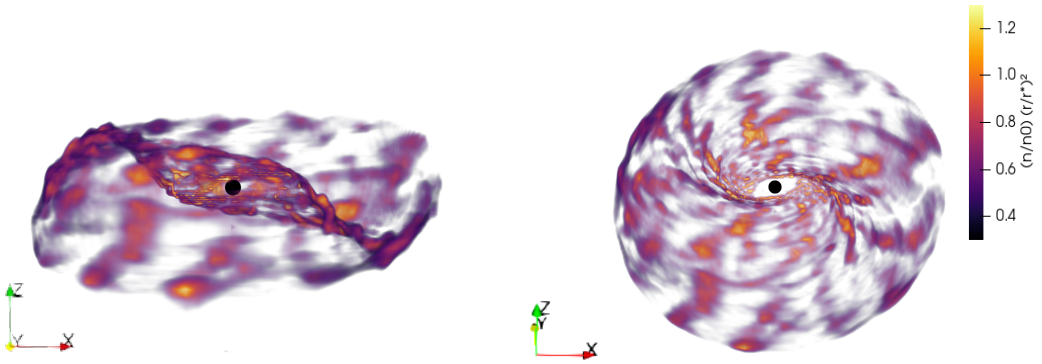

(c) pulsar and torus, $\alpha = 90°$

(d) pulsar and torus, $\alpha = 45°$

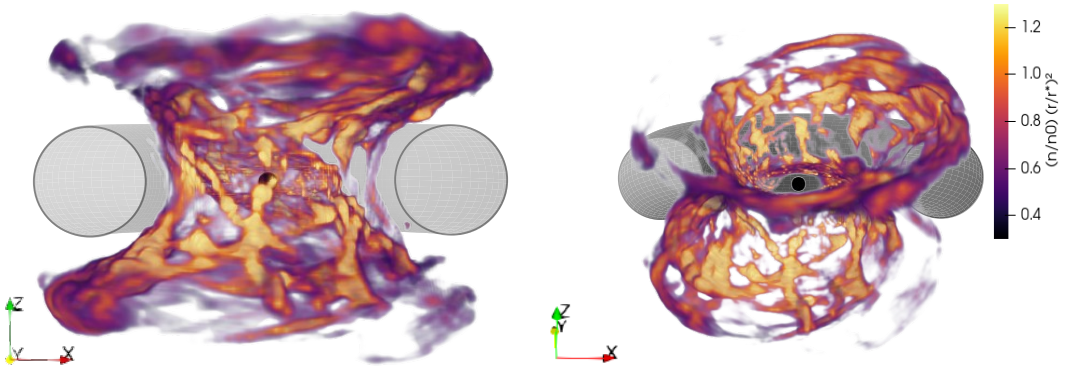

Figure 5.12: 3D particles density $(n/n_0)(r/r_\star)^2$ of a pulsar magnetosphere for a magnetic obliquity of $\chi = 15°$. The central black sphere is the neutron star and colors represent the particles density, normalized by $(r/r_\star)^2$ to compensate for the effects of expansion. The density is normalized by $n_0 = \kappa\, n_{\rm GJ}$, where $\kappa = 10$ is the plasma multiplicity and $n_{\rm GJ}$ is the Goldereich-Julian density, computed at the magnetic poles of the neutron star. α denotes the viewing angle. *Top panels:* side view $\alpha = 90°$ (left) and oblique view $\alpha = 45°$ (right) for an isolated pulsar. *Bottom:* side view $\alpha = 90°$ (left) and oblique view $\alpha = 45°$ (right) for a pulsar interacting with a torus (grey volume).

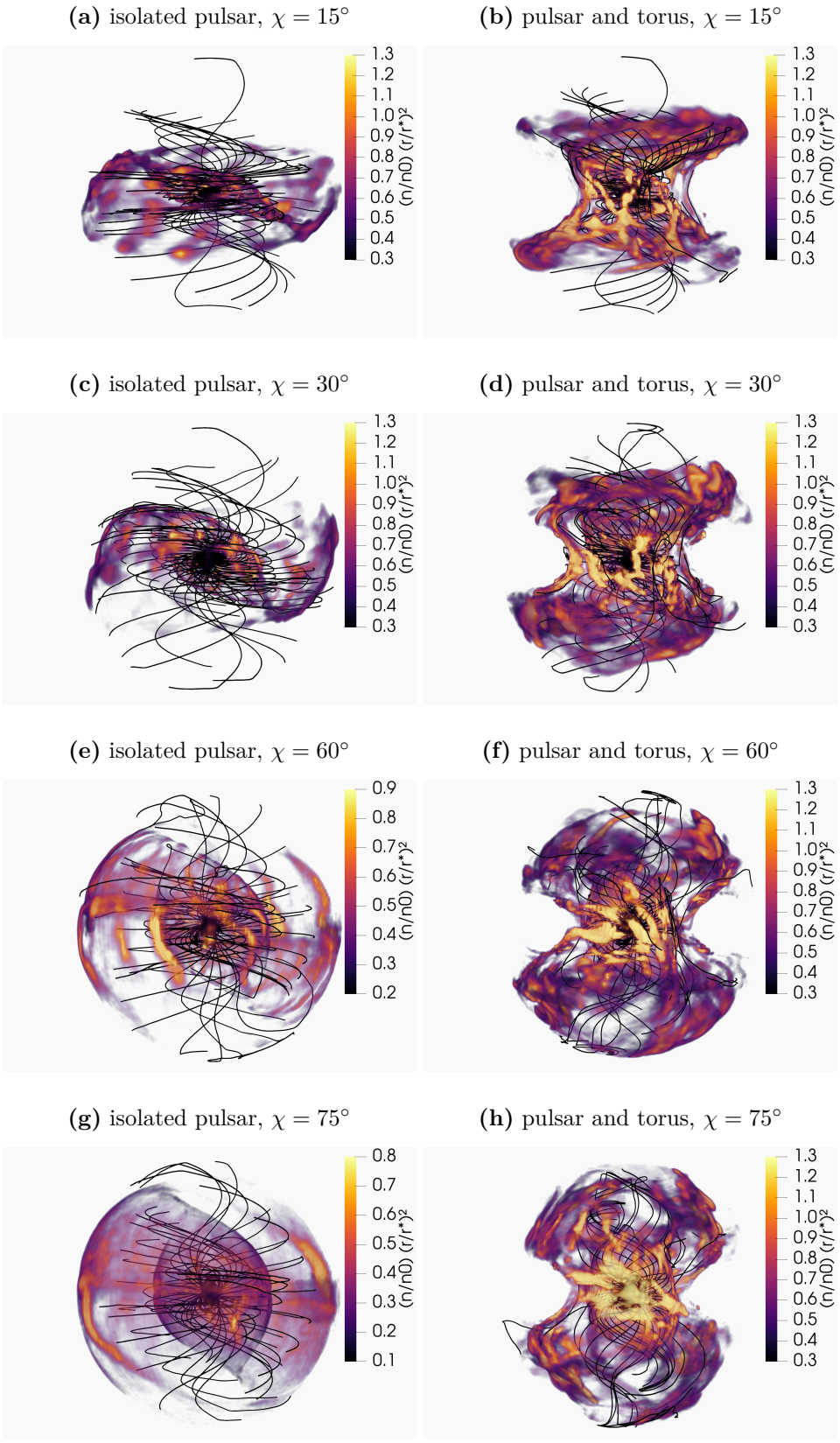

Figure 5.13: 3D particles density $(n/n_0)(r/r_\star)^2$ of the magnetosphere for magnetic obliquities of $\chi = 15°$, $30°$, $60°$ and $75°$. The density is normalized by $n_0 = \kappa\, n_{\rm GJ}$, where $\kappa = 10$ is the plasma multiplicity and $n_{\rm GJ}$ is the Goldereich-Julian density computed at the magnetic poles of the neutron star. The central black sphere is the neutron star. Field lines are shown in black. *Left:* isolated magnetosphere. *Right:* magnetosphere interacting with the disk.

right panels, the field lines are forced to bend when reaching the surface of the torus, in the ϕ-direction but also in the θ-direction, so as to circumvent the torus along its upper and lower sides. In all cases, we observe a significant enhancement of the plasma density, in particular at the latitudes spanned by the torus, and a vertical development of the magnetosphere as it is radially blocked by the torus, even though some plasma manages to reach higher radii by flowing along the field lines that circumvent the torus.

Interestingly, for pulsars with magnetic obliquities high enough such that their magnetic poles point toward the disk surface (with the threshold set by the disk aspect ratio), some open field lines originating from the polar cap appear to be periodically forced to close, before reopening again. This cyclic behavior influences the plasma dynamics and energy release, resulting in periodic retention and ejection. To illustrate this effect, Figure 5.14 shows, for the DISK_75 simulation, the temporal evolution of the net outgoing Poynting flux (blue curve) and the particle density (red curve), both evaluated at $r = R_{\rm LC}$, which is approximately the radius where the magnetosphere opens. Both quantities exhibit a quasi-synchronous modulation at the pulsar's spin period.

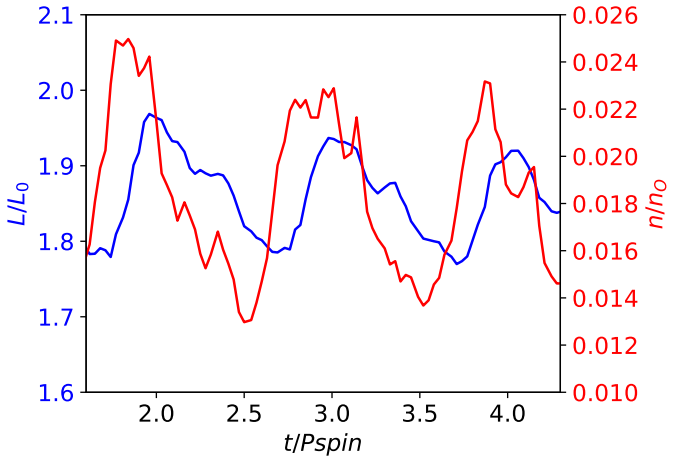

Figure 5.14: Time evolution of the net outgoing Poynting flux L/L_0 (blue curve, left y-axis) and the particle density n/n_0 (red curve, right y-axis), both evaluated at $r = R_{\rm LC}$, for the DISK_75 simulation. The Poynting flux is normalized by $L_0 = \mu^2\Omega^4/c^3$, which corresponds to the net radial Poynting flux for an aligned dipole (Eq. 2.78). The particle density is normalized by $n_0 = \kappa\, n_{\rm GJ}$, where $\kappa = 10$ is the plasma multiplicity and $n_{\rm GJ}$ is the Goldereich-Julian density, computed at the magnetic poles of the neutron star. A periodic modulation is observed in both the Poynting flux and the particle density at the light cylinder radius.

To better visualize the restructuring of the current sheet for all magnetic obliquities, we superimpose 2D poloidal cuts of the new density distributions over the current sheets originating from the isolated pulsars (see Figure 5.15). For all magnetic obliquities, the current sheet extends over larger latitudes. While for less inclined cases (see panel 5.15a) the plasma streams along the torus edges in a relatively laminar manner, higher inclined cases exhibit a less ordered and more turbulent structure. Indeed, for $\chi = 15°$, the original geometry of the current sheet closely follows the contour of the torus, thereby causing less alteration of the magnetic field structure. Conversely, for more highly inclined cases, the portion of the current sheet intersecting the torus becomes increasingly vertical, resulting in stronger perturbations to the field lines and matter flow, and leading to a more turbulent magnetospheric reconfiguration.

Figure 5.16 shows how the two spiral arms of the current sheet wrap more tightly around the pulsar than usual and merge at the inner edge of the torus. This implies a significant accumulation of plasma at this distance from the pulsar and may trigger an enhancement of

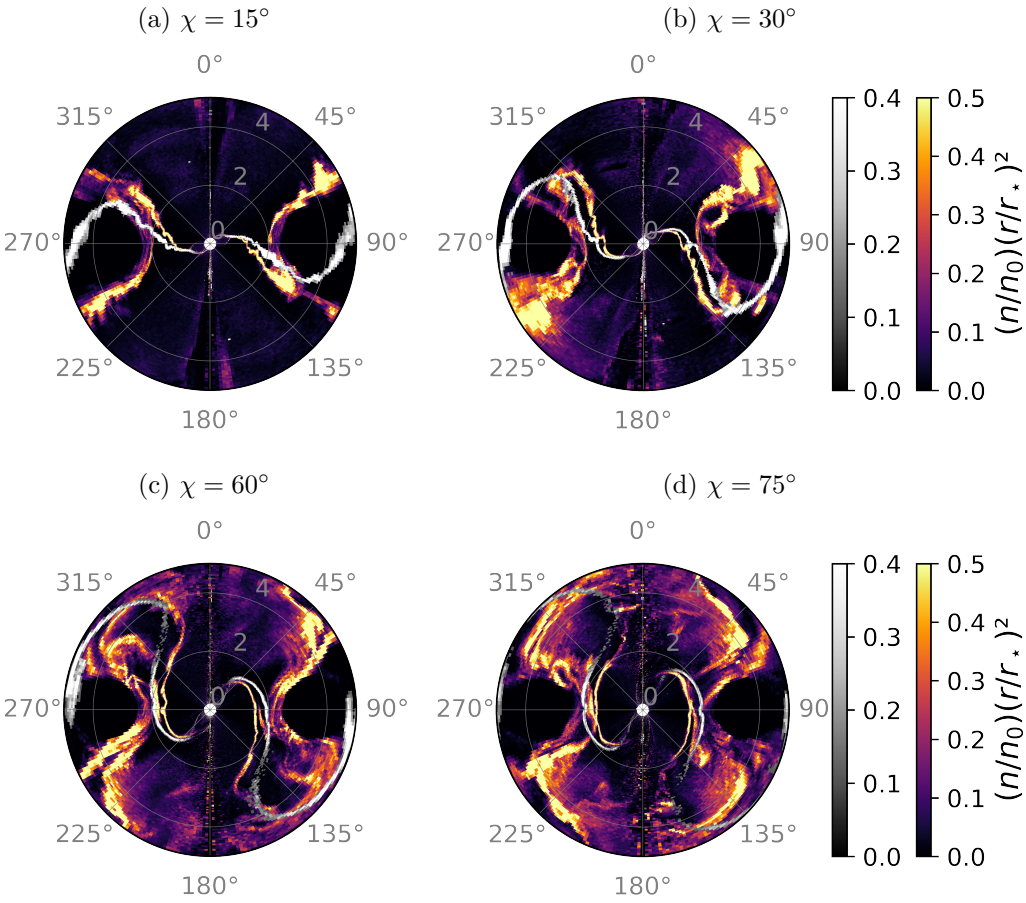

Figure 5.15: 2D poloidal maps of the plasma density $(n/n_0)(r/r_\star)^2$ for each magnetic obliquity. The density is normalized by $n_0 = \kappa\, n_{\rm GJ}$, where $\kappa = 10$ is the plasma multiplicity and $n_{\rm GJ}$ is the Goldereich-Julian density computed at the magnetic poles of the neutron star. The current sheet from the reference case (indicated by a grayscale colorbar) is superimposed on the plasma structure resulting from the pulsar-disk interaction (displayed in color), at the same time. Radii are given in units of the light cylinder radius.

energy dissipation in this zone.

The magnetic field is also strengthened by the presence of the disk. This is visible where the magnetic field lines hit the inner edge of the disk (see Figure 5.17), but the effect is not restricted to this surface alone. Indeed, we observe a global increase in the magnetic field strength throughout the entire computational domain, both in the poloidal and toroidal planes (Figure 5.18).

5.4.2 Particle acceleration

In light of Chapter 4, we expect the disk to act as an obstacle capable of bending the magnetic field lines and locally causing their compression, thereby intensifying energy dissipation through magnetic reconnection. We indeed observe an enhancement of particle acceleration at the disk surface, as shown in Figure 5.19. However, this effect might be limited by the enhanced cooling of particles, as will be detailed further on. The polar caps also emerge as preferential sites for particle acceleration. A likely explanation, drawing on a well-known mechanism in the context of isolated magnetospheres, is that the introduction of the conducting torus alters the plasma boundary conditions, particularly by increasing the charge required in the current sheet to circumvent the torus. To ensure charge conservation at the

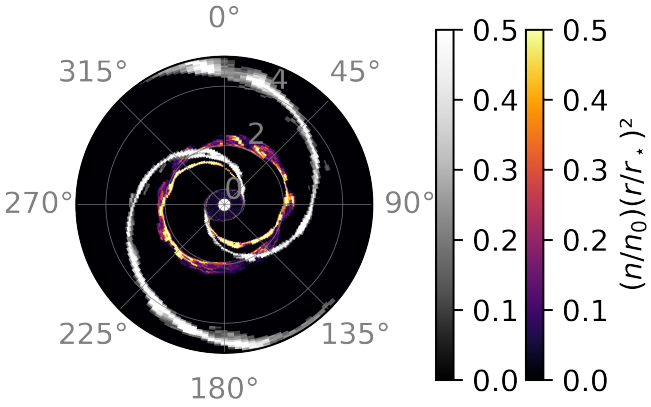

Figure 5.16: 2D equatorial map of the plasma density density $(n/n_0)(r/r_\star)^2$ for $\chi = 15°$. The current sheet from the reference case (indicated by a grayscale colorbar) is superimposed over the plasma structure resulting from the pulsar-disk interaction (displayed in color). Radii are given in units of the light cylinder radius. The two branches of the current sheet merge at the inner edge of the torus.

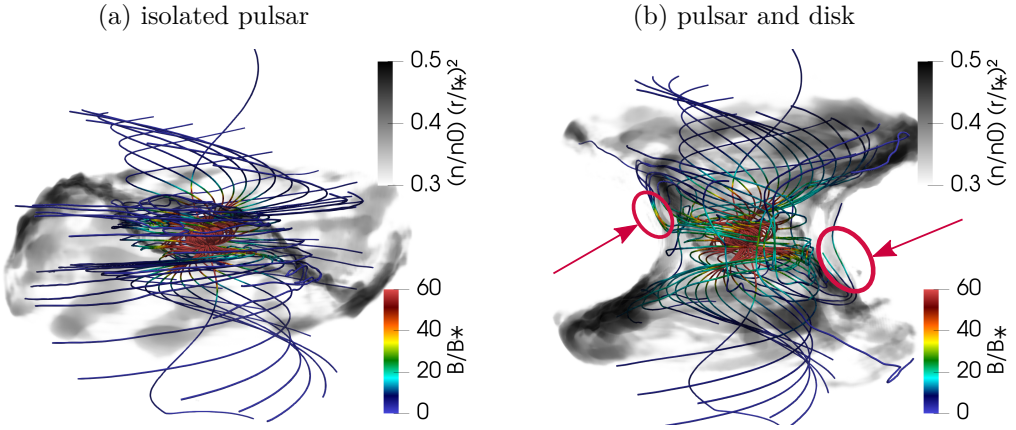

Figure 5.17: 3D rendering of the magnetic field strength $(B/B_\star)$ for $\chi = 15°$, in the reference case (left) and with the disk present (right). $B_\star$ corresponds to the norm of the magnetic field at the magnetic poles of the star. Colors indicate magnetic field strength, while plasma density is shown in gray. Compared to the reference case, the magnetic field is globally stronger, particularly near the disk surface (see pink arrows).

surface of the star, the currents along the open field lines at the polar caps need to adjust accordingly. For a fixed number of particles, this implies the acceleration of particles, until they reach the threshold required to produce pairs. Further investigation would be required to quantify the need for polar charges, but this goes beyond the scope of the present study.

5.4.3 Plasma isotropization

Another important consequence of the disk's presence is the isotropization of the plasma. In the striped wind of isolated magnetospheres, plasma predominantly flows along magnetic field lines, except in the current sheet, where particles escaping from X-points are accelerated and isotropized. Figure 5.20 shows the ratio between the effective magnetic field strength perpendicular to the particles momentum ($\tilde{B}_\perp$, defined in Eq. 2.102) to the total field strength (B), so as to illustrate $\sin\zeta$, where ζ is the pitch angle between the magnetic field and the particle's velocity. As expected, this ratio reaches its maximum value in the current layer.

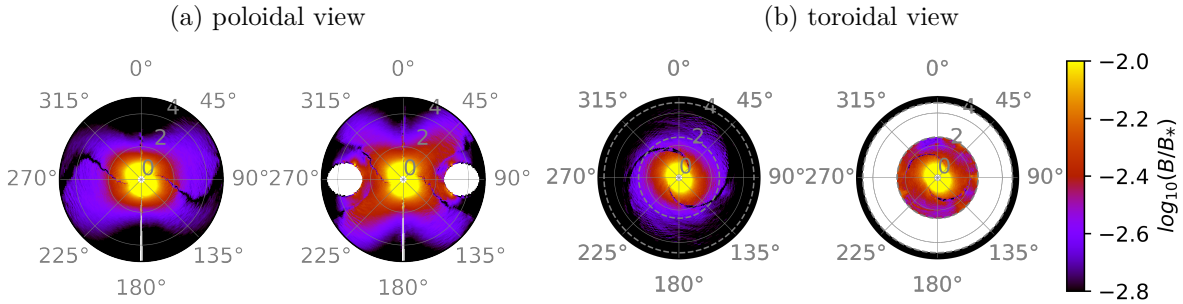

Figure 5.18: 2D maps of the magnetic field strength $log_{10}(B/B_\star)$ for $\chi = 15°$. $B_\star$ corresponds to the norm of the magnetic field at the magnetic poles of the star. Left: View in a poloidal plane. Right: View in the equatorial plane. For each observer's perspective, the reference case is shown on the left, and the interaction case on the right. The disk surface from panel 4 (white area) is traced by grey dashed lines on panel 3 (reference case) for easier comparison. Radii are given in units of the light cylinder radius.

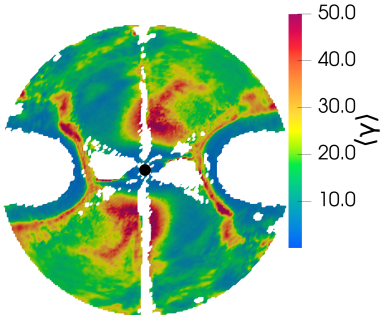

Figure 5.19: 2D poloidal map of the mean Lorentz factor of particles $\langle\gamma\rangle$, for run DISK_15. The presence of the disk induces an enhancement of particle acceleration at the disk surface. The central black sphere represents the neutron star.

Our results show that, when there is a disk, regardless of the pulsar's magnetic inclination, the pitch angle is amplified by at least a factor of 2 over a broad region surrounding the pulsar surface (note that the features observed along the rotation axis are artifacts). The effect is all the more pronounced for cases with the highest magnetic inclinations.

5.5 Synchrotron emission

5.5.1 Increase of the synchrotron emission due to the disk

In the previous section, we outlined the salient features of the magnetospheric structure that forms in the presence of a disk, with particular emphasis on the various factors that can contribute to enhanced synchrotron radiation. We saw that the plasma density in the inner parts of the wind is considerably increased. The residence time of particles near the light cylinder is considerably enhanced, leading them to cool in regions of strong magnetic field. The magnetic field itself is also amplified throughout the computational domain, particularly along the arc-like structures surrounding the inner edge of the torus. In these zones, particle acceleration is enhanced, accompanied by a net increase in the pitch angle.

Because the synchrotron power emitted by the magnetosphere is given by (Blumenthal and Gould, 1970):

$$\mathcal{P}_{\rm rad} = \frac{2}{3} n r_e^2 c \gamma^2 \tilde{B}_\perp^2 \,, \tag{5.9}$$

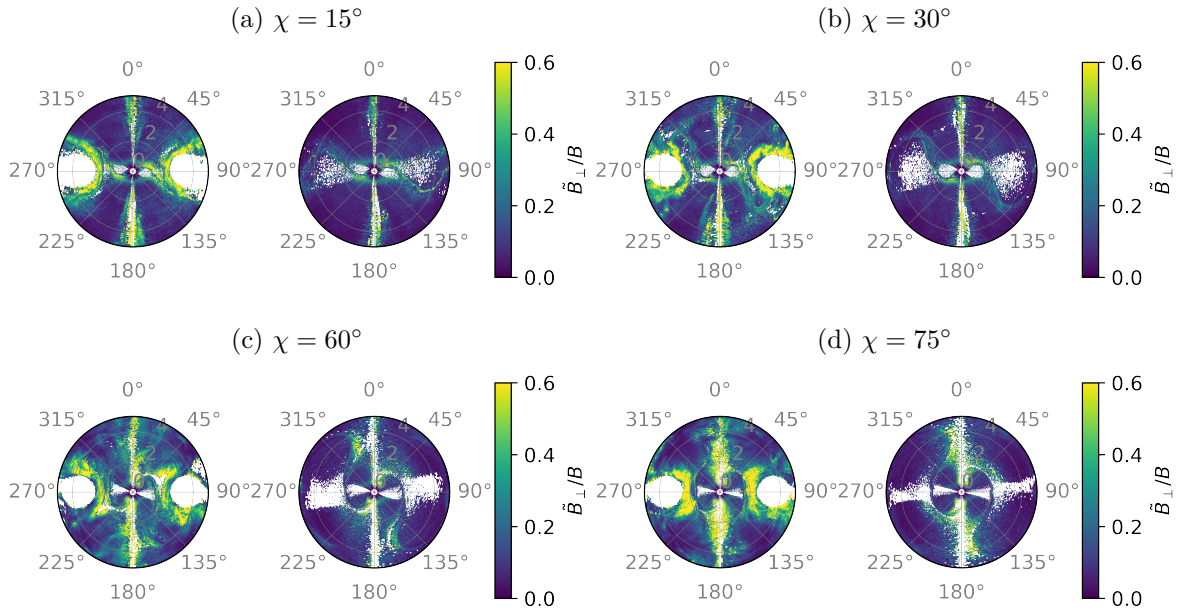

Figure 5.20: 2D poloidal maps of the ratio between the effective perpendicular magnetic field ($\tilde{B}_\perp$) to the total field strength (B). For each magnetic obliquity, the interaction case is shown on the left and the reference case is shown on the right. Radii are given in units of the light cylinder radius. The pitch angle of particles is significantly increased in the presence of the disk.

and based on all the elements discussed above, a significant increase in synchrotron emission is to be expected. This is indeed confirmed by our results: the presence of the disk not only enhances synchrotron radiation, but also alters the emission region itself, which now coincides with the disrupted current sheet rather than the standard one. Figure 5.21 shows, for all magnetic obliquities, the synchrotron emission in the presence of the disk (left), alongside its corresponding reference case (right).

Although these results appear similar regardless of the magnetic obliquity, a significant structural difference emerges between low and high-obliquity cases. Indeed, when analyzing the evolution of the synchrotron emission maps over a pulsar's spin period, we find that low and high-obliquity configurations behave differently. Figure 5.22 presents three snapshots of synchrotron emission maps, taken $0.25\,P_{\rm spin}$ apart, for the cases of $\chi = 15°$ (top) and $\chi = 75°$ (bottom). Let us fix a specific observer's viewing angle (α), as illustrated in the figure. In the low-obliquity case, each time one arm of the current sheet points in the observer's direction, a burst of radiation is emitted. Both arms of the current sheet sweep across all latitudes from $\pi/2 + \chi$ to $\pi/2 - \chi$ returning to the observer's angle once every spin period. As a result, the emission that escapes radially from the simulation box reaches a maximum flux at time t, followed by a minimum (see pink circles) at time $t + P_{\rm spin}/2$. On the opposite hemisphere, this pattern is shifted by $0.5\,P_{\rm spin}$. Hence, the emission appears modulated over one spin period of the pulsar, producing a single intensity peak per period. In contrast to low-obliquity cases, for $\chi = 75°$ and the same observer's angle, we detect two emission bursts per spin period, with an identical symmetric pattern on the opposite hemisphere. In such highly inclined configurations, the current sheet approaches the disk almost vertically and breaks apart in a symmetric manner. As a result, a burst of emission is produced every time an arm of the current sheet impacts the disk, i.e., every $0.5\,P_{\rm spin}$.

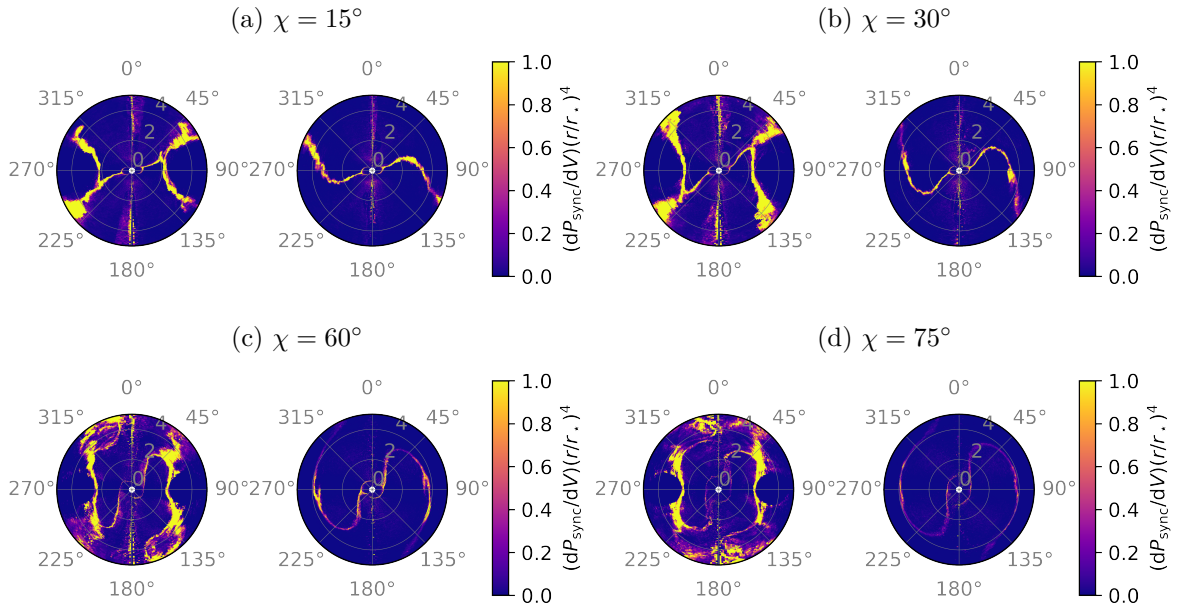

Figure 5.21: 2D poloidal maps of the normalized isotropic synchrotron power emitted by the particles per unit of volume $(\mathrm{d}P_{\rm sync}/\mathrm{d}V)(r/r_\star)^4$. Radii are given in units of the light cylinder radius. The synchrotron radiation is enhanced in the presence of the disk and the emission region itself is also altered, now corresponding to the disrupted current sheet.

5.5.2 Light curves

The skymaps originating from all simulations are reported in Figure 5.23, to better illustrate the effect highlighted above. All the forthcoming results are time-averaged over two pulsar spin periods, specifically between 1.4 and 3.4 $P_{\rm spin}$, after all simulations have converged. In Figure 5.23, the left column represents the reference cases (i.e., isolated pulsars), and the right column shows the pulsar-disk simulations. Each row corresponds to a different pulsar's magnetic obliquity. Five dashed lines are overlaid on each skymap, corresponding to five selected lines of sight. Below each skymap, the light curves corresponding to the five viewing angles are plotted. In the left column, we reproduce well-established results (see, for example, Cerutti et al. 2016), with emission originating primarily from the current sheet and a two-peak structure visible in the light curves (see Section 1.3.2 and Cerutti et al. 2025 for further explanations). Peaks are globally thin, although their width varies with the geometry of the current sheet intercepted by the line of sight: in the most inclined cases, the current sheet oscillates in the $\theta-$direction almost vertically and is intercepted almost perpendicularly by the line of sight, thereby explaining very narrow peaks. The results shown in the right column exhibit some common features, regardless of the magnetic obliquity. The first striking result is a significant enhancement of synchrotron emission at all latitudes throughout the entire spin period. A consistent colorbar is intentionally applied to all plots to emphasize the intensity contrast between reference cases and the others. Another common feature is the substantial broadening of the intensity peaks, compared to the reference cases. Furthermore, when two intensity peaks are present, they are spaced by about half a phase and their amplitudes slightly differ. Beyond these findings common to all obliquities, some fundamental differences appear between cases with different inclinations. First, although the inclination of $\chi = 60°$ seems to represent an optimum in terms of intensity, the global tendency shows an increase in intensity with the magnetic obliquity. Secondly, and importantly, we recover the behaviour described in Section 5.5.1. The least inclined case ($\chi = 15°$) exhibits a single intensity peak per spin period (for a fixed viewing angle), with a half-phase shift between the two hemispheres. In contrast,

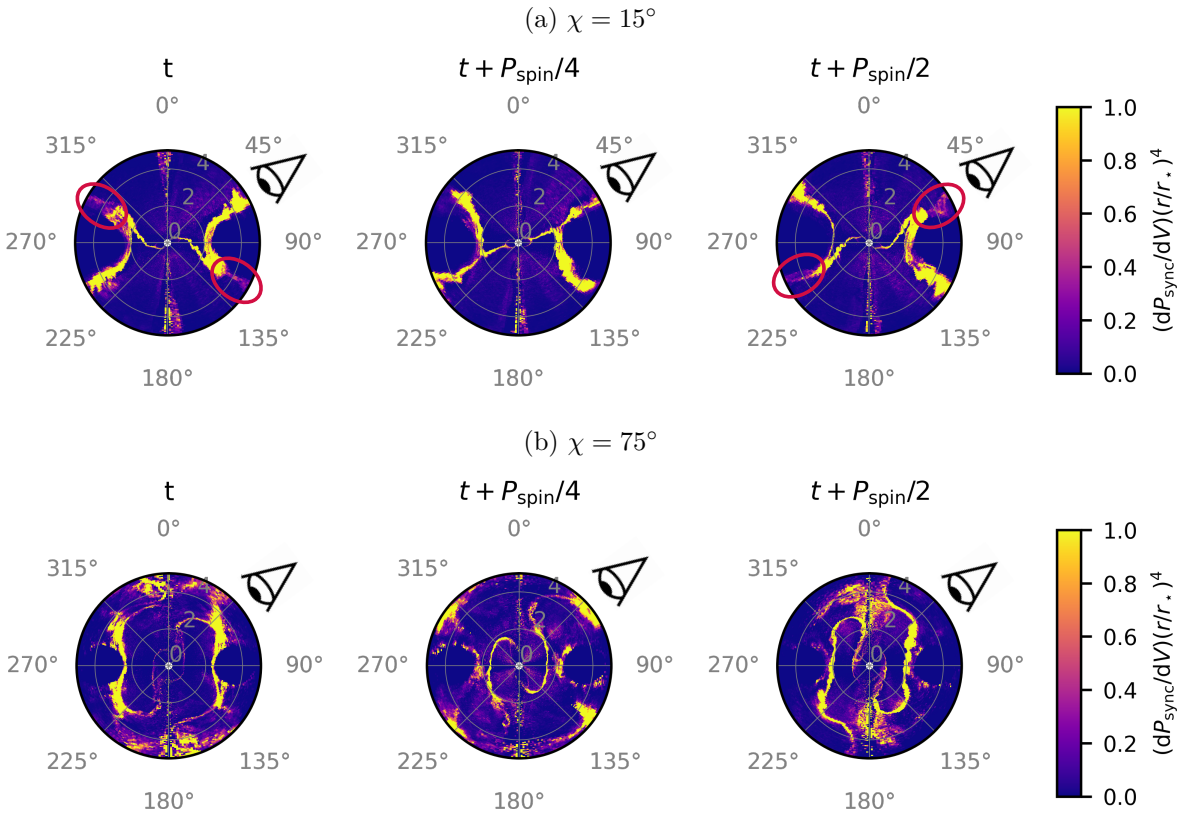

Figure 5.22: Temporal evolution of 2D poloidal synchrotron emission maps in the presence of the disk, for $\chi = 15°$ (top) and $\chi = 75°$ (bottom). We represent 2D snapshots of the normalized isotropic synchrotron power emitted by the particles per unit of volume $(\mathrm{d}P_{\mathrm{sync}}/\mathrm{d}V)(r/r_\star)^4$. The eye symbol indicates the observer's viewing angle considered in the analysis of these maps. Pink circles highlight emission minima. For low inclinations, one burst of light is emitted per spin period, whereas for high inclinations, two bursts of light are produced within each spin period. Radii are given in units of the light cylinder radius.

the most inclined case ($\chi = 75°$) displays two intensity peaks per period, aligned in phase across both hemispheres. In other words, the least inclined case displays central symmetry, whereas the most inclined cases appears symmetric with respect to the equatorial plane. The transition from one regime to the other occurs smoothly at intermediate obliquities, namely $\chi = 30°$ and $\chi = 60°$. As described in Section 5.1.4, observations of PSR J1023+0038 reveal two bright, broad peaks per spin period, separated by 180°, similarly to our most inclined case. This suggests that the observed system has a high magnetic obliquity. Consequently, the majority of the results that follow are shown for the case $\chi = 75°$.

In the following, we examine the energy dependence of these results. Although we present results for the case $\chi = 75°$, the energy dependence is found to be similar across all magnetic inclinations. We split the total energy range into four logarithmically equally spaced bins, as illustrated in Figure 5.24. Figure 5.25 presents the skymaps and light curves computed for each energy bin. Because the energy flux varies across different energy bins, each skymap is normalized to its own maximum intensity. Doing so enables us to compare the pulsed fraction across the different energy bins. It clearly appears that the pulsed fraction increases with energy.

Another important point that we wish to assess, is the displacement of peaks with energy. To better evaluate this aspect, we overlay the light curves obtained for the four energy bins, at a fixed viewing angle, in a single plot. Results being similar across all viewing angles, we show

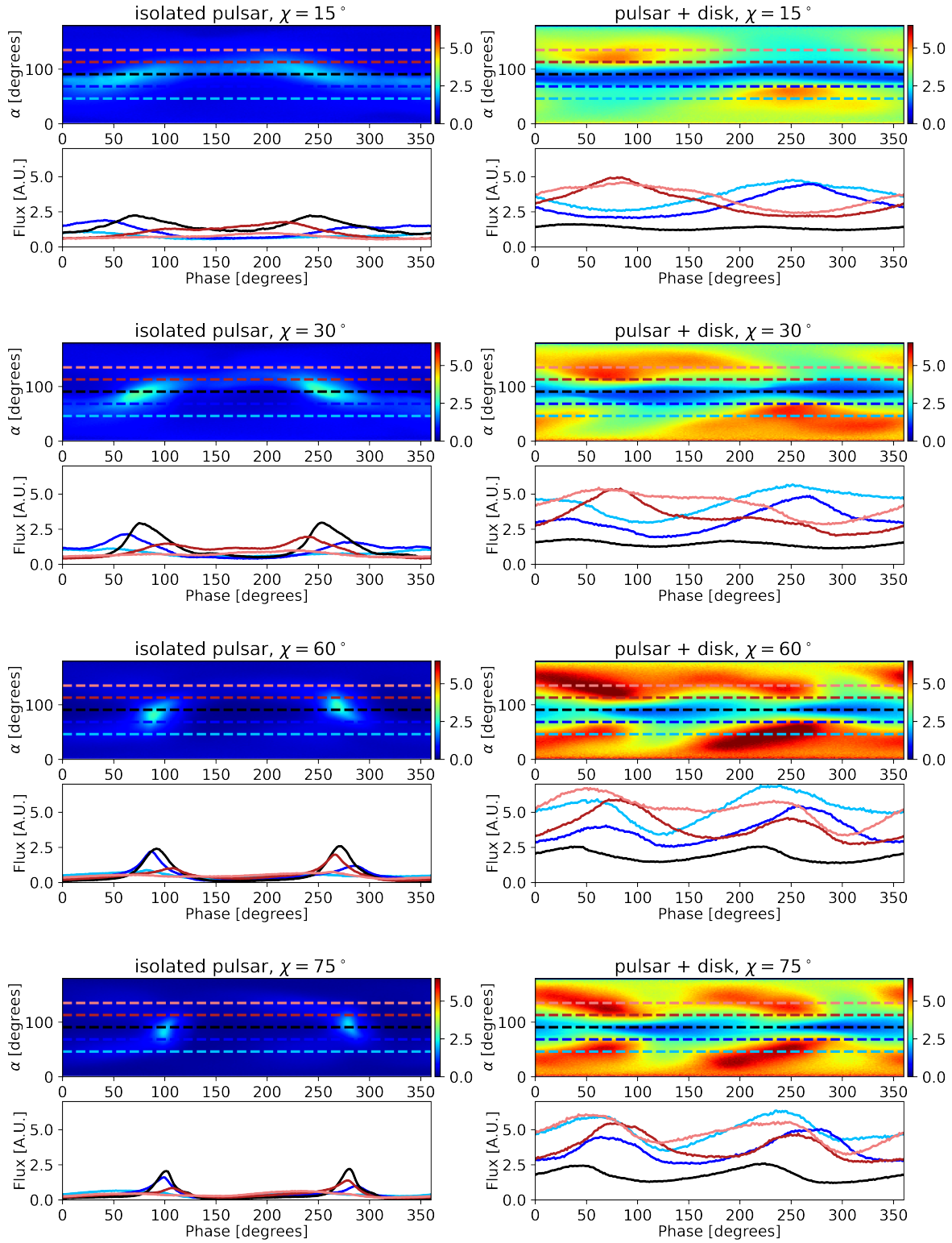

Figure 5.23: For each simulation, we show the skymap (as a function of the viewing angle, α, and of the pulsar's spin phase) and the light curves associated with five different observer angles (see dashed lines for the corresponding colors on the skymaps): $\alpha = 45°, 67.5°, 90°, 112.5°$ and $135°$. The colorbar shows the synchrotron flux normalized by the average flux of run REF_15 (top-left panel). Data are averaged over $2P_{\rm spin}$. The interaction with the disk induces a significant increase in intensity throughout the entire spin period and at all observer angles, and a net broadening of the pulses. Low magnetic obliquities give rise to a single intensity peak per period while high magnetic obliquities display two peaks per period.

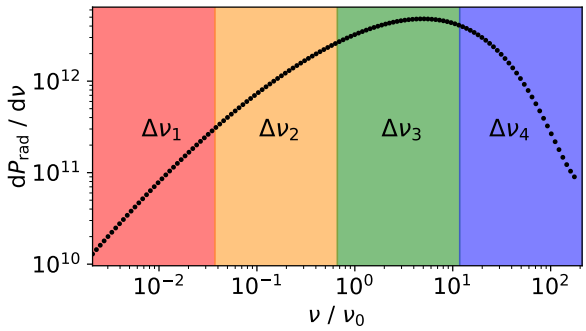

Figure 5.24: Synchrotron spectrum obtained for run DISK_75. The frequency ν is normalized by $\nu_0 = 3eB_\star/4\pi mc$. The frequency domain is divided into four logarithmically equally spaced bins: $\Delta\nu_1$, $\Delta\nu_2$, $\Delta\nu_3$, and $\Delta\nu_4$.

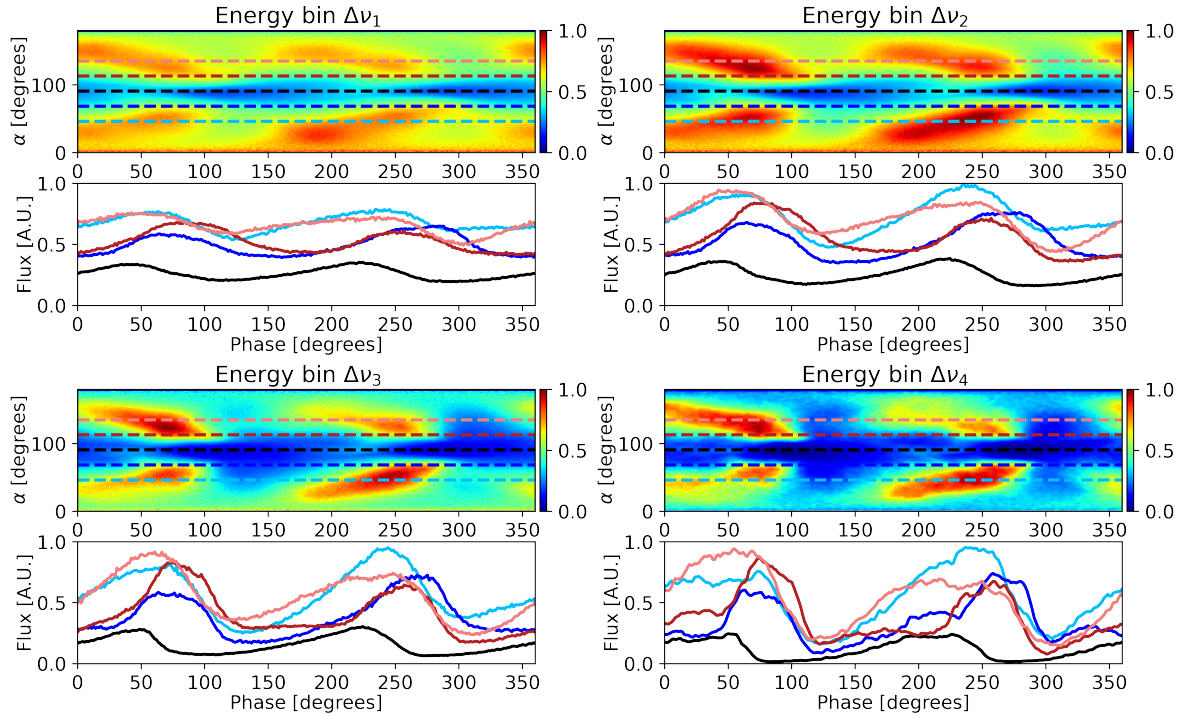

Figure 5.25: Skymaps of run DISK_75 obtained by integrating over four logarithmically equally spaced bins. The skymaps depend on the viewing angle, α, and the pulsar's spin phase. Below each skymap, we plot the light curves associated with five different viewing angles (see dashed lines for the corresponding colors on the skymaps): $\alpha = 45°, 67.5°, 90°, 112.5°$ and $135°$. The colorbar shows the synchrotron flux, and each skymap is normalized to its maximum value. Data are averaged over $2\,P_{\rm spin}$. The pulsed fraction is observed to increase with energy.

only those corresponding to the angle measured for PSR J1023+0038, i.e., 46.4° (Figure 5.26). For visualization purposes, each curve is normalized to its peak value. No significant shift in the phase of the peaks appears across energy bands, regardless of the viewing angle and the magnetic obliquity.

5.5.3 Polarization properties

As we have seen, the electromagnetic field topology undergoes a reconfiguration due to the interaction with the disk. This naturally raises the question of how its polarization properties

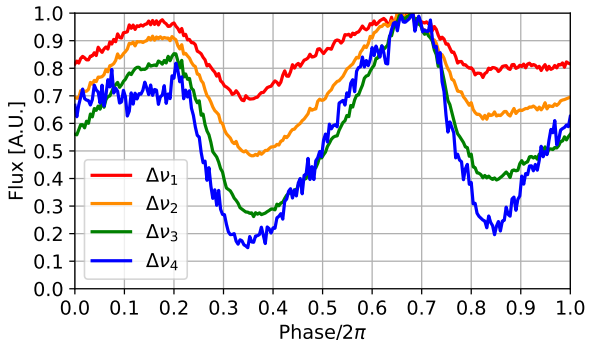

Figure 5.26: Light curves of run DISK_75 obtained by integrating over four logarithmically equally spaced frequency bins ($\Delta\nu_1$, $\Delta\nu_2$, $\Delta\nu_3$, and $\Delta\nu_4$), evaluated at a fixed viewing angle $\alpha = 46.4°$. This specific viewing angle corresponds to the one measured for the transitional millisecond pulsar PSR J1023+0038. Each curve its normalized to its own maximum value to facilitate comparison. Data are averaged over $2P_{\rm spin}$. We observe no significant phase shift in the peaks across energy bands.

may be affected. We remind the reader that the linear polarization degree (Π) and the polarization angle (PA) are defined as follows :

$$\Pi = \frac{\sqrt{Q^2+U^2}}{I} \quad \text{and} \quad \text{PA} = \frac{1}{2}\arctan\left(\frac{U}{Q}\right) , \tag{5.10}$$

where Q, U and I are the Stokes parameters and the polarization angle is defined as the angle between the rotation axis and the direction of the effective perpendicular magnetic field ($\tilde{\boldsymbol{B}}_\perp$; Eq. 2.102) projected on the plane of the sky for a given observer. A more detailed description of the main polarization quantities and their numerical modelling is provided in Cerutti et al. (2016). Before moving on to the new results, let us outline some salient polarization features obtained in the case of isolated magnetospheres. It is important to first note that ultra-relativistic particles emit only linearly polarized radiation (Ginzburg and Syrovatskii, 1965). Hence, the circular polarization component is not considered in such systems (i.e., the Stokes parameter V is neglected). As an example, Figure 5.27 shows the skymaps of the linear polarization degree and polarization angle for a magnetic obliquity of 75°. The polarization degree reaches $\sim$ 20%. A distinct drop in polarization is observed in the current sheet. Indeed, the magnetic field vanishes in this region due to magnetic reconnection, and particles escaping from the X-points are accelerated in various directions. The current sheet is also subject to instabilities, which can further disrupt the magnetic field topology at small scales and reduce the polarization degree. Due to the reversal of the magnetic field across the sheet, the polarization angle exhibits a sharp swing of $\sim$ 120° across the layer (see right panel in Figure 5.27). On both sides of the current sheet, the magnetic polarity shows little variation. Our results are consistent with a previous study dedicated to modeling polarized synchrotron emission from the equatorial current sheet, performed with `Zeltron` (Cerutti et al., 2016).

The inclusion of a disk in the pulsar wind significantly alters the polarization skymaps. Figure 5.28 presents our results for the degree of linear polarization at each magnetic obliquity. Even though the observed patterns vary with the pulsar's magnetic obliquity, we consistently observe a depolarization of the magnetosphere when the disk is present. This effect aligns with the disruption of the current sheet by the disk, which causes it to become thicker and more isotropized, thereby mixing regions of different polarities. A clear correlation emerges between the intensity peaks produced by the distorted current sheet (see Figure 5.23) and the local minima in polarization visible on the skymaps. Accordingly, for $\chi = 15°$, we recover the central symmetry observed in the intensity skymap, whereas for $\chi = 75°$, we recover symmetry with respect to the equatorial plane.

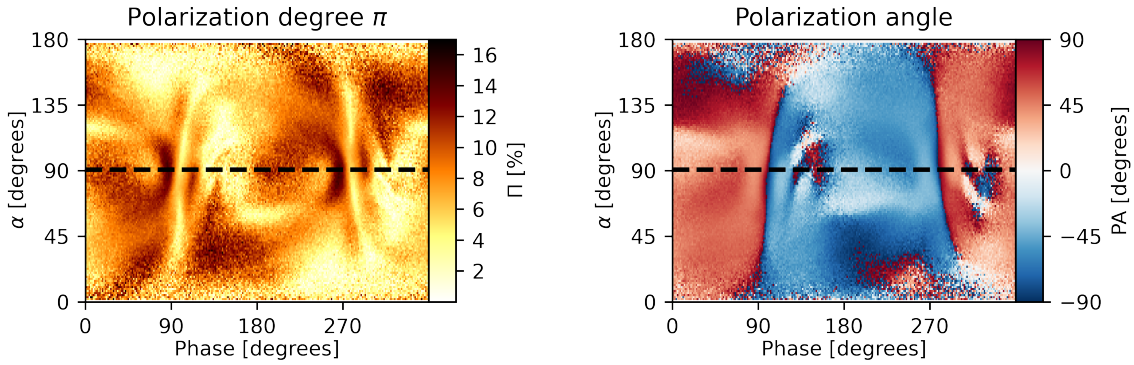

Figure 5.27: Skymaps of the polarization degree (left) and polarization angle (right) for an isolated pulsar with a magnetic obliquity of 75°. The maps are shown as a function of the viewing angle α and the pulsar phase. The dashed black line indicates the equatorial line of sight. Data are averaged over $2\,P_{\mathrm{spin}}$.

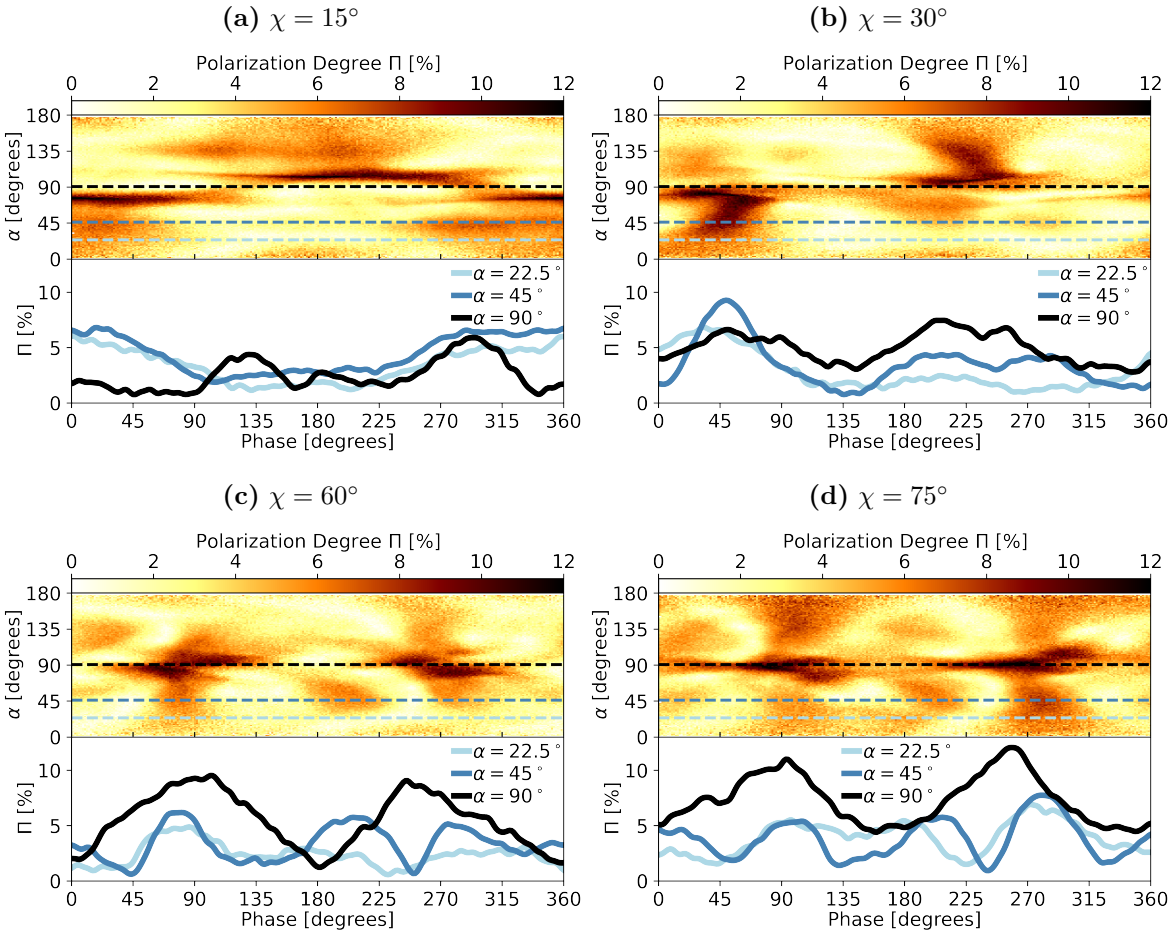

Figure 5.28: Skymaps of the linear polarization degree in the pulsar-disk interaction case, shown for all magnetic obliquities. The maps are presented as functions of the viewing angle α and the pulsar phase. The three dashed lines mark distinct viewing angles, with the corresponding curves displayed below each skymap. Data are averaged over $2\,P_{\mathrm{spin}}$. The polarization degree decreases in the presence of the disk, exhibiting an anticorrelation with the increase in light intensity.

As for the polarization angle, results are presented in Figure 5.29, for each magnetic obliquity. The equatorial regions appear somewhat blurred, and the polarization angle locally decreases in these areas due to the eclipse. We recall that, for any line of sight, we suppress all photons passing through the disk. Again, a central symmetry appears in the skymap for $\chi = 15°$, while cases with higher inclination tend to exhibit symmetry about the equatorial plane. However, some noise is present, caused by the disrupted current sheet, which occasionally results in local mixing of different polarities. We select three viewing angles for which we plot the corresponding curves below the skymaps. For $\alpha = 90°$, the polarization angle globally oscillates between $-50°$ and $50°$, with a smaller amplitude observed in the case of $\chi = 60°$. This viewing angle is affected by the disk eclipse. At higher latitudes (see curves for $\alpha = 45°$, corresponding to the maximum emission according to Figure 5.23, and curves for $\alpha = 22.5°$), the polarization angle rotates from approximately $-60°$ to $60°$ each time the disrupted current sheet is crossed. This behaviour is consistent across all magnetic obliquites. We infer that the presence of the disk does not lead to significant variations in the polarization angle rotation.

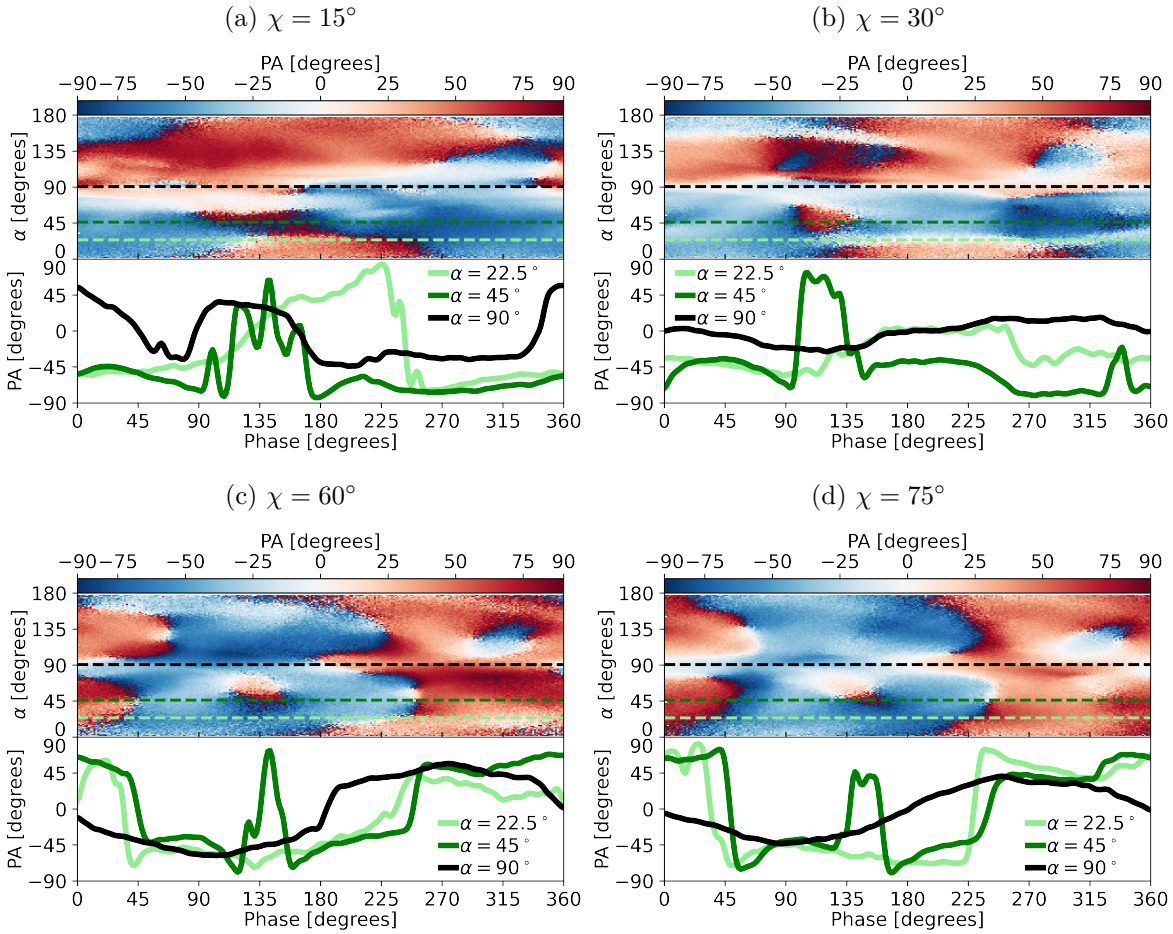

Figure 5.29: Skymaps of the polarization angle in the pulsar-disk interaction case, shown for all magnetic obliquities. The maps are presented as functions of the viewing angle α and the pulsar phase. The three dashed lines mark distinct viewing angles, with the corresponding curves displayed below each skymap. Data are averaged over $2\,P_{\rm spin}$. Apart from the equatorial regions distorted by the disk ecplipse, the polarization angle is shown to rotate from approximately $-60°$ to $60°$.

Similarly to the energy dependence study carried out for the intensity maps, we split the energy range into four logarithmically equally spaced bins (see Figure 5.24), denoted as $\Delta\nu_1$, $\Delta\nu_2$, $\Delta\nu_3$, and $\Delta\nu_4$. Since the results are similar regardless of the pulsar's magnetic obliquity,

we only show those corresponding to $\chi = 75°$. The linear polarization degree computed for each frequency bin is reported in Figure 5.30. A consistent colorbar is intentionally applied to all plots to emphasize the contrast between energy bins. It clearly appears that higher energies favor higher polarization degrees. The same procedure is applied to the polarization angle, and the energy-resolved results are presented in Figure 5.31. Again, although the effect is less pronounced than for the polarization degree, the polarization angle reaches higher absolute values at higher energies. In addition, the equatorial regions appear to be less affected by the disk eclipse at higher energies.

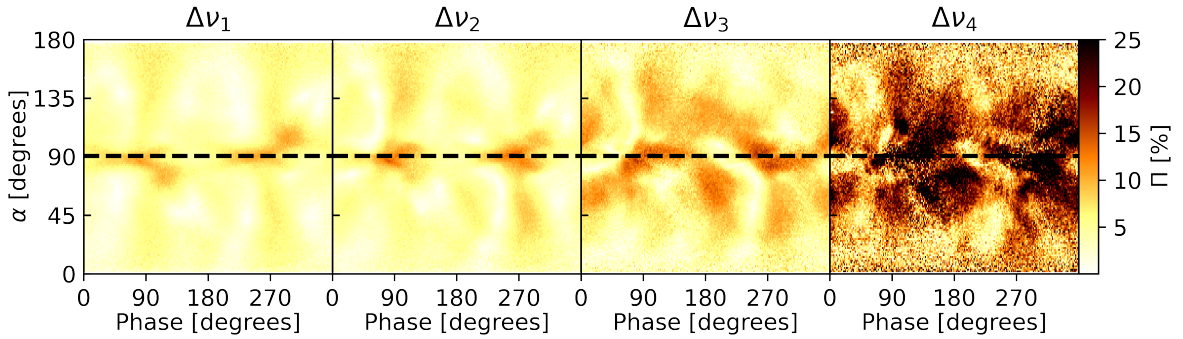

Figure 5.30: Skymaps of the linear polarization degree obtained by integrating over four logarithmically equally spaced bins ($\Delta\nu_1$, $\Delta\nu_2$, $\Delta\nu_3$, and $\Delta\nu_4$), in the presence of the disk, for $\chi = 75°$. The skymaps depend on the viewing angle, α, and the pulsar phase. The black dashed line marks the equatorial plane. Data are averaged over $2\,P_{\rm spin}$. The polarization degree is shown to increase with energy.

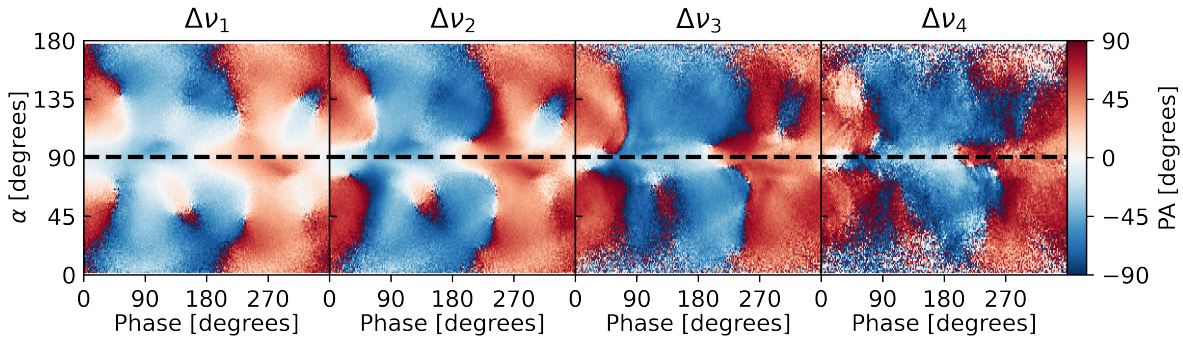

Figure 5.31: Skymaps of the linear polarization angle obtained by integrating over four logarithmically equally spaced bins ($\Delta\nu_1$, $\Delta\nu_2$, $\Delta\nu_3$, and $\Delta\nu_4$), in the presence of the disk, for $\chi = 75°$. The skymaps depend on the viewing angle, α, and the pulsar phase. The black dashed line marks the equatorial plane. Data are averaged over $2\,P_{\rm spin}$. The polarization angle reaches higher absolute values (and thus undergoes greater rotation) at higher energies.

Given the estimated viewing angle of PSR J1023+0038, namely 46.4° (Stringer et al., 2021), we adopt this value to plot and compare the polarization degree (Figure 5.32, left panel) and polarization angle (Figure 5.32, right panel) across all energy bins. This representation confirms both the increase in the linear polarization degree and the enhanced rotation of the polarization angle with energy.

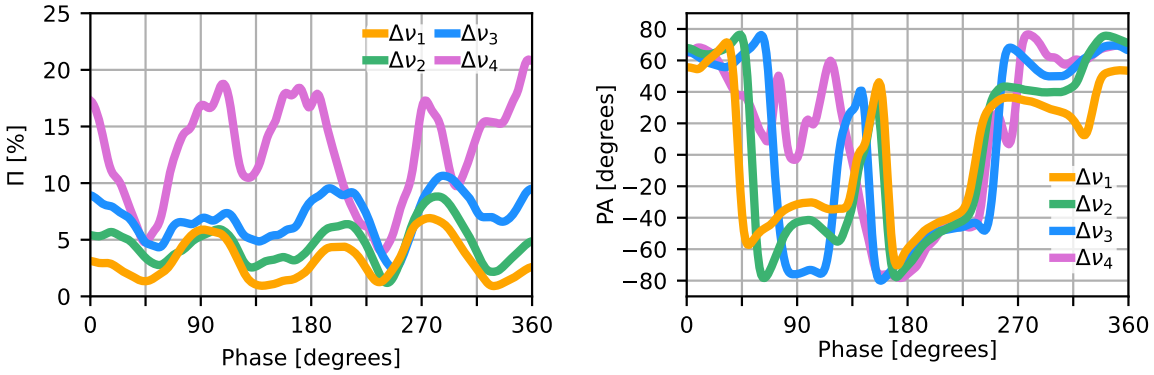

Figure 5.32: Polarization degrees (left) and polarization angles (right) for four logarithmically spaced energy bins ($\Delta\nu_1$, $\Delta\nu_2$, $\Delta\nu_3$, and $\Delta\nu_4$), derived from the DISK_75 simulation. They are computed at the viewing angle of PSR J1023+0038 ($\alpha = 46.4°$). Data are averaged over $2\,P_{\rm spin}$. Both the polarization degree and the amplitude of the polarization angle rotation increase with energy.

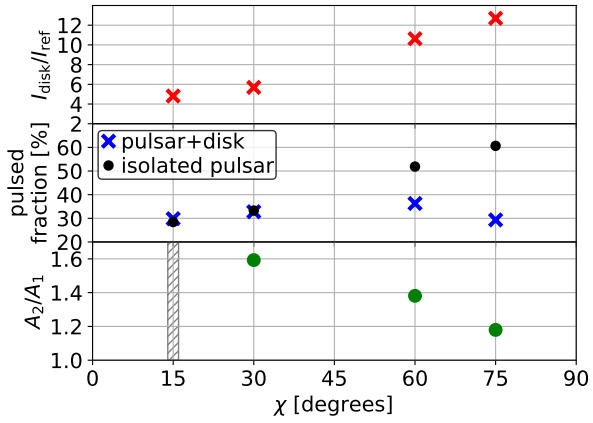

Figure 5.33: Characteristics of the synchrotron emission as a function of the magnetic obliquity χ. *Top panel:* flux ratios ($I_{\rm disk}/I_{\rm ref}$) between simulations including the disk and the reference simulations of isolated pulsars. *Middle panel:* pulsed fraction, computed by subtracting the continuum from the total luminosity and normalizing by the total luminosity. Blue crosses correspond to the pulsar-disk interaction cases, while black points refer to the isolated pulsar cases. *Bottom panel:* ratio of the peak amplitudes (A_2/A_1). The gray-shaded band indicates the absence of a second peak for $\chi = 15°$.

5.6 Discussion and conclusion

In this study, we investigate, through PIC simulations, how the interaction between a pulsar and a surrounding disk (located sufficiently close) alters the pulsar magnetosphere and modifies the emitted synchrotron light curves. Our results are consistent with the observations of the transitional millisecond system PSR J1023+0038 in its X-ray high mode, reported in Papitto et al. (2019). We find a significant increase in the total luminosity with respect to isolated pulsars, with amplification factors ranging from ~ 5 to ~ 12.5 depending on the magnetic obliquity of the pulsar (see top panel in Figure 5.33). We highlight the various factors contributing to the enhanced emission, including increased plasma density near the light cylinder radius, amplification of the magnetic field, plasma isotropization and enhanced particle acceleration.

Our parametric analysis, in which the magnetic obliquity angle is varied, reveals that the light curves can feature one or two peaks depending on the magnetic obliquity of the pulsar (χ), for a given disk aspect ratio (h/R). Indeed, low magnetic obliquities ($\tan^{-1}(h/R) \gtrsim \chi$) lead to the appearance of a single peak per phase, whereas high magnetic obliquities ($\tan^{-1}(h/R) \lesssim \chi$) display two peaks per period, separated by about half a rotation period (Figure 5.23). Intermediate magnetic obliquities exhibit a progressive evolution between these two regimes. A parametric study exploring various aspect ratios and disk distances would provide valuable support for these results. The observations of PSR J1023+0038 report a pulsed emission superimposed on a significant DC component, with two distinct peaks 180° apart. Therefore, the most relevant simulation for upcoming comparisons with observations of PSR J1023+0038 is the one that reproduces two broad peaks per period, corresponding to a pulsar magnetic obliquity of 75°, given our aspect ratio of $h/R = 0.3$.

In both the simulated and the observed data, the emission peaks are much broader than those typically seen in isolated pulsars, extending over half a rotational phase. We obtain a slight difference in the amplitudes of the peaks, similarly to the one reported in the observations. Figure 5.33 (bottom panel) presents the amplitude ratios (A_2/A_1) of the two peaks, computed after subtracting the DC component, for all magnetic obliquities. These ratios decrease from 1.6 to 1.2 as the magnetic obliquity increases. Papitto et al. (2019) reports background-subtracted RMS amplitudes for the two peaks (r_1 and r_2), yielding r_2/r_1 ratios of 1 in the optical and 3 in the X-ray band. We compute the pulsed fraction, by subtracting the continuous flux from the total flux before normalizing it by the total flux. Results are presented in Figure 5.33 (middle panel) for all magnetic obliquities. Because of the appearance of a strong continuous component, the pulsed fraction of the light curves is significantly diminished, compared to isolated pulsars light curves. As can be seen on the figure, it particularly deviates from the reference values for the highest magnetic obliquities and reaches $\sim 30\%$ for $\chi = 75°$. We find an increase in the pulsed fraction with energy (Figure 5.25). The observational data indicates a pulsed fraction[1] of $\sim 1\%$ for optical rays and $\sim 10\%$ for X-rays. Hence, numerical and observational results appear to follow the same general trend regarding both a decrease in the pulsed fraction with respect to isolated pulsars and an increase with energy. However, we cannot directly compare our computed pulsed fractions to observational data, since the majority of the detected optical emission is expected to originate from the irradiation of the disk or the donor star, and current observations do not allow us to determine what fraction of the optical emission actually originates from the immediate surroundings of the neutron star.

In addition to the new DC component that appears in our study, several other sources of continuous emission are neglected in our model and could account for the remaining discrepancy with the pulsed fraction inferred from observational data. PIC simulations are

[1] We note that our method for calculating the pulsed fraction differs from the one employed in the observational study.

well-suited for studying low-density and collisionless plasma environments, but are not appropriate for modeling denser and collisional plasma environments like the disk itself. Hence, we simulate the disk as a boundary condition for the pulsar magnetosphere. This implies that the emission coming from the disk is not captured in our analysis, although we would expect it to dominate the system's total emission. More generally, our model does not include the thermal emission, which could be significant when considering the disk. The irradiation of the companion star, both by the pulsar wind and the disk material, could also contribute to the thermal continuum component (in the optical and infrared bands). Such emission directly depends on the irradiated face of the companion and may also include a component modulated at the orbital period. Additionally, the presence of a compact jet in these systems has been discussed (Baglio et al., 2023) and might also contribute to the DC component. So far, we only investigated the synchrotron emission but we could also expect some inverse compton emission coming from the interaction between the pulsar wind and the photons from the disk (or the companion). Given the particle acceleration and the photon reservoir evidenced in our results, the system could also host synchrotron self-Compton processes. Contrary to what is observed in the optical and X-ray emissions from PSR J1023+0038 (see Papitto et al. 2019 and Illiano et al. 2023), we detect no significant phase shift between pulses when comparing light curves computed at different energies (Figure 5.26). The limitation of our study to the inner regions of the wind (up to $5.6\,R_{\rm LC}$) may partly explain this, as we do not capture the particles cooling occurring at larger distances.

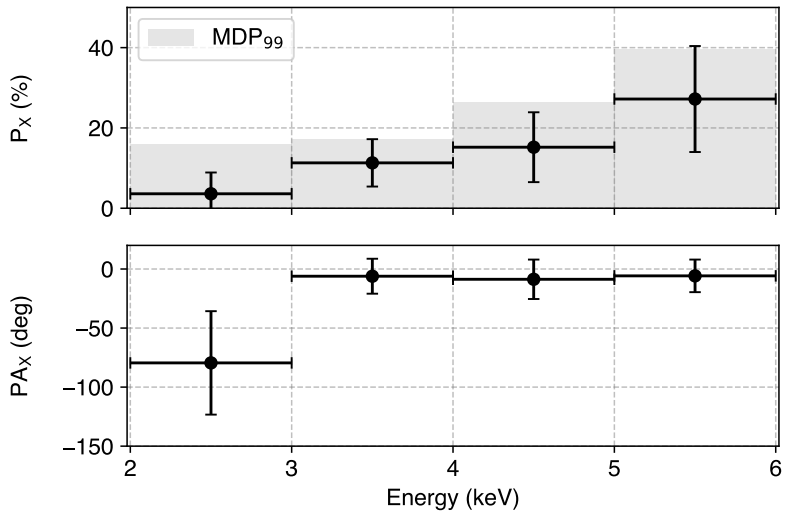

Figure 5.34: Energy dependence of the X-ray polarization properties in PSR J1023+0038. The top and bottom panels respectively show the polarization degree and polarization angle as a function of photon energy. Horizontal bars indicate the width of the energy bins used for the binned analysis and vertical error bars correspond to 1σ. Gray shaded areas represent the minimum detectable polarization at the 99% confidence level for each bin. Figure taken from Baglio et al. (2024).

The synchrotron radiation produced in our model is linearly polarized, although the presence of the disk leads to depolarization compared to the isolated case, especially in the regions where plasma accumulates. However, we observe a significant increase in the polarization degree with energy (Figure 5.32). Observations reveal that the pulsed flux and the polarized flux closely coincide across the spectrum, and report a polarization degree of $(1.4 \pm 0.04)\%$ in the optical band and $(12 \pm 3)\%$ at X-ray wavelengths (Baglio et al., 2024). In addition to that, Baglio et al. (2024) shows the increase in X-ray polarization with energy (see Figure 5.34), in agreement with our model's predictions. The modeled polarization angle features oscilla-

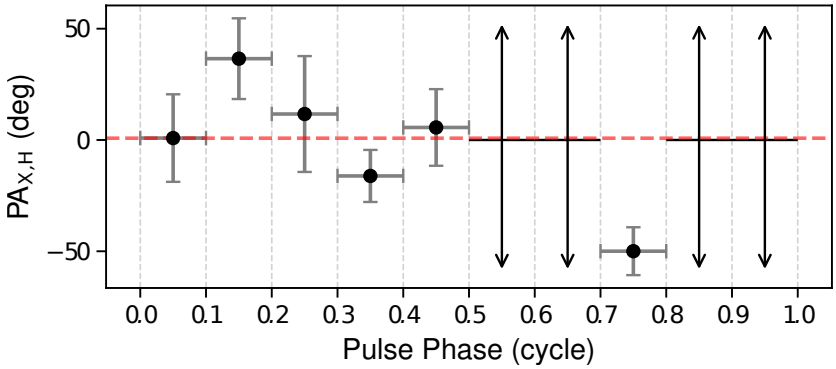

Figure 5.35: Polarization angle of PSR J1023+0038 in the high mode, as a function of the rotational phase. Results are sampled in 10 phase bins and obtained after background subtraction. Arrows indicate upper limits, reported at the 90% confidence level for bins compatible with null values at the 68% confidence level. The red horizontal dashed line traces the mean value. Figure taken from Baglio et al. (2024).

tions across the pulsar phase, regardless of the pulsar's magnetic obliquity, similarly to what is obtained for isolated pulsars. In particular, for $\chi = 75°$ and $\alpha = 46.4°$, the polarization angle varies from $\sim -60°$ and $\sim 60°$. The rotation of the polarization angle appears to be increasingly pronounced at higher energies (Figure 5.32). Observational data (Baglio et al., 2024) do not exclude such rotations of the polarization angle (Figure 5.35) and confirm the variation of the polarization angle with energy (Figure 5.34).

To conclude, we present the first numerical model that successfully reproduces the main characteristics of the optical and X-ray pulsed emission observed from PSR J1023+0038. Our results confirm the synchrotron origin of this peculiar signal and support the scenario in which the optical and X-ray pulses are produced by synchrotron radiation emitted as the pulsar's striped wind interacts with the inner edge of the accretion disk, located a few light-cylinder radii from the pulsar.

The present study does not simulate the disk, nor the possible mixing of particle populations from the pulsar wind and the accretion flow, and therefore does not address the establishment of equilibrium between the pulsar wind and the inner disk boundary during the transition to the sub-luminous disk state. Investigating these larger-scale processes would complement our scenario and provide deeper insight into the global conditions leading to this state. Polarimetric observations with higher statistics are expected in the coming years and will be valuable for further constraining emission models. The detection of new transitional systems, or the confirmation of already identified candidates, will be necessary to improve our understanding of the pulsar population involved. Increasing the sample of transitional millisecond pulsars will be particularly important to assess whether highly inclined pulsars are required to reach the subluminous disk state — that is, whether all detections consistently show a two-peaked pulsed signal, as predicted by our model. Alternatively, this study suggests that transitional systems may instead display single-peaked light curves in the case of low-inclination pulsars.

Chapter 6

Towards pulsar–black hole simulations

Contents

6.1 Electromagnetic precursors to neutron star mergers 123
6.1.1 Observations of neutron star mergers 123
6.1.2 Precursor radiative signatures 124
6.1.3 The special case of black hole–neutron star binaries 124
6.2 Existing models and key predictions 125
6.3 Off-center pulsar on a spherical grid 126
6.3.1 Electromagnetic fields implementation 126
6.3.2 Particles injection 128
6.4 Next steps towards binary implementation 130

This chapter presents ongoing work towards building the first GRPIC simulations of pulsar—black hole binaries. Implementing numerically such systems is a significant challenge in itself; therefore, even though no physical results are available yet, we present our motivations for this study, outline the numerical setup under development, some of the difficulties encountered so far, and the steps required to achieve a working model.

6.1 Electromagnetic precursors to neutron star mergers

6.1.1 Observations of neutron star mergers

Neutron star mergers, including both binary neutron stars and black hole–neutron star systems, are expected to be among the most common detectable multi-messenger transients (Burns et al., 2025). The evolution of binary neutron stars and black hole–neutron star binaries features three main phases: an inspiral phase, that can last millions of years and during which the two objects gradually lose energy and angular momentum through gravitational wave emission and possibly electromagnetic emission; a merger phase lasting about one millisecond; and a post-merger phase, lasting up to several seconds, during which any remaining matter is either ejected or accreted onto the remnant body, potentially accompanied by electromagnetic counterparts (see Figure 6.1 for an illustration).

The first joint detection of gravitational and electromagnetic signals from a binary neutron star merger (Abbott et al., 2017) demonstrated the importance of combining gravitational and electromagnetic observations to study such systems and provided insights across an exceptionally wide range of fields, including astrophysics, cosmology, gravitation and dense matter. The estimated binary neutron star merger rate ranges from 10 to 1700 $\mathrm{Gpc}^{-3}\ \mathrm{yr}^{-1}$ and the neutron star–black hole merger rate is expected to lie between 7.8 and 140 $\mathrm{Gpc}^{-3}\ \mathrm{yr}^{-1}$ (Abbott et al., 2023). Although the rate of binary black hole merger observations via gravitational waves is much higher than that of binary neutron star or black hole–neutron star mergers, the fourth Open Gravitational-wave Catalog (4-OGC; Nitz et al. 2023), which compiles data from the first three observing runs (O1, O2, O3a, and O3b) of the Advanced LIGO (LIGO Scientific Collaboration et al., 2015) and Advanced Virgo (Acernese et al., 2015) gravitational wave observatories, reports two binary neutron star events and two black hole–neutron star events. The Gravitational-Wave Transient Catalog 3 (GWTC-3) reports two more possible black hole–neutron star binaries, GW190426_152155 and GW190917_114630 (Abbott et al., 2023).

Among the neutron star mergers detected via gravitational waves, only the binary neutron star merger GW170817 (Abbott et al., 2017) has confirmed electromagnetic counterparts, observed during the post-merger phase. In particular, no electromagnetic counterparts have been observed for the black hole–neutron star mergers (Abbott et al., 2021).

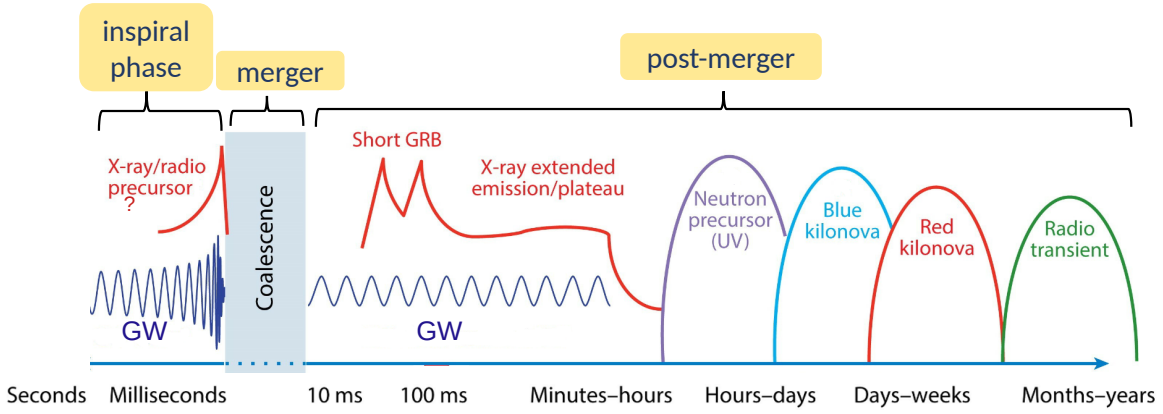

Figure 6.1: Temporal evolution of a neutron star (NS) merger, illustrating the corresponding observational signatures. Abbreviations: GRB – γ-ray burst; GW – gravitational wave. Gravitational waves have been observed both before and after the merger, whereas electromagnetic emissions have only been detected during the post-merger phase. Adapted from Fernández and Metzger (2016).

6.1.2 Precursor radiative signatures

To date, there are no confirmed electromagnetic detections preceding the coalescence of any neutron star merger. Electromagnetic emissions during the inspiral phase have been far less studied than those occurring after merger. Yet, several studies predict electromagnetic emissions prior to coalescence (e.g., see Fernández and Metzger 2016 and references therein for analytical or semi-analytical models, and Palenzuela et al. 2013; Most and Philippov 2020; Carrasco and Shibata 2020; Skiathas et al. 2025 for MHD models). Indeed, in the case of close neutron star or neutron star–black hole binaries, the interacting magnetosphere is expected to be all the more active since orbital motion adds to the intrinsic spin of each star. Nevertheless, many unknowns still remain concerning the nature of the precursor emission, such as its physical origin, whether it is thermal or not, its shape, its energy spectrum.

Modelling the expected radiation signatures is of considerable interest. Firstly, it could provide insights into the nature of the compact objects, including their physical properties prior to coalescence and their spins, as well as information about the merger event itself, such as the energies involved. Secondly, such modelling is valuable for localizing these events in the sky and could potentially serve as an early warning for the arrival of gravitational-wave signals.

6.1.3 The special case of black hole–neutron star binaries

In this study, we focus on the specific case of pulsar–black hole binaries. As mentioned before, two such systems have been detected in 2021, via gravitational waves, GW200105_162426 and GW200115_042309 (Abbott et al., 2021). So far, black hole–neutron star systems have only been observed through their mergers, since gravitational-wave detectors are sensitive only to the late inspiral and coalescence, and no black hole–neutron star binary has yet been identified electromagnetically (e.g., via pulsar timing or accretion). This is why observed black hole–neutron star systems so far always refer to merger events.

Since isolated black holes lack intrinsic magnetic fields, simulations involving them necessarily require assumptions about the origin and initial configuration of the magnetic field lines. In contrast, black hole–neutron star binaries are particularly interesting from a modeling perspective, as no assumptions are needed regarding the initial geometry of the system, the origin of the magnetic field, or the primary plasma, these being naturally provided by the neutron star. In this sense, a pulsar–black hole binary provides a well-constrained environment to probe the vicinity of a black hole.

The rotational energy of the black hole can be extracted by the neutron star's magnetic field lines, which are frozen into the magnetospheric plasma and thread the black hole's horizon. The spins of both objects (dominant at large separations) and the orbital motion (dominant near merger) twist and stretch these field lines, leading to their opening and subsequent magnetic reconnection. These reconnection events can accelerate particles and produce electron–positron pairs, potentially giving rise to precursor electromagnetic signals. The flux is expected to intensify as the two stars approach each other, since the orbital velocity increases and the binary separation decreases, causing the magnetic field strength at the black hole's horizon to grow roughly as the inverse cube of the separation (assuming a dipolar field for the neutron star).

If the black hole mass is sufficiently low and the black hole spin is sufficiently high, the system will merge without disruption of the neutron star. It is important to emphasize that, for non-disrupting black hole–neutron star binaries, magnetospheric interaction before the merger appears to be the only viable source of electromagnetic signals, highlighting the importance of studying this mechanism.

6.2 Existing models and key predictions

Several theoretical studies have investigated a unipolar induction model (see Section 2.3.1), where the black hole acts as a battery moving through the neutron star magnetic field, driving currents along connecting field lines and thus extracting energy from the system, potentially powering precursor electromagnetic signals (Hansen and Lyutikov, 2001; McWilliams and Levin, 2011; Lai, 2012; Piro, 2012; D'Orazio et al., 2016).

Since the 2010s, with the advent of numerical relativity simulations, several numerical models have been developed to study the magnetospheres of compact object binaries. Simulations of binary neutron star systems laid the groundwork for the first models of black hole–neutron star binaries, providing key insights and numerical techniques that were subsequently adapted to account for the additional complexities of black hole–neutron star systems.

Paschalidis et al. (2013) performed the first general-relativistic MHD simulations of such systems (see Figure 6.2), with an ideal MHD code reaching the force-free limit in the magnetosphere. They predict precursor electromagnetic emissions due to both the unipolar model and another energy-loss mechanism based on the orbital motion of the neutron star magnetic dipolar moment.

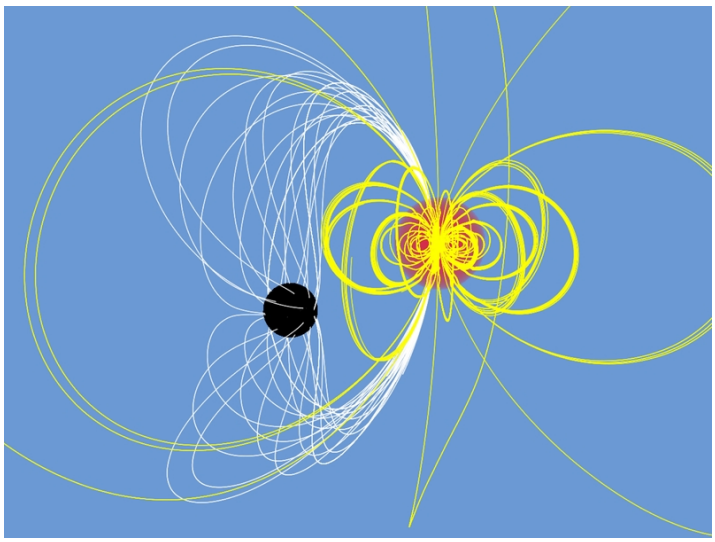

Figure 6.2: First general-relativistic MHD simulations of black hole–neutron star binaries. The neutron star (red sphere) magnetic field lines are shown in yellow, except for those threading the black hole horizon (black sphere), which are traced in white. Figure taken from Paschalidis et al. (2013).

East et al. (2021) and Most and Philippov (2023) both resort to a resistive general-relativistic MHD approach that recovers the force-free limit where appropriate (Palenzuela et al., 2013) to perform simulations of black hole–neutron star binaries. East et al. (2021) find that, additional to the unipolar inductor model emission, the intrinsic twisting of field lines in such systems leads to their opening and the appearance of reconnection layers accelerating particles and powering significant electromagnetic emission. Most and Philippov (2023) focus their study on closed magnetic flux tubes connecting the two objects, from their formation to their twisting and eruption, caused by the binary orbital motion. Based on this scenario, they predict electromagnetic precursor flaring activity, under the form of fast-radio transients and X-ray flares.

Carrasco et al. (2021) perform force-free simulations in fixed Kerr spacetime, confirming the previously mentioned results. They demonstrate the formation of large-scale current sheets, the creation of a flux-tube connecting both objects, and the emission of large-amplitude Alfvén wave perturbations (depending on the magnetic field inclination). Consequently, they

predict significant electromagnetic emissions prior to the merger, mainly powered by the binary's orbital motion. Indeed, both Carrasco et al. (2021) and Most and Philippov (2023) show that the black hole spin contributes far less to the electromagnetic luminosity than the orbital kinetic energy.

In all the previously mentioned MHD simulations, the Poynting flux is used to infer potential electromagnetic luminosities. However, predicting detectable signals requires modeling the microphysical processes responsible for dissipation, particularly in regions such as current sheets. To more accurately quantify the energy transfer between rotational power, electromagnetic power, and the kinetic energy of the magnetospheric plasma, so as to ultimately predict non-thermal electromagnetic emission, we must turn to PIC simulations.

6.3 Off-center pulsar on a spherical grid

To simulate a black hole–neutron star binary, we employ two specific configurations of the `Zeltron` code: a flat spacetime version in spherical coordinates displaying a central pulsar (Cerutti et al., 2013; Cerutti and Werner, 2019), and a general-relativistic version in Kerr spacetime, featuring a central black hole (Parfrey et al., 2019; Crinquand et al., 2021). Our objective is to merge these into a single, unified framework. More precisely, we aim to implement a pulsar into the general-relativistic `Zeltron` code, in orbit around the black hole, so as to preserve the Kerr metric in spherical coordinates. However, the code that includes the pulsar is inherently structured with the pulsar positioned at the center of the spherical grid. Consequently, relocating the pulsar off-center represents a significant numerical step in the implementation of the binary. This numerical work is carried out using the same 2D equatorial version of the `Zeltron` code as that employed in Chapter 4, and thus assuming flat spacetime. The original central pulsar now acts as the companion, serving as a proxy for the future black hole, while the previous companion is replaced by a pulsar. The current section outlines the main components of this numerical implementation, along with the challenges faced during its development. The forthcoming steps for the binary implementation, which remain to be completed, are presented in Section 6.4.

We define two reference frames: the first frame ($\mathcal{R}$), associated with the coordinates (r, θ, ϕ) and centered at the origin of the grid; and the second frame ($\mathcal{R}'$), defined by (r', θ', ϕ') and centered on the pulsar, whose center position is given by $(r_{\rm c,pulsar}, \theta_{\rm c,pulsar}, \phi_{\rm c,pulsar})$ (see Figure 6.3). The coordinate transformation between the two frames reads:

$$r' = \sqrt{(r\cos\phi - r_{\rm c,pulsar}\cos\phi_{\rm c,pulsar})^2 + (r\sin\phi - r_{\rm c,pulsar}\sin\phi_{\rm c,pulsar})^2}\,, \tag{6.1}$$

$$\theta' = \theta = \pi/2\,, \tag{6.2}$$

$$\phi' = \arctan\left(\frac{r\sin\phi - r_{\rm c,pulsar}\sin\phi_{\rm c,pulsar}}{r\cos\phi - r_{\rm c,pulsar}\cos\phi_{\rm c,pulsar}}\right)\,. \tag{6.3}$$

6.3.1 Electromagnetic fields implementation

We begin by implementing the electromagnetic fields. Due to the 2D equatorial setup considered, we adopt a split monopole configuration (see Section 2.3.3). Therefore, we impose the following magnetic field at $t = 0$:

$$\mathbf{B} = B_\star\left(\frac{r_\star}{r'}\right)\mathbf{e}'_r \tag{6.4}$$

$$= B_\star\left(\frac{r_\star}{r'}\right)^2(\cos\phi'\cos\phi + \sin\phi'\sin\phi)\,\mathbf{e}_r + B_\star\left(\frac{r_\star}{r'}\right)^2(-\cos\phi'\sin\phi + \cos\phi\sin\phi')\,\mathbf{e}_\phi\,, \tag{6.5}$$

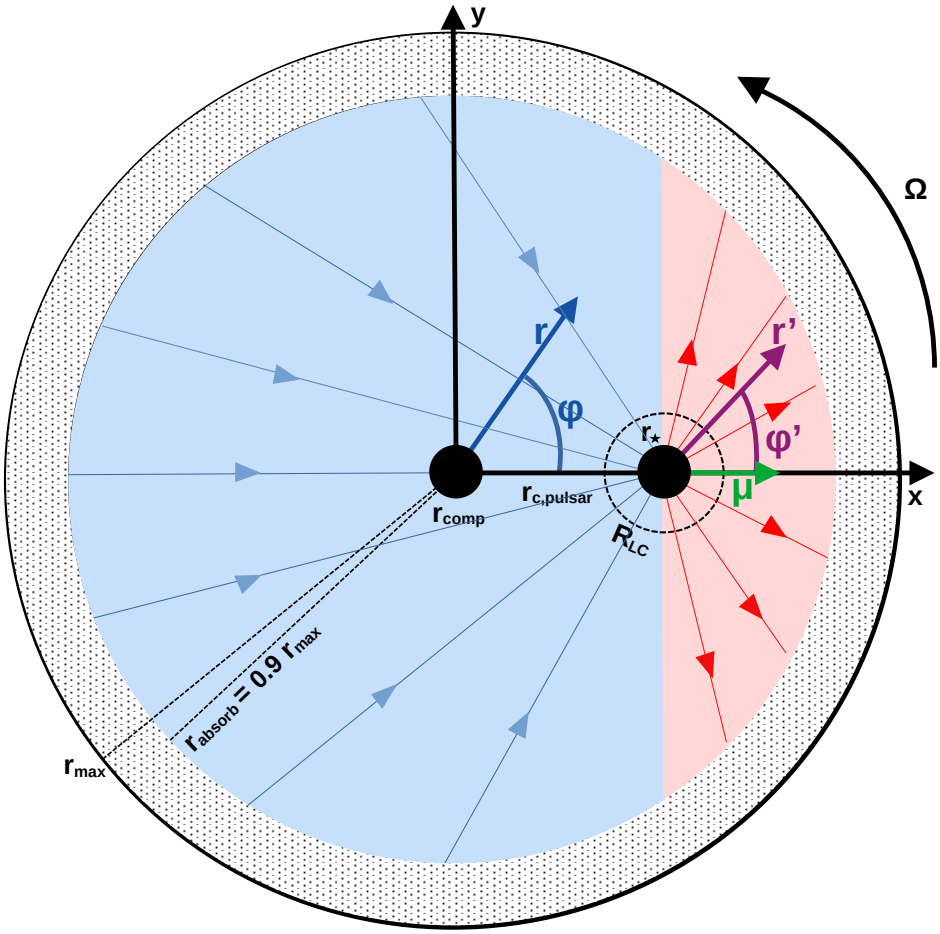

Figure 6.3: Initial numerical configuration. The pulsar, with radius $r_\star$, is offset from the center of the spherical simulation domain, which is defined in the reference frame $\mathcal{R}$ with coordinates (r, ϕ) centered at the origin. We introduce a second reference frame, $\mathcal{R}'$, with coordinates (r', ϕ') centered on the pulsar. The simulation domain extends to a radius $r_{\rm max}$, with an absorbing layer applied at $r_{\rm absorb} = 0.9\ r_{\rm max}$. A companion body of radius $r_{\rm comp}$ is placed at the center of the mesh. The domain is initially devoid of particles. Magnetic field lines (indicated by blue and red arrows) follow a split-monopole geometry: they are radially outward in one hemisphere (light red region) and radially inward in the other (light blue region). The hemispheres are separated by a plane orthogonal to the magnetic moment vector μ (green arrow) and parametrized by $\phi' = \Omega t \pm \pi/2$, where $\mathbf{\Omega}$ is the spin velocity of the pulsar. The light-cylinder radius $R_{\rm LC}$ is marked by a black dashed circle.

where $r_\star$ denotes the pulsar radius, and $B_\star$ the surface polar magnetic field. The magnetic field reverses across the two hemispheres: $\mathbf{B} \to -\mathbf{B}$. The pulsar rotates at an angular speed of $\Omega = c/R_{\rm LC}$, where $R_{\rm LC}$ is the light-cylinder radius. Hence, the plane separating the two hemispheres, across which the fields reverse, is defined by

$$r\cos(\Omega t - \phi) - r_{\rm c,pulsar}\cos(\Omega t - \phi_{\rm c,pulsar}) = 0\,. \tag{6.6}$$

For the centered pulsar configuration, we enforce the split monopole conditions at the pulsar boundary at every timestep. In the offset configuration, we also prescribe, at each timestep, the split monopole solution at the neutron star surface. Contrary to the configuration where the pulsar is located at the center of the mesh, its radius then defining the inner boundary of the simulation box, in this case the interior of the neutron star is included within the simulation domain. We must therefore prescribe the electromagnetic fields inside the star (i.e., at $r < r_\star$). However, we notice that enforcing all the electromagnetic field components inside the neutron star at each timestep prevents the expected inspiral split monopole solution to develop properly. Based on similar findings, Crinquand et al. (2019) noted that allowing an additional degree of freedom by letting B_ϕ evolve freely resolves the issue. In practice, we therefore impose all components except B_ϕ inside the pulsar, which proves to be satisfactory. To initiate the rotation of the magnetic field lines at $t = 0$, we additionnaly impose a corotating poloidal electric field at the pulsar surface:

$$E_\theta(r,\phi) = -\frac{r'}{R_{\rm LC}} B_\star \left(\frac{r_\star}{r'}\right)^2\,, \tag{6.7}$$

with the sign reversal across the two hemispheres and with $r'(r,\phi)$ given by Eq. (6.1). The stationary full split monopole solution in the $(\mathcal{R}')$ frame is given by Eqs. (2.71). After a coordinate transformation, the corresponding expressions in the $(\mathcal{R})$ frame are:

$$\begin{aligned}
B_r(r,\phi) &= B_\star \left(\frac{r_\star}{r'}\right)^2 (\cos\phi'\cos\phi + \sin\phi'\sin\phi) && (6.8)\\
&\quad -\frac{B_\star r_\star^2 \Omega \sin\theta}{rc}(-\sin\phi'\cos\phi + \cos\phi\sin\phi') && (6.9)\\
B_\theta(r,\phi) &= B'_\theta = 0 && (6.10)\\
B_\phi(r,\phi) &= B_\star \left(\frac{r_\star}{r}\right)^2 (-\cos\phi'\sin\phi + \sin\phi'\cos\phi) && (6.11)\\
&\quad -\frac{B_\star {r_\star}^2 \Omega}{r'c}(\sin\phi'\sin\phi + \cos\phi'\cos\phi) && (6.12)\\
E_r(r,\phi) &= 0 && (6.13)\\
E_\theta(r,\phi) &= B_\phi && (6.14)\\
E_\phi(r,\phi) &= 0\,. && (6.15)
\end{aligned}$$

Here again, the field reverses sign across the two hemispheres.

6.3.2 Particles injection

We inject particles from the stellar surface. In the centered version of the code, particles are injected in each θ cell around the surface, with a radial position uniformly distributed between $r_\star$ and $r_\star + {\rm d}r$ (where ${\rm d}r$ is the radial size of the first cell from the star surface), and an angular position uniformly distributed within the cell. In the offset pulsar configuration, since the pulsar interior is included in the simulation domain, we prescribe particle injection throughout the entire disk enclosed by the pulsar surface, i.e., for $r' < r_\star$. To prevent overinjection, which could excessively screen the electric field at the pulsar boundary, we clear the pulsar interior at each timestep before injecting new particles.

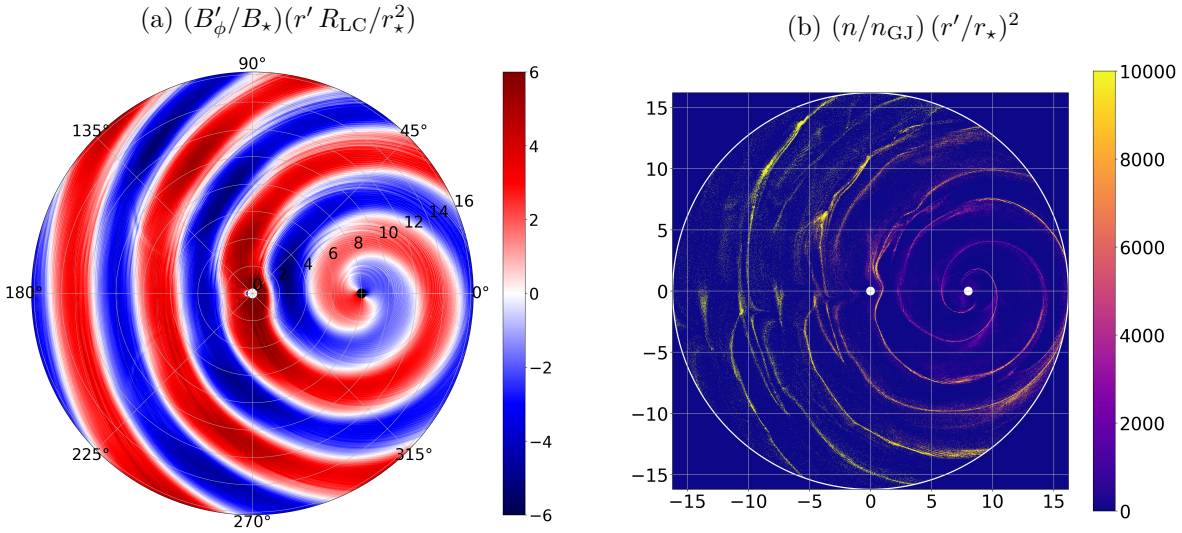

Figure 6.4: Toroidal magnetic field (left panel) and particle's density (right panel) evaluated in the $(\mathcal{R}')$ frame at $t = 5.3\ P_{\rm spin}$. The central white disk represents the absorbing companion while the disk located at 8 $R_{\rm LC}$ illustrates the pulsar. In the right panel, the white circle marks the boundary of the simulation domain. Radii are given in units of the light-cylinder radius.

We carried out several tests to determine the optimal particle injection prescription. In particular, we tried injecting particles within a thin layer around the pulsar surface, with the layer thickness ranging from 100 dr down to 5 dr and d$r = 2.6 \times 10^{-2}\, r_\star$. We found that the thinnest layer favored the best current sheet formation. However, injecting throughout the entire pulsar interior after cleaning particles at each timestep proved even more satisfactory. We are currently testing another injection prescription based on volumetric injection between $r_\star$ and 2 $R_{\rm LC}$, combined with a magnetization threshold ($\sigma_{\rm min}$). This approach allows particle pairs to be injected only in sufficiently magnetized regions, which are favorable for particle acceleration and pair creation, while avoiding overinjection in already dense areas.

Regardless of the particle injection prescription, we face several challenges due to the spherical structure of the grid. In particular, an asymmetry systematically arises between the pulsar boundaries facing the inner and outer edges of the simulation domain. Increasing the grid resolution helps reduce this issue to a reasonable level. Moreover, we observe some noise in the particle density, especially near the inner edge of the simulation box. This noise appears to be reduced when increasing the number of injected particles per cell. Contrary to the centered pulsar configuration, where the mesh is logarithmically spaced in radius, we prescribe a uniform radial spacing of the cells to reduce the asymmetry between different sides of the pulsar surface. With logarithmic radial spacing, we observe the formation of a potential barrier for particles near $r_{\rm min}$. When switching to a uniform radial spacing, this initially empty region around $r_{\rm min}$ becomes properly populated again.

We impose absorbing boundary conditions for both particles and fields at the surface of the central companion. Figure 6.4 shows the toroidal magnetic field (B'_ϕ) and the particle density, evaluated in the $(\mathcal{R}')$ frame at $t = 5.3\ P_{\rm spin}$. We recover the two inspiral branches of the current sheet and the stripes of alternating polarity, centered on the offset pulsar located at ($r_{\rm c,pulsar} = 8\ R_{\rm LC}$ and $\phi_{\rm c,pulsar} = 0$). The density plots also feature the two branches of the current sheet, as expected. As observed in Chapter 4, the current sheet bends when approaching the companion's surface. We present here the best solution obtained to date. However, some points still merit further investigation, such as the absence of clear plasmoids

and the presence of secondary current sheet branches. Both of these issues could possibly be resolved by increasing the number of particles per cell and by increasing the resolution.

6.4 Next steps towards binary implementation

In the following, we present a brief outline of the next steps required for the binary implementation.

- Implementation of the pulsar in the black hole magnetosphere: we aim to integrate the off-center pulsar in the general-relativistic version of the `Zeltron` code, displaying a central black hole. By construction, this code uses an axisymmetric and stationary Kerr metric, therefore excluding any perturbation, in particular gravitational waves, and neglecting the neutron star curvature. The code adopts the 3+1 formalism and the spherical Kerr-Schild coordinates (MacDonald and Thorne, 1982; Komissarov, 2004). For numerical reasons, we set $r_\star = r_{\rm BH}$, where $r_{\rm BH} = 2GM_{\rm BH}/c^2$ is the Schwarzschild radius of the black hole and $M_{\rm BH}$ denotes its mass. Indeed, the black hole radius determines the grid scale and should not be too large compared to the grid resolution Δr. Conversely, the pulsar radius must be sufficiently larger than Δr to be well resolved at its surface, which is especially important for particle injection, as previously mentioned. The simulation domain typically extends up to 15 $r_{\rm g}$, where $r_{\rm g} = 0.5\ r_{\rm BH}$ is the gravitational radius. We need to maintain sufficient distance between the pulsar and the black hole to allow the pulsar wind to form (including stripe formation), while also ensuring enough space beyond the pulsar to observe the magnetosphere's rearrangement and to assess the radiation processes involved. Consequently, we plan to keep orbital separations ranging from 3 to 6 $r_{\rm g}$. This means the black hole is effectively smaller and the pulsar is closer than in realistic astrophysical scenarios. Tidal effects are neglected in this study.

- Black hole spin parameter study: we aim to explore the impact, on the binary system, of the black hole's dimensionless Kerr spin parameter $a_{\rm BH} = J_{\rm BH}c/GM_{\rm BH}^2$, where $J_{\rm BH}$ is the black hole angular momentum. We plan to simulate the two limiting cases and the intermediate state: $a = 0$ for a Schwarzschild black hole, $a = 0.5$ and $a = 1$ for a maximally rotating black hole.

- Orbital motion implementation: after studying the fixed binary system, we aim to set the pulsar in motion around the black hole. We perform a change of the coordinate system to work in the corotating reference frame. This approach corresponds to introducing an additional β^ϕ term in the shift vector of the metric, to account for the Keplerian orbital velocity of the pulsar. By doing so, the coordinate system effectively rotates with the pulsar's orbital motion, allowing us to describe the system in the corotating frame without physically displacing the objects or the grid.

- Non-stationary orbital separation: although the `Zeltron` code does not yet model gravitational wave emission, we can estimate the associated energy losses and prescribe the corresponding decrease in orbital separation.

- Post-processing synchrotron analysis: photons emitted by synchrotron processes are saved by the simulation and propagated afterward via the `GeoKerr` module of the `Zeltron` code (Crinquand et al., 2021). Once the photons are extracted from the simulation output, the regions responsible for non-thermal emission can be identified, and the underlying kinetic processes leading to such emission can be characterized.

Conclusion and perspectives

Throughout this thesis, we tackled the fundamental yet complex subject of relativistic magnetospheres in binary systems, with a pulsar as the primary source of the magnetospheric interaction. Dramatic progress in the modeling of relativistic magnetospheres has been achieved over the last decades, primarily driven by the development of numerical approaches. Among these, the PIC approach has emerged as a preferred tool for conducting such studies, owing to its ability to capture both the global dynamics and the kinetic processes of the magnetosphere, which are intrinsically linked despite operating on very different temporal and spatial scales. Isolated compact-object environments are now increasingly well constrained, although some key questions remain unresolved to date. It is therefore timely to investigate their interaction with a companion within a binary system, a configuration that applies to a significant fraction of known objects. Understanding the high-energy phenomena originating from such systems requires modelling the global magnetospheric dynamics, as well as identifying and localizing the particle acceleration mechanisms at play, in order to ultimately predict the resulting emissions. In this thesis, we focused on the electromagnetic emission generated by such systems.

To adress this problem, we selected three case studies that exemplify the diversity of pulsar binary systems. In Chapter 4, we provided the first kinetic model of the interaction between a pulsar wind and a small, spherical and perfectly conducting companion, through 2D equatorial PIC simulations. This generic case has applications to pulsar – planet or pulsar – asteroid systems and serves as a proxy for modelling compact-object binaries, such as pulsar–white dwarf and pulsar–neutron star systems. We highlighted the role of the companion's position relative to the fast magnetosonic point in the shaping of the global magnetosphere and in the establishment of a shock. Moreover, we showed that, regardless of the companion's separation, the impact of the pulsar's current sheet on the companion's surface forces magnetic reconnection, resulting in a significant enhancement of particle acceleration. The successive spiral arms of the current sheet, upon hitting the companion's surface, divide on either side of the spherical body, forming two radial branches that surround the companion. Accelerated particles thereby emit synchrotron radiation in the form of an orbitally modulated hollow cone of light, whose intensity and aperture decrease with orbital separation and increase with the companion's size. This additional non-thermal emission greatly exceeds the pulsed synchrotron flux from an isolated pulsar magnetosphere and is expected to lie in the hard X-ray to soft gamma-ray band. Additionally, we predicted possible associated radio counterparts based on the significant triggering of fast magnetosonic modes in the companion's wake and on previous studies showing that such modes can escape as radio waves in a pulsar magnetosphere. These counterparts are naturally modulated over the orbital period, thereby providing a plausible scenario for long-period radio transients. This scenario is particularly relevant in the light of the recent detection of higher-energy counterparts to such transients, suggesting a common – or at least related – underlying mechanism, in contrast to the usual dichotomy between radio and gamma-ray emission processes in pulsar magnetospheres.

In contrast to systems with small or compact companions, interactions between a pulsar and a main-sequence star can result in the formation of a disk of matter around the pul-

sar. Chapter 5 is devoted to the study of the interaction between a pulsar wind and such a disk, where accretion is neglected. With 3D PIC simulations, we showed how the pulsar wind reconfigurates in the presence of the disk. We demonstrated that the pulsar's striped wind interaction with the inner edge of the disk induces an accumulation of plasma before its inner boundary, a strengthening of the magnetic field due to the confinement of magnetic field lines, an isotropization of the plasma and an enhancement of particle acceleration. The combination of all these effects leads to a substantial increase of non-thermal electromagnetic emission, through synchrotron radiation. In particular, the modeled light curves present a strong continuous component and either one or two broad peaks per pulsar's rotation period, depending on the pulsar's magnetic obliquity, for a given disk aspect ratio. Moreover, we predicted a depolarization of the signal with respect to isolated pulsar magnetospheres, along with an increase in both the polarization angle variation and the polarization degree with energy. This study is particularly relevant for transitional millisecond pulsars, systems with a main-sequence companion star that alternate between rotation-powered and accretion-powered states, featuring a third, intermediate state in which a disk is present without clear evidence of accretion. Our model successfully reproduces, for the first time, the optical and X-ray pulsations detected from the transitional millisecond pulsar PSR J1023+0038. It is also compatible with the associated polarization measurements.

Finally, we initiated the development of a numerical framework for modeling pulsar–black hole binaries, with the ultimate goal of simulating their electromagnetic emission in the pre-merger phase. To this end, we implemented an offset pulsar in the 2D spherical, flat-spacetime version of the `Zeltron` code, which was originally designed to place the pulsar at the center of the simulation domain. Offsetting the pulsar within the spherical grid introduced numerous numerical challenges, primarily due to the grid's asymmetry at the pulsar surface and to the inclusion of the stellar interior within the simulation domain, unlike in the centered configuration, where the inner boundary of the box coincides with the pulsar surface. We therefore carried out several tests to identify the most suitable prescriptions for the implementation of electromagnetic fields and particle injection.

This thesis work lays the groundwork for a number of follow-up investigations. First, it opens the way to the modeling of long-period radio transients. While Chapter 4 reports the manifest emission of fast magnetosonic modes in the presence of the companion, possibly exiting the wind as radio waves, we do not proceed to the quantification of the radio counterparts. Such quantification would deserve a dedicated study. Indeed, the isolation of the radio emission with respect to the background low-frequency emission is not trivial. One way to capture this effect would be to compute the general Stokes parameters defined on the simulation grid, using the Fourier decomposition technique presented in Robishaw and Heiles (2021) and recently applied by Benáček et al. (2025) to model radio emission from pulsar polar caps.

Moreover, the setup presented in Chapter 4 would benefit from being extended to 3D, as the mechanism identified in our study, responsible for particle acceleration, synchrotron emission and the formation of fast magnetosonic modes, is intrinsically linked to the confinement of magnetic field lines and of the current sheet ahead of the companion. This confinement could be partly altered when a third dimension is included. Additionnally, moving to 3D would allow us to probe other latitudes, especially those not reached by the striped wind, which are exclusively characterized by opened field lines and lack a current layer. Placing the companion at such latitudes could enable us to verify whether Alfvén wings form, as predicted by Mottez et al. (2020) in the context of modelling repeating fast radio bursts.

A new class of peculiar systems, known as "white dwarf pulsars", has been discovered over the past decade. These are non-accreting binary systems composed of a white dwarf in interaction with a low-mass companion star, and exhibiting pulsations from radio to X-rays that are modulated by the orbital motion of the companion. To date, only three such systems

have been identified. The first discovered and prototype of this class is AR Scorpii, a white dwarf − M dwarf binary which exhibits coherent radio pulsations together with higher-energy counterparts. AR Scorpii displays pulsations with a 1.97-minute period, corresponding to the white dwarf's spin, and a 3.56-hour modulation due to the orbital motion. Its emission is believed to be powered by the white dwarf's spin-down and to originate from synchrotron radiation produced by relativistic particles. Interestingly, this past year, two of the twelve confirmed long-period radio transients (LT J1101+5521 and GLEAM−X J0704−37) have been identified as originating from white dwarf − M dwarf binaries, in which the white dwarf's spin appears to be synchronized with the orbital motion (i.e., polars). Hence, it would be timely to model such white dwarf - M dwarf systems by replacing the central pulsar with a white dwarf and the offset companion by the red dwarf. This substitution would imply several fundamental changes compared to the current pulsar setup. Indeed, in the case of a white dwarf, the magnetospheric plasma is predominantly supplied by the companion. The physical regime would be drastically different, as the plasma would be moderately magnetized and relativistic, implying the suppression of pair creation. Instead, an ion-electron plasma should be injected from the companion's surface.

In both white dwarf pulsars and binary scenarios proposed for long-period radio transients, the companion is expected to lie within the light cylinder, given the observed orbital periods. This differs from the regime investigated in Chapter 4. In a separate study, we began investigating such close binary systems composed of a central pulsar and an orbiting companion. We used a 2D axisymmetric poloidal (r–z plane) version of the `Zeltron` code, featuring a central pulsar to which we added a perfectly conducting torus as a proxy for the spherical companion star. We carried out a parametric study varying the orbital speed relative to the intrinsic pulsar spin, so as to explore three regimes: no rotation ($\Omega_{\rm orb} = 0$ rad.s^{-1}), corotation ($\Omega_{\rm orb} = \Omega_{\rm spin}$), and super-rotation ($\Omega_{\rm orb} = 2\,\Omega_{\rm spin}$). Long-period radio transients would correspond to the corotation case, while white dwarf pulsars would correspond to an under-rotation scenario. Figure 6.5 illustrates how the topology of the magnetic field lines is affected by the companion. Colors indicate the toroidal magnetic field (B_ϕ), which provides insight intothe pulsar spin-down, since $L \propto B_\phi^2$ away from the pulsar surface. When orbital motion is negligible compared to the spin, the Y-shaped reconnection layer forms much farther from the central object than in the isolated case, which induces the broadening of the equatorial current sheet. In the corotation regime, the pulsar spin-down is reduced due to the reduction of open poloidal field lines. Conversely, the super-rotation regime significantly increases the intensity of B_ϕ and exhibits a magnetic field reversal on both sides of the usual reconnection zone. This arises from the faster rotation of field lines attached to the conductor's surface compared to the open field lines, giving rise to three current sheets. In light of these results on the global structure of the magnetosphere, the next step would now consist of studying the corresponding observational signatures.

Chapter 4 explores the interaction between a pulsar and a spherical companion, small enough to fit between two stripes of the pulsar wind. This configuration excludes the regime of spider pulsars, whose companion star is much larger than the stripe wavelength. The spider pulsar regime has been studied through PIC simulations by Cortés and Sironi (2024, 2025), where a plane-parallel striped wind is launched towards a companion star. Although their simulations also produce double-peaked light curves similar to those obtained in our work, with enhanced electromagnetic emission arising from particles accelerated through reconnection, their global magnetospheric structure differs markedly. In their case, particle acceleration results primarily from shock-driven reconnection. It would therefore be relevant to increase the size of our spherical companion to observe the transition between both regimes and verify that, in the spider regime, we recover the results of Cortés and Sironi (2025). In particular, including the pulsar itself within the simulation domain, and thus generating the pulsar wind self-consistently from first principles, would introduce a radial component to the pulsar wind

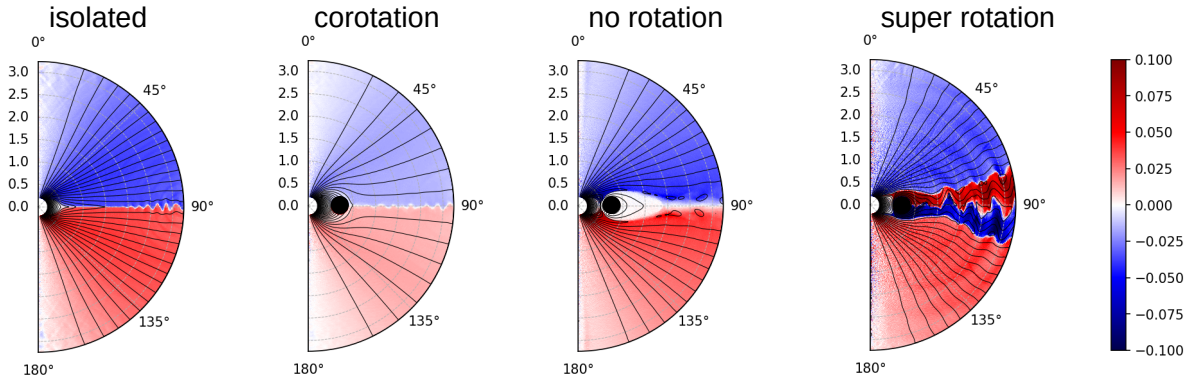

Figure 6.5: Maps of the toroidal magnetic field $(B_\phi/B_\star)(r/r_\star)$ at $t/P_{\rm spin} = 5.62$, for the isolated pulsar and for cases including a conducting torus, shown for all three rotational regimes. The black disk represents the companion. Black solid lines represent the poloidal magnetic field lines, while the color bar indicates the strength of the toroidal component. The radial extent of the simulation box is expressed in units of the light-cylinder radius ($R_{\rm LC}$). The addition of the torus alters the magnetic field structure differently depending on the rotation speed of the conductor.

that is suppressed in their plane-parallel approximation. We may then wonder whether this radial component could induce further asymmetry between the light-curve peaks. Regarding pulsar planets, to our knowledge, all confirmed detections so far involve millisecond pulsars, for which the stripe wavelength is theoretically smaller than the typical size of planets or compact companions. Notably, no planets have been detected around young pulsars. This may indicate that planet formation is more favorable around older pulsars, since pulsar planets in the Galactic field are thought to either form after the supernova explosion or survive it if they were already present beforehand (Kerr et al., 2015). Nonetheless, current evolutionary scenarios do not exclude the existence of planets around pulsars with longer spin periods, which could therefore fit between successive stripes of the pulsar wind. Future observational campaigns may therefore reveal such systems in the coming years.

None of the setups presented in this thesis include ions. Indeed, since we focused on non-thermal electromagnetic emissions, pair plasma dominates the emission. Nevertheless, from a multi-messenger perspective, one may ask whether the interaction between the pulsar wind and a companion could enhance cosmic-ray energies. Previous studies indicate that millisecond pulsars are expected to accelerate protons up to PeV energies, or even to ultra-high energies in the case of newly born millisecond pulsars (Guépin et al., 2020). It is therefore plausible that the presence of a companion could provide an additional energy boost, particularly if the companion is sufficiently massive (e.g., in spider systems).

The study presented in Chapter 5 represents a first major step in the kinetic modeling of transitional millisecond pulsars. The promising results obtained open the way for further developments of this approach. Priority directions for future work include assessing the impact of the disk's distance and aspect ratio, investigating the potential feedback of the produced emission on the companion star, and characterizing the interaction between the pulsar wind and the disk plasma populations, the latter being currently explored through MHD simulations. It would also be of particular interest to evaluate the role of inverse Compton scattering in the global emission. In particular, such systems constitute promising candidates for TeV emission arising from the inverse Compton scattering of UV photons by particles accelerated to TeV energies. Indeed, a TeV component due to inverse Compton scattering has already been detected in isolated systems such as the Crab and Vela pulsars (Ansoldi et al., 2016; H. E. S. S. Collaboration et al., 2023). Since transitional millisecond pulsars are shown to

emit substantially more UV flux, the corresponding TeV component produced via inverse Compton scattering is expected to be significantly enhanced. Expanding the sample of this peculiar class of systems and obtaining more comprehensive polarization data will be essential to further constrain their physical properties.

Among compact-object binaries, Chapter 6 focuses specifically on pulsar–black hole systems. However, this work also lays the groundwork for the modeling of binary neutron stars. In particular, although Chapter 6 modifies the properties of the central object in the perspective of a black-hole replacement, retaining the initial central pulsar and adding the offset pulsar to the simulation domain can be used to simulate a double pulsar system. To date, such a setup has never been implemented in fully 3D PIC models, although a simplified 2D model with aligned magnetic moments and rotation axes, hence neglecting orbital motion, has been proposed by Crinquand et al. (2019). Other models have been developed within the force-free electrodynamics framework, such as those by Most and Philippov (2020) and Skiathas et al. (2025).

Current and upcoming wide-field, high-sensitivity observatories dedicated to time-domain astronomy will drastically increase the number of detected transients. Among these are MeerKAT and SKA operating at radio frequencies, LSST at optical wavelengths, Athena, IXPE and the Einstein probe in the X-ray band, CTA, SVOM and LHAASO in the gamma-rays domain. In a multi-messenger perspective, the current LIGO-Virgo-Kagra network, dedicated to gravitational wave detection, will be folllowed by the next-generation facilities such as the Einstein Telescope, Cosmic Explorer, and LISA. For high-energy neutrinos, new and forthcoming observatories include IceCube-Gen2, KM3NeT, and GRAND, while HAWC, the Pierre Auger observatory and the Telescope Array and will search for (ultra-)high-energy cosmic rays. In this context, our models predict specific observational signatures that forthcoming observatories will be able to probe, thereby offering new prospects for identifying and characterizing high-energy transients. Concurrently, ongoing numerical developments, such as the coupling of kinetic and fluid approaches to address scale separation and the porting of codes to GPU-based architectures, are laying the foundation for more accurate and energy-efficient models of high-energy astrophysical phenomena.

Although numerical simulations are still often employed to address theoretical questions, this thesis has convinced me of their crucial role in supporting observational astrophysics, both in making predictions and in interpreting data. Building on these first results, I hope to contribute to unveiling and deciphering new cosmic signals by harnessing the synergy between observations and numerical modeling.

Bibliography

B. P. Abbott et al. GW170817: Observation of Gravitational Waves from a Binary Neutron Star Inspiral. *Phys. Rev. Lett.*, 119(16):161101, Oct. 2017. doi: 10.1103/PhysRevLett.119.161101.

R. Abbott et al. Observation of Gravitational Waves from Two Neutron Star-Black Hole Coalescences. *ApJ*, 915(1):L5, July 2021. doi: 10.3847/2041-8213/ac082e.

R. Abbott et al. Population of Merging Compact Binaries Inferred Using Gravitational Waves through GWTC-3. *Physical Review X*, 13(1):011048, Jan. 2023. doi: 10.1103/PhysRevX.13.011048.

Abhishek, N. Malusare, N. Tanushree, G. Hegde, and S. Konar. Radio pulsar sub-populations (II): The mysterious RRATs. *Journal of Astrophysics and Astronomy*, 43(2):75, Dec. 2022. doi: 10.1007/s12036-022-09862-3.

M. Abraham. Prinzipien der dynamik des elektrons. *Annalen der Physik*, 315:105 – 179, 03 1902. doi: 10.1002/andp.19023150105.

M. Abraham. Zur theorie der strahlung und des strahlungsdruckes. *Annalen der Physik*, 319: 236 – 287, 03 1904. doi: 10.1002/andp.19043190703.

F. Acernese et al. Advanced Virgo: a second-generation interferometric gravitational wave detector. *Classical and Quantum Gravity*, 32(2):024001, Jan. 2015. doi: 10.1088/0264-9381/32/2/024001.

S. Akiyama, J. C. Wheeler, D. L. Meier, and I. Lichtenstadt. The Magnetorotational Instability in Core-Collapse Supernova Explosions. *ApJ*, 584(2):954–970, Feb. 2003. doi: 10.1086/344135.

E. Amato. The theory of Pulsar Wind Nebulae: recent progress. *arXiv e-prints*, art. arXiv:2001.04442, Jan. 2020. doi: 10.48550/arXiv.2001.04442.

F. Ambrosino, A. Papitto, L. Stella, F. Meddi, P. Cretaro, L. Burderi, T. Di Salvo, G. L. Israel, A. Ghedina, L. Di Fabrizio, and L. Riverol. Optical pulsations from a transitional millisecond pulsar. *Nature Astronomy*, 1:854–858, Oct. 2017. doi: 10.1038/s41550-017-0266-2.

F. Ambrosino, A. Miraval Zanon, A. Papitto, F. Coti Zelati, S. Campana, P. D'Avanzo, L. Stella, T. Di Salvo, L. Burderi, P. Casella, A. Sanna, D. de Martino, M. Cadelano, A. Ghedina, F. Leone, F. Meddi, P. Cretaro, M. C. Baglio, E. Poretti, R. P. Mignani, D. F. Torres, G. L. Israel, M. Cecconi, D. M. Russell, M. D. Gonzalez Gomez, A. L. Riverol Rodriguez, H. Perez Ventura, M. Hernandez Diaz, J. J. San Juan, D. M. Bramich, and F. Lewis. Optical and ultraviolet pulsed emission from an accreting millisecond pulsar. *Nature Astronomy*, 5:552–559, June 2021. doi: 10.1038/s41550-021-01308-0.

B. C. Andersen et al. Sub-second periodicity in a fast radio burst. *Nature*, 607(7918):256–259, July 2022. ISSN 1476-4687. doi: 10.1038/s41586-022-04841-8. URL http://dx.doi.org/10.1038/s41586-022-04841-8.

S. Ansoldi et al. Teraelectronvolt pulsed emission from the Crab Pulsar detected by MAGIC. *A&A*, 585:A133, Jan. 2016. doi: 10.1051/0004-6361/201526853.

J. Antoniadis, P. C. C. Freire, N. Wex, T. M. Tauris, R. S. Lynch, M. H. van Kerkwijk, M. Kramer, C. Bassa, V. S. Dhillon, T. Driebe, J. W. T. Hessels, V. M. Kaspi, V. I. Kondratiev, N. Langer, T. R. Marsh, M. A. McLaughlin, T. T. Pennucci, S. M. Ransom, I. H. Stairs, J. van Leeuwen, J. P. W. Verbiest, and D. G. Whelan. A massive pulsar in a compact relativistic binary. *Science*, 340(6131), Apr. 2013. ISSN 1095-9203. doi: 10.1126/science.1233232. URL http://dx.doi.org/10.1126/science.1233232.

A. Anumarlapudi, D. L. Kaplan, N. Rea, N. Erasmus, D. Kelson, S. K. Ocker, E. Lenc, D. Dobie, N. Hurley-Walker, G. Sivakoff, D. A. H. Buckley, T. Murphy, J. Pritchard, L. Driessen, K. Rose, and A. Zic. ASKAP J144834-685644: a newly discovered long period radio transient detected from radio to X-rays. *MNRAS*, 542(2):1208–1232, Sept. 2025. doi: 10.1093/mnras/staf1227.

A. M. Archibald, I. H. Stairs, S. M. Ransom, V. M. Kaspi, V. I. Kondratiev, D. R. Lorimer, M. A. McLaughlin, J. Boyles, J. W. T. Hessels, R. Lynch, J. van Leeuwen, M. S. E. Roberts, F. Jenet, D. J. Champion, R. Rosen, B. N. Barlow, B. H. Dunlap, and R. A. Remillard. A Radio Pulsar/X-ray Binary Link. *Science*, 324(5933):1411, June 2009. doi: 10.1126/science.1172740.

A. M. Archibald, S. Bogdanov, A. Patruno, J. W. T. Hessels, A. T. Deller, C. Bassa, G. H. Janssen, V. M. Kaspi, A. G. Lyne, B. W. Stappers, S. P. Tendulkar, C. R. D'Angelo, and R. Wijnands. Accretion-powered Pulsations in an Apparently Quiescent Neutron Star Binary. *ApJ*, 807(1):62, July 2015. doi: 10.1088/0004-637X/807/1/62.

I. Arka and G. Dubus. Pulsed high-energy γ-rays from thermal populations in the current sheets of pulsar winds. *A&A*, 550:A101, Feb. 2013. doi: 10.1051/0004-6361/201220110.

J. Arons. Pulsar Wind Nebulae as Cosmic Pevatrons: A Current Sheet's Tale. *Space Sci. Rev.*, 173(1-4):341–367, Nov. 2012. doi: 10.1007/s11214-012-9885-1.

W. B. Atwood et al. The Large Area Telescope on the Fermi Gamma-Ray Space Telescope Mission. *ApJ*, 697(2):1071–1102, June 2009. doi: 10.1088/0004-637X/697/2/1071.

W. Baade and F. Zwicky. Cosmic Rays from Super-novae. *Proceedings of the National Academy of Science*, 20(5):259–263, May 1934. doi: 10.1073/pnas.20.5.259.

D. C. Backer. Pulsar Nulling Phenomena. *Nature*, 228(5266):42–43, Oct. 1970. doi: 10.1038/228042a0.

D. C. Backer, S. R. Kulkarni, C. Heiles, M. M. Davis, and W. M. Goss. A millisecond pulsar. *Nature*, 300(5893):615–618, Dec. 1982. doi: 10.1038/300615a0.

M. C. Baglio, F. Coti Zelati, S. Campana, G. Busquet, P. D'Avanzo, S. Giarratana, M. Giroletti, F. Ambrosino, S. Crespi, A. Miraval Zanon, X. Hou, D. Li, J. Li, P. Wang, D. M. Russell, D. F. Torres, K. Alabarta, P. Casella, S. Covino, D. M. Bramich, D. de Martino, M. Méndez, S. E. Motta, A. Papitto, P. Saikia, and F. Vincentelli. Matter ejections behind the highs and lows of the transitional millisecond pulsar PSR J1023+0038. *A&A*, 677:A30, Sept. 2023. doi: 10.1051/0004-6361/202346418.

M. C. Baglio, F. Coti Zelati, A. Di Marco, F. La Monaca, A. Papitto, A. K. Hughes, S. Campana, D. M. Russell, D. F. Torres, F. Carotenuto, S. Covino, D. de Martino, S. Giarratana, S. E. Motta, K. Alabarta, P. D'Avanzo, G. Illiano, M. M. Messa, A. Miraval Zanon, and N. Rea. Polarized multiwavelength emission from pulsar wind - accretion disk interaction in a transitional millisecond pulsar. *arXiv e-prints*, art. arXiv:2412.13260, Dec. 2024. doi: 10.48550/arXiv.2412.13260.

A. Bahramian, J. Strader, L. Chomiuk, C. O. Heinke, J. C. A. Miller-Jones, N. Degenaar, A. J. Tetarenko, V. Tudor, E. Tremou, L. Shishkovsky, R. Wijnands, T. J. Maccarone, G. R. Sivakoff, and S. Ransom. The maveric survey: A transitional millisecond pulsar candidate in terzan 5. *The Astrophysical Journal*, 864(1):28, Aug. 2018. ISSN 1538-4357. doi: 10.3847/1538-4357/aad68b. URL http://dx.doi.org/10.3847/1538-4357/aad68b.

X.-N. Bai and A. Spitkovsky. Modeling of Gamma-ray Pulsar Light Curves Using the Force-free Magnetic Field. *ApJ*, 715(2):1282–1301, June 2010. doi: 10.1088/0004-637X/715/2/1282.

J. Ballet, P. Bruel, T. H. Burnett, B. Lott, and T. F.-L. collaboration. Fermi large area telescope fourth source catalog data release 4 (4fgl-dr4), 2024. URL https://arxiv.org/abs/2307.12546.

E. D. Barr, A. Dutta, P. C. C. Freire, M. Cadelano, T. Gautam, M. Kramer, C. Pallanca, S. M. Ransom, A. Ridolfi, B. W. Stappers, T. M. Tauris, V. Venkatraman Krishnan, N. Wex, M. Bailes, J. Behrend, S. Buchner, M. Burgay, W. Chen, D. J. Champion, C.-H. R. Chen, A. Corongiu, M. Geyer, Y. P. Men, P. V. Padmanabh, and A. Possenti. A pulsar in a binary with a compact object in the mass gap between neutron stars and black holes. *Science*, 383(6680):275–279, Jan. 2024. ISSN 1095-9203. doi: 10.1126/science.adg3005. URL http://dx.doi.org/10.1126/science.adg3005.

C. G. Bassa, A. Patruno, J. W. T. Hessels, E. F. Keane, B. Monard, E. K. Mahony, S. Bogdanov, S. Corbel, P. G. Edwards, A. M. Archibald, G. H. Janssen, B. W. Stappers, and S. Tendulkar. A state change in the low-mass X-ray binary XSS J12270-4859. *MNRAS*, 441(2):1825–1830, June 2014. doi: 10.1093/mnras/stu708.

S. Bégin. A search for fast pulsars in globular clusters. Master's thesis, University of British Columbia, Canada, Oct. 2006.

M. A. Belyaev. Dissipation, energy transfer, and spin-down luminosity in 2.5D PIC simulations of the pulsar magnetosphere. *MNRAS*, 449(3):2759–2767, May 2015. doi: 10.1093/mnras/stv468.

M. A. Belyaev and K. Parfrey. Spatial Distribution of Pair Production Over the Pulsar Polar Cap. *ApJ*, 830(2):119, Oct. 2016. doi: 10.3847/0004-637X/830/2/119.

J. Benáček, A. Jessner, M. Pohl, T. Rievajová, and L. S. Oswald. On the origin of radio polarization in pulsar polar caps. *arXiv e-prints*, art. arXiv:2503.17249, Mar. 2025. doi: 10.48550/arXiv.2503.17249.

N. Bessho and A. Bhattacharjee. Collisionless Reconnection in an Electron-Positron Plasma. *Phys. Rev. Lett.*, 95(24):245001, Dec. 2005. doi: 10.1103/PhysRevLett.95.245001.

A. V. Bilous, T. T. Pennucci, P. Demorest, and S. M. Ransom. A Broadband Radio Study of the Average Profile and Giant Pulses from PSR B1821-24A. *ApJ*, 803(2):83, Apr. 2015. doi: 10.1088/0004-637X/803/2/83.

C. K. Birdsall and A. B. Langdon. *Plasma Physics via Computer Simulation*. 1991.

R. D. Blandford. To the Lighthouse. In M. Gilfanov, R. Sunyeav, and E. Churazov, editors, *Lighthouses of the Universe: The Most Luminous Celestial Objects and Their Use for Cosmology*, page 381, Jan. 2002. doi: 10.1007/10856495_59.

R. D. Blandford and R. L. Znajek. Electromagnetic extraction of energy from Kerr black holes. *MNRAS*, 179:433–456, May 1977. doi: 10.1093/mnras/179.3.433.

G. R. Blumenthal and R. J. Gould. Bremsstrahlung, Synchrotron Radiation, and Compton Scattering of High-Energy Electrons Traversing Dilute Gases. *Reviews of Modern Physics*, 42(2):237–271, Jan. 1970. doi: 10.1103/RevModPhys.42.237.

C. D. Bochenek, V. Ravi, K. V. Belov, G. Hallinan, J. Kocz, S. R. Kulkarni, and D. L. McKenna. A fast radio burst associated with a Galactic magnetar. *Nature*, 587(7832): 59–62, Nov. 2020. doi: 10.1038/s41586-020-2872-x.

S. Bogdanov and J. P. Halpern. Identification of the High-energy Gamma-Ray Source 3FGL J1544.6-1125 as a Transitional Millisecond Pulsar Binary in an Accreting State. *ApJ*, 803 (2):L27, Apr. 2015. doi: 10.1088/2041-8205/803/2/L27.

S. Bogdanov, A. Bahramian, C. O. Heinke, P. C. C. Freire, J. W. T. Hessels, S. M. Ransom, and I. H. Stairs. A Deep Chandra X-Ray Observatory Study of the Millisecond Pulsar Population in the Globular Cluster Terzan 5. *ApJ*, 912(2):124, May 2021. doi: 10.3847/1538-4357/abee78.

S. V. Bogovalov. On the physics of cold MHD winds from oblique rotators. *A&A*, 349: 1017–1026, Sept. 1999. doi: 10.48550/arXiv.astro-ph/9907051.

H. E. Bond, R. L. White, R. H. Becker, and M. S. O'Brien. FIRST J102347.6+003841: The First Radio-selected Cataclysmic Variable. *PASP*, 114(802):1359–1363, Dec. 2002. doi: 10.1086/344381.

A. Bransgrove, B. Ripperda, and A. Philippov. Magnetic Hair and Reconnection in Black Hole Magnetospheres. *Phys. Rev. Lett.*, 127(5):055101, July 2021. doi: 10.1103/PhysRevLett.127.055101.

A. Bransgrove, A. M. Beloborodov, and Y. Levin. Radio Emission and Electric Gaps in Pulsar Magnetospheres. *ApJ*, 958(1):L9, Nov. 2023. doi: 10.3847/2041-8213/ad0556.

R. P. Breton. Radio pulsars in binary systems, 2009.

R. Bühler and R. Blandford. The surprising Crab pulsar and its nebula: a review. *Reports on Progress in Physics*, 77(6):066901, June 2014. doi: 10.1088/0034-4885/77/6/066901.

M. Burgay, N. D'Amico, A. Possenti, R. N. Manchester, A. G. Lyne, B. C. Joshi, M. A. McLaughlin, M. Kramer, J. M. Sarkissian, F. Camilo, V. Kalogera, C. Kim, and D. R. Lorimer. An increased estimate of the merger rate of double neutron stars from observations of a highly relativistic system. *Nature*, 426(6966):531–533, Dec. 2003. ISSN 1476-4687. doi: 10.1038/nature02124. URL http://dx.doi.org/10.1038/nature02124.

M. Burgay, M. A. McLaughlin, and S. P. Reynolds. On the debated nature of Rotating RAdio Transients. In T. di Salvo, G. L. Israel, L. Piersant, L. Burderi, G. Matt, A. Tornambe, and M. T. Menna, editors, *The Multicolored Landscape of Compact Objects and Their Explosive Origins*, volume 924 of *American Institute of Physics Conference Series*, pages 607–612. AIP, Aug. 2007. doi: 10.1063/1.2774917.

E. Burns et al. Multidisciplinary science in the multimessenger era, 2025. URL https://arxiv.org/abs/2502.03577.

A. Burtovoi, L. Zampieri, M. Fiori, G. Naletto, A. Spolon, C. Barbieri, A. Papitto, and F. Ambrosino. Spin-down rate of the transitional millisecond pulsar PSR J1023+0038 in the optical band with Aqueye+. *MNRAS*, 498(1):L98–L103, Nov. 2020. doi: 10.1093/mnrasl/slaa133.

M. Caleb, I. Heywood, K. Rajwade, M. Malenta, B. W. Stappers, E. Barr, W. Chen, V. Morello, S. Sanidas, J. van den Eijnden, M. Kramer, D. Buckley, J. Brink, S. E. Motta, P. Woudt, P. Weltevrede, F. Jankowski, M. Surnis, S. Buchner, M. C. Bezuidenhout, L. N. Driessen, and R. Fender. Discovery of a radio-emitting neutron star with an ultra-long spin period of 76 s. *Nature Astronomy*, 6:828–836, May 2022. doi: 10.1038/s41550-022-01688-x.

M. Caleb, E. Lenc, D. L. Kaplan, T. Murphy, Y. P. Men, R. M. Shannon, L. Ferrario, K. M. Rajwade, T. E. Clarke, S. Giacintucci, N. Hurley-Walker, S. D. Hyman, M. E. Lower, S. McSweeney, V. Ravi, E. D. Barr, S. Buchner, C. M. L. Flynn, J. W. T. Hessels, M. Kramer, J. Pritchard, and B. W. Stappers. An emission-state-switching radio transient with a 54-minute period. *Nature Astronomy*, 8(9):1159–1168, June 2024. ISSN 2397-3366. doi: 10.1038/s41550-024-02277-w. URL http://dx.doi.org/10.1038/s41550-024-02277-w.

F. Camilo, S. M. Ransom, J. P. Halpern, J. Reynolds, D. J. Helfand, N. Zimmerman, and J. Sarkissian. Transient pulsed radio emission from a magnetar. *Nature*, 442(7105):892–895, Aug. 2006. doi: 10.1038/nature04986.

S. Campana and T. Di Salvo. Accreting Pulsars: Mixing-up Accretion Phases in Transitional Systems. In L. Rezzolla, P. Pizzochero, D. I. Jones, N. Rea, and I. Vidaña, editors, *Astrophysics and Space Science Library*, volume 457 of *Astrophysics and Space Science Library*, page 149, Jan. 2018. doi: 10.1007/978-3-319-97616-7_4.

S. Campana, A. Miraval Zanon, F. Coti Zelati, D. F. Torres, M. C. Baglio, and A. Papitto. Probing X-ray emission in different modes of PSR J1023+0038 with a radio pulsar scenario. *A&A*, 629:L8, Sept. 2019. doi: 10.1051/0004-6361/201936312.

F. Carrasco and M. Shibata. Magnetosphere of an orbiting neutron star. *Physical Review D*, 101(6):063017, Mar. 2020. doi: 10.1103/PhysRevD.101.063017.

F. Carrasco, M. Shibata, and O. Reula. Magnetospheres of black hole-neutron star binaries. *Phys. Rev. D*, 104(6):063004, Sept. 2021. doi: 10.1103/PhysRevD.104.063004.

B. W. Carroll and D. A. Ostlie. *An introduction to modern astrophysics, Second Edition.* 2017.

S. Çıkıntoğlu, K. Y. Ekşi, and L. Rezzolla. GRMHD simulations of accreting neutron stars I: Non-rotating dipoles. *MNRAS*, 517(3):3212–3226, Dec. 2022. doi: 10.1093/mnras/stac2510.

B. Cerutti. *Accélération de particules dans les magnétosphères relativistes.* Habilitation à diriger des recherches, Institut de Planétologie et d'Astrophysique de Grenoble, Jan. 2021.

B. Cerutti and A. M. Beloborodov. Electrodynamics of Pulsar Magnetospheres. *Space Sci. Rev.*, 207(1-4):111–136, July 2017. doi: 10.1007/s11214-016-0315-7.

B. Cerutti and A. A. Philippov. Dissipation of the striped pulsar wind. *A&A*, 607:A134, Nov. 2017. doi: 10.1051/0004-6361/201731680.

B. Cerutti and G. Werner. Zeltron: Explicit 3D relativistic electromagnetic Particle-In-Cell code. Astrophysics Source Code Library, record ascl:1911.012, Nov. 2019.

B. Cerutti, G. R. Werner, D. A. Uzdensky, and M. C. Begelman. Beaming and Rapid Variability of High-energy Radiation from Relativistic Pair Plasma Reconnection. *ApJ*, 754(2): L33, Aug. 2012. doi: 10.1088/2041-8205/754/2/L33.

B. Cerutti, G. R. Werner, D. A. Uzdensky, and M. C. Begelman. Simulations of Particle Acceleration beyond the Classical Synchrotron Burnoff Limit in Magnetic Reconnection: An Explanation of the Crab Flares. *ApJ*, 770(2):147, June 2013. doi: 10.1088/0004-637X/770/2/147.

B. Cerutti, A. Philippov, K. Parfrey, and A. Spitkovsky. Particle acceleration in axisymmetric pulsar current sheets. *Monthly Notices of the Royal Astronomical Society*, 448(1):606–619, Feb. 2015. ISSN 0035-8711. doi: 10.1093/mnras/stv042. URL http://dx.doi.org/10.1093/mnras/stv042.

B. Cerutti, J. Mortier, and A. A. Philippov. Polarized synchrotron emission from the equatorial current sheet in gamma-ray pulsars. *MNRAS*, 463(1):L89–L93, Nov. 2016. doi: 10.1093/mnrasl/slw162.

B. Cerutti, A. A. Philippov, and A. Spitkovsky. Modelling high-energy pulsar light curves from first principles. *Monthly Notices of the Royal Astronomical Society*, 457(3):2401–2414, Feb. 2016. ISSN 1365-2966. doi: 10.1093/mnras/stw124. URL http://dx.doi.org/10.1093/mnras/stw124.

B. Cerutti, A. A. Philippov, and G. Dubus. Dissipation of the striped pulsar wind and non-thermal particle acceleration: 3D PIC simulations. *A&A*, 642:A204, Oct. 2020. doi: 10.1051/0004-6361/202038618.

B. Cerutti, E. Figueiredo, and G. Dubus. Synthetic pulsar light curves from global kinetic simulations and comparison with the fermi-lat catalog. *A&A*, 695:A93, Mar. 2025. ISSN 1432-0746. doi: 10.1051/0004-6361/202451948. URL http://dx.doi.org/10.1051/0004-6361/202451948.

A. Y. Chen and A. M. Beloborodov. Electrodynamics of Axisymmetric Pulsar Magnetosphere with Electron-Positron Discharge: A Numerical Experiment. *ApJ*, 795(1):L22, Nov. 2014. doi: 10.1088/2041-8205/795/1/L22.

A. Y. Chen, F. Cruz, and A. Spitkovsky. Filling the magnetospheres of weak pulsars. *The Astrophysical Journal*, 889(1):69, Jan. 2020. ISSN 1538-4357. doi: 10.3847/1538-4357/ab5c20. URL http://dx.doi.org/10.3847/1538-4357/ab5c20.

K. Chen and M. Ruderman. Pulsar Death Lines and Death Valley. *ApJ*, 402:264, Jan. 1993. doi: 10.1086/172129.

Z.-C. Chen and L. Liu. Is psr j0514−4002e in a pbh-ns binary?, 2024.

A. Chernoglazov, H. Hakobyan, and A. Philippov. High-energy Radiation and Ion Acceleration in Three-dimensional Relativistic Magnetic Reconnection with Strong Synchrotron Cooling. *ApJ*, 959(2):122, Dec. 2023. doi: 10.3847/1538-4357/acffc6.

Chime/Frb Collaboration et al. Periodic activity from a fast radio burst source. *Nature*, 582 (7812):351–355, June 2020. doi: 10.1038/s41586-020-2398-2.

I. Cognard, J. A. Shrauner, J. H. Taylor, and S. E. Thorsett. Giant radio pulses from a millisecond pulsar. *The Astrophysical Journal*, 457(2):L81, feb 1996. doi: 10.1086/309894. URL https://dx.doi.org/10.1086/309894.

I. Contopoulos. The coughing pulsar magnetosphere. *A&A*, 442(2):579–586, Nov. 2005. doi: 10.1051/0004-6361:20053143.

I. Contopoulos, D. Kazanas, and C. Fendt. The Axisymmetric Pulsar Magnetosphere. *ApJ*, 511(1):351–358, Jan. 1999. doi: 10.1086/306652.

F. V. Coroniti. Magnetically Striped Relativistic Magnetohydrodynamic Winds: The Crab Nebula Revisited. *ApJ*, 349:538, Feb. 1990. doi: 10.1086/168340.

J. Cortés and L. Sironi. Global kinetic modeling of the intrabinary shock in spider pulsars. *The Astrophysical Journal*, 933(2):140, July 2022. ISSN 1538-4357. doi: 10.3847/1538-4357/ac74b2. URL http://dx.doi.org/10.3847/1538-4357/ac74b2.

J. Cortés and L. Sironi. Particle acceleration and non-thermal emission at the intrabinary shock of spider pulsars - I. Non-radiative simulations. *MNRAS*, 534(3):2551–2565, Nov. 2024. doi: 10.1093/mnras/stae2278.

J. Cortés and L. Sironi. Particle acceleration and nonthermal emission at the intrabinary shock of spider pulsars. II: Fast-cooling simulations. *MNRAS*, Feb. 2025. doi: 10.1093/mnras/staf284.

F. Coti Zelati, N. Rea, J. A. Pons, S. Campana, and P. Esposito. Systematic study of magnetar outbursts. *MNRAS*, 474(1):961–1017, Feb. 2018. doi: 10.1093/mnras/stx2679.

F. Coti Zelati, A. Papitto, D. de Martino, D. A. H. Buckley, A. Odendaal, J. Li, T. D. Russell, D. F. Torres, S. M. Mazzola, E. Bozzo, M. Gromadzki, S. Campana, N. Rea, C. Ferrigno, and S. Migliari. Prolonged sub-luminous state of the new transitional pulsar candidate CXOU J110926.4-650224. *A&A*, 622:A211, Feb. 2019. doi: 10.1051/0004-6361/201834835.

B. Crinquand, B. Cerutti, and G. Dubus. Kinetic modeling of the electromagnetic precursor from an axisymmetric binary pulsar coalescence. *A&A*, 622:A161, Feb. 2019. doi: 10.1051/0004-6361/201834610.

B. Crinquand, B. Cerutti, G. Dubus, K. Parfrey, and A. Philippov. Synthetic gamma-ray light curves of Kerr black hole magnetospheric activity from particle-in-cell simulations. *A&A*, 650:A163, June 2021. doi: 10.1051/0004-6361/202040158.

Z. G. Dai, J. S. Wang, X. F. Wu, and Y. F. Huang. Repeating fast radio bursts from highly magnetized pulsars traveling through asteroid belts. *The Astrophysical Journal*, 829(1):27, Sept. 2016. ISSN 1538-4357. doi: 10.3847/0004-637x/829/1/27. URL http://dx.doi.org/10.3847/0004-637X/829/1/27.

P. Das and O. Porth. Three-dimensional GRMHD Simulations of Neutron Star Jets. *ApJ*, 960(2):L12, Jan. 2024. doi: 10.3847/2041-8213/ad151f.

P. Das, O. Porth, and A. L. Watts. GRMHD simulations of accreting neutron stars with non-dipole fields. *MNRAS*, 515(3):3144–3161, Sept. 2022. doi: 10.1093/mnras/stac1817.

D. De Grandis, R. Turolla, T. S. Wood, S. Zane, R. Taverna, and K. N. Gourgouliatos. Three-dimensional Modeling of the Magnetothermal Evolution of Neutron Stars: Method and Test Cases. *ApJ*, 903(1):40, Nov. 2020. doi: 10.3847/1538-4357/abb6f9.

D. de Martino, M. Falanga, J. M. Bonnet-Bidaud, T. Belloni, M. Mouchet, N. Masetti, I. Andruchow, S. A. Cellone, K. Mukai, and G. Matt. The intriguing nature of the high-energy gamma ray source XSS J12270−4859. *A&A*, 515:A25, June 2010. doi: 10.1051/0004-6361/200913802.

D. de Martino, T. Belloni, M. Falanga, A. Papitto, S. Motta, A. Pellizzoni, Y. Evangelista, G. Piano, N. Masetti, J. M. Bonnet-Bidaud, M. Mouchet, K. Mukai, and A. Possenti. X-ray follow-ups of XSS J12270−4859: a low-mass X-ray binary with gamma-ray Fermi-LAT association. *A&A*, 550:A89, Feb. 2013. doi: 10.1051/0004-6361/201220393.

D. de Martino, J. Casares, E. Mason, D. A. H. Buckley, M. M. Kotze, J.-M. Bonnet-Bidaud, M. Mouchet, R. Coppejans, and A. A. S. Gulbis. Unveiling the redback nature of the low-mass x-ray binary xss j1227.0−4859 through optical observations. *Monthly Notices of the Royal Astronomical Society*, 444(4):3004–3014, 09 2014. ISSN 0035-8711. doi: 10.1093/mnras/stu1640. URL https://doi.org/10.1093/mnras/stu1640.

I. de Ruiter, K. Rajwade, C. Bassa, A. Rowlinson, R. Wijers, C. Kilpatrick, G. Stefansson, J. Callingham, J. Hessels, T. Clarke, et al. Sporadic radio pulses from a white dwarf binary at the orbital period. *Nature Astronomy*, pages 1–13, 2025.

V. Decoene, K. Kotera, and J. Silk. Fast radio burst repeaters produced via Kozai-Lidov feeding of neutron stars in binary systems. *A&A*, 645:A122, Jan. 2021. doi: 10.1051/0004-6361/202038975.

N. Degenaar, R. Wijnands, M. T. Reynolds, J. M. Miller, D. Altamirano, J. Kennea, N. Gehrels, D. Haggard, and G. Ponti. The Peculiar Galactic Center Neutron Star X-Ray Binary XMM J174457-2850.3. *ApJ*, 792(2):109, Sept. 2014. doi: 10.1088/0004-637X/792/2/109.

C. Dehman, D. Viganò, J. A. Pons, and N. Rea. 3D code for MAgneto-Thermal evolution in Isolated Neutron Stars, MATINS: the magnetic field formalism. *MNRAS*, 518(1):1222–1242, Jan. 2023. doi: 10.1093/mnras/stac2761.

C. D. Dermer and A. Atoyan. Collapse of Neutron Stars to Black Holes in Binary Systems: A Model for Short Gamma-Ray Bursts. *ApJ*, 643(1):L13–L16, May 2006. doi: 10.1086/504895.

A. J. Deutsch. The electromagnetic field of an idealized star in rigid rotation in vacuo. *Annales d'Astrophysique*, 18:1, Jan. 1955.

P. E. Dewdney, P. J. Hall, R. T. Schilizzi, and T. J. L. W. Lazio. The Square Kilometre Array. *IEEE Proceedings*, 97(8):1482–1496, Aug. 2009. doi: 10.1109/JPROC.2009.2021005.

P. A. M. Dirac. Classical theory of radiating electrons. *Proc. Roy. Soc. Lond. A*, 167:148–169, 1938. doi: 10.1098/rspa.1938.0124.

F. A. Dong, T. Clarke, A. P. Curtin, A. Kumar, I. Stairs, S. Chatterjee, A. M. Cook, E. Fonseca, B. M. Gaensler, J. W. T. Hessels, V. M. Kaspi, M. Lazda, K. W. Masui, J. W. McKee, B. W. Meyers, A. B. Pearlman, S. M. Ransom, P. Scholz, K. Shin, K. M. Smith, and C. M. Tan. The discovery of a nearby 421 s transient with chime/frb/pulsar, 2024. URL https://arxiv.org/abs/2407.07480.

D. J. D'Orazio, J. Levin, N. W. Murray, and L. Price. Bright transients from strongly-magnetized neutron star-black hole mergers. *Phys. Rev. D*, 94(2):023001, July 2016. doi: 10.1103/PhysRevD.94.023001.

G. Dubus. Gamma-ray binaries and related systems. *A&A Rev.*, 21:64, Aug. 2013. doi: 10.1007/s00159-013-0064-5.

W. E. East, L. Lehner, S. L. Liebling, and C. Palenzuela. Multimessenger Signals from Black Hole-Neutron Star Mergers without Significant Tidal Disruption. *ApJ*, 912(1):L18, May 2021. doi: 10.3847/2041-8213/abf566.

D. Eckert, M. Del Santo, A. Bazzano, K. Watanabe, A. Paizis, E. Bozzo, C. Ferrigno, I. Caballero, L. Sidoli, and L. Kuiper. IGR J18245-2452: a new hard X-ray transient discovered by INTEGRAL. *The Astronomer's Telegram*, 4925:1, Mar. 2013.

J. A. Eilek and T. H. Hankins. Radio emission physics in the Crab pulsar. *Journal of Plasma Physics*, 82(3):635820302, June 2016. doi: 10.1017/S002237781600043X.

K. Y. Ekşİ and M. A. Alpar. Disks Surviving the Radiation Pressure of Radio Pulsars. *ApJ*, 620(1):390–397, Feb. 2005. doi: 10.1086/425959.

T. Erber. High-Energy Electromagnetic Conversion Processes in Intense Magnetic Fields. *Reviews of Modern Physics*, 38(4):626–659, Oct. 1966. doi: 10.1103/RevModPhys.38.626.

P. Esposito, N. Rea, and G. L. Israel. Magnetars: A Short Review and Some Sparse Considerations. In T. M. Belloni, M. Méndez, and C. Zhang, editors, *Timing Neutron Stars: Pulsations, Oscillations and Explosions*, volume 461 of *Astrophysics and Space Science Library*, pages 97–142, Jan. 2021. doi: 10.1007/978-3-662-62110-3_3.

Event Horizon Telescope Collaboration et al. First M87 Event Horizon Telescope Results. I. The Shadow of the Supermassive Black Hole. *ApJ*, 875(1):L1, Apr. 2019. doi: 10.3847/2041-8213/ab0ec7.

Event Horizon Telescope Collaboration et al. First Sagittarius A* Event Horizon Telescope Results. I. The Shadow of the Supermassive Black Hole in the Center of the Milky Way. *ApJ*, 930(2):L12, May 2022. doi: 10.3847/2041-8213/ac6674.

R. Fernández and B. D. Metzger. Electromagnetic Signatures of Neutron Star Mergers in the Advanced LIGO Era. *Annual Review of Nuclear and Particle Science*, 66(1):23–45, Oct. 2016. doi: 10.1146/annurev-nucl-102115-044819.

F. Filbet and E. Sonnendrücker. Numerical methods for the vlasov equation. In F. Brezzi, A. Buffa, S. Corsaro, and A. Murli, editors, *Numerical Mathematics and Advanced Applications*, pages 459–468, Milano, 2003. Springer Milan. ISBN 978-88-470-2089-4.

A. S. Fruchter, D. R. Stinebring, and J. H. Taylor. A millisecond pulsar in an eclipsing binary. *Nature*, 333(6170):237–239, May 1988. doi: 10.1038/333237a0.

A. Gautam, R. M. Crocker, L. Ferrario, A. J. Ruiter, H. Ploeg, C. Gordon, and O. Macias. Millisecond pulsars from accretion-induced collapse as the origin of the Galactic Centre gamma-ray excess signal. *Nature Astronomy*, 6:703–707, Apr. 2022. doi: 10.1038/s41550-022-01658-3.

B. Giacomazzo and R. Perna. General Relativistic Simulations of Accretion Induced Collapse of Neutron Stars to Black Holes. *ApJ*, 758(1):L8, Oct. 2012. doi: 10.1088/2041-8205/758/1/L8.

V. L. Ginzburg and S. I. Syrovatskii. Cosmic Magnetobremsstrahlung (synchrotron Radiation). *ARA&A*, 3:297, Jan. 1965. doi: 10.1146/annurev.aa.03.090165.001501.

T. Gold. Rotating Neutron Stars as the Origin of the Pulsating Radio Sources. *Nature*, 218 (5143):731–732, May 1968. doi: 10.1038/218731a0.

P. Goldreich and W. H. Julian. Pulsar Electrodynamics. *ApJ*, 157:869, Aug. 1969. doi: 10.1086/150119.

S. P. Goodwin, J. Mestel, L. Mestel, and G. A. E. Wright. An idealized pulsar magnetosphere: the relativistic force-free approximation. *MNRAS*, 349(1):213–224, Mar. 2004. doi: 10.1111/j.1365-2966.2004.07481.x.

S. E. Gralla, A. Lupsasca, and A. Philippov. Pulsar Magnetospheres: Beyond the Flat Spacetime Dipole. *ApJ*, 833(2):258, Dec. 2016. doi: 10.3847/1538-4357/833/2/258.

A. Gruzinov. Stability in force-free electrodynamics, 1999. URL https://arxiv.org/abs/astro-ph/9902288.

A. Gruzinov. Power of an Axisymmetric Pulsar. *Phys. Rev. Lett.*, 94(2):021101, Jan. 2005. doi: 10.1103/PhysRevLett.94.021101.

C. Guépin, K. Kotera, E. Barausse, K. Fang, and K. Murase. Ultra-high-energy cosmic rays and neutrinos from tidal disruptions by massive black holes. *A&A*, 616:A179, Sept. 2018. doi: 10.1051/0004-6361/201732392.

C. Guépin, B. Cerutti, and K. Kotera. Proton acceleration in pulsar magnetospheres. *A&A*, 635:A138, Mar. 2020. doi: 10.1051/0004-6361/201936816.

C. Guerra, Z. Meliani, and G. Voisin. Hydrodynamical simulations of wind interaction in spider systems: A step toward understanding transitional millisecond pulsars. *A&A*, 690: A75, Oct. 2024. doi: 10.1051/0004-6361/202450638.

H. E. S. S. Collaboration et al. Discovery of a radiation component from the Vela pulsar reaching 20 teraelectronvolts. *Nature Astronomy*, 7:1341–1350, Nov. 2023. doi: 10.1038/s41550-023-02052-3.

H. Hakobyan, A. Philippov, and A. Spitkovsky. Magnetic Energy Dissipation and γ-Ray Emission in Energetic Pulsars. *ApJ*, 943(2):105, Feb. 2023. doi: 10.3847/1538-4357/acab05.

J. P. Halpern, E. Gaidos, A. Sheffield, A. M. Price-Whelan, and S. Bogdanov. Optical Observations of the Binary MSP J1023+0038 in a New Accreting State. *The Astronomer's Telegram*, 5514:1, Oct. 2013.

B. M. S. Hansen and M. Lyutikov. Radio and X-ray signatures of merging neutron stars. *MNRAS*, 322(4):695–701, Apr. 2001. doi: 10.1046/j.1365-8711.2001.04103.x.

B. Haskell and A. Melatos. Models of pulsar glitches. *International Journal of Modern Physics D*, 24(3):1530008, Jan. 2015. doi: 10.1142/S0218271815300086.

M. R. Hayashi, K. Shibata, and R. Matsumoto. X-Ray Flares and Mass Outflows Driven by Magnetic Interaction between a Protostar and Its Surrounding Disk. *ApJ*, 468:L37, Sept. 1996. doi: 10.1086/310222.

A. Hewish, S. J. Bell, J. D. H. Pilkington, P. F. Scott, and R. A. Collins. Observation of a Rapidly Pulsating Radio Source. *Nature*, 217(5130):709–713, Feb. 1968. doi: 10.1038/217709a0.

A. B. Hill, A. Szostek, S. Corbel, F. Camilo, R. H. D. Corbet, R. Dubois, G. Dubus, P. G. Edwards, E. C. Ferrara, M. Kerr, E. Koerding, D. Koziel, and Ł. Stawarz. The bright unidentified γ-ray source 1fgl j1227.9−4852: can it be associated with a low-mass x-ray binary? *MNRAS*, 415(1):235–243, July 2011. doi: 10.1111/j.1365-2966.2011.18692.x.

R. Hu and A. M. Beloborodov. Axisymmetric pulsar magnetosphere revisited. *The Astrophysical Journal*, 939(1):42, Nov. 2022. ISSN 1538-4357. doi: 10.3847/1538-4357/ac961d. URL http://dx.doi.org/10.3847/1538-4357/ac961d.

R. A. Hulse and J. H. Taylor. Discovery of a pulsar in a binary system. *ApJ*, 195:L51–L53, Jan. 1975. doi: 10.1086/181708.

N. Hurley-Walker, X. Zhang, A. Bahramian, S. J. McSweeney, T. N. O'Doherty, P. J. Hancock, J. S. Morgan, G. E. Anderson, G. H. Heald, and T. J. Galvin. A radio transient with unusually slow periodic emission. *Nature*, 601(7894):526–530, Jan. 2022. doi: 10.1038/s41586-021-04272-x.

N. Hurley-Walker, N. Rea, S. J. McSweeney, B. W. Meyers, E. Lenc, I. Heywood, S. D. Hyman, Y. P. Men, T. E. Clarke, F. Coti Zelati, D. C. Price, C. Horváth, T. J. Galvin, G. E. Anderson, A. Bahramian, E. D. Barr, N. D. R. Bhat, M. Caleb, M. Dall'Ora, D. de Martino, S. Giacintucci, J. S. Morgan, K. M. Rajwade, B. Stappers, and A. Williams. A long-period radio transient active for three decades. *Nature*, 619(7970):487–490, July 2023. doi: 10.1038/s41586-023-06202-5.

N. Hurley-Walker, S. McSweeney, A. Bahramian, N. Rea, C. Horváth, S. Buchner, A. Williams, B. Meyers, J. Strader, E. Aydi, et al. A 2.9 hr periodic radio transient with an optical counterpart. *The Astrophysical Journal Letters*, 976(2):L21, 2024.

IceCube Collaboration et al. Multimessenger observations of a flaring blazar coincident with high-energy neutrino IceCube-170922A. *Science*, 361(6398):eaat1378, July 2018. doi: 10.1126/science.aat1378.

A. F. Illarionov and R. A. Sunyaev. Why the Number of Galactic X-ray Stars Is so Small? *A&A*, 39:185, Feb. 1975.

G. Illiano, A. Papitto, F. Ambrosino, A. Miraval Zanon, F. Coti Zelati, L. Stella, L. Zampieri, A. Burtovoi, S. Campana, P. Casella, M. Cecconi, D. de Martino, M. Fiori, A. Ghedina, M. Gonzales, M. Hernandez Diaz, G. L. Israel, F. Leone, G. Naletto, H. Perez Ventura, C. Riverol, L. Riverol, D. F. Torres, and M. Turchetta. Investigating the origin of optical and x-ray pulsations of the transitional millisecond pulsar psr j1023+0038. *A&A*, 669:A26, Jan. 2023. ISSN 1432-0746. doi: 10.1051/0004-6361/202244637. URL http://dx.doi.org/10.1051/0004-6361/202244637.

G. Iorio, M. Mapelli, G. Costa, M. Spera, G. J. Escobar, C. Sgalletta, A. A. Trani, E. Korb, F. Santoliquido, M. Dall'Amico, N. Gaspari, and A. Bressan. Compact object mergers: exploring uncertainties from stellar and binary evolution with SEVN. *MNRAS*, 524(1):426–470, Sept. 2023. doi: 10.1093/mnras/stad1630.

H. Isobe, H. Takasaki, and K. Shibata. Measurement of the Energy Release Rate and the Reconnection Rate in Solar Flares. *ApJ*, 632(2):1184–1195, Oct. 2005. doi: 10.1086/444490.

J. D. Jackson. *Classical electrodynamics*. 1975.

B. A. Jacoby, M. Bailes, M. H. van Kerkwijk, S. Ord, A. Hotan, S. R. Kulkarni, and S. B. Anderson. Psr j1909-3744: A binary millisecond pulsar with a very small duty cycle. *The Astrophysical Journal*, 599(2):L99–L102, Dec. 2003. ISSN 1538-4357. doi: 10.1086/381260. URL http://dx.doi.org/10.1086/381260.

B. A. Jacoby, M. Bailes, S. M. Ord, H. S. Knight, and A. W. Hotan. Discovery of Five Recycled Pulsars in a High Galactic Latitude Survey. *ApJ*, 656(1):408–413, Feb. 2007. doi: 10.1086/509312.

A. Jaodand, A. M. Archibald, J. W. T. Hessels, S. Bogdanov, C. R. D'Angelo, A. Patruno, C. Bassa, and A. T. Deller. Timing Observations of PSR J1023+0038 During a Low-mass X-Ray Binary State. *ApJ*, 830(2):122, Oct. 2016. doi: 10.3847/0004-637X/830/2/122.

A. Jaodand, J. W. T. Hessels, and A. Archibald. A decade of transitional millisecond pulsars. *Proceedings of the International Astronomical Union*, 13(S337):47–51, Sept. 2017. ISSN 1743-9221. doi: 10.1017/s1743921317010407. URL http://dx.doi.org/10.1017/S1743921317010407.

T. J. Johnson, C. Venter, A. K. Harding, L. Guillemot, D. A. Smith, M. Kramer, Ö. Çelik, P. R. den Hartog, E. C. Ferrara, X. Hou, J. Lande, and P. S. Ray. Constraints on the Emission Geometries and Spin Evolution of Gamma-Ray Millisecond Pulsars. *ApJS*, 213 (1):6, July 2014. doi: 10.1088/0067-0049/213/1/6.

S. Johnston, R. W. Romani, F. E. Marshall, and W. Zhang. Radio and X-ray observations of PSR B0540-69. *MNRAS*, 355(1):31–36, Nov. 2004. doi: 10.1111/j.1365-2966.2004.08286.x.

P. B. Jones. Properties of condensed matter in very strong magnetic fields. *Monthly Notices of the Royal Astronomical Society*, 218:477–485, Feb. 1986. doi: 10.1093/mnras/218.3.477.

S. Kaci, G. Giacinti, F. Aharonian, and J.-S. Wang. Microquasars as the major contributors to Galactic cosmic rays around the "knee". *arXiv e-prints*, art. arXiv:2510.01369, Oct. 2025. doi: 10.48550/arXiv.2510.01369.

C. Kalapotharakos and I. Contopoulos. Three-dimensional numerical simulations of the pulsar magnetosphere: preliminary results. *A&A*, 496(2):495–502, Mar. 2009. doi: 10.1051/0004-6361:200810281.

C. Kalapotharakos, G. Brambilla, A. Timokhin, A. K. Harding, and D. Kazanas. Three-dimensional kinetic pulsar magnetosphere models: Connecting to gamma-ray observations. *The Astrophysical Journal*, 857(1):44, apr 2018. doi: 10.3847/1538-4357/aab550. URL https://dx.doi.org/10.3847/1538-4357/aab550.

C. Kalapotharakos, Z. Wadiasingh, A. K. Harding, and D. Kazanas. The Gamma-Ray Pulsar Phenomenology in View of 3D Kinetic Global Magnetosphere Models. *ApJ*, 954(2):204, Sept. 2023. doi: 10.3847/1538-4357/ace972.

D. Kasen and L. Bildsten. Supernova Light Curves Powered by Young Magnetars. *ApJ*, 717 (1):245–249, July 2010. doi: 10.1088/0004-637X/717/1/245.

V. M. Kaspi, A. G. Lyne, R. N. Manchester, F. Crawford, F. Camilo, J. F. Bell, N. D'Amico, I. H. Stairs, N. P. F. McKay, D. J. Morris, and A. Possenti. Discovery of a young radio pulsar in a relativistic binary orbit. *The Astrophysical Journal*, 543(1):321–327, Nov. 2000. ISSN 1538-4357. doi: 10.1086/317103. URL http://dx.doi.org/10.1086/317103.

M. Kerr, S. Johnston, G. Hobbs, and R. M. Shannon. Limits on Planet Formation Around Young Pulsars and Implications for Supernova Fallback Disks. *ApJ*, 809(1):L11, Aug. 2015. doi: 10.1088/2041-8205/809/1/L11.

J. G. Kirk and P. Duffy. TOPICAL REVIEW: Particle acceleration and relativistic shocks. *Journal of Physics G Nuclear Physics*, 25(8):R163–R194, Aug. 1999. doi: 10.1088/0954-3899/25/8/201.

J. G. Kirk, Y. Lyubarsky, and J. Petri. The Theory of Pulsar Winds and Nebulae. In W. Becker, editor, *Astrophysics and Space Science Library*, volume 357 of *Astrophysics and Space Science Library*, page 421, Jan. 2009. doi: 10.1007/978-3-540-76965-1_16.

K. I. I. Koljonen and M. Linares. SpiderCat: A Catalog of Compact Binary Millisecond Pulsars. *arXiv e-prints*, art. arXiv:2505.11691, May 2025. doi: 10.48550/arXiv.2505.11691.

S. Komissarov. Time-dependent, force-free, degenerate electrodynamics. *Monthly Notices of the Royal Astronomical Society*, 336:759 – 766, 10 2002. doi: 10.1046/j.1365-8711.2002.05313.x.

S. S. Komissarov. Electrodynamics of black hole magnetospheres. *MNRAS*, 350(2):427–448, May 2004. doi: 10.1111/j.1365-2966.2004.07598.x.

S. S. Komissarov. Simulations of the axisymmetric magnetospheres of neutron stars. *MNRAS*, 367(1):19–31, Mar. 2006. doi: 10.1111/j.1365-2966.2005.09932.x.

J. Krause-Polstorff and F. C. Michel. Pulsar space charging. *A&A*, 144:72–80, Mar. 1985a.

J. Krause-Polstorff and F. C. Michel. Electrosphere of an aligned magnetized neutron star. *MNRAS*, 213:43, Mar. 1985b. doi: 10.1093/mnras/213.1.43P.

R. Kyer, S. Roy, J. Strader, R. Urquhart, I. Molina, P. Craig, and L. Chomiuk. Multi-wavelength evidence for two new candidate transitional millisecond pulsars in the sub-luminous disk state: 4fgl j0639.1-8009 and 4fgl j1824.2+1231. *The Astrophysical Journal*, 983(2):112, Apr. 2025. ISSN 1538-4357. doi: 10.3847/1538-4357/adc128. URL http://dx.doi.org/10.3847/1538-4357/adc128.

D. Lai. DC Circuit Powered by Orbital Motion: Magnetic Interactions in Compact Object Binaries and Exoplanetary Systems. *ApJ*, 757(1):L3, Sept. 2012. doi: 10.1088/2041-8205/757/1/L3.

L. D. Landau. On the theory of stars. *Phys. Z. Sowjetunion*, 1:285, 1932. doi: 10.1016/B978-0-08-010586-4.50013-4.

L. D. Landau and E. M. Lifschitz. *The Classical Theory of Fields*, volume Volume 2 of *Course of Theoretical Physics*. Pergamon Press, Oxford, 1975.

A. Lange, J. Eagle, O. Kargaltsev, L. Kuiper, and J. Hare. The Vela Pulsar and Its Pulsar Wind Nebula Vela-X Using 13 Yr of Fermi-LAT Observations. *ApJ*, 988(2):200, Aug. 2025. doi: 10.3847/1538-4357/ade713.

M. I. Large, A. E. Vaughan, and B. Y. Mills. A Pulsar Supernova Association? *Nature*, 220 (5165):340–341, Oct. 1968. doi: 10.1038/220340a0.

G. Lavagetto, L. Burderi, F. D'Antona, T. Di Salvo, R. Iaria, and N. R. Robba. The different fates of a low-mass x-ray binary - i. conservative mass transfer. *Monthly Notices of the Royal Astronomical Society*, 348(1):73–82, Feb. 2004. ISSN 1365-2966. doi: 10.1111/j.1365-2966.2004.07299.x. URL http://dx.doi.org/10.1111/j.1365-2966.2004.07299.x.

LIGO Scientific Collaboration et al. Advanced LIGO. *Classical and Quantum Gravity*, 32(7):074001, Apr. 2015. doi: 10.1088/0264-9381/32/7/074001.

M. Linares. IGR J18245-2452: an accreting neutron star and thermonuclear burster in M28. *The Astronomer's Telegram*, 4960:1, Apr. 2013.

M. Linares, A. Bahramian, C. Heinke, R. Wijnands, A. Patruno, D. Altamirano, J. Homan, S. Bogdanov, and D. Pooley. The neutron star transient and millisecond pulsar in M28: from sub-luminous accretion to rotation-powered quiescence. *MNRAS*, 438(1):251–261, Feb. 2014. doi: 10.1093/mnras/stt2167.

D. R. Lorimer. Binary and millisecond pulsars. *Living Reviews in Relativity*, 11(1), Nov. 2008. ISSN 1433-8351. doi: 10.12942/lrr-2008-8. URL http://dx.doi.org/10.12942/lrr-2008-8.

D. R. Lorimer and M. Kramer. *Handbook of Pulsar Astronomy*, volume 4. 2004.

D. R. Lorimer, M. Bailes, M. A. McLaughlin, D. J. Narkevic, and F. Crawford. A Bright Millisecond Radio Burst of Extragalactic Origin. *Science*, 318(5851):777, Nov. 2007. doi: 10.1126/science.1147532.

A. G. Lyne and F. Graham-Smith. *Pulsar astronomy*. 1990.

A. G. Lyne, M. Burgay, M. Kramer, A. Possenti, R. Manchester, F. Camilo, M. A. McLaughlin, D. R. Lorimer, N. D'Amico, B. C. Joshi, J. Reynolds, and P. C. C. Freire. A double-pulsar system: A rare laboratory for relativistic gravity and plasma physics. *Science*, 303(5661):1153–1157, Feb. 2004. ISSN 1095-9203. doi: 10.1126/science.1094645. URL http://dx.doi.org/10.1126/science.1094645.

Y. E. Lyubarskii. A model for the energetic emission from pulsars. *A&A*, 311:172–178, July 1996.

Y. Lyubarsky. Radio emission of the Crab and Crab-like pulsars. *MNRAS*, 483(2):1731–1736, Feb. 2019. doi: 10.1093/mnras/sty3233.

D. MacDonald and K. S. Thorne. Black-hole electrodynamics - an absolute-space/universal-time formulation. *MNRAS*, 198:345–382, Jan. 1982. doi: 10.1093/mnras/198.2.345.

A. I. MacFadyen and S. E. Woosley. Collapsars: Gamma-ray bursts and explosions in "failed supernovae". *The Astrophysical Journal*, 524(1):262–289, Oct. 1999. ISSN 1538-4357. doi: 10.1086/307790. URL http://dx.doi.org/10.1086/307790.

R. N. Manchester, G. B. Hobbs, A. Teoh, and M. Hobbs. The Australia Telescope National Facility Pulsar Catalogue. *AJ*, 129(4):1993–2006, Apr. 2005. doi: 10.1086/428488.

J. C. McKinney. Relativistic force-free electrodynamic simulations of neutron star magnetospheres. *MNRAS*, 368(1):L30–L34, May 2006. doi: 10.1111/j.1745-3933.2006.00150.x.

M. A. McLaughlin, A. G. Lyne, D. R. Lorimer, M. Kramer, A. J. Faulkner, R. N. Manchester, J. M. Cordes, F. Camilo, A. Possenti, I. H. Stairs, G. Hobbs, N. D'Amico, M. Burgay, and J. T. O'Brien. Transient radio bursts from rotating neutron stars. *Nature*, 439(7078): 817–820, Feb. 2006. doi: 10.1038/nature04440.

S. T. McWilliams and J. Levin. Electromagnetic Extraction of Energy from Black-hole-Neutron-star Binaries. *ApJ*, 742(2):90, Dec. 2011. doi: 10.1088/0004-637X/742/2/90.

Z. Medin and D. Lai. Condensed surfaces of magnetic neutron stars, thermal surface emission, and particle acceleration above pulsar polar caps. *Monthly Notices of the Royal Astronomical Society*, 382(4):1833–1852, 11 2007. ISSN 0035-8711. doi: 10.1111/j.1365-2966.2007.12492.x. URL https://doi.org/10.1111/j.1365-2966.2007.12492.x.

F. C. Michel. Relativistic Stellar-Wind Torques. *ApJ*, 158:727, Nov. 1969. doi: 10.1086/150233.

F. C. Michel. Rotating Magnetospheres: an Exact 3-D Solution. *ApJ*, 180:L133, Mar. 1973. doi: 10.1086/181169.

F. C. Michel. Theory of pulsar magnetospheres. *Rev. Mod. Phys.*, 54:1–66, Jan 1982. doi: 10.1103/RevModPhys.54.1. URL https://link.aps.org/doi/10.1103/RevModPhys.54.1.

J. M. Miller, S. J. Swihart, J. Strader, R. Urquhart, E. Aydi, L. Chomiuk, K. C. Dage, A. Kawash, L. Shishkovsky, and K. V. Sokolovsky. A new candidate transitional millisecond pulsar in the subluminous disk state: 4fgl j0407.7–5702. *The Astrophysical Journal*, 904(1): 49, Nov. 2020. ISSN 1538-4357. doi: 10.3847/1538-4357/abbb2e. URL http://dx.doi.org/10.3847/1538-4357/abbb2e.

K. A. Miller and J. M. Stone. Magnetohydrodynamic Simulations of Stellar Magnetosphere-Accretion Disk Interaction. *ApJ*, 489(2):890–902, Nov. 1997. doi: 10.1086/304825.

A. Miraval Zanon, F. Ambrosino, F. Coti Zelati, S. Campana, A. Papitto, G. Illiano, G. L. Israel, L. Stella, P. D'Avanzo, and M. C. Baglio. UV and X-ray pulse amplitude variability in the transitional millisecond pulsar PSR J1023+0038. *A&A*, 660:A63, Apr. 2022. doi: 10.1051/0004-6361/202243180.

R. Mishra, M. Čemeljić, J. Varela, and M. Falanga. Auroras on planets around pulsars, 2023.

I. Mochol. *Pulsar Striped Winds*, page 135–159. Springer International Publishing, 2017. ISBN 9783319630311. doi: 10.1007/978-3-319-63031-1_7. URL http://dx.doi.org/10.1007/978-3-319-63031-1_7.

E. R. Most and A. A. Philippov. Electromagnetic Precursors to Gravitational-wave Events: Numerical Simulations of Flaring in Pre-merger Binary Neutron Star Magnetospheres. *ApJ*, 893(1):L6, Apr. 2020. doi: 10.3847/2041-8213/ab8196.

E. R. Most and A. A. Philippov. Electromagnetic Precursors to Black Hole-Neutron Star Gravitational Wave Events: Flares and Reconnection-powered Fast Radio Transients from the Late Inspiral. *ApJ*, 956(2):L33, Oct. 2023. doi: 10.3847/2041-8213/acfdae.

F. Mottez. Ab initio simulations of neutron stars' oblique electrospheres with realistic neutron star parameters. *A&A*, 684:A115, Apr. 2024. doi: 10.1051/0004-6361/202347692.

F. Mottez and J. Heyvaerts. Magnetic coupling of planets and small bodies with a pulsar wind. *A&A*, 532:A21, July 2011. ISSN 1432-0746. doi: 10.1051/0004-6361/201116530. URL http://dx.doi.org/10.1051/0004-6361/201116530.

F. Mottez and J. Heyvaerts. The magnetic coupling of planets and small bodies with a pulsar's wind. In S. Boissier, P. de Laverny, N. Nardetto, R. Samadi, D. Valls-Gabaud, and H. Wozniak, editors, *SF2A-2012: Proceedings of the Annual meeting of the French Society of Astronomy and Astrophysics*, pages 597–600, Dec. 2012. doi: 10.48550/arXiv.1210.0684.

F. Mottez and P. Zarka. Radio emissions from pulsar companions: a refutable explanation for galactic transients and fast radio bursts. *A&A*, 569:A86, Sept. 2014. doi: 10.1051/0004-6361/201424104.

F. Mottez, P. Zarka, and G. Voisin. Repeating fast radio bursts caused by small bodies orbiting a pulsar or a magnetar. *A&A*, 644:A145, Dec. 2020. doi: 10.1051/0004-6361/202037751.

A. Murguia-Berthier, K. Parfrey, A. Tchekhovskoy, and J. Jacquemin-Ide. From Feast to Famine: A Systematic Study of Accretion onto Oblique Pulsars with 3D GRMHD Simulations. *ApJ*, 961(1):L20, Jan. 2024. doi: 10.3847/2041-8213/ad16eb.

F. M. Neubauer. Nonlinear standing Alfvén wave current system at Io: Theory. *J. Geophys. Res.*, 85(A3):1171–1178, Mar. 1980. doi: 10.1029/JA085iA03p01171.

C. Y. Ng, J. Takata, G. C. K. Leung, K. S. Cheng, and P. Philippopoulos. High-energy Emission of the First Millisecond Pulsar. *ApJ*, 787(2):167, June 2014. doi: 10.1088/0004-637X/787/2/167.

A. H. Nitz, S. Kumar, Y.-F. Wang, S. Kastha, S. Wu, M. Schäfer, R. Dhurkunde, and C. D. Capano. 4-OGC: Catalog of Gravitational Waves from Compact Binary Mergers. *ApJ*, 946 (2):59, Apr. 2023. doi: 10.3847/1538-4357/aca591.

I. C. Niţu, M. J. Keith, B. W. Stappers, A. G. Lyne, and M. B. Mickaliger. A search for planetary companions around 800 pulsars from the Jodrell Bank pulsar timing programme. *Monthly Notices of the Royal Astronomical Society*, 512(2):2446–2459, 03 2022. ISSN 0035-8711. doi: 10.1093/mnras/stac593. URL https://doi.org/10.1093/mnras/stac593.

J. P. Ostriker and J. E. Gunn. On the Nature of Pulsars. I. Theory. *Astrophysical Journal*, 157:1395, Sept. 1969. doi: 10.1086/150160.

F. Pacini. Energy Emission from a Neutron Star. *Nature*, 216(5115):567–568, Nov. 1967. doi: 10.1038/216567a0.

F. Pacini. Rotating Neutron Stars, Pulsars and Supernova Remnants. *Nature*, 219(5150): 145–146, July 1968. doi: 10.1038/219145a0.

C. Palenzuela, L. Lehner, M. Ponce, S. L. Liebling, M. Anderson, D. Neilsen, and P. Motl. Electromagnetic and Gravitational Outputs from Binary-Neutron-Star Coalescence. *Phys. Rev. Lett.*, 111(6):061105, Aug. 2013. doi: 10.1103/PhysRevLett.111.061105.

C. Pallanca, E. Dalessandro, F. R. Ferraro, B. Lanzoni, and G. Beccari. The Optical Counterpart to the X-Ray Transient IGR J1824-24525 in the Globular Cluster M28. *ApJ*, 773 (2):122, Aug. 2013. doi: 10.1088/0004-637X/773/2/122.

A. Papitto and D. d. Martino. *Transitional Millisecond Pulsars*, page 157–200. Springer International Publishing, Nov. 2021. ISBN 9783030851989. doi: 10.1007/978-3-030-85198-9_6. URL http://dx.doi.org/10.1007/978-3-030-85198-9_6.

A. Papitto and D. F. Torres. A Propeller Model for the Sub-luminous State of the Transitional Millisecond Pulsar PSR J1023+0038. *ApJ*, 807(1):33, July 2015. doi: 10.1088/0004-637X/807/1/33.

A. Papitto, C. Ferrigno, E. Bozzo, N. Rea, L. Pavan, L. Burderi, M. Burgay, S. Campana, T. di Salvo, M. Falanga, M. D. Filipović, P. C. C. Freire, J. W. T. Hessels, A. Possenti, S. M. Ransom, A. Riggio, P. Romano, J. M. Sarkissian, I. H. Stairs, L. Stella, D. F. Torres, M. H. Wieringa, and G. F. Wong. Swings between rotation and accretion power in a binary millisecond pulsar. *Nature*, 501(7468):517–520, Sept. 2013. doi: 10.1038/nature12470.

A. Papitto, F. Ambrosino, L. Stella, D. Torres, F. Coti Zelati, A. Ghedina, F. Meddi, A. Sanna, P. Casella, Y. Dallilar, S. Eikenberry, G. L. Israel, F. Onori, S. Piranomonte, E. Bozzo, L. Burderi, S. Campana, D. de Martino, T. Di Salvo, C. Ferrigno, N. Rea, A. Riggio, S. Serrano, A. Veledina, and L. Zampieri. Pulsating in Unison at Optical and X-Ray Energies: Simultaneous High Time Resolution Observations of the Transitional Millisecond Pulsar PSR J1023+0038. *ApJ*, 882(2):104, Sept. 2019. doi: 10.3847/1538-4357/ab2fdf.

K. Parfrey and A. Tchekhovskoy. General-relativistic Simulations of Four States of Accretion onto Millisecond Pulsars. *ApJ*, 851(2):L34, Dec. 2017. doi: 10.3847/2041-8213/aa9c85.

K. Parfrey and A. Tchekhovskoy. Accreting Neutron Stars in 3D General-relativistic Magnetohydrodynamic Simulations: Jets, Magnetic Polarity, and the Interchange Slingshot. *ApJ*, 975(1):57, Nov. 2024. doi: 10.3847/1538-4357/ad737b.

K. Parfrey, A. M. Beloborodov, and L. Hui. Introducing PHAEDRA: a new spectral code for simulations of relativistic magnetospheres. *MNRAS*, 423(2):1416–1436, June 2012. doi: 10.1111/j.1365-2966.2012.20969.x.

K. Parfrey, A. Spitkovsky, and A. M. Beloborodov. Simulations of the magnetospheres of accreting millisecond pulsars. *MNRAS*, 469(3):3656–3669, Aug. 2017. doi: 10.1093/mnras/stx950.

K. Parfrey, A. Philippov, and B. Cerutti. First-Principles Plasma Simulations of Black-Hole Jet Launching. *Phys. Rev. Lett.*, 122(3):035101, Jan. 2019. doi: 10.1103/PhysRevLett.122.035101.

E. N. Parker. The Solar-Flare Phenomenon and the Theory of Reconnection and Annihiliation of Magnetic Fields. *ApJS*, 8:177, July 1963. doi: 10.1086/190087.

V. Paschalidis, Z. B. Etienne, and S. L. Shapiro. General-relativistic simulations of binary black hole-neutron stars: Precursor electromagnetic signals. *Phys. Rev. D*, 88(2):021504, July 2013. doi: 10.1103/PhysRevD.88.021504.

A. Patruno, A. M. Archibald, J. W. T. Hessels, S. Bogdanov, B. W. Stappers, C. G. Bassa, G. H. Janssen, V. M. Kaspi, S. Tendulkar, and A. G. Lyne. A New Accretion Disk around the Missing Link Binary System PSR J1023+0038. *ApJ*, 781(1):L3, Jan. 2014. doi: 10.1088/2041-8205/781/1/L3.

E. C. Pattie, T. J. Maccarone, C. T. Britt, C. O. Heinke, P. G. Jonker, D. R. Lorimer, G. R. Sivakoff, D. Steeghs, J. Strader, M. A. P. Torres, and R. Wijnands. An arcsecond view at 1-2 GHz into the Galactic Bulge. *MNRAS*, 531(2):2191–2212, June 2024. doi: 10.1093/mnras/stae1231.

J. Pétri, J. Heyvaerts, and S. Bonazzola. Diocotron instability in pulsar electrospheres. I. Linear analysis. *A&A*, 387:520–530, May 2002. doi: 10.1051/0004-6361:20020442.

T. D. Phan, G. Paschmann, C. Twitty, F. S. Mozer, J. T. Gosling, J. P. Eastwood, M. Øieroset, H. Rème, and E. A. Lucek. Evidence for magnetic reconnection initiated in the magnetosheath. *Geophys. Res. Lett.*, 34(14):L14104, July 2007. doi: 10.1029/2007GL030343.

A. Philippov and M. Kramer. Pulsar Magnetospheres and Their Radiation. *ARA&A*, 60:495–558, Aug. 2022. doi: 10.1146/annurev-astro-052920-112338.

A. Philippov, D. A. Uzdensky, A. Spitkovsky, and B. Cerutti. Pulsar Radio Emission Mechanism: Radio Nanoshots as a Low-frequency Afterglow of Relativistic Magnetic Reconnection. *ApJ*, 876(1):L6, May 2019. doi: 10.3847/2041-8213/ab1590.

A. Philippov, A. Timokhin, and A. Spitkovsky. Origin of Pulsar Radio Emission. *Phys. Rev. Lett.*, 124(24):245101, June 2020. doi: 10.1103/PhysRevLett.124.245101.

A. A. Philippov and A. Spitkovsky. Ab Initio Pulsar Magnetosphere: Three-dimensional Particle-in-cell Simulations of Axisymmetric Pulsars. *ApJ*, 785(2):L33, Apr. 2014. doi: 10.1088/2041-8205/785/2/L33.

A. A. Philippov and A. Spitkovsky. Ab-initio Pulsar Magnetosphere: Particle Acceleration in Oblique Rotators and High-energy Emission Modeling. *ApJ*, 855(2):94, Mar. 2018. doi: 10.3847/1538-4357/aaabbc.

A. A. Philippov, B. Cerutti, A. Tchekhovskoy, and A. Spitkovsky. Ab Initio Pulsar Magnetosphere: The Role of General Relativity. *ApJ*, 815(2):L19, Dec. 2015a. doi: 10.1088/2041-8205/815/2/L19.

A. A. Philippov, A. Spitkovsky, and B. Cerutti. Ab Initio Pulsar Magnetosphere: Three-dimensional Particle-in-cell Simulations of Oblique Pulsars. *ApJ*, 801(1):L19, Mar. 2015b. doi: 10.1088/2041-8205/801/1/L19.

A. D. Piazza. Exact solution of the landau-lifshitz equation in a plane wave, 2008.

A. L. Piro. Magnetic Interactions in Coalescing Neutron Star Binaries. *ApJ*, 755(1):80, Aug. 2012. doi: 10.1088/0004-637X/755/1/80.

J. Pétri. The pulsar force-free magnetosphere linked to its striped wind: time-dependent pseudo-spectral simulations. *Monthly Notices of the Royal Astronomical Society*, 424(1): 605–619, 07 2012. ISSN 0035-8711. doi: 10.1111/j.1365-2966.2012.21238.x. URL https://doi.org/10.1111/j.1365-2966.2012.21238.x.

J. Pétri. Theory of pulsar magnetosphere and wind. *Journal of Plasma Physics*, 82(5), Sept. 2016. ISSN 1469-7807. doi: 10.1017/s0022377816000763. URL http://dx.doi.org/10.1017/S0022377816000763.

J. Pétri and J. G. Kirk. Growth rates of the weibel and tearing mode instabilities in a relativistic pair plasma. *Plasma Physics and Controlled Fusion*, 49(11):1885, oct 2007. doi: 10.1088/0741-3335/49/11/009. URL https://dx.doi.org/10.1088/0741-3335/49/11/009.

N. Rea and D. De Grandis. Magnetars. *arXiv e-prints*, art. arXiv:2503.04442, Mar. 2025. doi: 10.48550/arXiv.2503.04442.

N. Rea, M. A. McLaughlin, B. M. Gaensler, P. O. Slane, L. Stella, S. P. Reynolds, M. Burgay, G. L. Israel, A. Possenti, and S. Chatterjee. Discovery of Extended X-Ray Emission Around the Highly Magnetic RRAT J1819-1458. *ApJ*, 703(1):L41–L45, Sept. 2009. doi: 10.1088/0004-637X/703/1/L41.

V. Richard-Romei and B. Cerutti. Enhanced particle acceleration in a pulsar wind interacting with a companion. *A&A*, 689:A251, Sept. 2024. doi: 10.1051/0004-6361/202450605.

V. Richard-Romei, B. Cerutti, A. Papitto, and R. La Placa. 3D particle-in-cell simulations of pulsar wind – disk interaction: application to the transitional millisecond pulsar PSR J1023+0038. 2026. in prep.

T. Robishaw and C. Heiles. *The Measurement of Polarization in Radio Astronomy*, page 127–158. WORLD SCIENTIFIC, May 2021. doi: 10.1142/9789811203770_0006. URL http://dx.doi.org/10.1142/9789811203770_0006.

A. C. Rodriguez. Spectroscopic detection of a 2.9-hour orbit in a long-period radio transient. *A&A*, 695:L8, Mar. 2025. doi: 10.1051/0004-6361/202553684.

F. Rohrlich. Dynamics of a charged particle. *Physical Review E*, 77(4), apr 2008. doi: 10.1103/physreve.77.046609.

M. M. Romanova, G. V. Ustyugova, A. V. Koldoba, and R. V. E. Lovelace. Magnetohydrodynamic Simulations of Disk-Magnetized Star Interactions in the Quiescent Regime: Funnel Flows and Angular Momentum Transport. *ApJ*, 578(1):420–438, Oct. 2002. doi: 10.1086/342464.

M. M. Romanova, O. D. Toropina, Y. M. Toropin, and R. V. E. Lovelace. Magnetohydrodynamic Simulations of Accretion onto a Star in the "Propeller" Regime. *ApJ*, 588(1): 400–407, May 2003a. doi: 10.1086/373990.

M. M. Romanova, G. V. Ustyugova, A. V. Koldoba, J. V. Wick, and R. V. E. Lovelace. Three-dimensional Simulations of Disk Accretion to an Inclined Dipole. I. Magnetospheric Flows at Different Θ. *ApJ*, 595(2):1009–1031, Oct. 2003b. doi: 10.1086/377514.

M. M. Romanova, A. K. Kulkarni, and R. V. E. Lovelace. Unstable Disk Accretion onto Magnetized Stars: First Global Three-dimensional Magnetohydrodynamic Simulations. *ApJ*, 673(2):L171, Feb. 2008. doi: 10.1086/527298.

M. M. Romanova, A. V. Koldoba, G. V. Ustyugova, A. A. Blinova, D. Lai, and R. V. E. Lovelace. 3D MHD simulations of accretion on to stars with tilted magnetic and rotational axes. *MNRAS*, 506(1):372–384, Sept. 2021. doi: 10.1093/mnras/stab1724.

M. Ronchi. Population synthesis of galactic pulsars with machine learning, 2024. URL https://arxiv.org/abs/2404.15953.

M. Ronchi, N. Rea, V. Graber, and N. Hurley-Walker. Long-period pulsars as possible outcomes of supernova fallback accretion. *The Astrophysical Journal*, 934(2):184, Aug. 2022. ISSN 1538-4357. doi: 10.3847/1538-4357/ac7cec. URL http://dx.doi.org/10.3847/1538-4357/ac7cec.

J. Roy, P. S. Ray, B. Bhattacharyya, B. Stappers, J. N. Chengalur, J. Deneva, F. Camilo, T. J. Johnson, M. Wolff, J. W. T. Hessels, C. G. Bassa, E. F. Keane, E. C. Ferrara, A. K. Harding, and K. S. Wood. Discovery of Psr J1227-4853: A Transition from a Low-mass X-Ray Binary to a Redback Millisecond Pulsar. *ApJ*, 800(1):L12, Feb. 2015. doi: 10.1088/2041-8205/800/1/L12.

M. Ruderman. Matter in superstrong magnetic fields. *Symposium - International Astronomical Union*, 53:117–131, 1974. doi: 10.1017/S0074180900099964.

M. A. Ruderman and P. G. Sutherland. Theory of pulsars: polar gaps, sparks, and coherent microwave radiation. *ApJ*, 196:51–72, Feb. 1975. doi: 10.1086/153393.

G. B. Rybicki and A. P. Lightman. *Radiative processes in astrophysics*. 1979.

K. Saitou, M. Tsujimoto, K. Ebisawa, and M. Ishida. Suzaku x-ray study of an anomalous source xss j12270–4859. *Publications of the Astronomical Society of Japan*, 61(4):L13–L16, Aug. 2009. ISSN 0004-6264. doi: 10.1093/pasj/61.4.l13. URL http://dx.doi.org/10.1093/pasj/61.4.L13.

V. F. Shvartsman. Neutron Stars in Binary Systems Should Not Be Pulsars. *AZh*, 48:438, Apr. 1971.

L. Sironi and B. Cerutti. Particle Acceleration in Pulsar Wind Nebulae: PIC Modelling. In D. F. Torres, editor, *Modelling Pulsar Wind Nebulae*, volume 446 of *Astrophysics and Space Science Library*, page 247, Jan. 2017. doi: 10.1007/978-3-319-63031-1_11.

L. Sironi and A. Spitkovsky. Relativistic Reconnection: An Efficient Source of Non-thermal Particles. *ApJ*, 783(1):L21, Mar. 2014. doi: 10.1088/2041-8205/783/1/L21.

L. Sironi, D. A. Uzdensky, and D. Giannios. Relativistic magnetic reconnection in astrophysical plasmas: A powerful mechanism of nonthermal emission. *Annual Review of Astronomy and Astrophysics*, 63(1):127–178, Aug. 2025. ISSN 1545-4282. doi: 10.1146/annurev-astro-020325-115713. URL http://dx.doi.org/10.1146/annurev-astro-020325-115713.

D. Skiathas, C. Kalapotharakos, Z. Wadiasingh, D. Kazanas, A. K. Harding, and P. T. Kolbeck. Magnetosphere Evolution and Precursor-Driven Electromagnetic Signals in Merging Binary Neutron Stars. *arXiv e-prints*, art. arXiv:2503.19884, Mar. 2025. doi: 10.48550/arXiv.2503.19884.

D. A. Smith et al. The third fermi large area telescope catalog of gamma-ray pulsars. *The Astrophysical Journal*, 958(2):191, Nov. 2023. ISSN 1538-4357. doi: 10.3847/1538-4357/acee67. URL http://dx.doi.org/10.3847/1538-4357/acee67.

A. Spitkovsky. Time-dependent force-free pulsar magnetospheres: Axisymmetric and oblique rotators. *The Astrophysical Journal*, 648(1):L51–L54, aug 2006. doi: 10.1086/507518. URL https://doi.org/10.1086%2F507518.

A. Spitkovsky and J. Arons. Simulations of Pulsar Wind Formation. In P. O. Slane and B. M. Gaensler, editors, *Neutron Stars in Supernova Remnants*, volume 271 of *Astronomical Society of the Pacific Conference Series*, page 81, Jan. 2002. doi: 10.48550/arXiv.astro-ph/0201360.

H. Spohn. The critical manifold of the lorentz-dirac equation. *Europhysics Letters (EPL)*, 50 (3):287–292, may 2000. doi: 10.1209/epl/i2000-00268-x.

D. H. Staelin and E. C. Reifenstein, III. Pulsating Radio Sources near the Crab Nebula. *Science*, 162(3861):1481–1483, Dec. 1968. doi: 10.1126/science.162.3861.1481.

B. W. Stappers, M. Bailes, A. G. Lyne, R. N. Manchester, N. D'Amico, T. M. Tauris, D. R. Lorimer, S. Johnston, and J. S. Sandhu. Probing the Eclipse Region of a Binary Millisecond Pulsar. *ApJ*, 465:L119, July 1996. doi: 10.1086/310148.

B. W. Stappers, A. M. Archibald, J. W. T. Hessels, C. G. Bassa, S. Bogdanov, G. H. Janssen, V. M. Kaspi, A. G. Lyne, A. Patruno, S. Tendulkar, A. B. Hill, and T. Glanzman. A State Change in the Missing Link Binary Pulsar System PSR J1023+0038. *ApJ*, 790(1):39, July 2014. doi: 10.1088/0004-637X/790/1/39.

R. Stein et al. A tidal disruption event coincident with a high-energy neutrino. *Nature Astronomy*, 5(5):510–518, Feb. 2021. ISSN 2397-3366. doi: 10.1038/s41550-020-01295-8. URL http://dx.doi.org/10.1038/s41550-020-01295-8.

J. Strader, K.-L. Li, L. Chomiuk, C. O. Heinke, A. Udalski, M. Peacock, L. Shishkovsky, and E. Tremou. A new $\gamma-$ray loud, eclipsing low-mass x-ray binary. *The Astrophysical Journal*, 831(1):89, Oct. 2016. ISSN 1538-4357. doi: 10.3847/0004-637x/831/1/89. URL http://dx.doi.org/10.3847/0004-637X/831/1/89.

J. Strader, S. J. Swihart, R. Urquhart, L. Chomiuk, E. Aydi, A. Bahramian, A. Kawash, K. V. Sokolovsky, E. Tremou, and A. Udalski. Multiwavelength evidence for a new flare-mode transitional millisecond pulsar. *The Astrophysical Journal*, 917(2):69, Aug. 2021. ISSN 1538-4357. doi: 10.3847/1538-4357/ac0b47. URL http://dx.doi.org/10.3847/1538-4357/ac0b47.

J. G. Stringer, R. P. Breton, C. J. Clark, G. Voisin, M. R. Kennedy, D. Mata Sánchez, T. Shahbaz, V. S. Dhillon, M. van Kerkwijk, and T. R. Marsh. Optical photometry of two transitional millisecond pulsars in the radio pulsar state. *Monthly Notices of the Royal Astronomical Society*, 507(2):2174–2191, 07 2021. ISSN 0035-8711. doi: 10.1093/mnras/stab2167. URL https://doi.org/10.1093/mnras/stab2167.

P. A. Sturrock. A Model of Pulsars. *ApJ*, 164:529, Mar. 1971. doi: 10.1086/150865.

P. A. Sweet. The Neutral Point Theory of Solar Flares. In B. Lehnert, editor, *Electromagnetic Phenomena in Cosmical Physics*, volume 6 of *IAU Symposium*, page 123, Jan. 1958.

P. Szkody, O. Fraser, N. Silvestri, A. Henden, S. F. Anderson, J. Frith, B. Lawton, E. Owens, S. Raymond, G. Schmidt, M. Wolfe, J. Bochanski, K. Covey, H. Harris, S. Hawley, G. R.

Knapp, B. Margon, W. Voges, L. Walkowicz, J. Brinkmann, and D. Q. Lamb. Cataclysmic Variables from the Sloan Digital Sky Survey. II. The Second Year. *AJ*, 126(3):1499–1514, Sept. 2003. doi: 10.1086/377346.

S. Takasao, K. Tomida, K. Iwasaki, and T. K. Suzuki. A Three-dimensional Simulation of a Magnetized Accretion Disk: Fast Funnel Accretion onto a Weakly Magnetized Star. *ApJ*, 857(1):4, Apr. 2018. doi: 10.3847/1538-4357/aab5b3.

M. Tamburini, F. Pegoraro, A. Di Piazza, C. H. Keitel, and A. Macchi. Radiation reaction effects on radiation pressure acceleration. *New Journal of Physics*, 12(12):123005, Dec. 2010. doi: 10.1088/1367-2630/12/12/123005.

A. Tchekhovskoy, A. Spitkovsky, and J. G. Li. Time-dependent 3D magnetohydrodynamic pulsar magnetospheres: oblique rotators. *MNRAS*, 435:L1–L5, Aug. 2013. doi: 10.1093/mnrasl/slt076.

T. Thongmeearkom, C. J. Clark, R. P. Breton, M. Burgay, L. Nieder, P. C. C. Freire, E. D. Barr, B. W. Stappers, S. M. Ransom, S. Buchner, F. Calore, D. J. Champion, I. Cognard, J. M. Grießmeier, M. Kramer, L. Levin, P. V. Padmanabh, A. Possenti, A. Ridolfi, V. V. Krishnan, and L. Vleeschower. A targeted radio pulsar survey of redback candidates with MeerKAT. *MNRAS*, 530(4):4676–4694, June 2024. doi: 10.1093/mnras/stae787.

A. N. Timokhin. On the force-free magnetosphere of an aligned rotator. *MNRAS*, 368(3):1055–1072, May 2006. doi: 10.1111/j.1365-2966.2006.10192.x.

A. N. Timokhin. Time-dependent pair cascades in magnetospheres of neutron stars - I. Dynamics of the polar cap cascade with no particle supply from the neutron star surface. *MNRAS*, 408(4):2092–2114, Nov. 2010. doi: 10.1111/j.1365-2966.2010.17286.x.

A. N. Timokhin and J. Arons. Current flow and pair creation at low altitude in rotation-powered pulsars' force-free magnetospheres: space charge limited flow. *MNRAS*, 429(1):20–54, Feb. 2013. doi: 10.1093/mnras/sts298.

A. N. Timokhin and A. K. Harding. On the Maximum Pair Multiplicity of Pulsar Cascades. *ApJ*, 871(1):12, Jan. 2019. doi: 10.3847/1538-4357/aaf050.

H. Tong. Discussions on the Nature of GLEAM-X J162759.5-523504.3. *ApJ*, 943(1):3, Jan. 2023. doi: 10.3847/1538-4357/aca7fa.

D. F. Torres, L. Ji, J. Li, A. Papitto, N. Rea, E. de Oña Wilhelmi, and S. Zhang. A Search for Transitions between States in Redbacks and Black Widows Using Seven Years of Fermi-LAT Observations. *ApJ*, 836(1):68, Feb. 2017. doi: 10.3847/1538-4357/836/1/68.

R. Torres, T. Grismayer, F. Cruz, R. Fonseca, and L. Silva. Osiris-gr: General relativistic activation of the polar cap of a compact neutron star. *New Astronomy*, 112:102261, Nov. 2024. ISSN 1384-1076. doi: 10.1016/j.newast.2024.102261. URL http://dx.doi.org/10.1016/j.newast.2024.102261.

M. Turchetta, B. Sen, J. A. Simpson, M. Linares, R. P. Breton, J. Casares, M. R. Kennedy, and T. Shahbaz. Discovery of the variable optical counterpart of the redback pulsar psr j2055+1545. *Monthly Notices of the Royal Astronomical Society*, 538(1):380–394, Feb. 2025. ISSN 1365-2966. doi: 10.1093/mnras/staf293. URL http://dx.doi.org/10.1093/mnras/staf293.

D. A. Uzdensky and A. Spitkovsky. Physical Conditions in the Reconnection Layer in Pulsar Magnetospheres. *ApJ*, 780(1):3, Jan. 2014. doi: 10.1088/0004-637X/780/1/3.

D. A. Uzdensky, N. F. Loureiro, and A. A. Schekochihin. Fast Magnetic Reconnection in the Plasmoid-Dominated Regime. *Phys. Rev. Lett.*, 105(23):235002, Dec. 2010. doi: 10.1103/PhysRevLett.105.235002.

M. P. van Haarlem et al. LOFAR: The LOw-Frequency ARray. *A&A*, 556:A2, Aug. 2013. doi: 10.1051/0004-6361/201220873.

A. Veledina, J. Nättilä, and A. M. Beloborodov. Pulsar Wind-heated Accretion Disk and the Origin of Modes in Transitional Millisecond Pulsar PSR J1023+0038. *ApJ*, 884(2):144, Oct. 2019. doi: 10.3847/1538-4357/ab44c6.

D. Viganò, A. Garcia-Garcia, J. A. Pons, C. Dehman, and V. Graber. Magneto-thermal evolution of neutron stars with coupled Ohmic, Hall and ambipolar effects via accurate finite-volume simulations. *Computer Physics Communications*, 265:108001, Aug. 2021. doi: 10.1016/j.cpc.2021.108001.

E. Vurgun, D. García-Senz, M. Linares, and K. Y. Ekşi. An energy approach to pulsar–disc interaction: disc stability and implications for transitional millisecond pulsars. *MNRAS*, 540(4):3625–3641, July 2025. doi: 10.1093/mnras/staf854.

Y. Wang, P. A. Uttarkar, R. M. Shannon, Y. W. J. Lee, D. Dobie, Z. Wang, K. W. Bannister, M. Caleb, A. T. Deller, M. Glowacki, J. N. Jahns-Schindler, T. Murphy, R. Anna-Thomas, N. D. R. Bhat, X. Deng, V. Gupta, A. Jaini, C. W. James, and J. Tuthill. The Discovery of a 41 s Radio Pulsar PSR J0311+1402 with ASKAP. *ApJ*, 982(2):L53, Apr. 2025. doi: 10.3847/2041-8213/adbe61.

Z. Wang, A. M. Archibald, J. R. Thorstensen, V. M. Kaspi, D. R. Lorimer, I. Stairs, and S. M. Ransom. SDSS J102347.6+003841: A Millisecond Radio Pulsar Binary That Had a Hot Disk During 2000-2001. *ApJ*, 703(2):2017–2023, Oct. 2009. doi: 10.1088/0004-637X/703/2/2017.

Z. Wang et al. Detection of x-ray emission from a bright long-period radio transient. *Nature*, 642(8068):583–586, May 2025. ISSN 1476-4687. doi: 10.1038/s41586-025-09077-w. URL http://dx.doi.org/10.1038/s41586-025-09077-w.

T. C. Weekes, M. F. Cawley, D. J. Fegan, K. G. Gibbs, A. M. Hillas, P. W. Kowk, R. C. Lamb, D. A. Lewis, D. Macomb, N. A. Porter, P. T. Reynolds, and G. Vacanti. Observation of TeV Gamma Rays from the Crab Nebula Using the Atmospheric Cerenkov Imaging Technique. *ApJ*, 342:379, July 1989. doi: 10.1086/167599.

G. R. Werner, D. A. Uzdensky, B. Cerutti, K. Nalewajko, and M. C. Begelman. The Extent of Power-law Energy Spectra in Collisionless Relativistic Magnetic Reconnection in Pair Plasmas. *ApJ*, 816(1):L8, Jan. 2016. doi: 10.3847/2041-8205/816/1/L8.

A. Wolszczan. Discovery of pulsar planets. *New A Rev.*, 56(1):2–8, Jan. 2012. doi: 10.1016/j.newar.2011.06.002.

D. G. Yakovlev, P. Haensel, G. Baym, and C. Pethick. Lev Landau and the concept of neutron stars. *Physics Uspekhi*, 56(3):289-295, Mar. 2013. doi: 10.3367/UFNe.0183.201303f.0307.

K. Yee. Numerical solution of initial boundary value problems involving maxwell's equations in isotropic media. *IEEE Transactions on Antennas and Propagation*, 14(3):302–307, May 1966. doi: 10.1109/TAP.1966.1138693.

C. Zanni and J. Ferreira. MHD simulations of accretion onto a dipolar magnetosphere. I. Accretion curtains and the disk-locking paradigm. *A&A*, 508(3):1117–1133, Dec. 2009. doi: 10.1051/0004-6361/200912879.

C. Zanni and J. Ferreira. MHD simulations of accretion onto a dipolar magnetosphere. II. Magnetospheric ejections and stellar spin-down. *A&A*, 550:A99, Feb. 2013. doi: 10.1051/0004-6361/201220168.

L. M. Zelenyi and V. V. Krasnoselskikh. Relativistic Modes of Tearing Instability in a Background Plasma. *Soviet Ast.*, 23:460, Aug. 1979.

S. Zenitani and M. Hoshino. The Generation of Nonthermal Particles in the Relativistic Magnetic Reconnection of Pair Plasmas. *ApJ*, 562(1):L63–L66, Nov. 2001. doi: 10.1086/337972.

H. Zhang, L. Sironi, and D. Giannios. Fast Particle Acceleration in Three-dimensional Relativistic Reconnection. *ApJ*, 922(2):261, Dec. 2021. doi: 10.3847/1538-4357/ac2e08.

D. A. Zyuzin, A. V. Karpova, A. Y. Kirichenko, Y. A. Shibanov, I. F. Bikmaev, M. R. Gilfanov, E. N. Irtuganov, M. A. Gorbachev, M. V. Suslikov, R. Karimov, M. M. Veryazov, and M. Pereyra. Is the Fermi source 4FGL J1824.2+1231 a transitional millisecond pulsar? *A&A*, 699:A21, July 2025. doi: 10.1051/0004-6361/202555365.

Résumé de la thèse en français

Chapitre 1 – Introduction

Une multitude de phénomènes à haute énergie est observée à travers l'Univers et joue un rôle central dans l'essor récent de l'astronomie multi-messagers, car ces phénomènes impliquent souvent plusieurs des quatre "messagers" provenant du cosmos : les signaux électromagnétiques, les rayons cosmiques (principalement des noyaux et des protons se propageant dans l'espace), les neutrinos et les ondes gravitationnelles. La plupart de ces phénomènes à haute énergie trouvent leur origine dans les environnements d'objets extrêmement compacts ou dans des processus qui leur sont associés. Les naines blanches, les étoiles à neutrons et les trous noirs constituent ce que l'on appelle des objets compacts, classés ici par ordre de compacité croissante, laquelle reflète l'intensité de leur champ gravitationnel. Tous représentent des stades ultimes de l'évolution stellaire, déterminés par la masse de l'étoile progénitrice avant son effondrement gravitationnel. Cependant, ils peuvent également se former par la fusion d'objets moins compacts : par exemple, la coalescence de deux naines blanches peut donner naissance à une étoile à neutrons, tandis que la fusion de naines blanches ou d'étoiles à neutrons peut conduire à la formation d'un trou noir. L'interaction entre les effets relativistes, les champs magnétiques intenses et la rotation rapide engendre la formation des magnétosphères relativistes autour des objets compacts. Ces magnétosphères abritent le lancement d'écoulements de plasma fortement magnétisés et relativistes (comme des vents relativistes ou des jets collimatés), la création de paires électron-positron, ainsi que l'accélération efficace de particules de différentes espèces (ions, électrons, positrons et neutrinos), ce qui conduit à l'émission d'un rayonnement électromagnétique non thermique. Les étoiles à neutrons combinent naturellement tous ces ingrédients et constituent ainsi les environnements de référence pour de telles magnétosphères. Les naines blanches, en revanche, peuvent posséder des champs magnétiques intenses, mais ceux-ci sont généralement plus faibles que ceux des étoiles à neutrons, et leur rotation plus lente engendre des magnétosphères essentiellement non relativistes. Les trous noirs, pour leur part, ne possèdent pas de champ magnétique intrinsèque ; cependant, ils peuvent développer une magnétosphère relativiste induite lorsqu'ils sont plongés dans un champ magnétique et un plasma externes,fournis par exemple par un disque d'accrétion ou un vent relativiste.

Les phénomènes de haute énergie impliquant des magnétosphères relativistes peuvent être classés en trois catégories majeures. Les phénomènes les plus évidents sont ceux induits par des processus purement magnétosphériques. Parmi les exemples les plus significatifs figurent les pulsars, c'est-à-dire des étoiles à neutrons en rotation rapide émettant un rayonnement pulsé périodique et produisant de puissants vents relativistes. D'autres systèmes emblématiques de l'activité magnétosphérique sont les magnétars, des étoiles à neutrons dotées de champs magnétiques exceptionnellement intenses, capables de générer occasionnellement des éruptions géantes et des sursauts électromagnétiques (Coti Zelati et al., 2018). Les magnétars (et, dans une moindre mesure, les magnétosphères des pulsars) ont également été proposés comme sources possibles des sursauts radio rapides (Lorimer et al., 2007), des impulsions radio extrêmement énergétiques mais de très courte durée. Une classe émergente de transitoires

radio de longue période (Hurley-Walker et al., 2022, 2023) – des sources d'impulsions radio présentant des périodicités allant de quelques minutes à plusieurs heures, parfois accompagnées de contreparties à plus haute énergie (Anumarlapudi et al., 2025) – est très probablement associée à des pulsars, des magnétars ou des naines blanches, qu'ils soient isolés ou situés dans des systèmes binaires (Hurley-Walker et al., 2024; de Ruiter et al., 2025). L'accrétion peut également révéler, voire stimuler, l'activité magnétosphérique. Un exemple frappant en est fourni par les noyaux actifs de galaxies, correspondant à des trous noirs supermassifs accrétant de la matière au centre des galaxies. Ces objets constituent les sources persistantes de rayonnement électromagnétique les plus lumineuses de l'Univers. Certaines de ces magnétosphères de trous noirs engendrent des jets relativistes fortement collimatés (Blandford and Znajek, 1977), appelés blazars lorsque leur axe est orienté vers la Terre. De plus, les événements de rupture par effet de marée, caractérisés par la destruction d'étoiles ou de naines blanches par des trous noirs supermassifs, associent une accrétion transitoire à une activité magnétosphérique, pouvant parfois aboutir à l'éjection de jets relativistes. Enfin, les binaires X, composées d'une étoile donneuse et d'un objet compact accrétant, émettent un rayonnement X intense alimenté par l'accrétion et gouverné par la magnétosphère de l'accréteur. Les binaires X englobent une grande diversité de phénomènes, parmi lesquels figurent les pulsars milliseconde transitionnels (Papitto and Martino, 2021). L'effondrement gravitationnel et la coalescence d'objets compacts constituent une autre catégorie de processus influencés par les magnétosphères. Les supernovae à effondrement de cœur, explosions stellaires puissantes résultant de l'effondrement du cœur d'une étoile massive, incluent les supernovae magnéto-rotationnelles (Akiyama et al., 2003) et les supernovae alimentées par un magnétar (Kasen and Bildsten, 2010), toutes deux pouvant être fortement influencées par les magnétosphères relativistes impliquées. Selon le scénario bien établi du collapsar (MacFadyen and Woosley, 1999), un sous-ensemble de supernovae à effondrement de cœur conduit à la formation d'un trou noir entouré d'un disque d'accrétion, capable d'alimenter des jets relativistes par activité magnétosphérique, produisant ainsi des sursauts gamma longs. De manière similaire, les fusions d'objets compacts engendrent des ondes gravitationnelles et des signaux électromagnétiques post-coalescence, incluant des sursauts gamma courts. Les fusions impliquant au moins une étoile à neutrons et donnant naissance à un trou noir peuvent générer des magnétosphères transitoires qui s'éteignent progressivement, comme l'ont montré Bransgrove et al. (2021). Des émissions électromagnétiques précurseures, résultant de l'interaction des magnétosphères binaires, sont également prédites, bien qu'elles n'aient pas encore été observées (Most and Philippov, 2020, 2023; Carrasco and Shibata, 2020; Carrasco et al., 2021). De plus, plusieurs des phénomènes évoqués ci-dessus sont à l'origine de l'accélération de neutrinos de haute énergie et de rayons cosmiques de très ou d'ultra-haute énergie. Par conséquent, la description de ces phénomènes à haute énergie et des processus qui leur sont associés requiert une compréhension approfondie des environnements d'objets compacts. Au-delà du domaine de l'astrophysique des hautes énergies, ces systèmes constituent d'excellents laboratoires pour l'étude de la physique extrême, permettant d'explorer entre autres la gravité forte, les plasmas relativistes et hautement magnétisés, ce qui souligne leur importance pour de nombreux domaines théoriques de la physique. Alors que les observations astrophysiques des siècles passés étaient principalement limitées aux signaux électromagnétiques – d'abord dans le domaine optique, puis progressivement étendues à l'ensemble du spectre multi-longueurs d'onde (radio, infrarouge, ultraviolet, rayons X et rayons gamma) – le XXIe siècle a vu l'émergence de l'astronomie multi-messagers, dans laquelle les instruments peuvent observer et combiner différents messagers issus d'un même événement astrophysique. Au cours des deux dernières décennies, les premières détections simultanées de plusieurs messagers provenant d'un seul événement ont marqué un tournant : l'événement d'ondes gravitationnelles GW170817 (Abbott et al., 2017), accompagné d'un rayonnement électromagnétique, ou encore l'association d'un neutrino de haute énergie avec le blazar TXS 0506+056 (IceCube Collaboration et al.,

2018). Cette nouvelle ère a été rendue possible non seulement par le développement de détecteurs dédiés aux rayons cosmiques, aux neutrinos et aux ondes gravitationnelles, mais aussi par les progrès majeurs de l'instrumentation dédiée à l'observation électromagnétique, tels que l'amélioration de la sensibilité, de la précision temporelle, de la couverture spectrale, de la résolution spatiale et spectrale, ainsi que des mesures de polarisation. Ces avancées observationnelles ont naturellement entraîné un besoin croissant d'études théoriques visant à interpréter les signaux détectés. Des progrès considérables en modélisation ont été accomplis au cours des dernières décennies, principalement grâce à la montée en puissance des approches numériques, qui permettent de surmonter les fortes limitations des méthodes purement analytiques. L'augmentation des capacités de calcul, portée par le développement rapide du calcul haute performance, combinée à la mise au point de méthodes numériques avancées – telles que la magnétohydrodynamique (MHD) relativiste, les codes particle-in-cell (PIC) ou encore les techniques de raffinement de maillage adaptatif – a rendu possible l'étude de problèmes de plus en plus complexes, tridimensionnels, non linéaires, relativistes et multi-échelles. En conséquence, les simulations numériques sont devenues un outil prédominant tant pour la prédiction que pour l'interprétation des observations astrophysiques. Comme il sera détaillé par la suite, les simulations PIC se sont progressivement imposées comme un outil essentiel en astrophysique des hautes énergies, car elles permettent de capturer les phénomènes non thermiques à l'origine de l'accélération des particules et du rayonnement de haute énergie, produisant ainsi les composantes les plus énergétiques des spectres observés.

Les magnétosphères de pulsars englobent un large éventail des phénomènes introduits précédemment et constituent le cas canonique des magnétosphères relativistes. Elles présentent un intérêt particulier, car elles combinent champs magnétiques extrêmes, rotation rapide et dynamique de plasma relativiste, en faisant des environnements privilégiés pour l'étude de processus fondamentaux tels que l'accélération des particules et le rayonnement électromagnétique, notamment à haute énergie. À ce jour, plus de 4000 pulsars ont été découverts. Bien qu'ils aient été initialement identifiés grâce à leurs pulsations radio, on a progressivement découvert que leur magnétosphère émettait sur l'ensemble du spectre électromagnétique. Les régions magnétosphériques responsables de l'émission diffèrent selon la fréquence observée, reflétant la diversité des processus physiques à l'origine du rayonnement. En effet, tandis que l'émission radio proviendrait principalement des régions de la calotte polaire, situées près de la surface de l'étoile (la feuille de courant constituant néanmoins une zone d'émission secondaire, comme décrit en détail au Chapitre 2), le rayonnement de haute énergie est émis majoritairement depuis les régions externes de la magnétosphère. Les pulsars se divisent en deux grandes catégories : d'une part, les pulsars jeunes, caractérisés par des périodes typiques d'environ 0,6 s et des champs magnétiques de l'ordre de 10^{12} G, souvent associés à des rémanents de supernova ; et d'autre part, les pulsars plus anciens, dits recyclés, présentant des périodes de l'ordre de la milliseconde et des champs d'environ 10^{8} G. Ces derniers ont vu leur rotation accélérée par l'accrétion de moment angulaire provenant d'une étoile compagnon. Les étoiles à neutrons sont également classées selon leur principale source de rayonnement : les pulsars peuvent être alimentés par la rotation (i.e., "rotation-powered pulsars"), par le champ magnétique, par l'accrétion ou par leur chaleur interne. La plupart des pulsars sont alimentés par leur rotation, leur émission résultant donc principalement de l'extraction d'énergie de rotation de l'étoile.

Cette thèse se concentre essentiellement sur les pulsars gamma. Tous les pulsars gamma découverts à ce jour sont alimentés par la rotation et peuvent être des pulsars jeunes ou des pulsars milliseconde, ces derniers étant le plus souvent situés dans des systèmes binaires. Bien que les pulsars aient été historiquement découverts via leur émission radio, la majeure partie de leur puissance rayonnée et émise sous forme de rayons gamma. En effet, entre 1 % et 100 % de leur puissance de ralentissement (spin-down power) est émise sous forme de rayons gamma au-dessus de 100 MeV, contre moins de 10^{-6} pour l'émission radio (Cerutti

et al., 2025). Modéliser cette émission gamma revient donc à comprendre les principaux processus dissipatifs qui gouvernent les phénomènes de haute énergie – tels que l'accélération des particules et leur rayonnement – tout en fournissant des informations précieuses sur la structure globale et la dynamique des magnétosphères de pulsars. Le télescope spatial Fermi, dédié aux rayons gamma et lancé en 2008, est le premier à effectuer chaque jour un relevé complet du ciel et demeure le télescope gamma le plus sensible en orbite. Il a révolutionné l'étude des sources de rayons gamma de haute énergie, en particulier celle des pulsars, faisant passer le nombre de pulsars gamma connus d'une douzaine à environ 300 (Troisième Catalogue de Pulsars ; Smith et al. 2023). Les pulsars gamma se retrouvent aussi bien parmi les pulsars jeunes que parmi les pulsars milliseconde.

Au cours des dernières décennies, des avancées considérables ont été réalisées dans la compréhension des magnétosphères de pulsars. Les simulations numériques ont complété les modèles théoriques existants, et l'avènement des méthodes PIC a apporté un éclairage nouveau sur ces systèmes. Ces simulations ont permis d'aborder des questions fondamentales relatives à la structure générale des magnétosphères de pulsars isolés, aux processus cinétiques en jeu et à l'origine du rayonnement de haute énergie. Plusieurs études ont modélisé des magnétosphères de pulsars isolés à l'aide de la méthode PIC, aussi bien dans des configurations alignées (Philippov and Spitkovsky, 2014; Chen and Beloborodov, 2014; Cerutti et al., 2015; Belyaev, 2015; Hu and Beloborodov, 2022) qu'inclinées (Philippov et al., 2015b; Cerutti et al., 2016; Kalapotharakos et al., 2018). Ces modèles ont montré qu'une fraction significative de la puissance de ralentissement est dissipée sous forme d'énergie cinétique, principalement via des processus de reconnexion magnétique, et ont identifié la feuille de courant dans le vent comme principal site d'accélération des particules. Ces simulations ont également reproduit les signatures radiatives des magnétosphères de pulsars, en tenant compte du rayonnement synchrotron émis par les particules accélérées s'échappant des couches de reconnexion (Cerutti et al., 2016; Philippov and Spitkovsky, 2018; Kalapotharakos et al., 2018). Cependant, une fraction importante des pulsars se trouve dans des systèmes binaires, en particulier parmi les pulsars milliseconde, or peu d'études se sont intéressées à l'interaction entre le vent d'un pulsar et son compagnon. Ces systèmes suscitent un grand intérêt au sein de la communauté astrophysique, car ils sont susceptibles de produire des signaux multi-messagers et d'abriter de nouveaux sites d'accélération de particules, pouvant engendrer des signatures radiatives inédites et une émission électromagnétique accrue par rapport aux magnétosphères de pulsars isolés. Prédire leurs propriétés observationnelles peut ainsi orienter les futures détections, aider à coordonner les campagnes multi-longueurs d'onde et multi-messagers, et, en définitive, fournir des informations essentielles sur la population de pulsars. De plus, ces systèmes offrent une occasion unique d'explorer l'environnement proche des pulsars, généralement inaccessible dans le cas des pulsars isolés. Dans cette thèse, nous cherchons à apporter un éclairage sur certains cas spécifiques de systèmes binaires impliquant des pulsars alimentés par la rotation. L'objectif est d'améliorer la compréhension de leur structure magnétosphérique, de leurs mécanismes et sites d'accélération des particules, ainsi que de leur émission électromagnétique.

Chapitre 2 – Théorie des magnétosphères de pulsars

Les étoiles à neutrons résultent de l'effondrement d'étoiles ordinaires de type O ou B massives (environ 8 à 25 $M_\odot$) en fin de vie. Elles représentent les résidus stellaires les plus compacts pouvant rester stables sous l'effet de la gravité, avec une compacité de $\Xi = 0.2$ pour une masse de $M = 1.4\,M_\odot$ et un rayon de $R = 10$ km. Bien que la structure interne des étoiles à neutrons demeure un domaine de recherche ouvert, il est généralement admis que, en première approximation, elles peuvent être considérées comme des conducteurs parfaits, en raison de l'abondance de charges libres en leur sein. Le tableau suivant résume les ordres de grandeur typiques des propriétés fondamentales des pulsars.

Ordres de grandeur typiques pour les pulsars.

Grandeur physique	**Symbole**	**Ordre de grandeur**
Masse de l'étoile à neutrons	$M_\star$	$1.4\ M_\odot$
Rayon de l'étoile à neutrons	$R_\star$	10^6 cm
Compacité	Ξ	0.2
Densité volumique moyenne	$\rho_\star = 3M_\star/(4\pi R_\star^3)$	$10^{14}\ \mathrm{g\,cm^{-3}}$
Température de surface	$T_\star$	10^6 K
Période de rotation	P	1 ms − 10 s
Dérivée de la période de rotation	$\dot{P}$	$10^{-21} - 10^{-12}$
Vitesse angulaire	$\Omega = 2\pi/P$	$0.6 - 6 \times 10^3\ \mathrm{rad\,s^{-1}}$
Champ magnétique de surface	$B_\star$	$10^8 - 10^{15}$ G
Rayon du cylindre de lumière	$R_{\mathrm{LC}} = c/\Omega$	$5 \times 10^6 - 5 \times 10^{10}$ cm
Moment d'inertie	I	$10^{45}\ \mathrm{g\,cm^2}$
Puissance de freinage	$\dot{E}_{\mathrm{rot}} = 4\pi^2 I \dot{P} P^{-3}$	$10^{31} - 10^{38}\ \mathrm{erg\,s^{-1}}$
Facteur de Lorentz typique des particules	γ	$10 - 10^7$
Densité typique de particules magnétosphériques	n	$10^{12} - 10^{17}\ \mathrm{cm^{-3}}$

Les magnétosphères de pulsars sont remplies de plasma présentant les caractéristiques suivantes : quasi-neutre, relativiste, sans collisions, majoritairement froid et dominé par le champ magnétique. Le paramètre de magnétisation, qui exprime le rapport entre l'énergie électromagnétique et l'énergie cinétique des particules, vérifie $\sigma \gg 1$ à l'intérieur des magnétosphères de pulsars. Dans le cadre de la MHD idéale, les perturbations du plasma se décomposent en trois modes d'ondes linéaires fondamentaux : les ondes d'Alfvén, les ondes magnétoacoustiques lentes et rapides. On peut diviser l'environnement d'un pulsar en trois parties principales.

La magnétosphère, ou zone du cylindre de lumière, s'étend jusqu'au rayon du cylindre de lumière $R_{\mathrm{LC}} = c/\Omega$, défini comme la distance à laquelle un objet en corotation autour de l'étoile atteindrait la vitesse de la lumière, c étant la vitesse de la lumière et Ω la vitesse angulaire du pulsar. Au-delà du cylindre de lumière se trouve le vent du pulsar, qui s'étend du cylindre de lumière jusqu'au choc terminal, où une onde de choc quasi stationnaire se forme lorsque le vent du pulsar rencontre le milieu environnant. Enfin, la nébuleuse de vent de pulsar occupe la région située au-delà du choc terminal. Les premiers modèles de magnétosphères de pulsars considèrent une étoile à neutrons en rotation, parfaitement conductrice, placée dans le vide et dotée d'un moment magnétique dipolaire centré et aligné avec l'axe de rotation. Ces modèles montrent qu'une forte force électrique agissant à la surface de l'étoile devrait extraire à la fois des électrons et des ions, remplissant ainsi la magnétosphère de plasma. En raison de cela, Goldreich and Julian (1969) ont développé un modèle de MHD idéale décrivant cette extraction de plasma, jusqu'à ce que la densité magnétosphérique devienne suffisante pour écranter le champ électrique parallèle. Cette densité est appelée la densité de Goldreich–Julian. Bien que, dans le modèle de Goldreich–Julian, la magnétosphère soit supposée remplie en tout point d'une quantité de charges nécessaire pour satisfaire $\boldsymbol{E} \cdot \boldsymbol{B} = 0$, la solution obtenue pour un rotateur aligné diffère des attentes initiales, notamment en raison de l'absence de création de paires. En effet, au lieu d'obtenir une magnétosphère uniformément remplie de plasma, une solution stationnaire se met en place, constituée d'une accumulation d'électrons au-dessus des pôles (le "dôme") et d'ions dans la région équatoriale (le "disque"). Cette solution séparée en charges est appelée électrosphère et est considérée comme un modèle possible pour les vieux pulsars inactifs (situés au-delà de la ligne de mort), bien qu'elle ne parvienne pas à reproduire le ralentissement et le comportement magnétosphérique observés pour des pulsars. Ces résultats suggèrent que la production de paires est à l'œuvre dans les magnétosphères de pulsars actifs. Cette hypothèse est confirmée par les observations et

les modèles de nébuleuses de vent de pulsar, qui indiquent que les magnétosphères devraient présenter des densités de plasma supérieures à la densité de Goldreich–Julian. Dans un tel cas, la quantité de charges attendue ne peut pas être entièrement extraite de la surface de l'étoile, et la création de paires devient alors nécessaire au sein de la magnétosphère. Bien que la présence de petites régions localisées où le champ électrique parallèle n'est pas écranté soit nécessaire à la production de paires, ce régime – fondé sur une magnétosphère remplie de plasma – est bien décrit par une limite fortement magnétisée de la MHD relativiste idéale, appelée "électrodynamique force-free" (force-free electrodynamics). Le modèle force-free s'est avéré être une bonne approximation dans le cas des magnétosphères de pulsars (voir Cerutti and Philippov 2017 et les références qui y sont citées). Cette limite repose sur l'hypothèse que la force de Lorentz domine tous les autres termes dans l'équation de conservation de la quantité de mouvement en MHD, ce qui conduit à la condition suivante: $\rho\boldsymbol{E} + \boldsymbol{J} \times \boldsymbol{B} = \boldsymbol{0}$, où ρ et $\boldsymbol{J}$ sont les densités de charge et de courant, respectivement. Cette limite impose donc un compromis concernant la densité du plasma (Komissarov, 2002) : le plasma doit être suffisamment dense pour écranter le champ électrique parallèle, mais assez diffus pour que son inertie puisse être négligée. Sous les hypothèses de stationnarité et d'axisymétrie, la magnétosphère force-free est gouvernée par la solution d'une équation différentielle partielle non linéaire, connue sous le nom d'"équation du pulsar". Michel (1973) a proposé une solution analytique à cette équation, appliquée à un monopôle en rotation, appelée la solution du "monopôle scindé" ("split monopole solution"). Il a été montré que cette solution fournit une bonne approximation du vent du pulsar au-delà du cylindre de lumière ($r \gg R_{\rm LC}$), c'est pourquoi elle continue d'être utilisée dans des études modernes (par exemple, voir le Chapitre 4). La solution présente une inversion des champs et des courants à travers l'équateur, donnant naissance à une feuille de courant qui transporte le courant de retour afin de garantir un courant net nul à travers la surface stellaire et, par conséquent, une charge stellaire globale neutre. Près de la surface de l'étoile, les lignes de champ magnétique sont presque radiales ; à proximité du rayon du cylindre de lumière, les composantes poloidale et toroïdale sont d'ordre comparable ; et loin dans le vent pulsar, le champ magnétique devient presque purement toroïdal. La solution du monopôle scindé donne lieu à un flux de Poynting sortant non nul, correspondant à la puissance de freinage extraite de l'étoile. En raison de la complexité de l'équation du pulsar, aucune solution analytique n'existe pour le cas d'un dipôle en rotation aligné ; toutefois, plusieurs solutions numériques ont été obtenues (Contopoulos et al., 1999; Contopoulos, 2005; Goodwin et al., 2004; Gruzinov, 2005; Timokhin, 2006). Ces simulations représentent la base de la structure des magnétosphères de pulsars actuellement acceptée. Des simulations force-free dépendentes du temps réalisées par la suite, pour des rotateurs alignés (Komissarov, 2006; McKinney, 2006; Spitkovsky, 2006; Parfrey et al., 2012) et obliques (Spitkovsky, 2006; Kalapotharakos and Contopoulos, 2009; Pétri, 2012; Tchekhovskoy et al., 2013), confirment la structure générale de la solution stationnaire et axisymétrique.

À l'intérieur de la feuille de courant, le champ magnétique s'annule (puisqu'il s'inverse de part et d'autre de la feuille) et l'approximation force-free, fondée sur la domination magnétique et la négligence de la pression et de l'inertie du plasma, n'est plus valable. De plus, la présence de cavités électriques (electric gaps) et la physique de la production de paires ne peuvent pas être prises en compte dans le cadre de l'approximation force-free. Cela motive le développement d'approches cinétiques (méthode Particle-in-Cell), capables de modéliser de manière auto-cohérente la magnétosphère globale tout en incluant l'accélération des particules, la création de paires et le rayonnement (Philippov and Spitkovsky, 2014; Chen and Beloborodov, 2014; Philippov et al., 2015a,b; Cerutti et al., 2015, 2016; Belyaev, 2015). Nous soulignons que des modèles globaux de magnétosphères sont essentiels, car le problème est intrinsèquement non-local.

Voici un résumé des principales caractéristiques des magnétosphères de pulsars, basé sur

l'état actuel des connaissances. La magnétosphère se caractérise par trois régions principales : (i) une zone de lignes de champ magnétique fermées autour de la région équatoriale, s'étendant jusqu'au rayon du cylindre de lumière et en corotation avec le pulsar, garantissant ainsi la corotation du plasma piégé ; (ii) une zone où les lignes de champ magnétique, ancrées près des pôles stellaires, s'étendent au-delà du cylindre de lumière et, du fait de la rotation, s'ouvrent à l'infini, entraînant des courants de volume directs ; (iii) une couche de courant en forme de Y, qui conduit les courants de retour, séparant les zones ouvertes et fermées à l'intérieur de $R_{\rm LC}$ et qui, au-delà de $R_{\rm LC}$, divise les lignes de champ ouvertes de polarité opposée à travers le plan équatorial. Alors que les dipôles alignés développent une feuille de courant équatoriale plane au-delà du cylindre de lumière, les moments magnétiques inclinés produisent une feuille de courant oscillant en θ autour du plan équatorial, avec une amplitude déterminée par l'angle d'inclinaison χ et une longueur d'onde de $2\pi R_{\rm LC}$.

Dans le plan équatorial, la feuille de courant prend la forme de deux branches en spirale séparant des bandes magnétiques de polarité alternée, d'où l'appellation "vent strié" ("striped wind"). Les simulations PIC ont montré que la feuille de courant au-delà du point Y est le site principal de dissipation du flux de Poynting via la reconnexion magnétique, ce qui constitue la principale source d'accélération de particules dans les magnétosphères de pulsars (Chen and Beloborodov, 2014; Philippov et al., 2015b). La reconnexion magnétique correspond à une réorganisation topologique du champ magnétique à grande échelle, provoquée par des processus microscopiques dans le plasma, en particulier par la rupture et la reconnexion de lignes de champ magnétique de polarité opposée. Environ 1 à 10% de la puissance de freinage est dissipée dans la feuille de courant (Cerutti et al., 2020), la majeure partie de la dissipation ayant lieu dans la région interne du vent, du point Y jusqu'à quelques $R_{\rm LC}$. La reconnexion magnétique est un mécanisme puissant d'accélération de particules non thermiques, produisant un spectre d'énergie en loi de puissance. La feuille de courant est instable à diverses instabilités, la principale étant l'instabilité de "tearing" et l'instabilité "drift-kink" (ou instabilité de type "flux-rope" en 3D). Les particules accélérées dans la feuille de courant émettent via des processus synchrotron. Leur temps de refroidissement est court, ce qui conduit à l'émission de photons de haute énergie et à l'alimentation de la majeure partie du rayonnement de haute-énergie provenant des magnétosphères de pulsars, avec des efficacités radiatives de l'ordre de $L_\gamma/L_{\rm spin-down} \sim 1-10\%$. La compréhension actuelle de la structure magnétosphérique permet d'expliquer l'émission pulsée observée dans les bandes GeV et TeV (Bai and Spitkovsky, 2010; Cerutti et al., 2016; Philippov and Spitkovsky, 2018; Hakobyan et al., 2023). Les pulsations radio observées simultanément aux pulsations à haute énergie sont également liées à la dissipation magnétique dans la feuille de courant, bien qu'attribuées à un mécanisme radiatif différent (Uzdensky and Spitkovsky, 2014; Lyubarsky, 2019; Philippov et al., 2019; Bransgrove et al., 2023).

Chapitre 3 – Méthodes numériques

La variété des processus physiques impliqués dans les magnétosphères relativistes, combinée à l'interaction complexe et non linéaire entre champs et particules, rend un traitement analytique extrêmement difficile, voire impossible. Seules des configurations très simplifiées ou très spécifiques peuvent être traitées analytiquement. Les autres problèmes, plus complexes, ne peuvent être abordés que numériquement. Le traitement numérique consiste à discrétiser le temps et l'espace et à itérer dans le temps pour approximer la solution des équations différentielles à chaque pas de temps, en se basant sur la solution au pas de temps précédent. En utilisant des ressources informatiques capables de gérer un très grand nombre de pas de temps et de points de grille, il est possible, à condition que les critères de stabilité et de convergence soient respectés, de construire des modèles représentatifs (c'est-à-dire des "simulations") de magnétosphères relativistes. Pour les modèles de plasma, deux approches principales sont

couramment employées : les simulations magnétohydrodynamiques (MHD) ou les simulations force-free, qui traitent le plasma comme un fluide, ou bien les simulations cinétiques, qui modélisent la dynamique des particules individuelles et leurs interactions via le champ électromagnétique. Les approches MHD ont été employées avant les approches cinétiques, car elles étaient beaucoup moins exigeantes en termes de calcul et se sont néanmoins révélées très instructives pour reproduire la structure macroscopique des magnétosphères relativistes. Par exemple, elles permettent d'estimer l'énergie de rotation extraite des pulsars et convertie en flux de Poynting sortant. Cependant, elles ne permettent pas de saisir les processus microphysiques à l'œuvre, responsables de l'accélération des particules, de la création de paires et du rayonnement non thermique. En particulier, elles ne permettent pas d'estimer la fraction de l'énergie de freinage convertie en rayonnement de haute énergie. En revanche, les simulations cinétiques sont particulièrement adaptées aux plasmas non-collisionnels qui peuplent les magnétosphères relativistes, car elles permettent de capturer de manière auto-cohérente la dynamique de la magnétosphère ainsi que les processus liés à l'accélération des particules et au rayonnement, qui opèrent à des échelles microscopiques (c'est-à-dire l'épaiseur de peau, le rayon de Larmor et les échelles de refroidissement), appelées "échelles cinétiques". L'évolution d'un plasma non-collisionnel est régie, pour chaque espèce, par l'équation de Vlasov. Les approches cinétiques numériques consistent soit à résoudre directement l'équation de Vlasov (codes de type Vlasov), soit à la résoudre indirectement par une approximation particulaire, en échantillonnant la fonction de distribution avec un ensemble de "macro-particules" (codes Particle-in-Cell). Les codes de type Vlasov sont des solveurs de l'équation de Vlasov basés sur une grille, dans lesquels la fonction de distribution des particules évolue sur une grille d'espace des phases. Plusieurs schémas numériques peuvent être employés à cette fin, notamment les méthodes spectrales, les méthodes conservatrices en volumes finis ou en différences finies, et les méthodes semi-Lagrangiennes (voir Filbet and Sonnendrücker 2003 pour une revue). Bien que les codes Vlasov présentent un bruit numérique plus faible que les méthodes particulaires, car ils n'échantillonnent pas le plasma avec des macro-particules, la nature six-dimensionnelle du problème (trois dimensions spatiales plus trois dimensions pour l'impulsion) conduit à un coût en calcul et en mémoire extrêmement élevé pour des systèmes aussi grands que les magnétosphères, en particulier en 2D ou 3D. Par conséquent, les méthodes basées sur les particules sont beaucoup plus couramment utilisées. Parmi ces approches particulaires, la méthode Particle-in-Cell (PIC) est de loin la plus largement employée en astrophysique.

L'essence de l'approche PIC consiste à représenter les macro-particules dans un espace des phases continu (approche lagrangienne) tout en calculant les moments de la distribution (densités de charge et courants) et les champs électromagnétiques sur une grille (approche eulérienne). Cela permet de réduire drastiquement le coût numérique des interactions. La méthode PIC repose sur trois étapes numériques principales effectuées à chaque pas de temps : (i) la résolution de l'équation de Newton pour chaque particule afin d'obtenir sa nouvelle position dans l'espace des phases ; (ii) le dépôt des densités de charge et de courant sur la grille ; (iii) la résolution des équations de Maxwell pour faire évoluer les champs sur la grille. La contrainte de divergence nulle du champ magnétique est vérifiée en tout temps, à condition qu'elle soit respectée à $t = 0$ dans la simulation. En revanche, la loi de Gauss n'est pas automatiquement satisfaite par l'algorithme `Zeltron` présenté jusqu'ici, et la charge n'est pas conservée lorsqu'elle est déposée sur la grille. `Zeltron` corrige donc périodiquement le champ électrique via une méthode itérative de Gauss-Seidel. De plus, la reproduction des processus microphysiques du plasma nécessite que la longueur de Debye et la fréquence plasma soient résolues. Enfin, les codes PIC globaux conçus pour modéliser les magnétosphères relativistes doivent être parallélisés afin de traiter à la fois les grands domaines spatiaux et les longs temps d'intégration.

Le code existe en plusieurs versions ; dans cette thèse, nous nous concentrons sur les configurations conçues pour modéliser une magnétosphère de pulsar, à laquelle nous ajoutons

un compagnon différent dans chacun des chapitres suivants. Les simulations PIC globales de magnétosphères de pulsars doivent couvrir une énorme gamme d'échelles de longueur, allant des échelles cinétiques jusqu'aux dimensions macroscopiques du système. Il en est de même pour la gamme d'énergies à reproduire. Il est impossible d'atteindre de telles séparations d'échelle numériquement, ce qui nécessite de re-échelonner certains paramètres physiques clés, tels que le rayon de l'étoile à neutrons, l'intensité du champ magnétique et le rapport des masses des particules, afin de réduire la séparation des échelles de plusieurs ordres de grandeur. Cependant, la hiérarchie réaliste des échelles spatiales et énergétiques doit impérativement être préservée. La version du code utilisée pour la modélisation des pulsars emploie une grille sphérique et non cartésienne, car beaucoup mieux adaptée à cette application, le pulsar étant modélisé comme une sphère au centre du domaine de simulation.

Chapitre 4 – Interaction entre vent de pulsar et compagnon

Comme expliqué dans les chapitres précédents, d'importants progrès ont été réalisés au cours des dernières décennies dans notre compréhension des magnétosphères de pulsars isolés. Cependant, une fraction des pulsars galactiques se trouve dans des systèmes binaires (Lorimer, 2008; Breton, 2009). Alors que de nombreuses études ont exploré le couplage magnétique des étoiles à neutrons dans des systèmes binaires rapprochés (Hansen and Lyutikov, 2001; Palenzuela et al., 2013; Crinquand et al., 2019; Most and Philippov, 2020), bien moins nombreuses sont celles qui se sont intéressées aux interactions entre le vent du pulsar et son compagnon. À ce jour, les fondements de telles interactions demeurent mal compris. Dans ce travail, nous visons à modéliser une magnétosphère de pulsar inclinée, ainsi que les régions internes de son vent, interagissant avec un compagnon sphérique et non magnétisé, immergé dans le vent du pulsar. À notre connaissance, de tels systèmes n'ont encore jamais été modélisés à l'aide de simulations MHD ou PIC. Nous nous concentrons sur des compagnons dont le diamètre est inférieur à la demi-longueur d'onde du vent strié, excluant ainsi le régime des pulsars araignées. Cette configuration est destinée à représenter un cas générique pouvant s'appliquer à divers types de compagnons, parmi lesquels des planètes de pulsars, des astéroïdes, et des objets plus compacts tels que des étoiles à neutrons ou des naines blanches.

Nous utilisons la version 2.5D du code électromagnétique relativiste `Zeltron` (Cerutti et al., 2013; Cerutti and Werner, 2019), implémentée en coordonnées sphériques et restreinte au plan équatorial (Cerutti et al., 2015, 2016). Le domaine de calcul est constitué d'un disque comportant (4096×4096) cellules. Les particules sont confinées au plan $r\phi$, tandis que les trois composantes spatiales des champs électromagnétiques et des vitesses particulaires sont conservées. La surface de l'étoile, $r = r_\star$, définit la limite interne du domaine de calcul, qui s'étend radialement jusqu'à 24 $R_{\rm LC}$, le rayon du cylindre de lumière étant fixé à $R_{\rm LC} = 3\, r_\star$. L'étoile à neutrons centrale est modélisée comme un conducteur parfait sphérique en rotation à vitesse angulaire constante. Le champ magnétique est modélisé par un monopôle scindé (split monopole ; Michel 1973; Bogovalov 1999). Un compagnon est ajouté dans le vent du pulsar. Il est modélisé comme un conducteur parfait non magnétisé, sans rotation et sans vent intrinsèques. La séparation pulsar–compagnon est constante au cours du temps, et le compagnon est au repos dans la simulation (rotation orbitale nulle). Nous réalisons différentes simulations pour diverses séparations binaires et différents rayons du compagnon, afin d'étudier leur impact sur la réorganisation du vent et sur les processus cinétiques qui en résultent. En faisant varier la séparation du compagnon, nous pouvons sonder différentes régions du vent et, en particulier, explorer deux régimes distincts selon que le compagnon se situe à l'intérieur ou à l'extérieur du rayon magnétosonique rapide. Ce point correspond au rayon au-delà duquel la vitesse du vent dépasse la vitesse d'Alfvén (Michel, 1969; Kirk et al., 2009).

À titre de référence, pour évaluer les effets du compagnon et afin de s'assurer que notre

configuration reproduit les caractéristiques bien établies des pulsars isolés, nous réalisons une simulation d'une magnétosphère de pulsar isolé en utilisant des paramètres numériques identiques à ceux employés dans les simulations d'interaction avec le compagnon. Les cartes que l'on obtient du facteur de Lorentz moyen du vent en présence du compagnon montrent que, lorsque le compagnon est situé à l'intérieur de la surface magnétosonique rapide, le vent est décéléré dans l'ensemble du domaine, l'effet devenant plus isotrope et plus marqué pour des séparations orbitales plus faibles. En effet, dans ce régime, les perturbations se propagent plus rapidement que le vent sortant, affectant ainsi l'ensemble de la magnétosphère et empêchant la formation d'un choc. À l'inverse, lorsque le compagnon se trouve au-delà de la surface magnétosonique rapide, une chute brutale du facteur de Lorentz apparaît systématiquement le long d'un cône se formant au niveau du compagnon, marquant ainsi la formation d'un choc. Toutes les perturbations restent confinées à l'intérieur de ce cône, car elles sont entraînées par le vent du pulsar. Lorsqu'un choc se forme, nous parvenons à relier l'angle d'ouverture du cône au nombre de Mach alfvénique évalué au sommet du cône.

Indépendamment de la formation d'un choc, la présence du compagnon augmente l'accélération des particules, quelle que soit la séparation du compagnon. Ce phénomène résulte de la compression des lignes de champ magnétique atteignant la surface du compagnon au fur et à mesure de la progression radiale du vent, conduisant à une reconnexion forcée. En heurtant la surface du compagnon, la feuille de courant se fragmente autour de l'obstacle, et deux branches d'accélération de particules renforcée émergent et se propagent vers l'extérieur, formant deux flux radiaux distincts. Dans le régime sous-magnétosonique, bien qu'aucun choc ne se forme, on observe également deux directions privilégiées le long desquelles les particules accélérées se propagent. L'introduction du compagnon engendre une bosse localisée dans les spectres d'énergie des particules, dont l'énergie au pic varie en fonction de la séparation du compagnon.

Les pertes synchrotron représentent la contribution dominante à l'émission de haute énergie du système. L'ajout d'un compagnon introduit une nouvelle composante à l'émission synchrotron, qui domine largement l'émission totale. Nous reproduisons les courbes de lumière orbitales pour toutes les séparations et tailles du compagnon. Toutes les courbes de lumière présentent deux larges pics, correspondant aux instants où la ligne de visée de l'observateur croise les bords du cône creux d'émission. L'émission synchrotron totale intégrée sur une orbite décroît avec la séparation du compagnon ($d_{\rm comp}$), suivant une loi de puissance en $d_{\rm comp}^{-0.56}$. La séparation en phase orbitale entre les deux pics diminue également avec la séparation du compagnon, suivant une loi de puissance en $d_{\rm comp}^{-0.68}$. Nous montrons que cette loi d'échelle est la même que celle des inverses des facteurs de Lorentz ($1/\Gamma$) correspondants, calculés au sommet du cône de choc pour chaque simulation. De plus, nous montrons que le décalage angulaire entre le centre du cône creux d'émission et l'axe pulsar-compagnon, mesuré pour chaque séparation du compagnon, correspond au rapport des vitesses de dérive du vent ($V_\phi/V_r = R_{\rm LC}/r$) calculé à la position du compagnon à partir de la solution analytique du monopôle de Michel (1973).

Pour conclure, nous prédisons une nouvelle composante de haute énergie modulée orbitalement, qui apparaît lorsqu'un petit compagnon — tel qu'une planète, un astéroïde ou une étoile à neutrons faiblement magnétisée — orbite autour du pulsar. Cette émission devrait être principalement détectable dans les systèmes observés à proximité du plan orbital. Nous prédisons que la fréquence caractéristique de cette composante non thermique se situe dans le domaine des rayons gamma mous. Par conséquent, ces transitoires sont susceptibles d'être détectables uniquement à des distances galactiques.

Notre modèle prédit également des contreparties radio associées, bien qu'elles ne soient pas encore entièrement quantifiées. Nous montrons que la présence d'un compagnon déclenche une émission importante d'ondes magnétosoniques rapides (nettement plus importante que pour les pulsars isolés), principalement le long de deux directions orbitales spécifiques. Comme des

études précédentes ont montré que de telles ondes peuvent s'échapper de la magnétosphère sous forme d'émission radio cohérente, ce mécanisme combiné prédit des transitoires radio périodiques observables à deux phases orbitales distinctes. Ces contreparties radio périodiques galactiques seraient d'un intérêt particulier, notamment à la lumière des différentes classes de transitoires radio observés dont les origines restent incertaines (par exemple, les long-period radio transients, les rotation radio transients, ou encore les sursauts radio rapides périodes).

Chapitre 5 – Interaction entre vent de pulsar et disque

Depuis le début des années 2000, certaines binaires impliquant un pulsar milliseconde ont été observées en train d'alterner entre des états dont l'accrétion est la source d'énergie dominante et des états dont la rotation est la source d'énergie dominante, ces transitions dépendant des variations du taux d'accrétion de masse provenant du compagnon (étoile de faible masse). Cette nouvelle classe d'objets, appelée pulsars millisecondes transitionnels (tMSPs), fait le lien entre les pulsars millisecondes radio et ceux en phase d'accrétion (voir Jaodand et al. 2017; Campana and Di Salvo 2018; Papitto and Martino 2021 pour des revues). À ce jour, seules trois sources ont été confirmées comme des pulsars millisecondes transitionnels : PSR J1023+0038, IGR J18245−2452 et XSS J12270−4859. Depuis ces découvertes, de nombreuses recherches ont tenté d'élargir l'échantillon de tMSPs confirmés, menant à l'identification de plusieurs candidats potentiels. En plus des états alimentés par l'énergie de rotation rotation ou par l'accrétion, les tMSPs présentent également un troisième état intermédiaire, appelé état de disque sous-lumineux (sub-luminous disk state). Cet état doit son nom à la luminosité en rayons X qui le caractérise : plus élevée que celle observée pour les pulsars milliseconde alimentés par la rotation du pulsar (MSPs) et les pulsars milliseconde accrétants en quiescence (AMXPs), mais plus faible que celle atteinte lors des sursauts d'accrétion des AMXPs. Une caractéristique particulièrement remarquable de ces systèmes est leur transition rapide entre deux modes d'intensité en rayons X, appelés mode "haut" et mode "bas", parfois entrecoupés de brèves éruptions indépendantes. PSR J1023+0038 est observé dans le mode haut environ 80 % du temps. Dans cet état, des pulsations cohérentes en rayons X et dans le domaine optique, quasi simultanées, ont été détectées – en faisant le premier pulsar milliseconde jamais observé émettant des pulsations dans le domaine optique. Les profils de pulsations optiques et en rayons X sont similaires, présentant deux larges pics espacés d'environ 180° par période de rotation du pulsar. Les pulsations optiques sont en retard de 0,11 $P_{\rm spin}$ par rapport aux pulsations en rayons X. Les observations montrent que les pulsations optiques et X proviennent de la même région d'émission, et que leurs spectres pulsés peuvent être ajustés par la même loi de puissance. De plus, le spectre de l'émission polarisée correspond au spectre de l'émission pulsée, à la fois dans le domaine optique et en rayons X. L'ensemble de ces résultats observationnels pointe vers un mécanisme commun à l'origine de l'émission pulsée en rayons X et dans le domaine optique.

De nombreuses études ont tenté de mettre en évidence le mécanisme sous-jacent à l'origine de ce phénomène, que ce soit à travers des modèles phénoménologiques ou des simulations numériques. Cependant, aucune des approches employées n'est parvenue à reproduire simultanément la dynamique globale de l'interaction pulsar-disque et les processus cinétiques responsables de l'accélération des particules et de leur rayonnement. C'est donc la principale motivation de notre travail, ce qui justifie le recours aux simulations particle-in-cell (PIC).

Nous réalisons des simulations 3D à l'aide de la version espace-temps plat du code `Zeltron`. Le domaine de simulation est sphérique et s'étend jusqu'à $r_{\rm max} = 5.6\,R_{\rm LC}$, avec $R_{\rm LC} = 5\,r_\star$. L'étoile à neutrons est modélisée comme un conducteur parfait avec un champ magnétique dipolaire ancré à sa surface. Le disque est, quant à lui, modélisé comme un tore parfaitement conducteur. Nous effectuons différentes simulations pour plusieurs obliquités magnétiques du pulsar, tandis que le rapport d'aspect du disque est fixé à $h/R = 0.3$ pour toutes les

simulations.

L'ensemble de la magnétosphère est modifié et contraint de se reconfigurer sous l'effet de la présence du disque. Les lignes de champ magnétique sont forcées de se courber lorsqu'elles atteignent la surface du tore, de manière à le contourner. On observe une forte augmentation de la densité de plasma, celui-ci étant confiné par le bord interne du tore, notamment aux latitudes couvertes par celui-ci. Cela induit un développement vertical de la magnétosphère. Pour les pulsars dont l'obliquité magnétique est suffisamment élevée pour que leurs pôles magnétiques soient orientés vers la surface du disque (le seuil étant fixé par le rapport d'aspect du disque), certaines lignes de champ ouvertes, issues de la calotte polaire, semblent être périodiquement forcées à se refermer, avant de se rouvrir à nouveau. Ce comportement cyclique influence la dynamique du plasma et la libération d'énergie, entraînant une rétention et une éjection périodiques. L'intensité du champ magnétique est renforcée par la présence du disque. Nous observons également une augmentation de l'accélération des particules à la surface du disque. Enfin, la présence du disque entraîne une isotropisation du plasma. En conséquence de l'ensemble de ces effets, l'émission synchrotron est considérablement amplifiée, avec des facteurs d'amplification allant d'environ 5 à 12,5, selon l'obliquité magnétique du pulsar. La présence du disque modifie également la géométrie de la région d'émission, qui coïncide désormais avec la feuille de courant perturbée. Les courbes de lumière correspondantes sont donc altérées par rapport à celles des pulsars isolés. En effet, on observe une ou deux pics par période de rotation, selon l'obliquité magnétique du pulsar, pour un rapport d'aspect du disque donné. Ces pics sont considérablement élargis par rapport au cas de référence, sont espacés d'environ une demi-phase, et leurs amplitudes diffèrent légèrement. La fraction pulsée augmente avec l'énergie. Cependant, aucun décalage significatif n'apparaît entre les pics obtenus pour des bandes d'énergie différentes. De plus, on observe systématiquement une dépolarisation de la magnétosphère en présence du disque. Le degré de polarisation linéaire et la rotation de l'angle de polarisation augmentent avec l'énergie.

Nos résultats reproduisent avec succès, pour la première fois, les principales caractéristiques des courbes de lumière optiques et X observées pour PSR J1023+0038, telles que rapportées dans Papitto et al. (2019). Nous confirmons l'origine synchrotron de ce signal particulier et soutenons le scénario selon lequel les pulsations optiques et X sont produites par le rayonnement synchrotron émis lorsque le vent strié du pulsar interagit avec le bord interne du disque d'accrétion, situé à quelques rayons du cylindre de lumière du pulsar.

Chapitre 6 – Vers les simulations de binaires pulsar – trou noir

Les fusions d'étoiles à neutrons, incluant à la fois les binaires d'étoiles à neutrons et les systèmes trou noir–étoile à neutrons, sont considérées comme parmi les transitoires multi-messagers les plus fréquemment détectables (Burns et al., 2025). L'évolution des binaires d'étoiles à neutrons et des binaires trou noir–étoile à neutrons se déroule en trois phases principales : une phase spiralante, qui peut durer plusieurs millions d'années, au cours de laquelle les deux objets perdent progressivement de l'énergie et du moment angulaire par émission d'ondes gravitationnelles et éventuellement par émission électromagnétique ; une phase de fusion, d'une durée d'environ une milliseconde ; et une phase post-fusion pouvant durer jusqu'à plusieurs secondes, durant laquelle la matière résiduelle est soit éjectée, soit accrétée sur l'objet résultant de la fusion, et potentiellement accompagnée de contreparties électromagnétiques. Dans cette étude, nous nous concentrons sur le cas spécifique des binaires pulsar–trou noir. Deux tels systèmes ont été détectés en 2021 par ondes gravitationnelles, GW200105_162426 et GW200115_042309 (Abbott et al., 2021). Le Gravitational-Wave Transient Catalog 3 (GWTC-3) rapporte deux autres binaires trou noir–étoile à neutrons possibles, GW190426_152155 et GW190917_114630 (Abbott et al., 2023). Jusqu'à présent, les systèmes trou noir–étoile à neutrons n'ont été observés qu'au moment de leur fusion, les

détecteurs d'ondes gravitationnelles étant sensibles uniquement à la fin de la phase spiralante et à la coalescence, et aucune binaire trou noir–étoile à neutrons n'a encore été identifiée par détection électromagnétique. En particulier, à ce jour, aucune détection électromagnétique précédant la coalescence d'une fusion de binaire trou noir–étoile à neutrons n'a été confirmée. Les émissions électromagnétiques durant la phase spiralante ont été beaucoup moins étudiées que celles survenant après la fusion. Cependant, plusieurs travaux prédisent l'existence d'émissions électromagnétiques avant la coalescence (voir par exemple Fernández and Metzger 2016 et les références qui y sont citées pour des modèles analytiques ou semi-analytiques, ainsi que Palenzuela et al. 2013; Most and Philippov 2020; Carrasco and Shibata 2020; Skiathas et al. 2025 pour des modèles MHD). En effet, dans le cas de binaires rapprochées formées d'étoiles à neutrons ou de systèmes trou noir–étoile à neutrons, l'interaction magnétosphérique devrait être d'autant plus intense que le mouvement orbital s'ajoute à la rotation intrinsèque de chaque étoile. Néanmoins, de nombreuses incertitudes subsistent quant à la nature exacte de l'émission précurseure. La modélisation des signatures radiatives attendues présente un intérêt considérable. D'une part, elle peut fournir des informations précieuses sur la nature des objets compacts, notamment sur leurs propriétés physiques avant la coalescence et sur leurs vitesses de rotation, ainsi que sur l'événement de fusion lui-même, comme les énergies mises en jeu. D'autre part, une telle modélisation est essentielle pour localiser ces événements dans le ciel et pourrait potentiellement servir d'alerte précédant l'arrivée d'ondes gravitationnelles. Les trous noirs isolés étant dépourvus de champ magnétique intrinsèque, les simulations qui leur sont consacrées nécessitent inévitablement des hypothèses sur l'origine et la configuration initiale des lignes de champ magnétique. En revanche, les binaires trou noir–étoile à neutrons présentent un intérêt particulier du point de vue de la modélisation, car aucune hypothèse n'est requise concernant la géométrie initiale du système, l'origine du champ magnétique ou la nature du plasma primaire, ces éléments étant naturellement fournis par l'étoile à neutrons. En ce sens, une binaire pulsar–trou noir constitue un environnement bien contraint pour sonder les environs immédiats d'un trou noir.

Des études théoriques puis numériques (depuis les années 2010), se sont progressivement intéressées aux magnétosphères des binaires d'objets compacts, en particulier depuis l'essor des simulations numériques relativistes. Plusieurs approches magnétohydrodynamiques (MHD) ou force-free, incluant les effets de la relativité générale, ont instauré les bases des premiers modèles de binaires trou noir–étoile à neutrons. Dans l'ensemble de ces simulations MHD, le flux de Poynting est utilisé pour estimer la potentielle luminosité électromagnétique émise. Cependant, la prédiction de signaux détectables nécessite de modéliser les processus microphysiques responsables de la dissipation, en particulier dans les régions telles que les feuilles de courant. Afin de quantifier plus précisément le transfert d'énergie entre la puissance rotationnelle, la puissance électromagnétique et l'énergie cinétique du plasma magnétosphérique, et ainsi prédire l'émission électromagnétique non thermique, il est nécessaire de recourir aux simulation Particle-in-Cell (PIC).

Pour simuler une binaire trou noir–étoile à neutrons, nous utilisons deux configurations spécifiques du code `Zeltron` : une version en espace-temps plat en coordonnées sphériques présentant un pulsar central (Cerutti et al., 2013; Cerutti and Werner, 2019), et une version en relativité générale dans l'espace-temps de Kerr, incluant un trou noir central (Parfrey et al., 2019; Crinquand et al., 2021). Notre objectif est de fusionner ces deux configurations dans une même version du code. Plus précisément, nous visons à implémenter un pulsar dans le code GR `Zeltron` , en orbite autour du trou noir, de manière à préserver la métrique de Kerr en coordonnées sphériques. Cependant, le code incluant le pulsar est initialement structuré avec celui-ci positionné au centre de la grille sphérique. Par conséquent, le déplacement du pulsar hors du centre constitue une étape numérique majeure dans la modélisation de la binaire. Ce travail numérique est réalisé en utilisant la même version 2D équatoriale du code `Zeltron` que celle employée au Chapitre 4, et suppose donc un espace-temps plat. Le pulsar central

originel joue désormais le rôle du compagnon, servant de substitut au futur trou noir, tandis que le compagnon initial est remplacé par un pulsar.

Nous montrons deux cartes (champ magnétique et densité) correspondant à la meilleure solution obtenue à ce jour pour l'implémentation d'un pulsar excentré. Sur la carte de champ magnétique, nous retrouvons les deux branches en spirale de la feuille de courant ainsi que les bandes magnétiques de polarité alternée, centrées sur le pulsar décalé. Les cartes de densité présentent également les deux branches de la feuille de courant, comme attendu. Cependant, certains points méritent encore une étude plus approfondie, tels que l'absence de plasmoïdes clairement définis et la présence de branches secondaires dans la feuille de courant. Ces deux problèmes pourraient éventuellement être résolus en augmentant le nombre de particules par cellule et en améliorant la résolution spatiale.

Nous présentons plusieurs problèmes auxquels nous avons été confrontés. Certains sont liés à l'inclusion du pulsar à l'intérieur du domaine de simulation, contrairement au cas centré où la frontière interne du domaine correspond à la surface du pulsar. D'autres sont dus à la structure sphérique de la grille et à l'asymétrie systématique qui en résulte, entre les frontières du pulsar faisant face aux bords interne et externe du domaine de simulation. Nous rendons également compte des différentes approches d'injection de particules qui ont été testées.

Les prochaines étapes pour l'implémentation de la binaire incluent : (i) l'implémentation du pulsar excentré dans la version GR du code `Zeltron`, incluant un trou noir central ; (ii) une étude paramétrique de spin du trou noir ; (iii) l'implémentation du mouvement orbital du pulsar ; (iv) l'implémentation d'une séparation orbitale non stationnaire ; (v) une analyse en post-traitement de l'émission synchrotron résultante.

Conclusion

Tout au long de cette thèse, nous avons abordé le sujet fondamental mais complexe des magnétosphères relativistes dans les systèmes binaires, avec un pulsar comme source principale de l'interaction magnétosphérique. L'approche PIC s'est imposée comme un outil de choix pour la modélisation de tels systèmes, en raison de sa capacité à reproduire à la fois la dynamique globale et les processus cinétiques de la magnétosphère. Les environnements d'objets compacts isolés sont désormais de mieux en mieux contraints, bien que certaines questions clés restent non résolues à ce jour. Il est donc maintenant opportun d'étudier leur interaction avec un compagnon au sein d'un système binaire, configuration qui s'applique à une fraction significative des objets connus. Dans cette thèse, nous nous sommes concentrés sur la modélisation de l'émission électromagnétique générée par de tels systèmes, au moyen de simulations PIC.

Pour aborder ce problème, nous avons sélectionné trois cas d'étude illustrant la diversité des systèmes binaires impliquant un pulsar. Dans le Chapitre 4, nous avons présenté le premier modèle cinétique de l'interaction entre un vent de pulsar et un compagnon petit, sphérique et parfaitement conducteur, à l'aide de simulations PIC 2D dans le plan équatorial. Ce cas générique s'applique aux systèmes pulsar–planète ou pulsar–astéroïde et vise à servir de première étape vers la modélisation des binaires d'objets compacts, tels que les systèmes pulsar–naine blanche et pulsar–étoile à neutrons. Nous avons mis en évidence le rôle de la position du compagnon par rapport au point magnétosonique rapide dans la configuration globale de la magnétosphère et dans l'établissement d'un choc. De plus, nous avons montré que, quelle que soit la séparation du compagnon, l'impact de la feuille de courant sur la surface du compagnon entraîne une reconnexion magnétique forcée, se traduisant par une augmentation significative de l'accélération des particules. Les bras spiraux successifs de la feuille de courant, en frappant la surface du compagnon, se divisent de part et d'autre du corps sphérique, formant deux branches radiales dans le sillage du compagnon. Les particules ainsi accélérées émettent un rayonnement synchrotron sous la forme d'un cône creux de lumière modulé orbitalement, dont l'intensité et l'ouverture diminuent avec la séparation

orbitale et augmentent avec la taille du compagnon. Cette émission non thermique supplémentaire dépasse largement le flux synchrotron pulsé d'une magnétosphère de pulsar isolé et devrait se situer dans la gamme des rayons X durs ou gamma mous. De plus, nous avons prédit d'éventuelles contreparties radio associées, basées sur l'émission accrue de modes magnétosoniques rapides dans le sillage du compagnon et sur des études antérieures montrant que ces modes peuvent s'échapper sous forme d'ondes radio dans une magnétosphère de pulsar. Ces contreparties sont naturellement modulées par la période orbitale, fournissant ainsi un scénario plausible pour les transitoires radio de longue période (Hurley-Walker et al., 2022, 2023). Ce scénario est particulièrement pertinent au vu de la détection récente de contreparties à plus haute énergie pour ces transitoires radio, suggérant un mécanisme sous-jacent commun – ou du moins lié –, contrairement à la dichotomie habituelle entre les processus d'émission radio et gamma dans les magnétosphères de pulsars.

Le Chapitre 5 est consacré à l'étude de l'interaction entre un vent de pulsar et un disque, où l'accrétion est négligée. Nous avons montré que l'interaction du vent strié du pulsar avec le bord interne du disque induit une accumulation de plasma devant le bord interne, un renforcement du champ magnétique dû au confinement des lignes de champ, une isotropisation du plasma et une augmentation de l'accélération des particules. La combinaison de tous ces effets conduit à une augmentation significative de l'émission électromagnétique non thermique, via du rayonnement synchrotron. En particulier, les courbes de lumière modélisées présentent une composante continue bien plus élevée que dans le cas d'un pulsar isolé et un ou deux pics étendus par période de rotation du pulsar, selon l'obliquité magnétique du pulsar, pour un rapport hauteur sur rayon du disque donné. De plus, nous avons prédit une dépolarisation du signal par rapport aux magnétosphères de pulsars isolés, ainsi qu'une augmentation à la fois de la variation de l'angle de polarisation et du degré de polarisation avec l'énergie. Cette étude est particulièrement pertinente pour les pulsars millisecondes transitionnels, des systèmes possédant une étoile de la séquence principale comme compagnon, qui alternent entre un état où l'énergie de rotation domine l'émission et un état où l'énergie d'accrétion domine, et présentent un troisième état intermédiaire dans lequel un disque est présent sans preuve claire d'accrétion. Notre modèle reproduit avec succès, pour la première fois, les pulsations optiques et X des pulsars millisecondes transitionnels PSR J1023+0038. Il est également compatible avec les mesures de polarisation associées.

Enfin, nous avons initié le développement d'un dispositif numérique visant à modéliser les binaires pulsar–trou noir, dans le but de simuler leur émission électromagnétique précurseure à la coalescence (Chapitre 6). À cette fin, nous avons implémenté un pulsar excentré dans la version 2D sphérique en espace-temps plat du code `Zeltron`, initialement structurellement conçue avec le pulsar au centre du domaine de simulation. Le fait d'excentrer le pulsar au sein de la grille sphérique a introduit de nombreux défis numériques, principalement dûs à l'asymétrie de la grille au niveau de la surface du pulsar et à l'inclusion de l'intérieur stellaire dans le domaine de simulation. Nous avons donc réalisé plusieurs tests afin d'identifier les prescriptions les plus adaptées pour l'implémentation des champs électromagnétiques et de l'injection de particules. Nous montrons la meilleure solution obtenue à ce jour.

Ce travail de thèse ouvre la voie à plusieurs études futures. Nous détaillons en conclusion plusieurs de ces perspectives et présentons des résultats préliminaires concernant une modélisation dédiée à des systèmes binaires rapprochés, susceptibles d'émettre des transitoires radio de longue période.

Les observatoires à large champ et à haute sensibilité, actuels et à venir, vont considérablement augmenter le nombre de transitoires détectés. Dans ce contexte, nos modèles prédisent des signatures observationnelles spécifiques que ces futurs observatoires seront en mesure de sonder, offrant ainsi de nouvelles perspectives pour l'identification et la caractérisation des transitoires à haute énergie. Parallèlement, les développements numériques en cours, tels que le couplage des approches cinétique et fluide pour traiter la séparation d'échelles et le portage

des codes sur des architectures GPU, permettront l'émergence de modèles plus précis et plus économes en énergie appliqués aux phénomènes astrophysiques à haute énergie. Bien que les simulations numériques soient encore souvent utilisées pour traiter des questions théoriques, cette thèse m'a convaincue de leur rôle crucial comme complément à l'astrophysique observationnelle, tant pour formuler des prédictions que pour interpréter les données. En m'appuyant sur ces premiers résultats, j'espère contribuer à révéler et déchiffrer de nouveaux signaux cosmiques en tirant parti de la synergie entre observations et modélisation numérique.